Doctoral Dissertations   Graduate School

8-2022

Remote Human Vital Sign Monitoring Using Multiple-Input Multiple-Output Radar at Millimeter-Wave Frequencies

Toan Khanh Vo Dai
University of Tennessee, Knoxville, tvodai@vols.utk.edu

Follow this and additional works at: https://trace.tennessee.edu/utk_graddiss

Part of the Electromagnetics and Photonics Commons, and the Signal Processing Commons

Recommended Citation

To the Graduate Council:

I am submitting herewith a dissertation written by Toan Khanh Vo Dai entitled "Remote Human Vital Sign Monitoring Using Multiple-Input Multiple-Output Radar at Millimeter-Wave Frequencies." I have examined the final electronic copy of this dissertation for form and content and recommend that it be accepted in partial fulfillment of the requirements for the degree of Doctor of Philosophy, with a major in Electrical Engineering.

Ozlem Kilic, Major Professor

We have read this dissertation and recommend its acceptance:

Ozlem Kilic, Aly Fathy, Nicole McFarlane, Darren Maczka

Accepted for the Council:

Dixie L. Thompson

Vice Provost and Dean of the Graduate School

(Original signatures are on file with official student records.)

Remote Human Vital Sign Monitoring Using Multiple-Input Multiple-Output Radar at Millimeter-Wave Frequencies

A Dissertation Presented for the

Doctor of Philosophy

Degree

The University of Tennessee, Knoxville

Toan Khanh Vo Dai

August 2022

DEDICATION

To my parents, Loi Vo Dai and Tuyet Hoang, my beloved wife, Bich Tran, my sisters, Nhi Vo and Chi Vo whose unconditional love and supports have made this dissertation possible. To my dedicated teacher, Thong Nguyen Van, who always encourage me not to be afraid of math.

ACKNOWLEDGEMENTS

ABSTRACT

Non-contact respiration rate (RR) and heart rate (HR) monitoring using millimeter-wave (mmWave) radars has gained lots of attention for medical, civilian, and military applications. These mmWave radars are small, light, and portable which can be deployed to various places. To increase the accuracy of RR and HR detection, distributed multi-input multi-output (MIMO) radar can be used to acquire non-redundant information of vital sign signals from different perspectives because each MIMO channel has different fields of view with respect to the subject under test (SUT). This dissertation investigates the use of a Frequency Modulated Continuous Wave (FMCW) radar operating at 77-81 GHz for this application. Vital sign signal is first reconstructed with Arctangent Demodulation (AD) method using phase change's information collected by the radar due to chest wall displacement from respiration and heartbeat activities. Since the heartbeat signals can be corrupted and concealed by the third/fourth harmonics of the respiratory signals as well as random body motion (RBM) from the SUT, we have developed an automatic Heartbeat Template (HBT) extraction method based on Constellation Diagrams of the received signals. The extraction method will automatically spot and extract signals' portions that carry good amount of heartbeat signals which are not corrupted by the RBM. The extracted HBT is then used as an adapted wavelet for Continuous Wavelet Transform (CWT) to reduce interferences from respiratory harmonics and RBM, as well as magnify the heartbeat signals. As the nature of RBM is unpredictable, the extracted HBT may not completely cancel the interferences from RBM. Therefore, to provide better HR detection's accuracy, we have also developed a spectral-based HR selection method to gather frequency spectra of heartbeat signals from different MIMO channels. Based on this gathered spectral information, we can determine an accurate HR even if the heartbeat signals are significantly concealed by the RBM. To further improve the detection's accuracy of RR and HR, two deep learning (DL) frameworks are also investigated. First, a Convolutional Neural Network (CNN) has been proposed to optimally select clean MIMO channels and eliminate MIMO channels with low SNR of heartbeat signals. After that, a Multi-layer Perceptron (MLP) neural network (NN) is utilized to reconstruct the heartbeat signals that will be used to assess and select the final HR with high confidence.

TABLE OF CONTENTS

LIST OF TABLES

LIST OF FIGURES

CHAPTER I

INTRODUCTION

Vital signs can be monitored in a medical setting, such as by a doctor or nurse practitioner or at home using vital signs monitoring equipment. It is used to assess subjects' wellbeing, diagnose a medical issue, or even suggest lifestyle change. Monitoring vital signs is crucial to live longer and healthy life as it can indicate signs of an infection, early or prevent a misdiagnosis. Commonly, blood pressure, heart rate, respiration rate, and oxygen level are tracked. In this dissertation, we will only focus on respiration rate and heart rate detection, keeping in mind that a normal heart rate is between 60 and 100 beats per minute, and normal respiration rate for adults range from 12 to 20 breaths a minute [1].

1.1 Human Vital Sign Monitoring

Traditional human vital sign monitoring systems to capture respiratory rate (RR) and heart rate (HR) requires contact devices to subjects' chest. Figure 1.1 and Figure 1.2 illustrate some popular systems for measuring RR and HR from human subjects. For example, to measure the RR of the patients, belt sensors that wrap around patients' lower chests can be used which employ several sensors such as piezo-electric sensors [2], inductive sensors [3], capacitive sensors [4] and fiber optic sensors [5], etc. These systems measure the changes of pressure induced to the sensors by the chest movements during inhaling/exhaling periods. The pressure waveforms can then be used to estimated RR from the subjects under test (SUT). For HR measurement, multi-lead Electrocardiogram (ECG) devices shown in Figure 1.2 are usually used in hospitals or clinics facilities. These wearable systems, however, require contact with patients' chests and are not convenient under scenarios in which the patients have serious chest injury or when long-term
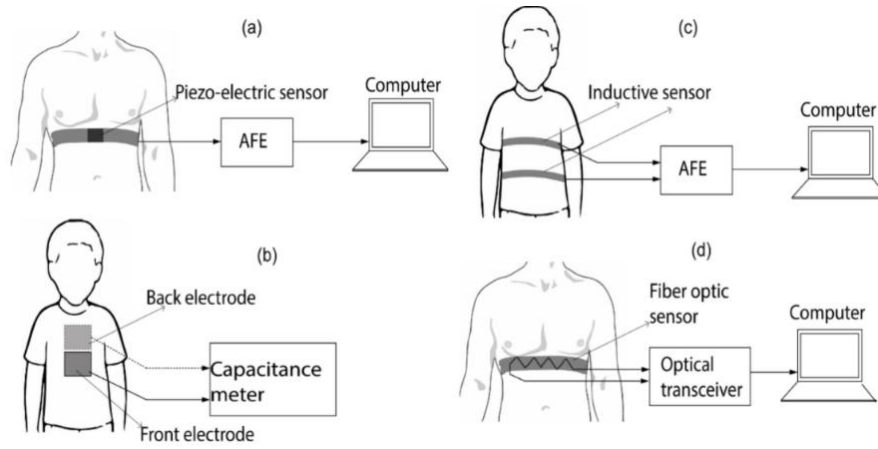
Figure 1.1. Contact Belt Sensor to Respiration Rate using a) Piezo-electric sensor [2], b) Back Electrode [3], c) Inductive sensor [4], and d) Fiber optic sensor [5].
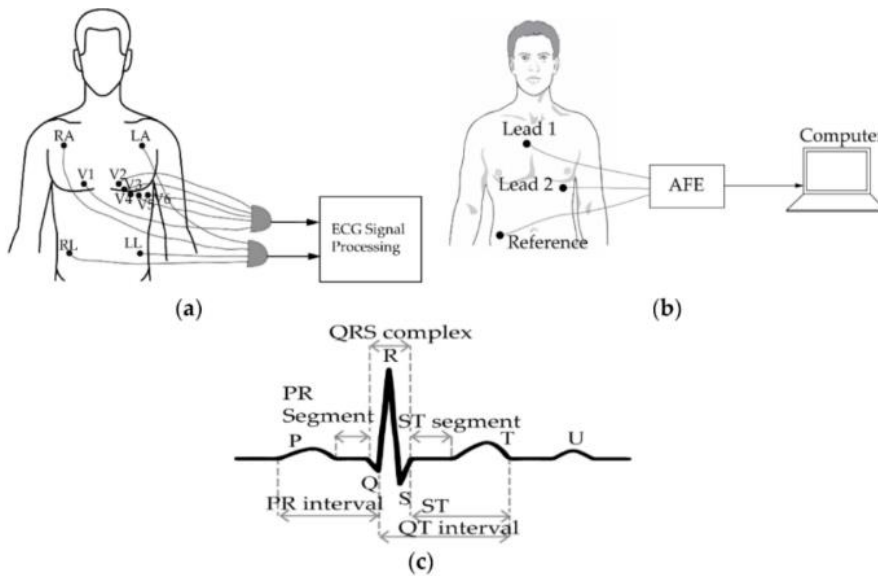
Figure 1.2. Contact ECG system to measure heart rate [6-7], a) 12-lead ECG system, b) ambulatory ECG system, and c) typical ECG waveform.

continuous monitoring is needed. Fig. 1.2c shows a typical ECG signal that can be used to measure HR as well as diagnose heart symptoms such as arrhythmias or coronary heart disease [6-7].

Another type of wearable devices used for HR measurement is electro-optic devices to measure the tissue blood volume changes in the microvascular tissue bed underneath the skin [8]. These devices measure photoplethysmogram (PPG) signals and can be used to estimate HR as well as assist clinicians to evaluate various cardiovascular-related diseases [8]. Although this technique has good potential as an innovative way to access cardiac pulsation, it is still inconvenient in daily monitoring of HR as the person must wear these devices 24/7. Furthermore, the accuracy is limited in tracking the PPG signals during daily activities and light physical exercises [8]. Figure 1.3 shows some PPG measuring devices such as finger pulse sensors, Apple iWatch or Fitbit devices, etc. Therefore, to overcome the inconveniences of traditional contact vital signs sensors discussed above, the non-contact measurement of human vital sign has the potential to improve many applications in different areas such as medical [9-10], civil [11, 13], and military [14]. Figure 1.4 illustrates some of the practical uses of a remote vital sign monitoring system. These systems can be deployed in public places such as airports or hospitals to monitor vital signs of multiple subjects.

Current state-of-the-art systems employ technologies such as camera- [15-16] or radar-based [9-12] techniques for monitoring patients' vital sign from a distance. Table 1.1 summarizes the technologies that are currently under considerations for remote vital sign monitoring application along with the advantages and limitations of these systems. It can be shown from Table 1.1 that although both systems have similar limitations such as their vulnerability to motion artifacts, the camera-based systems are more sensitive to lighting conditions, patients' skin colors as well as its incapability to penetrate materials for through-wall detection. Therefore, radar-based monitoring system is more attractive in wider range of applications/use cases as it offers precise localization

3

Figure 1.3. Wearable LED-based sensor for measuring human vital sign. a) Finger sensor, b) Apple iWatch, and c) Fitbit devices. *Sources obtained from Google Images.*
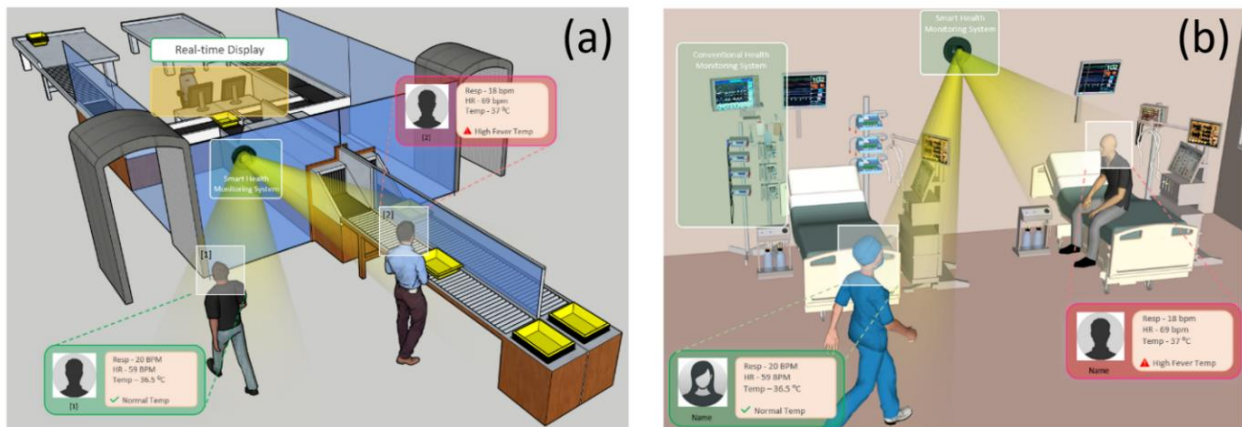
Figure 1.4. Remote vital sign monitoring system in a) airports, b) hospital or clinical facilities.

Table 1.1. Current Technologies for Remote Vital Sign Monitoring [9-12, 15-16]

Technologies	Principles	Advantages	Limitations
Video Camera-based Techniques	Measures induced movement of the chest by quantifying variation of image intensities over time	Non-contact, unobtrusive, ability to perform remote measurements via low-cost webcams.	Susceptible to motion artifacts, sensitive to lighting condition/skin colors, privacy issues to patients, unable to penetrate materials.
Radar	Detect movements of the chest caused by breathing and heartbeat.	Non-contact, ability to penetrate materials, precise localization of SUT.	Vulnerable to motion artifacts signal attenuation by high body fat and low SNR of heartbeat.

of patients, ability to penetrate materials for through-wall monitoring applications without invading the privacy of patients. Our objective is to develop a highly accurate non-contact RR/HR portable monitoring system based on radar techniques. Hence, we will utilize and study the newly developed mmWave radar systems. In this dissertation, we propose the use of a compact, portable, widely distributed MIMO radar system operating at 77-81 GHz to improve the accuracy of RR/HR detection results. It will be shown that by using more widely distributed MIMO channel, better estimation accuracy especially for HR can be achieved compared with single channel systems. As shown in Table 1.1, radar-based techniques for RR/HR detection suffer from two main challenging issues: low SNR and RBM. In the next sections, we discuss these challenges in details and literature surveys on solutions to tackle these issues.

1.2 Current Challenges of Radar-based Techniques for Vital Sign Detection

Since the concept of remote vital sign detection using a portable system at mmWave frequencies is based on sensing physiological motion of the chest's skin, several external factors might corrupt the vital sign signals captured by the radar. These include random motions during the measurements that add noises to the reading of vital sign signals and significantly degrade the SNR especially of the heartbeat signal that makes the detection more challenging. Following are the literature surveys on dealing with the Random Motions effects as well as methods for improving the SNR of vital sign signals.

1.2.1 Improving SNR of Heartbeat Signals

Although mmWave sensors with significantly reduced size have made remote human vital signs monitoring more feasible and portable to be deployed in public places, they severely suffer from

EM propagation loss and multipath interferences, which eventually cause errors in reading human vital signs. HR detection in particular suffers more, since reflected EM signals from chest displacement due to heartbeat are smaller compared to respiration and respiratory spurious harmonics [9-12]. There are a number of solutions in the literature to improve the signal to noise ratio (SNR) of the received vital signs signals. In [17,18], a directional horn antenna with a 20-dBi gain was used. Their HR estimation results show less than 2% error compared to a standard contact sensor. However, directive antennas reduce the field of view of the radar and make it impractical to work effectively in public places for multi-subject monitoring. Implementation of advanced signal processing algorithms at the receiver side is another solution for boosting SNR. A stepped-frequency continuous wave (SFCW) radar operating within 2-4 GHz is used with Arctangent Demodulation (AD) and State-Space Method (SSM) to enhance the SNR of the heart signals to 12dB [19-21]. Their results show a deviation of <1.5% from the estimated HR using a standard contact sensor when the subject is 0.8 m away from the transceiver. In [22], CWT and cross-correlation methods between two CW radars operated at 10 GHz were used to improve the SNR of heart signals. This method has improved the detection accuracy of HR by up to 14% compared to conventional CWT. In [23-24], an adaptive scale selection method with CWT is used to eliminate random body motion and noise components. They show an improvement of up to 40% in HR estimation accuracy. While their signal processing can be utilized at mmWave, these systems are successful, but still operate at low frequencies and are bulky so they do not offer portability.

Progress has also been made with mmWave FMCW radar [25-28], where processing techniques have been proposed to improve the quality of HR estimation. In [25], a 77-GHz FMCW radar is used with pre-processing methods such as noise/motion corrupted segment removal, windowing

and gain control, etc. to increase the quality of vital sign signal before estimation methods such as FFT and inter-peak estimation are employed to guarantee high accuracy. The work from [26-27] and [28] employ similar hardware but uses different processing chain such as maximum likelihood (ML) [26-27] and SSM [28] for HR estimation. Although producing accurate results, these approaches use single TX-RX antenna pair which does not take full advantages of the MIMO radar hardware. Mm-wave antennas and components can now be integrated into small circuitry to form a phased-array with steering capabilities [29-31]. In [29], two uniform linear arrays (ULA) are used with digital phase shifters to physically steer the TX-RX beams to the angular positions of subjects. An average SNR of 15 dB is achieved when a subject is detected. Recently, self-injection-locked radar [30-31] has also been used for vital sign applications. The radar operates at 2.4 GHz and transmits the output signal via one TX antenna. The echo signal is received by a 4-element ULA supported by 0°/90° digital phase shifter. Although HR estimation accuracy is not fully reported, the proposed system worked up to 3.6 m and 120° angular position.

While a phased-array with steering capability enhances the SNR of detected signal, it is still considered a single TX-RX pair and does not take advantage of spatial diversity. With L-TX and M-RX to form a MIMO configuration with $L \times M$ diverse channels; an opportunity for spatial diversity is offered. While the main advantage of phased-array radar is the coherent processing gain at the transmitting side, studies show that MIMO radars may offer enhanced performance with better tolerance to fading as they utilize spatially diverse transmitters and receivers [32-34]. Given that the target's radar cross section (RCS) at the aspect angle is varied, MIMO radar systems could outperform phased-array radar systems in higher SNR environments. Several works in literature takes advantage of MIMO radar for vital sign applications [35-36]. A 4 TX - 4 RX, FMCW MIMO radars with 7-GHz bandwidth are employed in [36] where the four TX-RX pairs

8

are placed at four corners of a room. The superposition of FFT magnitude from these TX-RX pairs is performed. Results from [36] show a 6% improvement in HR estimation accuracy compared with a single TX-RX pair.

In [37-40], the authors employ Maximal Ratio Combining (MRC) methods to combine the captured signals from separate TX-RX pairs to increase the SNR of the heartbeat signals. They show that with increase SNR, the HR accuracy rate is improved by 18% in [39] and 8% in [40]. One limitation from this approach is, however, after the combining processes, it is hard to identify the interferences of random motions from the combined signals especially for the cases where random motions are subtly induced to the vital sign signals. Table 1.2 summarizes the methods discussed above for improving the SNR of vital sign signal. It can be observed that most of the proposed work in literatures do not take advantage of the spatial diversity of MIMO radar configuration in further increasing the SNR of vital sign signals, especially the heartbeat signal. Although the authors in [39, 41] employs mmWave MIMO radar configuration in improving heartbeat's SNR using MRC, random motion is difficult to deal with when all signals are combined into one. Thus, in this dissertation, we will investigate the use of MIMO configuration to see if it can help increase the SNR of the vital sign signals and to deal with subtly induced random motions. As a result, improvements of RR/HR detection accuracy can be achieved.

1.2.2 Random Motion Cancellation on Vital Sign Detection

During the experiments, interferences from Random Motion (RM) certainly impacts the accuracy of RR and HR monitoring. This interference remains to be the most difficult challenge to address to date. There have been numerous works in the literature that proposed approaches to address this issue and a brief discussion will be given here. Generally, RM can be divided into two

Table 1.2. Proposed Solutions in Literature for SNR Improvement of Heartbeat Signal

Research Groups	Methods	Advantages	Limitations
Li, et al. [12]	High Gain Antennas	Increase SNR of heartbeat Signal	Single TX-RX, Decrease fields of view, Large Size Radar
Ren et al. [21]	State-spaced method	Increase SNR of heartbeat Signal	Single TX-RX, Large Size Radar
Tateishi et al. [22]	Wavelet Transform and Cross-correlation		
Shoichiro et al. [23]	Wavelet Transform		
Alizadeh et al. [27]	Maximum Likelihood	Increase SNR of heartbeat Signal, Compact Size Radar	Single TX-RX
Oleksak et al. [28]	State-spaced method		
Mehrdad et al. [29]	Phased-array	Increase SNR of heartbeat Signal, target localization	Complex Hardware, single TX-RX
Sakamoto et al. [39]	Maximal Ratio Combining Methods	Increase SNR of heartbeat signal, portable Radar.	Difficult to identify existing random motion
Dai et al. [41]			

categories: 1) from the radar itself [42-43] and 2) from the subject under test (SUT) [44-54]. We will briefly discuss these RM categories along with solutions proposed in literatures to deal with them as well as their advantages and limitation in the next sections. Most of the time random motions from the radar itself are caused by operators in which they create shaky/vibrating motions during the measurements. To deal with these random motions, authors in [42] places a motion sensor onto the hand-held radar to record any unwanted vibration caused by hand-shakes. Thus, the hand-shake vibration can be cancelled based on motion-sensor data. While [42] uses additional sensors to capture the radar's unwanted shaky motions, the authors in [43] proposed the use of Empirical Mode Decomposition (EMD) technique to identify and cancel out the unwanted vibrations as they have different spectral characteristics that can be realized from Intrinsic Mode Functions (IMFs). Thus, by removing the IFM featuring the RM and only using the remaining IMFs, the vital sign signal without hand-shake vibration effects can be recovered. As discussed from [42-43], while the mechanical hand-shake motions from the radar side might affect the accuracy of HR estimation, they can be canceled either by using extra hardware for capturing the interfered motions or by using a signal decomposition method such as EMD to identify and cancel these unwanted motions. In this dissertation, we thus focus on investigating the second category of RM where the interfered motions come directly from the SUT.

   While the nature of RM in the first category is more predictable and easier to overcome, it is not the case for the second category in which the motion comes from the body of the SUT. In [12, 44], the authors use two separate radar systems placed in front and back of the SUT to cancel out the RM as each radar captures the same RM but in opposite direction. It can be seen that for this approach, the measurement has to be performed simultaneously from both sides to cancel out the random body drifts. Thus, the complexity of hardware requirement makes this type of approach

not suitable for deploying the system at public places. Furthermore, alignment of the dual radars is also important to make sure the RBM signal is captured equally by the two radars so that the RM can be completely canceled from the combined signal. A different antenna configuration is proposed in [45-46] in which the self-injection locked (SIL) antennas have different gain features and are placed side-by-side rather than being located in front and back of the patient. Since the body and vital sign movements are not uniform over the entire chest, the signals that are captured by these two antennas have different amplitude ratios between the body motion and vital sign components. Although experimental results show that this approach reveals a body motion signal cancellation of around 85% [45], it still possesses several limitations. Firstly, it is critical for antennas to align with each other as they need to capture similar random body motion for the SUT to be able to successfully cancel them. Secondly, the experimental setup requires the high-gain antenna to be tilted, which makes the hardware system complicated for practical use. Similar approach of using dual radars has also been proposed in [47]. However, ultra-wideband radars with patch antennas are used instead of the CW radars with helical antennas in [45]. The difference in the setup between [47] and [48] is that the antenna configuration in [47] forms an up-down placement system while the system in [48] forms a left-right system. This approach assumes the radar on the SUT's left side captures both vital sign and RM signals while the one on the SUT's right side captures only RM signals as it does not look directly at the heart's chest area. Thus, by subtracting the signals captured from these two radars, only heartbeat signal remains. By properly combining the signals from the two radars, they show that the heartbeat spectrum SNR is enhanced and easier to detect. One main disadvantage of these approaches in [45-48], however, is that if the RBM is not received equally by both radars, these interferences cannot be totally eliminated.

Meanwhile in [49], the authors use four radars in front, back, left, right directions of the SUT

and the combination of the four signals can be used for cancelling the random body motion. This approach is also based on a concept proposed in [12] with the enhancement that the pair of radars in the right-left direction can also help to increase the SNR of the vital sign signals in the presence of RBM. However, deployment of a system with four separate radars will limit the use of this system at public places due to the complexity of hardware requirements. As an alternative approach, [50-51] employs a hybrid system where iPhone camera is used to capture the RM from SUT and the radar-measured signal is compensated based on a camera-measured RBM to acquire vital signs. A limitation of this approach is that accurate monitoring relies on RM data captured by the camera, which can be easily affected by lighting conditions in the room. Therefore, this type of hybrid systems is more suitable for laboratory use than in practice.

Progress has been made for a variety of advanced signal processing techniques that have been developed and proposed to combat RBM problems. In [25], for example, a 77-GHz FMCW radar is used with a simple thresholding method that eliminates large amplitude motion from the physiological signals that would exceed a certain threshold. The captured signals are divided into 1-second segments and the energy in each segment is computed for a window size of 1 second. If the energy within this segment exceeds a certain pre-defined threshold, all samples in the segment are discarded. However, this method is limited as it only helps removing any impulse-like motion due to sudden changes in SUT's position. With an RBM that subtly induces noises to the physiological signal, this method would provide an inadequate performance. In [52], a deep neural network (DNN) is proposed to predict the respiration pattern of SUT in the presence of RBM. Due to its powerful capability, DNN is employed to directly model the nonlinear relationship between the expected features of the respiration and the signal mixtures that contain RBM. Thus, the trained DNN model can still predict the respiration motion based on the relationship between random-

motion-interfered signals and clean respiratory signals that it learned from the training process. The authors from [52] showed that the original signal fluctuates due to interferences of RBM while the predicted signal can recover the respiratory pattern and increase the SNR of respiratory signal in the frequency domain. One limitation of this publication is that they only tried to recover respiratory information. The authors in [53] introduced matched filters to retrieve the respiratory and heartbeat spectra interfered by large scale RBM, where the templates that contain heartbeat information is first acquired and applied to the output physiological signal to cancel out RBM. From their experimental results, the authors showed that matched filtering method is useful against the passive RBM from unintentional body swaying effect during the measurement. One limitation in this approach, however, is the fact that the templates are extracted manually and might be challenging for real-time application.

It can be seen that most of the hardware-based methods require either complex hardware which takes up a lot of spaces and are not practical in use at public places or hybrid systems with camera which is highly sensitive to lighting conditions. For the software-based methods, the proposed techniques are generic and do not cover subtly induced RM [25], or only recover respiratory signals [52]. Thus, it is challenging in employing these methods to improve the HR estimation accuracy in practical scenarios.

1.3 Contributions

My major contributions include:

- Propose the use of a compact, widely distributed MIMO radar system to improve the respiratory rate and heart rate detection results. It will be shown that by using more widely distributed MIMO channels, better estimation accuracy especially for heart rate can be

achieved compared with single channel systems even in scenarios where there are pronounced random body-swaying motion (RBSM) that interfere with the heartbeat signals. The exploration of this device on monitoring vital sign of human subjects have not been widely published in the literature and this dissertation is one of the first work that investigate the use of this device.

- Proposes a novel automatic heartbeat template (HBT) extraction method based on constellation diagram of the received radar signal to adaptively identify the corrupted signal portions due to random swaying body motion and extract the templates that contain heartbeat signal to magnify its magnitude. The idea of using heartbeat template and matched filtering for magnifying heartbeat signals is not novel. However, the works in the literature require human intervention to extract a heartbeat template which are certainly not practical for real-time operation while our method is completely automatic and does not require human intervention.

- Develop a spectral-based heart rate selection to adaptively search for accurate heart rate based on the spectral characteristics of the wavelet transformed signal to address the interfered random body-swaying motion. Under the strong impact from the random body-swaying motion, the power spectral density of the heartbeat signals can be concealed by the interferences that simply picking the highest peak within the frequency spectrum do not guarantee accurate heart rate estimation. While most of the work using MIMO in the literature are not fully taking use of the spatial diversity of the system, our developed spectral-based heart rate selection can be used in different widely distributed MIMO device to improve accuracy of the heart rate estimation.

- Develop and analyze a convolutional neural network (CNN) for channel classification in which channels with low signal-to-noise ratio of heartbeat signals are identified and excluded from

the estimating procedure to reduce the error of HR detection. Currently in the literature, deep learning frameworks are mostly applied for single-channel radar which results in the requirement for large amount of data sets for certain tasks. With the advantages of having more information from different radar channels, we are among the first research groups that steers the effort of using deep learning for simpler tasks such as channel classification where there is no need for extensive amounts of data while still improving heart rate estimation's accuracy.

- We also utilize a multi-layer perceptron neural network to reconstruct the heartbeat signals and predict heart rates from subjects under test. While there has been works in the literature that use neural network for heartbeat signals' reconstruction, most of them uses single-channel radar which eventually requires an extensive amount of data for reconstructing the heartbeat signals, especially under scenarios with moving subjects under test. Our proposed framework addresses the challenge that extensive amount of radar data collected from human do not currently exist, hence by using more information from different MIMO channels and extracted information about our heartbeat template extraction method, we reduce the amount of training data needed while still achieve satisfactory performance for heartbeat signals reconstruction.

1.4 Organization of the Dissertation

The rest of the dissertation is organized as follows:

Chapter 2 discusses an introduction of different radar architectures that have been used in remote RR/HR monitoring applications. Comparison between these radar architectures will be discussed to select the most appropriate radar architectures for our study. An overview of the basic theory of Multiple-Input Multiple-Output (MIMO) radar configuration which employs Time Division Multiplexing (TDM) to separate the transmitted signals from different transmitters (TX) is also discussed.

Chapter 3 discusses the state of the art of compact radar systems from different manufacturers. For this dissertation, an FMCW-MIMO radar system from Texas Instruments is proposed as it offers MIMO configuration with widely distributed channels. Design details of the system such as antennas characteristics, output power, FMCW chirp timing configuration will be presented.

Chapter 4 discusses mathematic model of human chest wall displacement due to respiration, heartbeat as well as random body-swaying motion to aid in the development and validation of proposed processing chain. This chapter describes the mathematic model of the displacement of human chest wall due to the above signals as well as received radar signal with an FMCW radar employing TDM-MIMO configuration.

Chapter 5 introduces a processing chain for monitoring RR and HR from subjects under quasi-static scenarios in which the subjects have low random body-swaying motion. We first show a mathematic model of received signals using a TDM-MIMO radar for this application. Next, the processing chain including 2D-FFT for target selection, Arctangent Demodulation (AD), Constellation Correction for extracting and correcting the vital sign signals will be shown. Next, Maximal Ratio Combining (MRC) technique which is used to reduce complexity of the estimating process by combining the signal from separate MIMO channels will be discussed. This chapter will show that by employing more widely separated MIMO channels, better accuracy of HR estimation is achieved compared with single radar channel. To help reduce the interferences of respiratory harmonics, automatic HBT extraction and adapted CWT will also be presented. Experimental results with scenarios where the SUTs lie down on bed or sit down on chairs in front of radar will be shown followed by the results discussion and some concluding remarks of this chapter.

To propose a solution for the negative impact of random body-swaying motion, Chapter 6 shows

that while SUTs are standing, the interferences from the random body-swaying motion (RBSM) severely affect the HR estimation results. In this dissertation, we only address the impact of RBSM in which the upper body of the SUT unintentionally sways back and forth during the experiment. Thus, we must modify the processing chain to deal with the strong interferences from RBSM. A spectral-based HR selection is added to help select the HR from multiple MIMO channels. We first show that with simulated mathematic models, our proposed HBT extraction and adapted CWT method help suppress these unwanted interferences and significantly improve HR estimation accuracy compared with conventional methods. Experimental results for standing subjects will be shown next to validate the robustness of our modified processing chain compared with conventional methods and several published results. Discussion on results and concluding remarks are presented at the end of this chapter.

Chapter 7 discusses the Deep Learning Framework using CNN and MLP neural network that can be used to aid on channel classification and HR prediction. These modules are shown to be useful in improving the HR estimation accuracy. Training and testing results with synthesized data and experimental data to train these neural networks are shown to indicate their usefulness in our application followed by discussion and concluding remarks from this chapter.

Chapter 8 summarizes the dissertation and puts forward several directions of potential future works.

CHAPTER II

RADAR ARCHITECTURES AND CONFIGURATION

There are different radar architectures that have been proposed in literature for radar-based respiratory rate and heart rate monitoring applications. While each radar architecture has its own advantages and limitations, selecting a radar configuration that fits our intended use cases is important so that it can provide optimal capability of detection for our system. This chapter briefly introduces different radar architectures that have been recently proposed in the literature and how with emphasis on employing FMCW radar architecture. Furthermore, we also investigate MIMO radar configuration with widely distributed antennas and how its use impacts on improving the accuracy of detection.

2.1 Introduction to Different Radar Architectures

2.1.1 Continuous Wave (CW) Radars

Continuous Wave (CW) radars are the first popular type which can be used to extract respiratory rate and heart rate information from the subjects under test (SUT). In the CW radar architecture, single frequency signal is transmitted and received to capture the displacement from the patients' chest movement caused by respiration and heartbeat [12, 54]. Although CW radars are simple to implement and low-cost, they do not offer range detection capability which measures the distances of patients from the radar. Without range-detecting capability, CW radar cannot measure respiratory rate and heart rate in scenarios where there is more than one patient. Therefore, we want to opt for a different radar architecture that has this range-detection capability.

2.1.2 Ultra-Wideband (UWB) Radars

The second type of radar architecture that can be used for this application is UWB radar in which the radars send narrow pulses in a scale of nanosecond. By capturing the reflected pulses, we can detect the distances of objects with high range resolution [55-56]. Therefore, any tiny changes on the patients' chest such as periodic expansion and contraction can be detected by the UWB radars. It should be noted that UWB radars have power limitation and since it operates on a wide band, the system noises are relatively higher resulting in lower SNR compared with other types of radars. Furthermore, UWB radars require high-speed analog-to-digital converters (ADC), which will complicate the hardware design and increase the overall cost.

2.1.3 Stepped-frequency Continuous Wave (SFCW) Radars

Stepped-frequency Continuous Wave (SFCW) radar is another type of radar that can be used for vital sign detection application. Instead of transmitting a single frequency signal as in the CW radar or narrow pulse as in UWB radar, SFCW radar transmits a series of discrete tones in a stepwise manner to realize a large effective bandwidth. Therefore, by analyzing the received data on the frequency domain, SFCW radars offer range detection which enables multi-subject detection capability. Compared with impulse UWB radar, SFCW radar has a narrow instantaneous bandwidth so that lower-speed ADCs can be used and the hardware requirements for the receiver become less stringent [57]. Additionally, the receiver instantaneous bandwidth would be much smaller, resulting in a lower noise bandwidth and a higher signal-to-noise ratio (SNR). However, it is necessary to receive multiple tones before any processing is initiated, thus conventional SFCW radar suffers from a serious drawback that the data acquisition time to step over many frequencies is too long for many applications [57].

2.1.4 Frequency-Modulated Continuous Wave (FMCW) Radars

The last radar architecture that can be used for contactless vital sign detection is Frequency Modulate Continuous Wave (FMCW). For this architecture, the FMCW radar transmits a chirp signal which is a sinusoid whose frequency increases linearly with time. The transmitted chirp is reflected off the subjects and is received at the receiver. By analyzing the reflected chirp signal, range information as well as any physiological motions can be revealed [25, 58]. The noises bandwidth from FMCW radars are also lower than that of UWB radars as they employ narrower bandwidth.

2.2 A Focus on FMCW Radar

To summarize the advantages and limitation of the radar architectures that are discussed above, Table 2.1 shows a comparison between different types of radars architectures in terms of localization capability, multi-subject detection, ADC speed requirements, system noises and data acquisition time. Although each of them offers several advantages and disadvantages for using in vital sign monitoring applications, FMCW is shown to be a good candidate when used for this purpose. Thus, in this dissertation, we focus our investigation on the use of a FMCW radar configuration as it offers precise localization for multiple subject detection which CW radar is not capable of. Furthermore, FMCW radar generally has lower system noises than UWB radars as they require narrower instantaneous operating bandwidth and lower required data acquisition time compared with SFCW radars as they do not have to wait for complete reception of multiple single-frequency signals prior to processing. In the next chapter, we will discuss in detail about the FMCW radar we want to use as well as its antenna configuration.

Table 2.1. Comparison between different radar architectures

	CW	UWB	SFCW	FMCW
Localization	No	Yes	Yes	Yes
Multiple Subjects	No	Yes	Yes	Yes
ADC Speed	Low	Fast	Low	Low
System Noises	Low	High	Low	Low
Data Acquisition Time	Fast	Fast with high ADC speed	Slow	Fast

2.3 Principle of MIMO Configuration and Virtual Antenna Array

The MIMO radar systems consists of multiple transmitters and receivers which allows transmitting and receiving noncoherent waveforms [59-60]. Figure 2.1 demonstrates a typical MIMO radar in remote sensing applications such as target detection or localization [24]. Compared with the use of a single-input single-output (SISO) configuration, MIMO radars offer spatial diversity advantages to overcome target scintillation [60]. As the target radar cross section (RCS) can vary significantly with viewing angles, by deploying antennas that are widely distributed in space, the target can be illuminated and viewed at different spatial aspects. Thus, the signal-to-noise ratio (SNR) can be improved and results in the enhancements of detection performance. For a MIMO radar that can be considered as widely-spaced such that each element can view the target at different view aspect, the inter-element spacing d_t between the radar element has to satisfy the following condition [60]:

$$d_t \geq \frac{\lambda R}{D} \tag{2.1}$$

where λ is the operating wavelength, R is the distance from the radar to the target and D is the size of target. If this condition is satisfied, each element of MIMO array can then receive the reflected signals from the target via an independent path which helps to overcome the target scintillation issue.

Another advantage of a MIMO radar is its capability to differentiate closely spaced targets with high resolution by forming a virtual array configuration based on the MIMO array geometry [61-62]. While a SISO radar does not have the capability of finding the target's angles in space, i.e. angle of arrival (AoA), a single-input multiple-output (SIMO) radar can still do it but with lower number of antennas than an equivalent MIMO radar. This is demonstrated in Figures 2.2 and 2.3

23
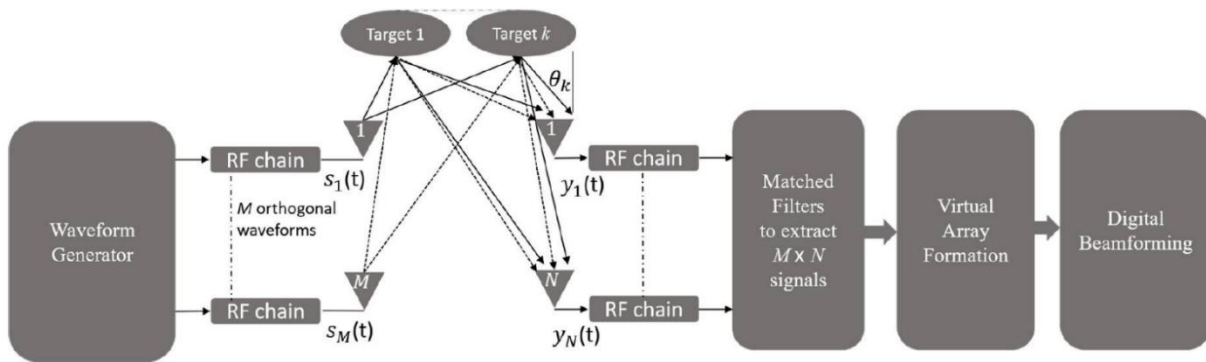
Figure 2.1. General MIMO radar system illuminating the targets with different transmitters and receiving the reflected signals with different receivers [60].
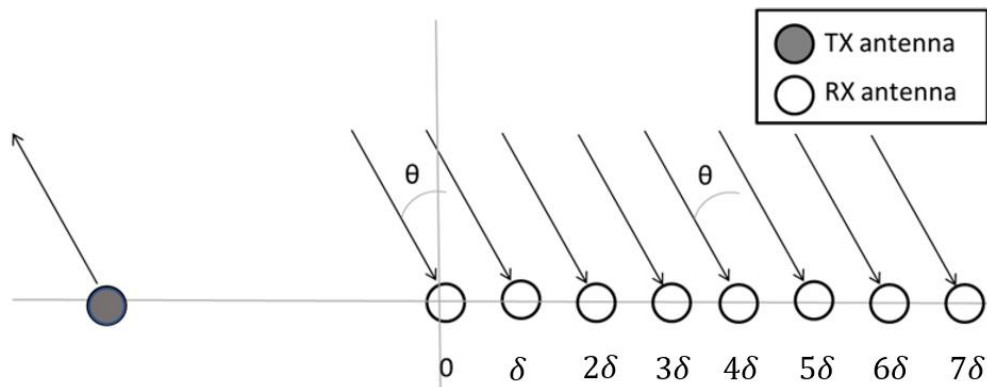
Figure 2.2. SIMO radar with single transmitter and 8 receivers [63].
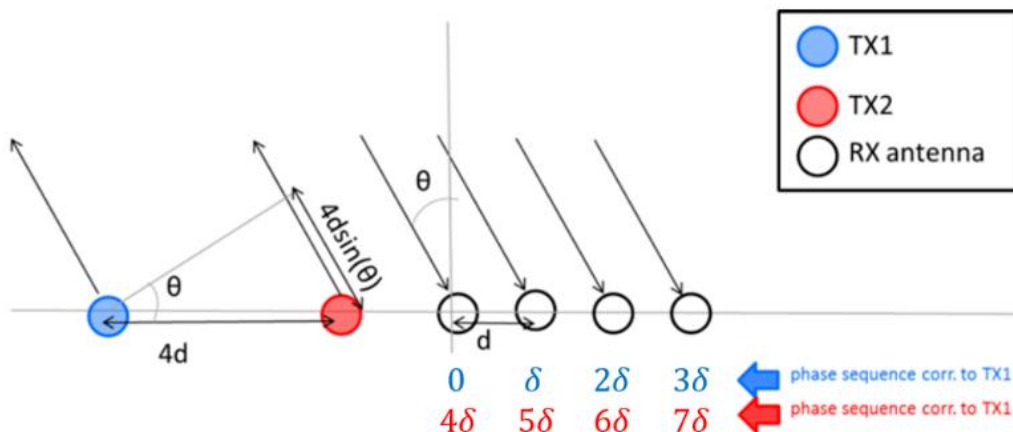
Figure 2.3. MIMO radar with 2 transmitters and 4 receivers [63].

in which the angle resolution of the MIMO radar with N_{TX} transmitting antennas and N_{RX} receiving antennas can be made equivalent to a SIMO radar with $N_{TX} \times N_{RX}$ receiving antennas [62]. Angle resolution θ_{res} of a MIMO radar system is the minimum angle separation for the two objects to be distinguished as separate peaks and is given by [63]:

$$\theta_{res} = \frac{\lambda}{Ndcos(\theta)} \tag{2.2}$$

where λ is the operating wavelength, $N = N_{TX} \times N_{RX}$ is the number of virtual antennas which depends on the number of physical antennas, d is the inter-element spacing of the virtual antennas and θ is the target's angle.

As shown in Figure 2.2, a transmission from the transmitter (TX) results in the phase of $[0\ \delta\ 2\delta\ ...\ 7\delta]$ at all of the eight receivers (RX). Also, it requires 9 antennas (1 TX – 8 RX) to be able to have a good angle resolution for a given target angle θ. In the MIMO case in Figure 2.3, the transmission of TX1 results in the phase of $[0\ \delta\ 2\delta\ 3\delta]$ at the four RX. Since the TX2 is 4d away from TX1, transmitted signal from TX2 travels an additional path length of $4dsin(\theta)$. Thus, the phase of the signal at the four RX due to transmission from TX2 is $[4\delta\ 5\delta\ 6\delta\ 7\delta]$. It can be shown that with MIMO configuration, it only uses 6 antennas (2 TX – 4 RX) to obtain the same resolution. Figure 2.2 and 2.3 shows that the MIMO configuration offers lower hardware cost for angle estimation compared with the SIMO configuration while maintaining the same angle resolution for target localization.

The principle of using MIMO configuration to form a virtual array can also be extended to multidimensional arrays. Figure 2.4 shows an example where a MIMO configuration can form a 2D virtual array with azimuth and elevation angle estimation capability.
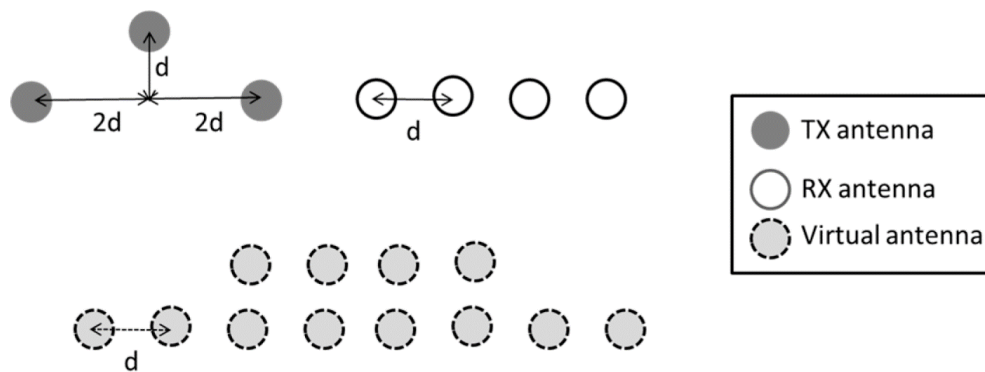
Figure 2.4. An example of using MIMO configuration to form a 2D virtual array for azimuth and elevation estimation capability.

To summarize the advantages of MIMO configuration over SIMO or SISO, Table 2.2 compares these configurations in terms of angle estimation capability, angle resolution, spatial diversity, and hardware costs assuming the same inter-element spacing and number of receivers. It can be seen from Table 2.2 that MIMO provides better spatial diversity as well as lower cost to produce the same angle resolution as with the SIMO configuration. Therefore, in this dissertation, we focus on investigating the use of MIMO radar to improve the SNR of received signal. Although we will not focus on the investigation of angle resolution in this dissertation, MIMO radar configuration also provides a higher angle resolution compared with other configuration which is beneficial in applications where it is required to detect multiple reflected radar signals from multiple targets in the scene.

2.4 Time Division Multiplexing (TDM) Strategies for MIMO Configuration

For MIMO configuration, it is important for the RX antennas to be able to separate the signals corresponding to different TX antennas (i.e. by having different TX antennas transmit on orthogonal channels). In this dissertation, TDM-MIMO is employed to separate signals from multiple TX antennas as it is the simplest way to implement in FMCW radar. In TDM-MIMO, there will be a time delay between sperate TX antennas to make sure they do not transmit at the same time. Each transmitting frame consists of several blocks, with each block consisting of several time slots T_r each corresponding to transmission by one of the numbers of the TX antennas [38]. As an example, in Figure 2.5, an FMCW radar with two time slots alternate time slots are dedicated to TX1 and TX2. Therefore, it guarantees that transmitted signals from different TX do not interfere with each other's.

Table 2.2. Comparison between different radar configurations

	SISO	SIMO	MIMO
Angle Estimation	No	Yes	Yes
Angle Resolution[1]	—	High	High
Spatial Diversity[2]	—	Low	High
Hardware Cost[3]	—	High	Low
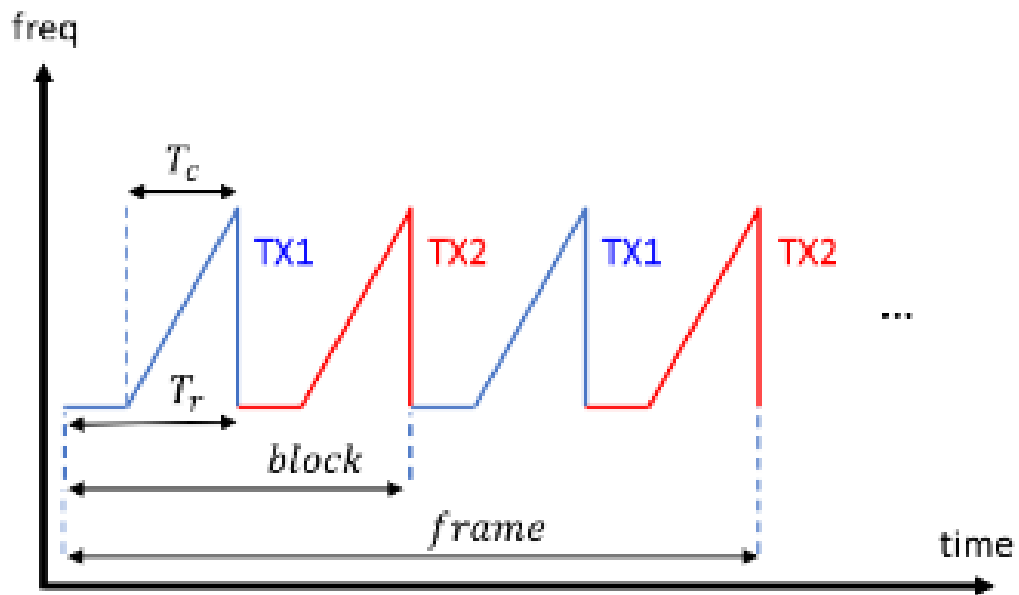
Figure 2.5. TDM-MIMO concept demonstration.

CHAPTER III

COMPACT ON-CHIP RADAR SYSTEMS

This chapter discusses the current state-of-the-art compact, integrated devices that are developed for mmWave radar from various manufacturers. As discussed in Chapter 2, since we are investigating radars with FMCW architectures and MIMO configuration, we can narrow down the search for available commercial devices that such capabilities. We will then give a brief introduction of the device of interest and the hardware setup for our application.

3.1 Current State of the Art

As the size of the antennas shrinks when the operating frequency increases and since we want to reduce the size of the radars so that it is more practical for the system to be deployed at public places or even portable, we opt for the use of millimeter-wave (mmWave) sensors. This frequency range attains a compact radar size that is enough for use as a handheld device while maintaining a high range resolution which is the main capability and advantage of the radar in distinguishing multiple subjects in space. Furthermore, with the size of the antennas significantly decreases in the mmWave frequencies, larger numbers of antennas can be integrated to the system without changing the overall size of the radar system, this enables a larger MIMO configuration in which various multiple antennas illuminate and receive the reflected signals from the subjects under test at different spatial angles. This helps to increase the accuracy of vital sign detection as there are multiple versions of captured signals from different angles. Figure 3.1 shows some available on-chip mmWave MIMO radar system that can be used for remote sensing applications in general.
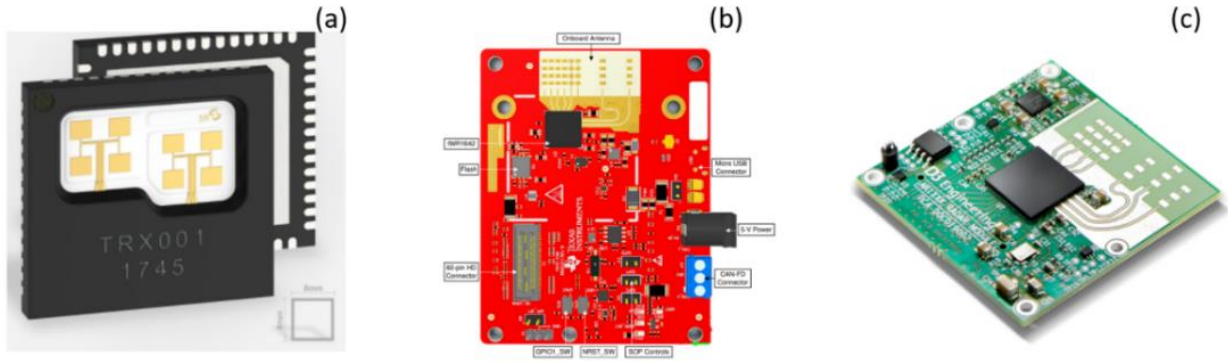
Figure 3.1. On-chip MIMO radar for remote sensing applications. *Sources from Google Images.*

Table 3.1 shows current state of the art mmWave radar system with MIMO configuration. The table shows the operation frequency of the system, the type of radar and the number of transmitters (TX) and receivers (RX). It should be noticed that there are other vendors who offer mmWave radar as well but are not listed here as their products do not support MIMO configuration. As seen from this list, we adopt the Texas Instrument (TI) MMWCAS-RF-EVM because it uses FMCW architectures which enable the range detection of the subjects. It also carries 12 TXs and 16 RXs antennas which vastly improves the spatial diversity for better signals realization as well as increases the angle solution of the radar in cases where we need to localize multiple subjects in the scene.

3.2 System Hardware

The Texas Instrument (TI) MMWCAS-RF-EVM; which is a four-device cascaded array of AWR2243, operating across 77-81 GHz frequency range. The Evaluation Module (EVM) for the MMWCAS-RF-EVM is shown in Figure 3.2 [64].

3.2.1 Antenna Structure

Figures 3.3, 3.4 and 3.5 show the TX-RX antenna structures of the radar system. The structure includes 12 TXs and 16 RXs resulting in a total of 192 separate channels. For the RX antennas, there are three groups which are RX Array A, RX Array B and C as shown in Figure 3.3. The spacing between antennas in each group is $\frac{\lambda_0}{2}$ in which λ_0 is the wavelength at 77 GHz. Separation between the three RX groups denoted as A2, A3 and A4 are listed in Table 3.2. These separations are designed to meet the cascading requirement between different chips [64].

Among the 12 TX antennas shown in Figure 3.4, there are 3 TXs from the master chip are placed

Table 3.1. State of the art mmWave radar with MIMO configuration

Manufacturer	Type	Frequency	# of TX – RX
Texas Instruments (TI)	FMCW	60 GHz – 64 GHz	3 TX – 4 RX
Texas Instruments (TI)	FMCW	77 GHz – 81 GHz	3 TX – 4 RX
Texas Instruments (TI)	**FMCW**	**77 GHz – 81 GHz**	**12 TX – 16 RX**
Sivers IMA	CW	57 GHz – 71 GHz	16 TX – 16 RX
NXP	FMCW	76 GHz – 81 GHz	3 TX – 4 RX
RFbeam Microwave GmbH	FMCW	76 GHz – 77 GHz	4 TX – 6 RX
ST Microelectronics	FMCW	76 GHz – 81 GHz	3 TX – 4RX
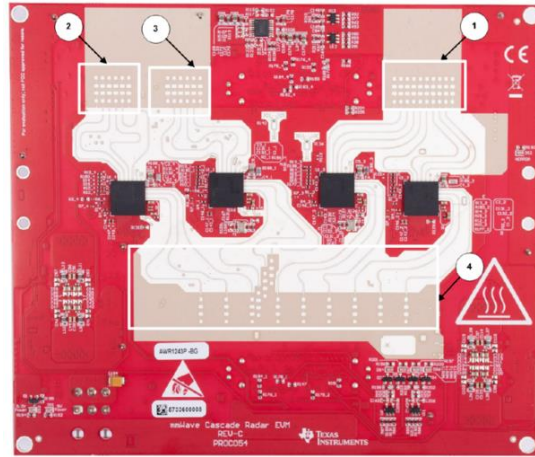
Figure 3.2. MMWCAS-RF EVM, (1) RX Array A – 8, $\lambda_0/2$, linear elements, (2) RX Array B – 4, $\lambda_0/2$, linear elements, (3) RX Array C – 4, $\lambda_0/2$, linear elements, (4) TX Array – 9, $2\lambda_0$, linear elements in azimuth, 4 elements in elevation.

in vertical direction to enable elevation estimation. The other 9 TXs are placed in the horizontal plane for azimuth angle estimation. The 9 azimuth TXs are placed $2\lambda_0$ apart so that together with the 16 RXs, they form a virtual array within MIMO mode with 86 virtual antennas in azimuth direction and provide an angle resolution of up to $1.4°$. The elevation angle resolution is equivalent to the resolution achieved with 7 antennas, which is approximately $18°$ [64].

Figure 3.5 shows the overall separation between TX antenna array and RX antenna array groups. As the vertical spacing between TX and RX groups is $19\lambda_0$. This hardware is a good candidate to study the efficiency of spatial diversity for HR estimation.

Figure 3.6 shows the TX-RX antennas along with the dimensions shown in Table 3.3. The antennas are 4-element series-fed patches. It has 12 dBi gain and its 3dB-beamwidths are approximately $70°$ for E-plane ($\phi = 0°$) and $20°$ for H-plane ($\phi = 90°$).

Figure 3.7 shows the 3D radiation pattern of the antenna and its 2D radiation pattern cuts in the E-plane and H-plane [64].

3.2.2 RF Front End

The MMWCAS-RF EVM is implemented by cascading four AWR2243 which is a self-contained FMCW transceiver single-chip solution operating across 76 to 81 GHz band. The AWR2243 is built on low-power 45-nm RFCMOS process to enable a monolithic implementation of a three TXs and four RXs system with built-in Phase-Locked Loop (PLL) and Analog-to-Digital Converters (ADC). Figure 3.8 shows the functional block diagram of a single AWR2243 device [64]. As discussed in the manufacturer's documentations of the hardware in [64], each AWR2243 device consists of three TXs and four RXs. Firstly, a ramp generator along with a local synthesizer of 20 GHz will generate a chirp profile. Each TX includes a programable 6-bit phase shifter ($5.625°$
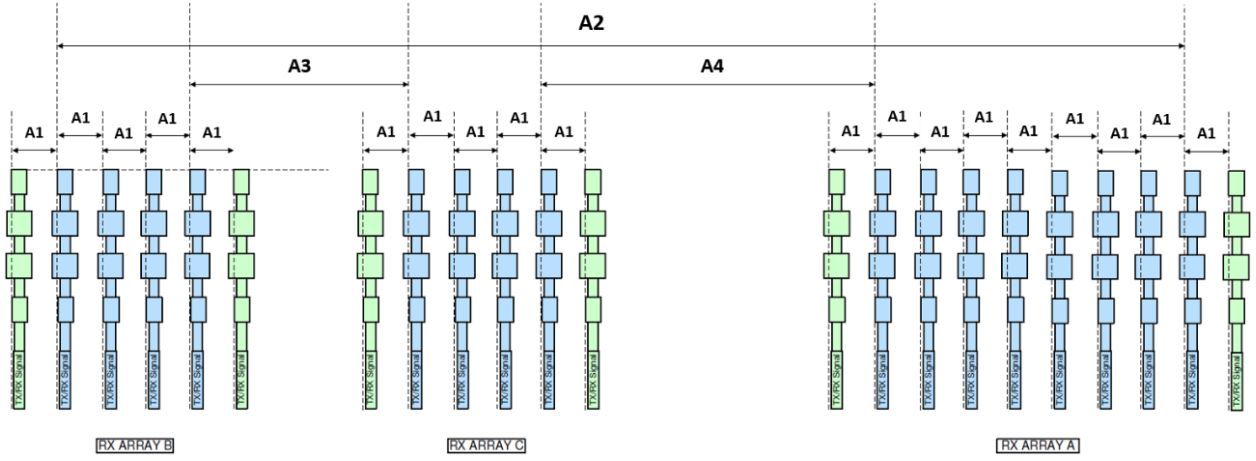
Figure 3.3. RX Antenna Array Dimensions of TI MMWCAS-RF-EVM
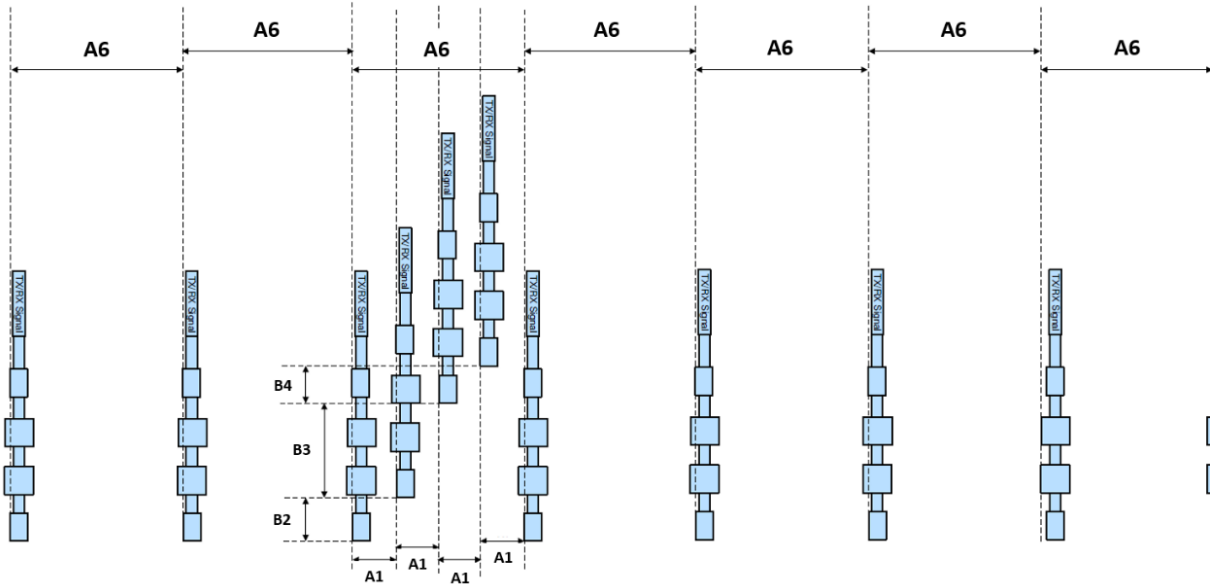
Figure 3.4. TX Antenna Array Dimensions of TI MMWCAS-RF-EVM
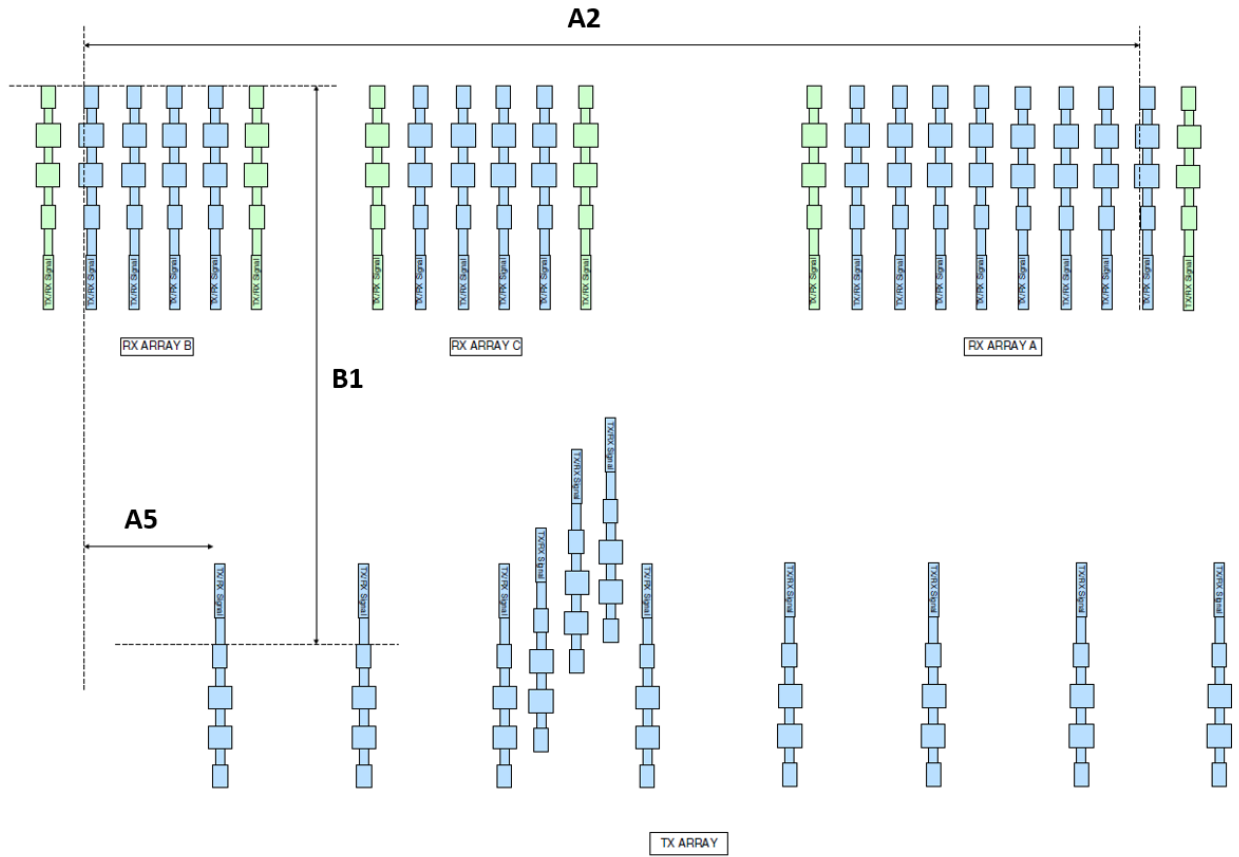
Figure 3.5. TX and RX Antenna Relative Dimensions of TI MMWCAS-RF-EVM
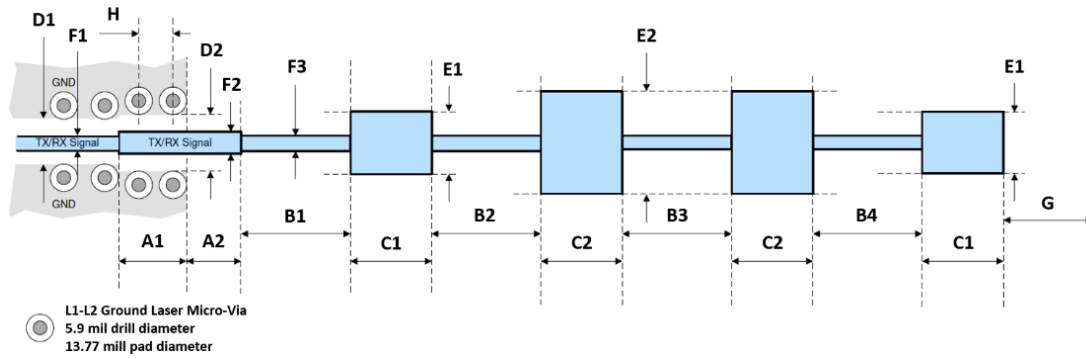
Figure 3.6. Series-Fed, Microstrip Patch Array Antenna Element and Dimensions of TI MMWCAS-RF-EVM
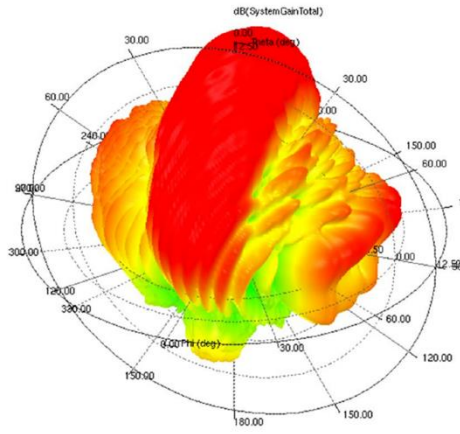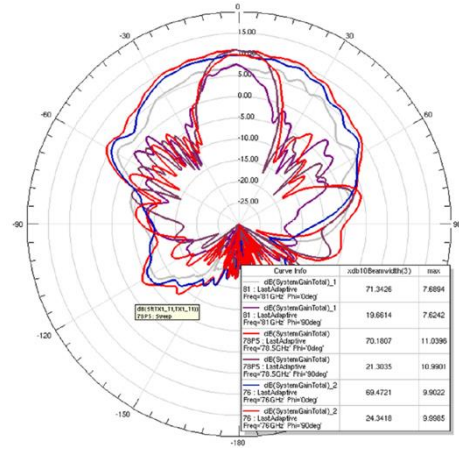
| (a) | (b) |

Figure 3.7. a) 3D Antenna Pattern @78.5 GHz Operation, b) 2D slices of E-plane and H-plane @76 GHz, 78.5 GHz and 81 GHz Operation of the Series-Fed, Microstrip Patch Array Antenna.

Table 3.2. TX – RX Antenna Array Dimensions of TI MMWCAS-RF-EVM [64]

Dimension Label	Dimension (mils)	Dimension (77 GHz, λ_0)
A1	76.78	0.5
A2	4069.34	26.5
A3	614.24	4.0
A4	2456.96	16.0
A5	1191.5	7.759
A6	307.12	20
B1	2928.84	19.072
B2	76.78	0.5
B3	230.36	1.5
B4	153.56	1.0

Table 3.3. Series-Fed, Microstrip Patch Array Antenna Element Dimensions of TI MMWCAS-

RF-EVM [64]

Dimension Label	Dimension (mils)
A1	27.568
A2	11.802
B1	47.24
B2	49.21
B3	45.27
B4	49.21
C1	42.52
C2	40.95
D1	16.722
D2	20.002
E1	39.38
E2	55.12
F1	8.4
F2	10.62
F3	3.94
G	>78.7402
H	<=20.67
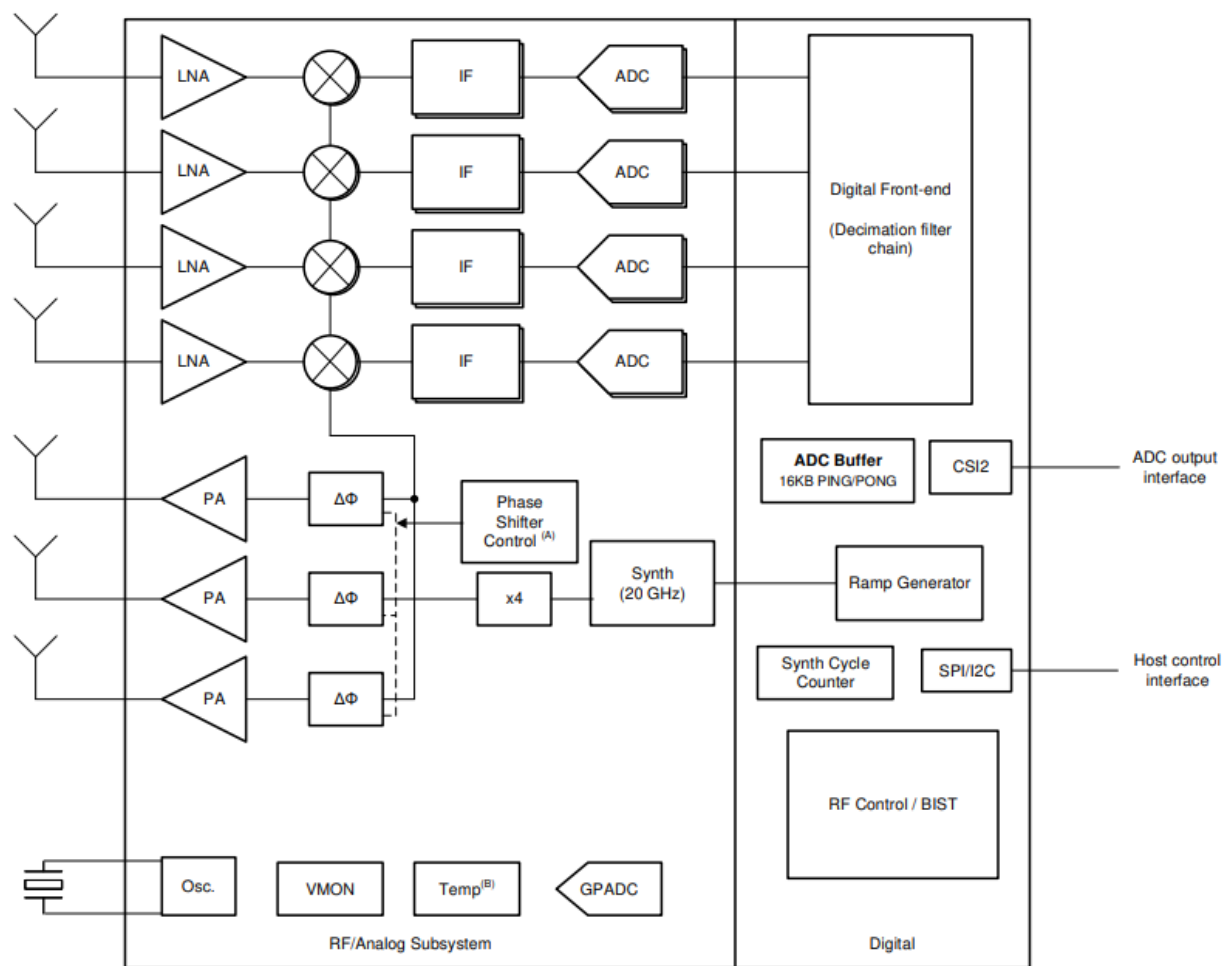
Figure 3.8. Functional Block Diagram of single AWR2243 device

step) to enable beam-forming applications. Following the phase shifters are power amplifiers (PA) and transmit antennas. On the receiving side the receiving antennas and low noise amplifiers (LNA) are placed. The output from the LNA will be passed through mixers along with the original chirp to reconstruct the baseband signals which have the information of range and movement of the subject under test. The output power of each AWR2243 is 10 dBm. For each series-fed antenna element with a 12-dBi gain, a total of 22 dBm Equivalent Isotropically Radiated Power (EIRP, which is the product of transmission power and gain in a direction relative to an isotropic antenna) will be realized. This is well below the restricted level for this type of device under FCC Part 15.255 and FCC Part 15.256 in which the peak EIRP should be less than 40 dBm and 33 dBm, correspondingly. Figure 3.9 shows a simplified functional block diagram of the MMWCAS-RF-EVM which is a cascade of four AWR2243 devices and their associated power, clocking, synchronization, local oscillator, and RF circuits. The AWR22243 devices are separated into master and slave devices in which the master device will use its built-in local oscillator distribution, clock distribution and frame synchronization to communicate and synchronize with other three slave devices. This allows the system to generate and receive coherent FMCW chirps across all master and slave devices. Each AWR2243 device on the board also has a 4-port CSI2.0 transmitter to send radar data to a host processor for data storage and processing. The MMWCAS-RF-EVM accepts 5V DC, 8 A (max) power through the host board connectors. The primary 5V system rails will then be converted into various AWR2243 device rails by a pair of LP87524P, quad-channel, monolithic, buck-converters.

3.3 Chirp Configuration and Related Parameters

3.3.1 Chirp Timing Parameters

The configuration of the FMCW chirp profile (such as frequency slope, sweep bandwidth, chirp

cycle time, etc.) directly affects the interpretation of measurement results as well as important capabilities of the system such as target distance, range resolution, and velocity resolution. Figure 3.10 depicts a single chirp and the associated timing parameters [65]. Within a slow-time frame, as the active chirp time is much shorter than the frame time, it is possible to use a series of chirps within a frame to stabilize the radar performance. The maximum number of chirps per frame will be dependent on the active chirp time and frame time. Figure 3.11 shows an example of a frame structure that consists of a series of chirps.

3.3.2 Maximum Detectable Range and Range Resolution

The maximum and minimum distance over which a radar can detect objects is an important parameter for a radar sensor. The max range information is determined from the sampling frequency, f_s, and the chirp sweeping slope, S [65].

$$Range_{max} = \frac{f_s \times c_0}{2 \times S} \tag{3.1}$$

where c_0 is the speed of light in m/s. The f_s is also dependent on the ADC sampling frequency used.

While the max range calculated in (3.1) is theoretical range merely based on chirp profile and can be used as a rule of thumb when designing the chirp. There are other aspects that can limit the max range of the radar sensor in practice. These aspects include output power from TX, noise figures from RX, chirp duration, number of chirps per frame, TX-RX antenna gain in the direction of interest, object characteristics like Radar Cross Section (RCS) as well as the minimum SNR
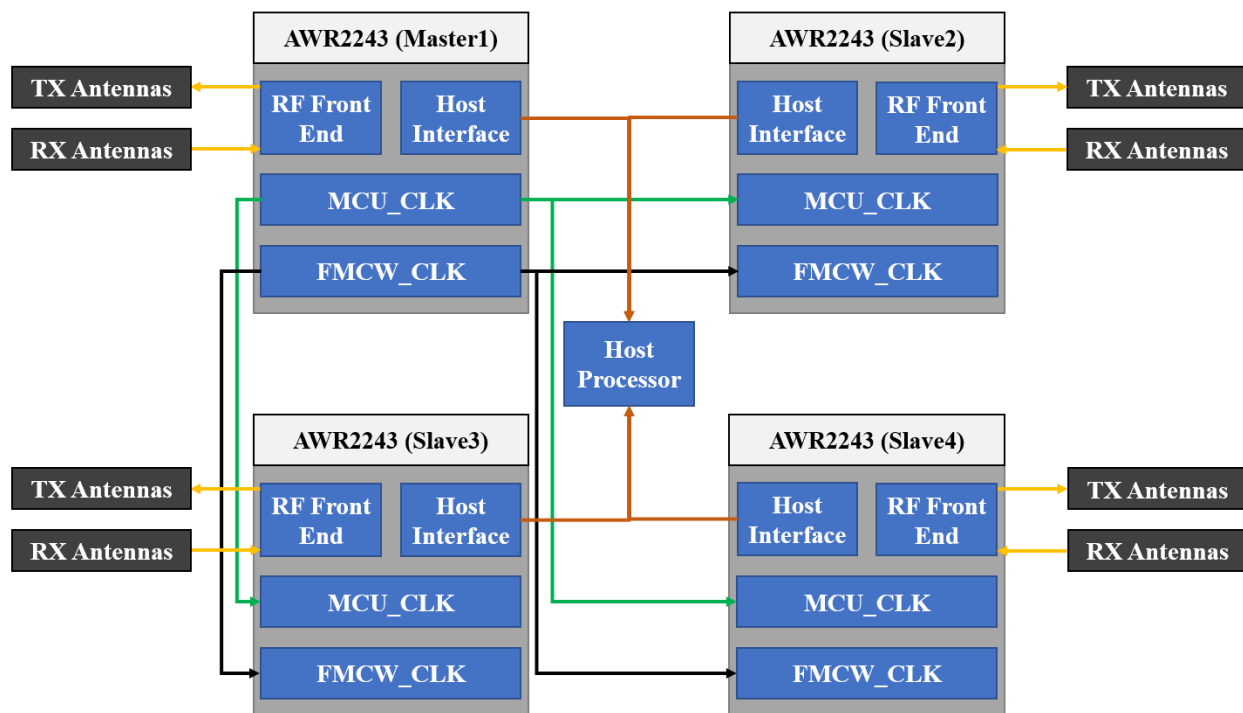
Figure 3.9. Simplified Functional Block Diagram of MMWCAS-RF-EVM consisting of a master AWR2243 device and three slaves AWR2243 devices.
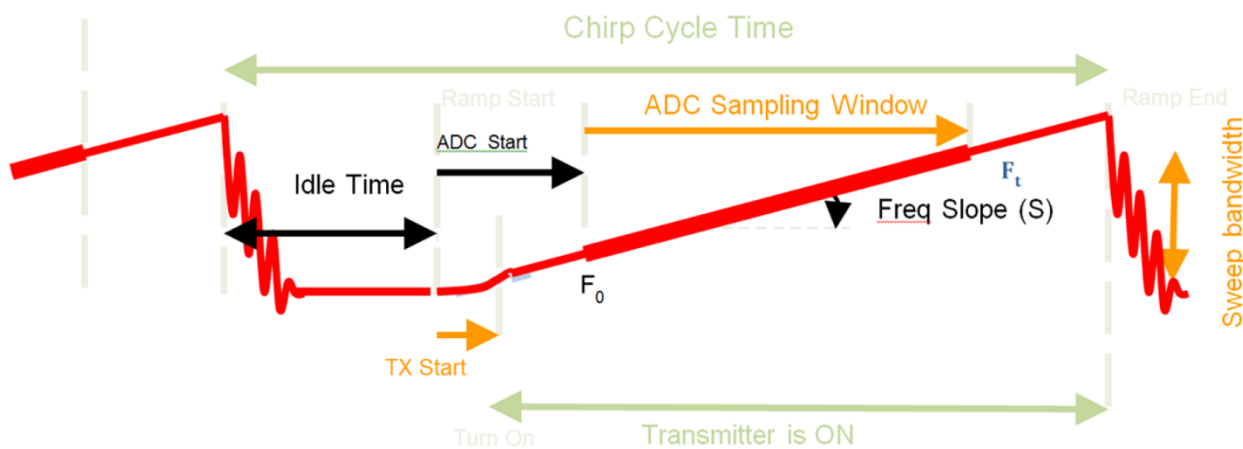
Figure 3.10. Typical FMCW Chirp Timing Setup [65]
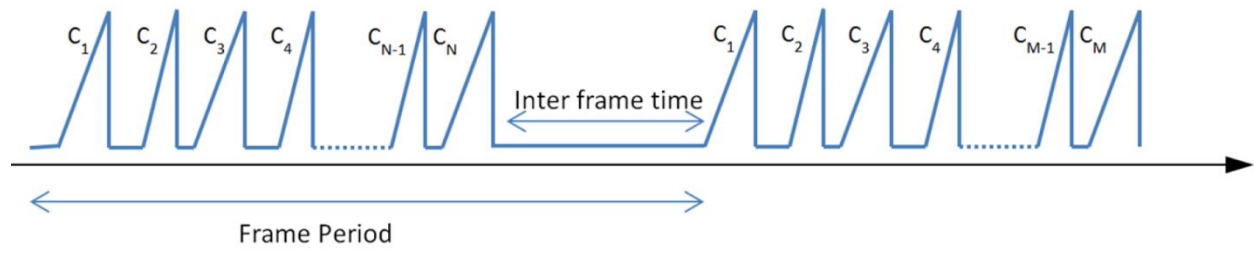
Figure 3.11. Typical FMCW Frame Structure

required by the detection algorithm to detect the target. Therefore, a more robust way to calculate max range is [65]:

$$Range_{max,SNR} = \sqrt[4]{\frac{P_t \times G_{TX} \times G_{RX} \times \sigma_{target} \times N_{chirp} \times T_{chirp} \times c_0^2}{f_0^2 (4\pi)^3 \times kT_{det} \times NF_{RX} \times SNR_{det}}}$$ (3.2)

where P_t is the TX output power, G_{TX}, G_{RX} are the TX and RX Antenna Gain, σ_{target} is the RCS of the target, N_{chirp} is the number of chirps per frame, T_{chirp} is the active chirp time, f_0 is the operating frequency, k is Boltzmann constant, T_{det} is the ambient temperature, NF_{RX} is the noise figure of the RX and SNR_{det} is the minimum SNR required by the algorithm to detect a target.

In scenarios where there are multiple subjects, the radar must be able to resolve two closely separated subjects. The smallest distance between two subjects that allows them to be detected separately is referred as the range resolution. This parameter depends on the chirp sweep bandwidth. This explains why the continuous wave (CW) radar does not have the capability of measuring range information as it only transmits single frequency signal. Range resolution is calculated as:

$$Range_{resolution} = \frac{c_0}{2 \times B}$$ (3.3)

where B is the sweep bandwidth of FMCW chirp. As seen from (3.3), the larger the sweep bandwidth, the better the range resolution. For MMWCAS-RF-EVM, the maximum sweep bandwidth is 4 GHz which is equivalent to a theoretical range resolution of approximately 4 cm.

3.3.3 Maximum Detectable Velocity and Velocity Resolution

The maximum detectable velocity of the radar sensor is also dependent on the chirp cycle time, which is the difference between the start of two consecutive chirps. This in turn depends on how fast the frequency sweep can be performed and the minimum inter-chirp time allowed. The maximum unambiguous velocity is calculated as [65]:

$$Velocity_{max} = \frac{\lambda_0}{4T_{chirp}} \tag{3.4}$$

where λ_0 is the operating wavelength, T_{chirp} is the total chirp time including active chirp time and idle time. For vital sign monitoring application, the detection of high-speed target is not required. Thus, the choice of T_{chirp} is significantly relaxed. In scenarios where there are multiple moving targets, the radar sensor might need to separate out targets with small velocities differences. This is where a good velocity resolution is necessary. The velocity resolution can be calculated as:

$$Velocity_{resolution} = \frac{\lambda_0}{2N_{chirp}T_{chirp}} \tag{3.5}$$

where N_{chirp} is the number of chirps per frame, T_{chirp} is the total chirp time and λ_0 is wavelength.

3.3.4 Angular Resolution

Apart from the angular field of view, it is also important to resolve two objects at that are close by angles. Therefore, having a good angular resolution is also important for a radar in many applications. In general, the angle resolution measurements depend on the number of receiver

antennas available. The larger the number of available antennas, the better angular resolution. The angular resolution can be calculated as:

$$Angular_{resolution} = \frac{\lambda_0}{d \times N_{RX} cos\theta} \times \frac{180}{\pi} \qquad (3.6)$$

where d is the spacing between receiving antennas, N_{RX} is the number of receiving antennas and θ is the angle at which the objects are present.

3.3.5 Chirp Configurations for RR/HR Monitoring Applications

The most common applications for radar include the short-range radar and mid- or long-range radar. For our application, the chirp configuration can be selected to adapt the short-range radar because if the SUTs are too far away from the radar, it may be difficult to detect heartbeat signals because their magnitudes are relatively weak compared with other interferences such as respiratory and random body-swaying motion signals.

Table 3.4 shows so the chirp timing configuration and other parameters that we are using for our RR/HR monitoring applications with the MMWCAS-RF-EVM device. Because the typical heart rate of human subjects is in range 0.75 – 2.5 Hz, the slow-time sampling frequency f_s is chosen as 20 Hz to satisfy Nyquist requirement. Since the active chirp time $T_c \simeq 40\mu s$ << the slow-time sampling time T_s, multiple chirps can be used in one slow-time frame to increase the SNR of received chirp and stabilize the target range bin identification. Theoretical maximum unambiguous range and range resolution calculated using equations (3.1) and (3.2) based on the chirps' timing parameters are 3.83 cm and 3.3 m, respectively. With these values of maximum unambiguous range and range resolution, the radar hardware should be able to acquire sufficient vital sign information when the radar is within this range.

Table 3.4. Chirp Timing and General Parameters used in this dissertation

Start Frequency, f_c (GHz)	77
Frequency Slope, S (MHz/µs)	98
Idle Time (µs)	250
TX Start Time (µs)	1
ADC Start Time (µs)	10
ADC Samples	64
ADC Sampling Frequency (MHz)	2.2
Ramp End Time (µs)	40
Number of Chirp Per Frame	8
Slow-time Sampling Frequency, $f_s = 1/T_s$ (Hz)	20
Range resolution (cm)	3.83
Maximum unambiguous range (m)	3.3

CHAPTER IV

SIMULATION OF VITAL SIGN AND RADAR SIGNALS

To aid in the development and validation of proposed processing chain, mathematical modeling of human chest wall displacement due to respiration, heartbeat as well as random body-swaying motion are necessary. This chapter describes the mathematical model of the displacement of human chest wall due to the above signals as well as received radar signal with an FMCW radar employing TDM-MIMO configuration.

4.1 Chest Wall Displacement Model due to Respiration and Heartbeat

The chest wall displacement due to respiration ΔR_r can be modeled as a periodic sequence of quadratic inhalation and exponential exhalation waveform. This is a result of fitting functions to published measurements of pressure induced by respiration muscles [66-67].

$$\Delta R_r(t) = \begin{cases} -\dfrac{K_b}{T_i T_e} t^2 + \dfrac{K_b T}{T_i T_e} t, & for\ t \in [0, T_i] \\ \dfrac{K_b}{1 - e^{-\frac{T_e}{\tau}}} \left[e^{-\frac{t - T_i}{\tau}} - e^{-\frac{T_e}{\tau}} \right], & for\ t \in [T_i, T] \end{cases} \tag{4.1}$$

where K_b is the minimum end-inspiratory pressure value representing the amplitude of the inspiratory effort, T_i and T_e are the durations of inspiratory and expiratory phases, $T = T_i + T_e = \frac{1}{f_{RR}}$ is the respiratory period of corresponding respiratory frequency f_{RR}, τ is the time constant of the exponential expiratory profile. Typical displacement amplitudes K_b are 4-12 mm [67] and typical RR of adults are 8-20 breaths per minute (BRPM). As the above model is a quadratic

waveform, it will introduce higher-order harmonic components that interfere with the heartbeat signals.

Since the heartbeat signals are narrowband, the chest wall displacement due to heartbeat ΔR_h can be modeled as a pure sinewave [12, 53]:

$$\Delta R_h(t) = A_h sin(2\pi f_{HR}t + \varphi_h) \tag{4.2}$$

where A_h is the displacement of the chest induced by heartbeat, f_{HR} is the heartbeat frequency and φ_h is the initial phase of the heartbeat signals. Typical HR of adults are $50 - 100$ beats per minute (BPM) [68].

To illustrate an example of our simulated chest displacement waveform, Table 4.1 lists several simulating parameters for respiratory rate, heart rate, maximum displacement due to respiration and heartbeat activity along with other timing parameters to simulate the waveform. Furthermore, as the chest displacement waveforms are time-variant, we introduce noises into the simulated waveform in which Gaussian noises are added to the following parameters $f_{RR}, f_{HR}, K_b, T_i, T_e, \tau, A_h$ during the 20-second simulation so that the simulated waveforms are more practical.

Figure 4.1 shows the simulated waveforms from the given set of parameters discussed in Table 4.1. It can be shown in Figure 4.1 that due to the added noises to the parameters in Table 4.1, the displacements of both respiratory and heartbeat signals are not uniform across the time domain, which is more realistic for analysis of interferences from harmonic components of the respiratory signal.

Table 4.1. Simulated Parameters for Chest Displacement due to Respiration and Heartbeat

f_{RR} (Hz)	f_{HR} (Hz)	K_b (mm)	T_i (s)	T_e (s)	τ (s)	A_h (mm)
0.25	1.1	4.3	1.95	1.95	0.27	0.15
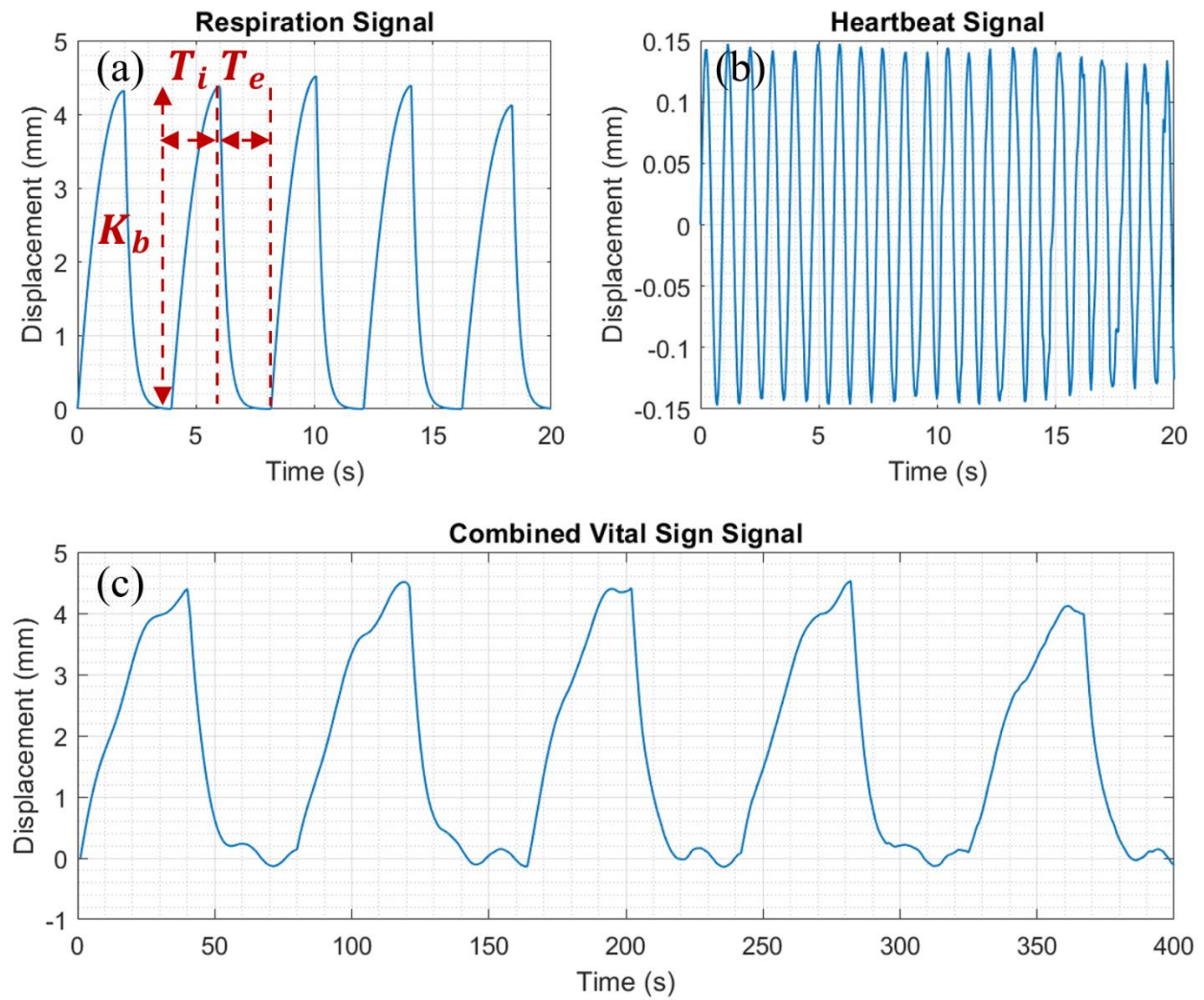
Figure 4.1. Simulated chest displacement due to a) Respiration, b) Heartbeat, c) Combination of respiration and heartbeat.

4.2 Interferences Model due to Random Body-Swaying Motion

Previous studies show that the spectra of random body-swaying motions are essentially wideband [53], which extend beyond the spectrum of heartbeats from the DC frequency. As the radar sees the body-swaying motion as a back-and-forth motion, we can model it as a series of triangular pulses with varying amplitude and lengths [53].

$$
\Delta_{RBSM}(t) = \begin{cases}
A_1 - \dfrac{2A_1 \left| t - \frac{T_1}{2} - t_{d1} \right|}{T_1}, \\
\quad t_{d1} \leq t \leq T_1 + t_{d1} \\[2em]
A_2 - \dfrac{2A_2 \left| t - \frac{T_2}{2} - T_1 - t_{d1} - t_{d2} \right|}{T_2}, \\
\quad T_1 + t_{d1} + t_{d2} \leq t \leq T_1 + T_2 + t_{d1} + t_{d2} \\[2em]
\quad\quad\quad\quad\quad\quad \vdots \\[1em]
A_n - \dfrac{2A_n \left| t - \frac{T_n}{2} - T_1 - \cdots - T_{n-1} - t_{d1} - \cdots - t_{dn} \right|}{T_n}, \\
T_1 + \cdots + T_{n-1} + t_{d1} + t_{dn} \leq t \leq T_1 + \ldots + T_n + t_{d1} + t_{dn}
\end{cases}
\tag{4.3}
$$

where $T_1, T_2, \ldots, T_n$ are the lengths of different triangular pulses with corresponding magnitudes of $A_1, A_2, \ldots, A_n$, $t_{d1}, t_{d2}, \ldots, t_{dn}$ are time delay between the triangular pulses. For unintentional body-swaying motion that we are considering in this dissertation, the body displacement A_n is approximately 5-15mm and the length T_n of these back-and-forth motions is about 0.5-1.5s [53]. To illustrate an example where chest displacement waveforms are corrupted by RBSM, Table 4.2 lists several parameters of two RBSM. Gaussian noises are added to the following parameters T_n, A_n during the 20-second simulation. Figure 4.2 shows the vital sign signal from Figure 4.1, the RBSM and the combined signals between them.

Table 4.2. Simulated Parameters for Two RBSM for 20 seconds

A_1 (mm)	A_2 (mm)	T_1 (s)	T_2 (s)	t_{d1} (s)	t_{d2} (s)
11	12	1.1	1	2.9	9.7
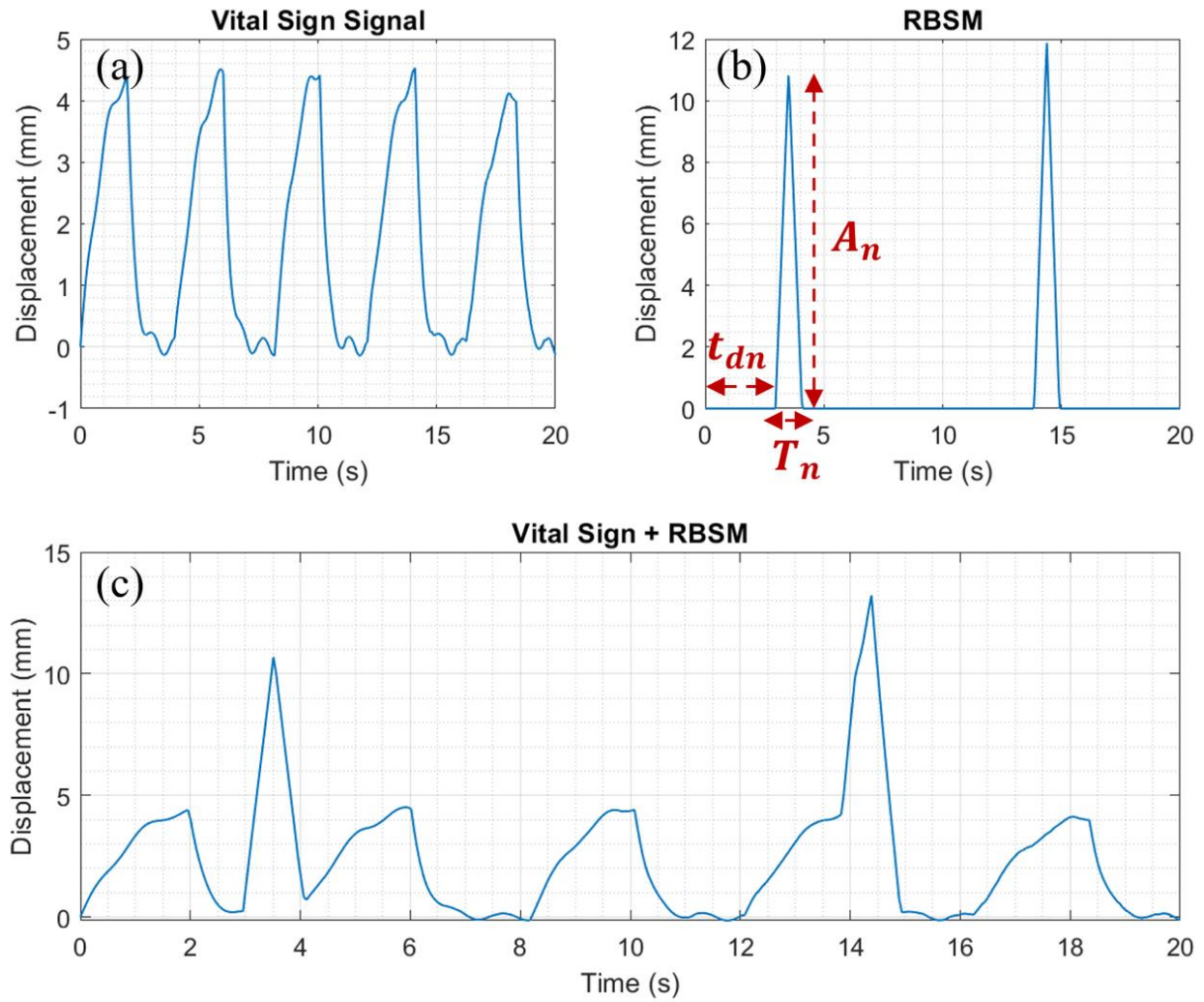
Figure 4.2. a) Simulated chest displacement due to respiration and heartbeat, b) Interferences from two RBSM, c) Combination of both.

To show the impact of on RR/HR estimation due to wideband RBSM noise, in Figure 4.3 we show the frequency spectrum of the signals on two passbands 0.1 – 0.6 Hz and 0.75 – 2.5 Hz in Figure 4.2a and 4.2c, respectively. These are the passbands that are used to determine RR and HR. Figures 4.3a shows that without RBSM, we can clearly obtain the RR in the passband 0.1 – 0.6 Hz. However, the RBSM seems to interfere with the spectrum of heartbeat signal in the passband 0.75 – 2.5 Hz as shown in Figure 4.3b. Therefore, it can be observed that while the RR estimation is not significantly affected, the estimation of HR in the presence of RBSM is inaccurate if we only use conventional peak picking of the spectrum. Therefore, to accurately estimated HR in the presence of RBSM, new approach needs to be developed.

4.3 FMCW Radar Equation for TDM-MIMO

As discussed in Chapter 2, an FMCW radar transmits a series of linear frequency ramps. When a TDM-MIMO is applied, the active TX is switched after each transmission to separate the transmitted signals between TXs. An example with two TXs is shown in Figure 4.4. Following is the formulation to show the phase error at each TX-RX pair. Supposed the FMCW transmitted signal is [25]:

$$x_{transmitted}(t) = A_T cos \left[2\pi f_c t + \frac{\pi B}{T_c} t^2 + \phi(t) \right]$$
(4.4)

where A_T is the transmitted power, f_c is the chirp starting frequency, B is the chirp bandwidth, T_c is the chirp duration and $\phi(t)$ is the phase noise from the transmitter.
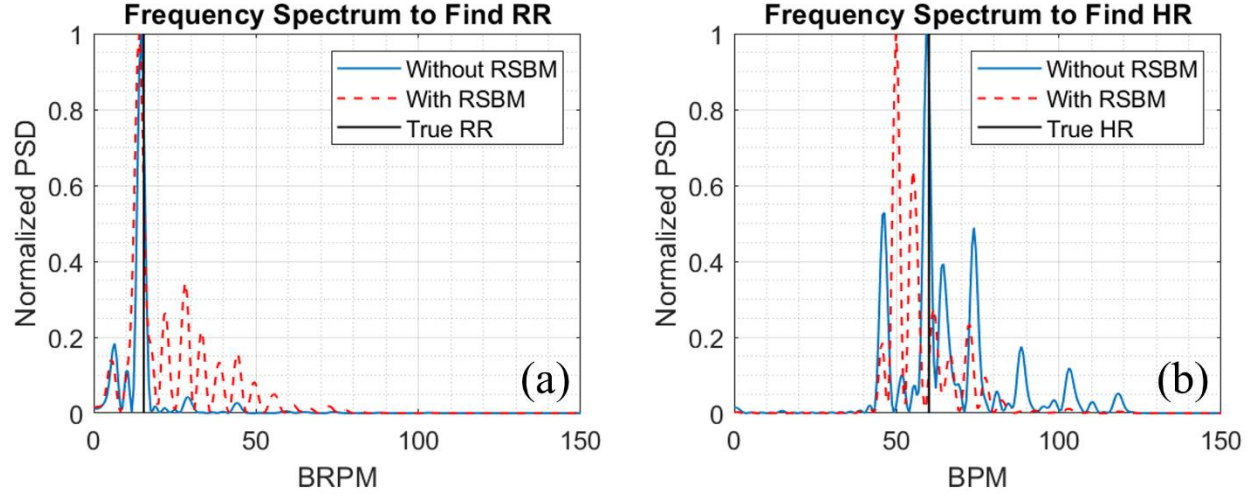
Figure 4.3. Frequency spectrum comparison between signals with and without RBSM. a) In the region 0.1 – 0.6 Hz, b) In the region 0.75 – 2 Hz.
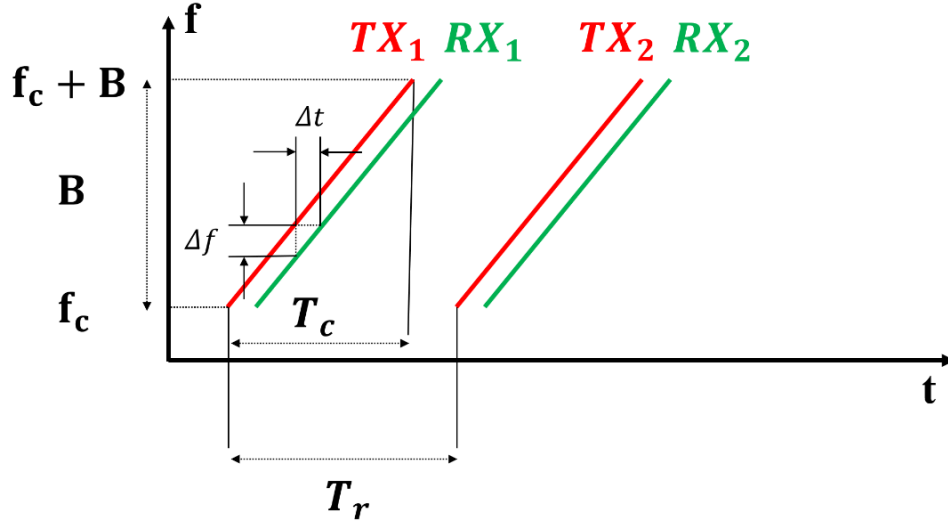
Figure 4.4. In the TDM-MIMO scheme, the TXs operate in an alternative way.

If multiple TX antennas in TDM-MIMO scheme are used, where m^{th} TX location is $d_m = (m-1)d_{TX}$ and d_{TX} is the separation between two TX antennas. Based on (4.4), the transmitted signal at m^{th} TX is:

$$x_m(t) = A_{Tm}\cos\left\{2\pi f_c[t-(m-1)T_r] + \frac{\pi B}{T_c}[t-(m-1)T_r]^2 + \frac{2\pi}{\lambda}d_m\sin\theta_{TX}\phi_m(t)\right\} \quad (4.5)$$

where T_r is the switching time between TX antennas in TDM scheme and θ_{TX} is the departure angle from m^{th} TX to target. The signal received, at n^{th} RX at location $d_n = (n-1)d_{RX}$ where d_{RX} is the separation between two RXs, is:

$$x_{mn}(t) = \alpha_n A_{Tm}\cos\left\{2\pi f_c[t-(m-1)T_r-t_d] + \frac{\pi B}{T_c}[t-(m-1)T_r-t_d]^2 + \frac{2\pi}{\lambda}d_m\sin\theta_{TX}\right.$$

$$\left. + \frac{2\pi}{\lambda}d_n\sin\theta_{RX} + \phi_{mn}(t)\right\} \quad (4.6)$$

where α_n is reflection coefficient of a target, $t_d = 2R(t)/c$ is the range-dependent time delay from the target at range $R(t)$ and θ_{RX} is the arrival angle from the target to n^{th} RX antenna. The received signal in (4.6) is mixed with transmitted signal in (4.4) and after I/Q mixing the signal is approximated as:

$$f_{mn}(t) = A_{mn}e^{j\left\{2\pi f_c[(m-1)T_r+t_d] + \frac{\pi B}{T_c}[(m-1)T_r+t_d]^2 + 2\pi f_b t + \Delta\phi_{mn}(t)\right\}}$$

$$\times e^{j\left[\frac{2\pi}{\lambda}(d_m\sin\theta_{TX}+d_n\sin\theta_{RX})\right]} \quad (4.7)$$

where A_{mn} is the received signal power at (m^{th}, n^{th}) TX-RX pair, $f_b = B[(m-1)T_r + t_d]/T_c$ is the beat frequency. The residual phase noise $\Delta\phi_{mn}(t)$ and the term $\frac{\pi B}{T_c}[(m-1)T_r + t_d]^2$ can be neglected in short range radar practical applications [19]. The beat signal after I/Q sampling can be expressed for the kth ADC sample and l^{th} chirp as [19]:

$$f_{mn}(k,l) = A_{mn}e^{j\left\{2\pi f_c(m-1)T_r + 2\pi f_b kT_f + \frac{4\pi}{\lambda}R\left(kT_f + lT_s\right)\right\}} \times e^{j\left[\frac{2\pi}{\lambda}(d_m sin\theta_{TX} + d_n sin\theta_{RX})\right]} \qquad (4.8)$$

where T_f is fast-time ADC sampling interval and T_s is slow-time sampling interval. Since the chest displacement due to vital sign is slow (typically < 3 Hz), no changes in phase during chirp time (fast-time axis) could occur. Therefore, one only needs to measure phase changes between successive chirps (slow-time axis) for a vital sign estimation. If the target is stationary at range R_{target}, then from [19]:

$$R\left(kT_f + lT_s\right) \approx R_{target} + R(lT_s) \qquad (4.9)$$

The phase shift received for (m^{th}, n^{th}) TX-RX pair is then:

$$\phi_{mn}(lT_s) = \frac{4\pi R(lT_s)}{\lambda} + \frac{4\pi R_{target}}{\lambda} + \frac{2\pi}{\lambda}(d_m sin\theta_{TX} + d_n sin\theta_{RX}) + 2\pi f_c(m-1)T_r \qquad (4.10)$$

From (4.10), the first term is the phase change due to chest displacement on slow-time axis. The latter three terms affect the phase induced from vital sign if there are large body motion. Therefore, it is necessary to compensate for these phase errors in imaging or velocity extraction applications. The first term of (4.10) can be expressed as:

$$R(lT_s) = \Delta R_r(lT_s) + \Delta R_h(lT_s) + \Delta R_{RBSM}(lT_s) \qquad (4.11)$$

where ΔR_r, ΔR_h are chest displacements due to respiration, heartbeat and ΔR_{RBSM} is the body displacement due to RBSM that are modeled in (4.1) – (4.3).

4.4 Received Radar Signal from Vital Sign Signal and RBSM

From (4.8), assuming the signal received at $TX_1 - RX_1$ pair (i.e. $m = n = 1$), the I/Q signal

sampled by the ADC at the target distance R_{target} along the slow-time axis can be simplified as:

$$I(t) = A_I \cos \left[\frac{4\pi}{\lambda} \left(\Delta R_h(t) + \Delta R_r(t) + \Delta R_{RBSM}(t) \right) + \phi_I \right] + n_I \qquad (4.12)$$

$$Q(t) = A_Q \sin \left[\frac{4\pi}{\lambda} \left(\Delta R_h(t) + \Delta R_r(t) + \Delta R_{RBSM}(t) \right) + \phi_Q \right] + n_Q \qquad (4.13)$$

where A_I, n_I, ϕ_I and A_Q, n_Q, ϕ_Q are magnitude, phase, and DC offsets from the I/Q channels of ADC. Due to imbalance issues which are usually present in the hardware ADC, these parameters may not be equal between I/Q channels, and it requires compensation methods to correct these imbalances. However, in the MMWCAS-RF-EVM radar device that we are using in this dissertation, the IQ imbalance issue has been corrected internally using a frequency-independent algorithm that adapts blindly with the received signal [68]. Therefore, we can assume that the level of differences between of A_I, n_I, ϕ_I and A_Q, n_Q, ϕ_Q exist but are negligible in this radar device. On the complex plane, because $A_I \simeq A_Q$ since there is negligible I/Q imbalance issue in this radar device, the I/Q components will form a constellation that presents the circular shape due to the oscillation of the periodic terms such as $\Delta R_r(t)$ and $\Delta R_h(t)$. However, if a different radar device is used and if the I/Q imbalances on that hardware is severe, i.e. $A_I \neq A_Q$, the constellation is no longer circular but is deformed into elliptical shapes [69]. For $\Delta R_{RBSM}(t)$, as it is not a periodic component, it will cause a drift in the original circular constellation to a new origin [70]. Figure 4.5 shows a comparison between the constellation of the same signal in Figures 4.1 and 4.2 with and without RBSM. It can be shown in Figure 4.5a that if we assume $\Delta R_{RBSM}(t) = 0$, $A_I \simeq A_Q$, $\phi_I \simeq \phi_Q$, $n_I \simeq n_Q \simeq 0$, in (4.12) and (4.13), then the constellation is a clean circular shape at the origin (0,0). If there is $\Delta R_{RBSM}(t)$ and small level of n_I and n_Q, the same constellation is shifted
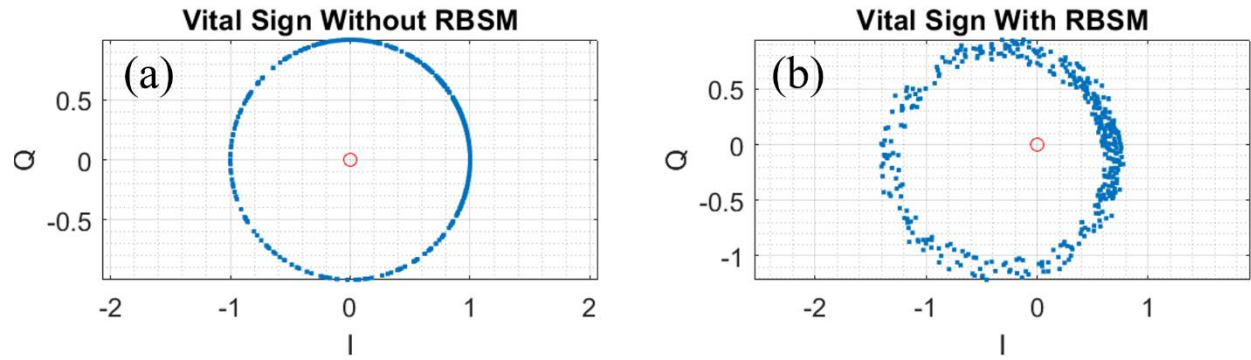
Figure 4.5. Simulated Constellation Diagram for received radar signals a) without RBSM and hardware noises, b) with RBSM and hardware noises.

to the new origin as shown in Figure 4.5b and the constellation points vary in a tolerable region. It will be discussed in the next chapter that the constellation shift due to body drifts also affects the accuracy of RR/HR estimation. Thus, it is necessary to correct the constellation as a pre-processing step prior to estimation of RR/HR. The shifted constellation can be expressed as:

$$I_{withRBSM}(t) = I(t) + dc_i \qquad (4.14)$$

$$Q_{withRBSM}(t) = Q(t) + dc_q \qquad (4.15)$$

where dc_i and dc_q represent the new origin of the shifted constellation.

CHAPTER V

PROPOSED SIGNAL PROCESSING TECHNIQUES

This chapter describes our proposed signal processing chain to accurately estimate RR/HR of SUTs under quasi-static scenarios. We show that by employing multiple MIMO channels, we can achieve better accuracy compared with single channel radar. To reduce the complexity and computational time, Maximal Ratio Combining (MRC) is employed to combine signals from separate channels into one for processing RR/HR information. In scenarios where the $3^{th} - 4^{th}$ harmonic components from respiratory signals can interfere with the heartbeat signals and make it more difficult to estimate HR, we introduce an automatic HBT extraction technique and continuous wavelet transform to help reduce the harmonic levels and increase the magnitude of heartbeat signal. Simulated results will first be shown to analyze and validate the proposed HBT extraction technique. Then, experimental results for quasi-static SUT will be shown to demonstrate the robustness of our signal processing chain. Analysis and results for SUTs under scenarios with higher RBSM interferences will be shown in the next chapter.

5.1 RR/HR Estimation in Quasi-Static Scenarios

In this chapter, we consider the scenarios where there are minimal interferences of RBSM. Therefore, the term ΔR_{RBSM} in equation (4.11) can be negligible and the radar should capture only chest displacement due to respiration $\Delta R_r(t)$ and heartbeat $\Delta R_h(lT_s)$. Since the respiratory signal is several orders of magnitude larger compared with heartbeat signal and is not purely sinusoidal, there are multiple harmonics of respiratory signals that also have higher magnitudes than heartbeat signal. Therefore, even though there are minimal random body motion in this case, respiratory

59

harmonics need to be suppressed to ensure high accuracy of HR estimation which will be shown in the next example. Processing chain on received radar signals in equation (4.8) from MIMO channels for estimating RR/HR is visualized in Figure 5.1.

As shown in the block diagram, the first step is to localize subject under test (SUT) in the scene by performing a range FFT of the complex ADC data in equation (4.8). This would result in a range profile of all objects in the scene. As the SUT is in front of the radar, their reflected signals should be strongest compared with other background clutters. Therefore, the range information of the SUT, i.e. their range bins, can be obtained on all MIMO channels. Next, the complex range profile values at the SUT's range bin will be extracted. This complex value is referred as a constellation point and similar to the equations (4.12) – (4.13). By extracting the constellation point as a function of time, we can determine the SUT's chest displacement due to respiration and heartbeat. As discussed in Chapter 4, a constellation correction technique must first be applied to shift the constellation back to the origin (0,0). This is because even under quasi-static scenarios, there are still body drift that make the original constellation shifted to a random origin. After the constellation correction step, phase extraction and impulse-like noise removal are then applied to obtain a clean chest displacement signal which contain information of RR and HR.

In scenarios which the SUTs are lying on beds or sitting on chairs, the interferences from RBSM, especially with upper body, should be minimal. Thus, the Maximal Ratio Combining (MRC) can be used to effectively combine chest displacement signals captured by all MIMO channels together. This helps to reduce the computational complexity as only one combined signal will be processed for RR and HR instead of multiple separate MIMO channels. To determine RR, the combined signal is passed through a band-pass filter (BPF) with passband $0.1 – 0.6$ Hz to remove any DC components. Then, RR can be found by finding the peak of frequency spectrum of the
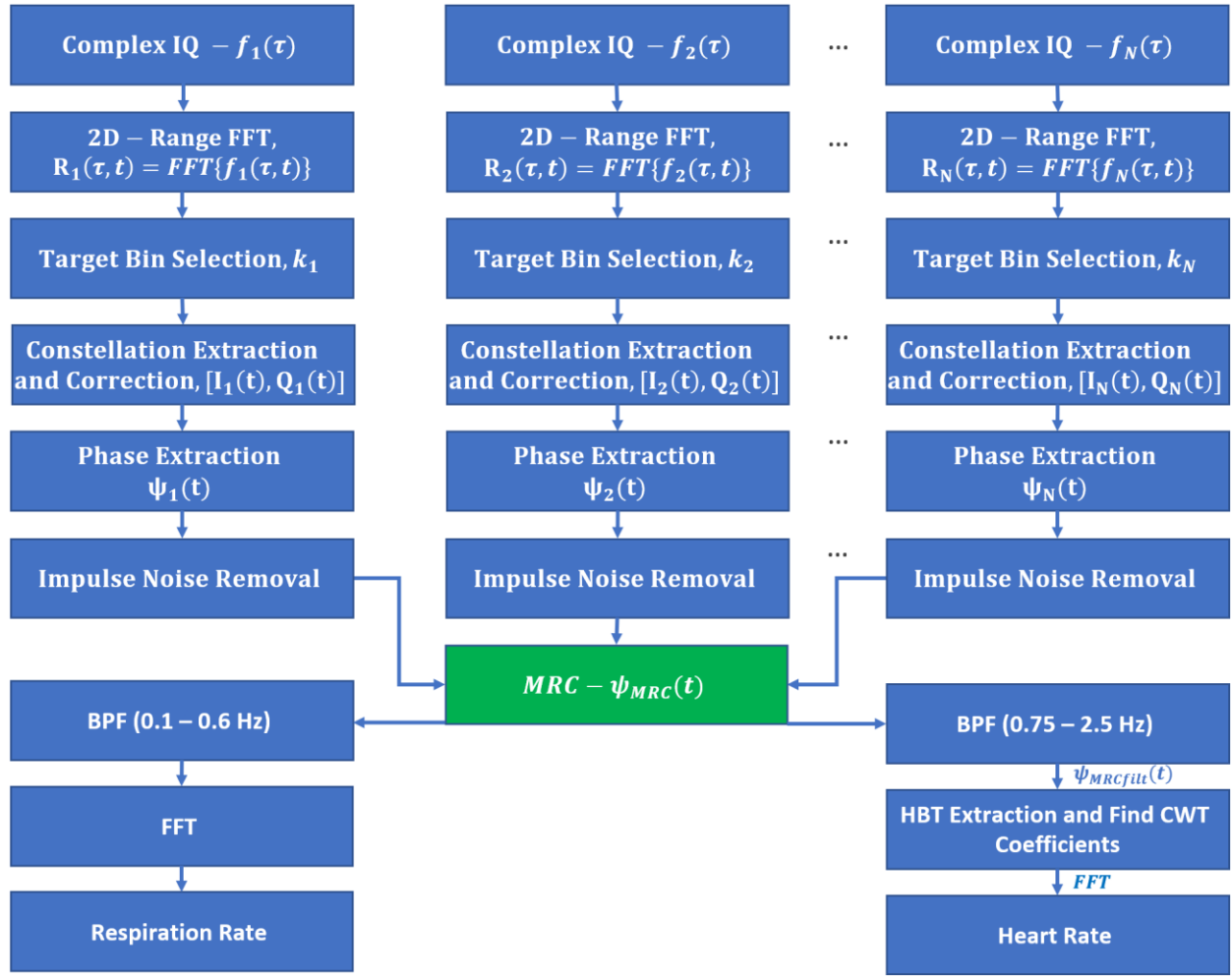
Figure 5.1. Proposed Chain of Signal Processing for RR/HR Estimation.

filtered signal. For HR estimation, the combined signal is passed through another BPF with passband 0.75 – 2.5 Hz. Then, we extract an HBT based on the constellation diagram from a separate channel. This HBT will be used to magnify the heartbeat signals by calculating CWT coefficient. Finally, accurate HR is determined by finding the peak from the frequency spectrum of the CWT coefficient signal. In the next sections, we discuss in detail the processing steps above.

5.2 Range FFT and Target Range Bin Selection

The Range FFT is performed separately on each channel's complex IQ data to obtain the range profile of the scenario under test. The range bin of the target will then be selected at which the variance of the magnitude of Range FFT is maximum. It should also be noted that the selected range bins are expected to be slightly different for separate MIMO channels. This is because the radar being used is a distributed MIMO system, propagating round-trip delay between certain TX-RX pairs might be slightly different which results in the slightly different detected range bin of the SUT between these TX-RX pairs. Figure 5.2 shows some examples for certain MIMO channels.

5.3 Chest Displacement Signal Extraction and Correction

5.3.1 Constellation Correction with Non-linear Least Square (NLLS) Method

As discussed in Chapter 4, the constellation is generally shifted from the origin (0,0) because of the body drift. This has nothing to do with the hardware but is dependent on the SUTs as shown in equations (4.12) – (4.15). For the state-of-the-art radar devices, the IQ channels of the ADC should not have any unbalancing issues. Thus, if the constellation is not properly corrected, they may distort the chest displacement signal extracted at the SUT's range bin which results in increase in harmonics level and make it harder for accurate RR/HR estimation [26-27]. With FMCW radar,
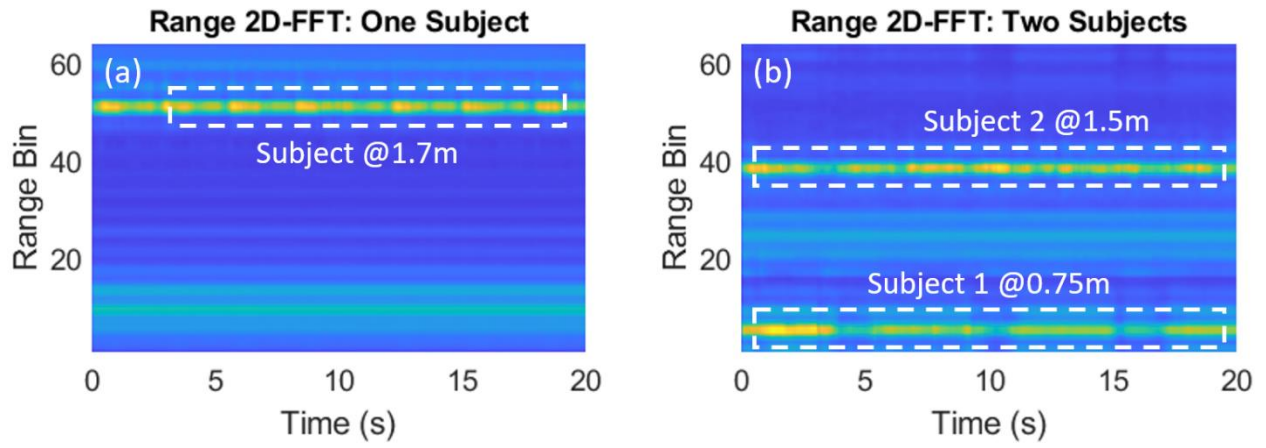
Figure 5.2. Range 2D-FFT matrix from a MIMO channel a) single subject, b) two-subject scenario.

constellation is corrected on the complex range profile at the selected range bin, i.e. $R_i(k_i, t)$. The extracted chest displacement signal (or phase variation to the radar due to chest displacement) is [12]:

$$\Psi_i(t) = arctan\left[\frac{Q(t) + dc_Q}{I(t) + dc_I}\right] \neq arctan\left[\frac{Q(t)}{I(t)}\right] \tag{5.1}$$

where (dc_I, dc_Q) are the shifted origin of constellation points cloud as discussed in Chapter 4. Figures 5.3 shows an example of the constellation before and after correction along with their corresponding phase variation. It can be observed in Figure 5.3b that without correction, the uncorrected constellation produces an inaccurate phase variation. To shift the constellation to the origin, the center (dc_I, dc_Q) of the constellation needs to be estimated. We adopted the NLLS method proposed in [26] to minimize the squared error between the radius and distance of sample points to the hypothetical center point of the cloud. If $\boldsymbol{a_j} = \begin{bmatrix} I[j]+dc_I \\ Q[j]+dc_Q \end{bmatrix}$ is the jth constellation point, then the optimum solution of the hypothetical radius $R_{constellation}$ and shifted center (dc_I, dc_Q) is:

$$\begin{bmatrix} R_{constellation} \\ dc_I \\ dc_Q \end{bmatrix} = (A^T A)^{-1} A^T \boldsymbol{b} \tag{5.2}$$

where $A = \begin{bmatrix} 1 & -2\boldsymbol{a_1^T} \\ 1 & -2\boldsymbol{a_1^T} \\ \vdots & \vdots \\ 1 & -2\boldsymbol{a_M^T} \end{bmatrix}$ is a full column rank matrix for M > 3 and M is the number of constellation

points in the cloud, and $\boldsymbol{b}$ is calculated as $\boldsymbol{b} = \begin{bmatrix} -\|a_1\|^2 \\ -\|a_2\|^2 \\ \vdots \\ -\|a_M\|^2 \end{bmatrix}$.

5.3.2 Arctangent Demodulation (AD)

AD is a sub-category of phase-based method used to extract the phase variation of radar signals due to the oscillatory motion of a target [12]. The output of AD algorithm is the unwrapped phase after constellation correction step when the constellation cloud is shifted back to the origin (0,0). Phase unwrapping is performed on the extracted phase to remove any phase drifts greater than $\pm\pi$ when $\Psi(t)$ is between the boundary of two adjacent quadrants. This is done by adding/subtracting 2π if the phase drift occurs. The extracted phase as the function of time can be calculated as follow which is the angle of each constellation point with respect to the horizontal (real) axis on the complex plane:

$$\Psi_i(t) = unwrap\left\{ arctan\left[\frac{Q(t)}{I(t)}\right]\right\} \tag{5.3}$$

5.3.3 Impulse-like Noise Removal

If the phase drifts still exist; but does not exceed $\pm\pi,$ the phase unwrapping would not obviously remove these phase drifts. As a result, they affect the periodicity of the extracted phase and eventually affects the accuracy of RR/HR estimation. These impulse-like noises are removed by computing a forward $\Psi(t+1) - \Psi(t)$ phase difference for each $\Psi(t)$. If the phase difference exceeds a threshold, then $\Psi(t+1)$ is replaced by an extrapolated value $\Psi_{extrap}(t+1)$ using three-point Lagrange interpolation with previous three values [25]. Figure 5.4 shows the effect of noise removal for several channels and corresponding phases before and after the removal procedure.
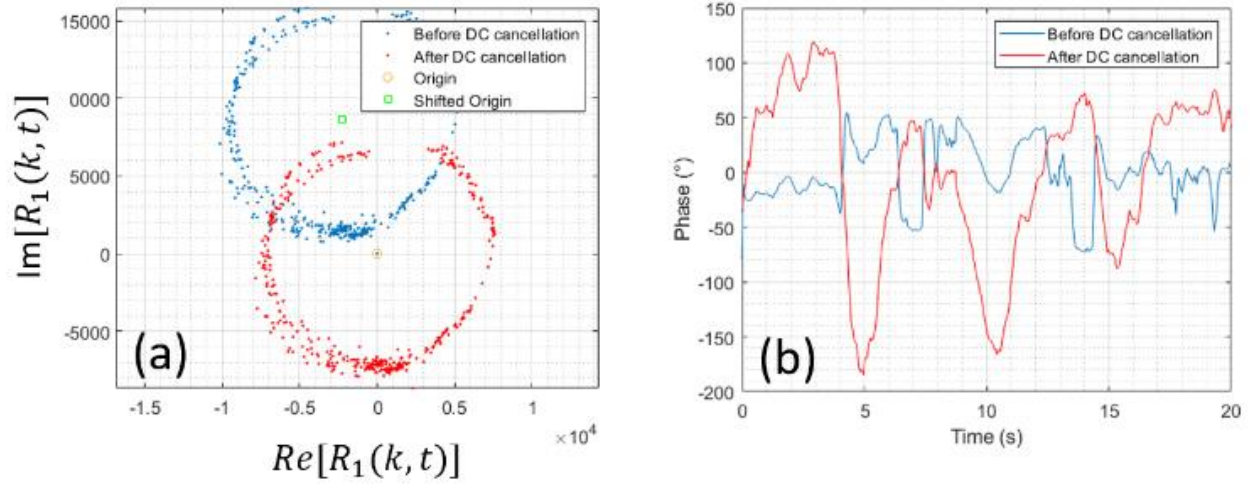
Figure 5.3. a) Constellation correction of the complex signal at the selected target bin, b) Corresponding extracted phase variation due to chest displacement.
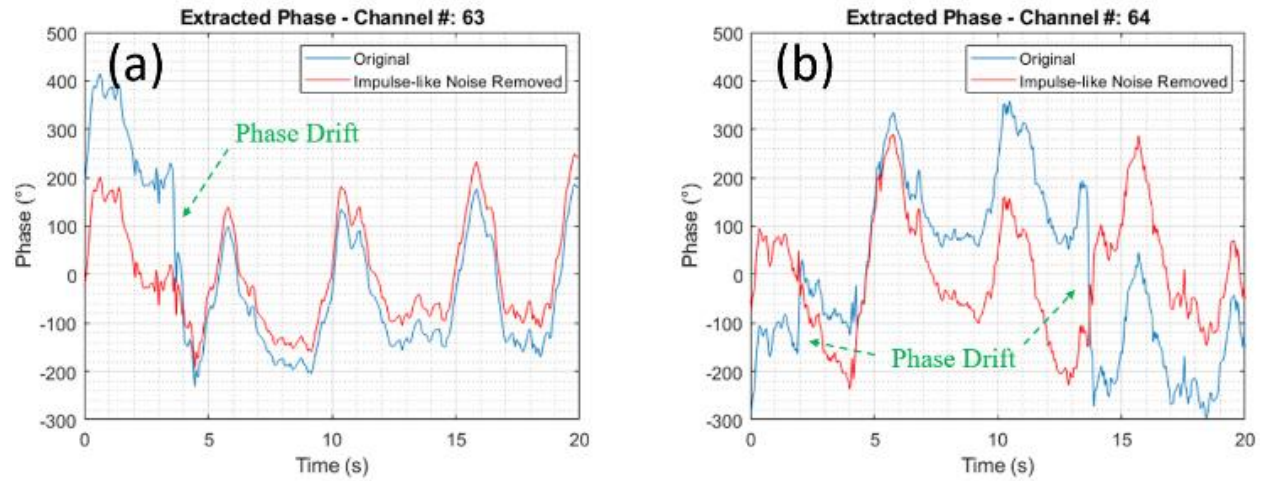
Figure 5.4. Example of Impulse-like Noise Removal on phase variation signals from a) Channel #63, b) Channel #64.

5.4 Maximal Ratio Combining (MRC)

The goal of MRC is to enhance the SNR of respiratory and heart signals by optimally combining the extracted phase variation signals $\Psi_i(t)$ calculated in equation (5.3) from different MIMO channels. Because AD method extracts relative chest displacement on the slow-time axis within separate MIMO channels, each channel produces its own independent version of $\Psi_i(t)$, and since the phase $\Psi_i(t)$ are not affected by their relative antennas' positions and target, there is no need to perform phase compensation to correct the beat FMCW signal. Detailed formulation of MRC is shown below [39-40]:

$$\Psi_{MRC}(t) = \sum_{i=1}^{N} w_i \Psi_i(t) \tag{5.4}$$

where w_i is a weighted coefficient for the ith channel which is directly proportional to the channel SNR. To determine w_i, a cross-correlation matrix is formed based on the time domain signals of the various channels $[\Psi_1(t), \dots, \Psi_N(t)]$:

$$R_{ij} \simeq \int \Psi_i(t)\Psi_j^*(t)dt \tag{5.5}$$

After forming the cross-correlation matrix, eigenvalue decomposition is performed resulting in:

$$R_{ij} = [v_1 v_2 \dots v_N] diag[\sigma_1 \sigma_2 \dots \sigma_N][v_1^* v_2^* \dots v_N^*]^T \tag{5.6}$$

where $\boldsymbol{\sigma_{1-N}}$ are eigenvalues, $\boldsymbol{v_{1-N}}$ are eigenvectors for each channel. MRC method uses the first eigenvector as weights, i.e. $\boldsymbol{w} = \boldsymbol{v_1^H}$, to combine all channels such that:

$$\Psi_{MRC}(t) = v_1^H \Psi(t) \tag{5.7}$$

where H represents a complex conjugate transpose. The eigenvector $\boldsymbol{v_1}$ is normalized; so that its norm is 1.

Identifying and eliminating some bad channels (or outliers) is good practice in improving MRC performance [37]. This process is referred as channel selection. It helps to reduce the contribution of bad channels as manifested in the weights' calculation. Thus, combined $\Psi_{MRC}(t)$ carries only useful information and is not corrupted by noise factors from the bad channels. In this chapter, since we are considering scenarios with minimal interferences from RBSM, channel selection is performed simply as:

1. Find weights vector $\boldsymbol{w}$ with $\Psi_i(t)$ as input to MRC using equations (5.5) and (5.7).

2. Find maximum value w_{max} of the absolute vector $|\boldsymbol{w}|$.

3. For a given threshold $w_{th} = \alpha w_{max}$ with $\alpha = [0,1]$, eliminate the channel i^{th} where $|w_i| < w_{th}$. Higher value of α results in more channels elimination. The idea is to make sure phases $\Psi_i(t)$ from certain channels that possess strong periodic patterns due to chest displacement are selected. For scenarios where there are more interferences from RBSM, more robust approach should be employed for channel classifications so that higher accuracy can be achieved.

5.5 RR Estimation

Under scenarios where there are minimal interferences from RBSM, the radar only captures chest displacement due to respiration and heartbeat. As the magnitude of respiratory signal is significantly higher than that of heartbeat signal, RR can be estimated by first passing the combined signal $\Psi_{MRC}(t)$ through a band-pass filter (BPF) with passband frequency 0.1 – 0.6 Hz. This is because the possible RR of a normal human subject is within this range. In this dissertation, 8th-order Infinite Impulse Response (IIR) bandpass filters are used. Next, the Fast Fourier Transform (FFT) of the filtered signal is calculated and the maximum of the spectrum should occurr at the

respiratory frequency. Figure 5.5a shows the magnitude response of the BPF used for RR estimation. Figures 5.5b and 5.5c show the raw phase variation and its filtered version along with their frequency spectrum. It can be seen that the peak of the spectrum occurs at the respiratory frequency which can be validated by the ground truth result.

5.6 HR Estimation using HBT Extraction and CWT

Typical heart waveform includes a dicrotic notch created due to the closing of the cardiac valve and reflections of the vasodile blood wave at blood vessels and forks [71]. In some cases, a second notch caused by the venous pulse effect produces another local maximum prior to the main maximum of a heartbeat signal [71]. Since there are several effects on the thorax area, the shape of heartbeat signal can be different for various subjects [53, 71-72]. Therefore, if we can adaptively extract a HBT that contains significant amount of heartbeat signal from the SUTs, the accuracy of heart rate detection can be significantly improved [53]. This section discusses our proposed approach for an automatic HBT extraction using information from the constellation diagram to improve the accuracy of HR estimation.

5.6.1 Heartbeat Template (HBT) Extraction

As discussed in Section 4.4 from Chapter 4 and Section 5.3.1 above, the constellation diagram [I(t),Q(t)] contains information not only about respiratory and heartbeat signals but also RBSM signals. Ideally, a periodic motion would result in a perfect circle on the constellation diagram. However, this is not the case for the physiological motions caused by heart and lungs as there are induced noises from body drifts that distorts these signals. To investigate the correlation between constellation diagram and its phase variations, Figure 5.6 shows an example of signals acquired

69
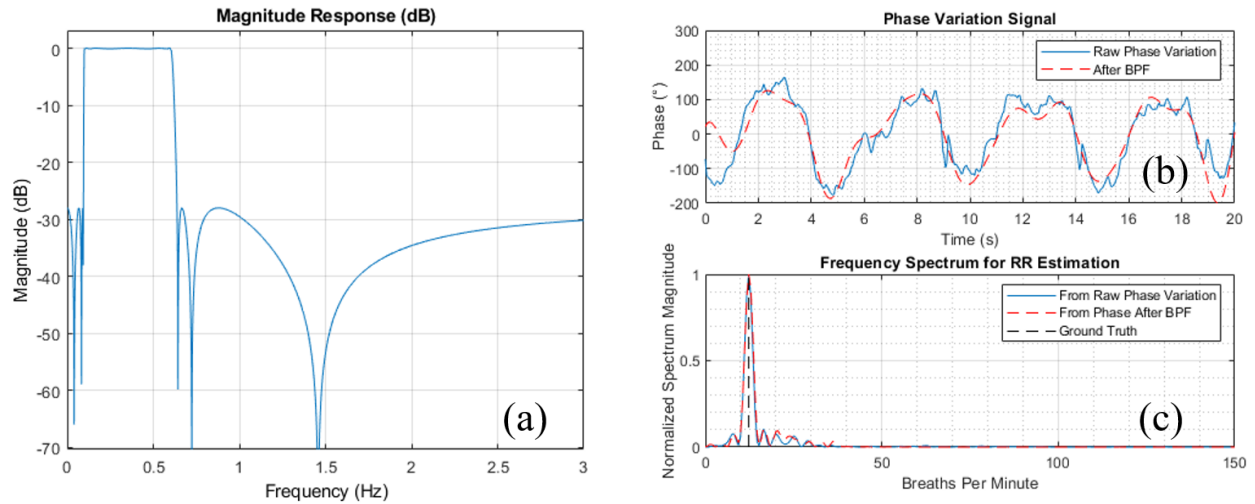
Figure 5.5. a) Magnitude Response in dB of the BPF with passband 0.1 Hz – 0.6 Hz used for RR estimation, b) An example of raw phase variation signal and filtered signal, c) Frequency spectrum of the signals in Figure 5.5b and results from ground truth.

from a sitting SUT with minimal RBSM. Let P_j be a constellation points where j^{th} is the time-frame number, then the distance between two adjacent constellation points j^{th} and $(j+1)^{th}$ in time is defined as $d_{j,j+1}$. Additionally, the angle $\theta_{j,j+1,j+2}$ is defined as the angle between two vectors formed by three consecutive constellation points in frames j^{th}, $(j+1)^{th}$ and $(j+2)^{th}$. Figure 5.6a shows an example of the chest displacement signal obtained using AD method for a sitting subject. With the frame rate of 20 Hz, a 20-second duration signal is equivalent to 400 frames. For the analysis of HBT extraction, we use frame number so that it is easier to identify and track the frames. Figure 5.6b shows the corresponding constellation diagram $[I(t), Q(t)]$ obtained from the target range bin k^{th}. It can be seen that the constellation diagram can be divided into two main regions where the distances of the points are further away (larger radius curvature) in one and closer (smaller radius curvature) in the other. Figure 5.6c zooms into few specific frames $112^{th} - 115^{th}$ and $139^{th} - 142^{th}$, in which they correspond to both the respiratory and heartbeat signals. This is because the frames $112^{th} - 115^{th}$ belongs to the exhaling period of respiration while $139^{th} - 142^{th}$ belongs to the resting period after exhalation that we can see the modulating heartbeat signal. It can be observed in Figure 5.6d that the distances between consecutive points in the heartbeat signals region are small $\left(d_{139,140} = 0.018, d_{140,141} = 0.008, d_{141,142} = 0.004\right)$ while the changes in angles between consecutive vectors are faster (from $23°$ to $112°$). This is opposite in respiration signals' region where distances between consecutive points are larger $\left(d_{112,113} = 0.27, d_{112,113} = 0.19, d_{114,115} = 0.14\right)$ and the changes in angles are slower (from $154°$ to $162°$). This can be explained by the fact that the heartbeat signals have significantly smaller magnitude (represented by the displacements/distances between consecutive constellation points) than respiratory/RBSM signals. Thus, the arc created by heartbeat's constellation points is relatively small, which makes the angles between consecutive vectors change their directions faster
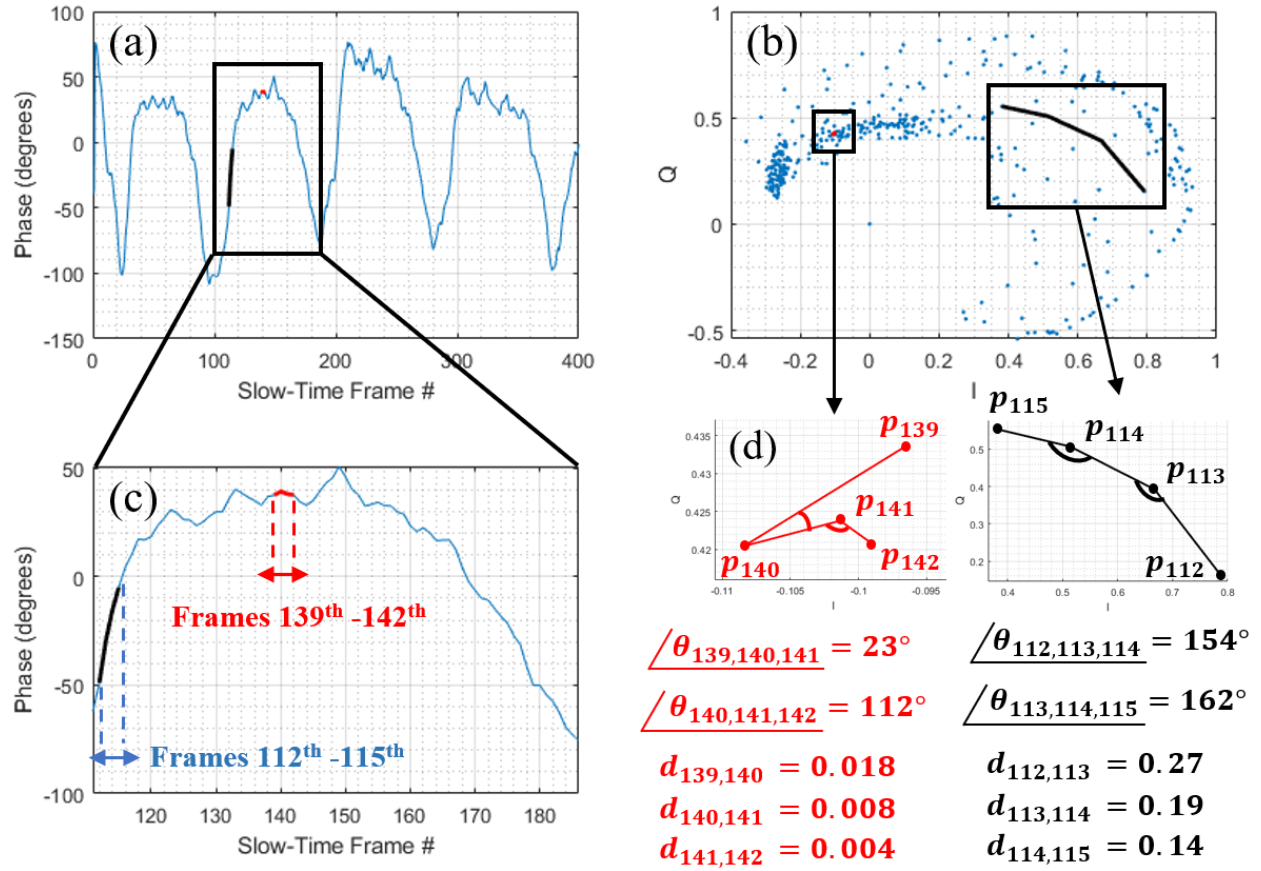
Figure 5.6. a) Chest displacement obtained using Arctangent Demodulation (AD) method, b) Corresponding Constellation Diagram, c) A zoom-in of frames $112^{th} - 115^{th}$ and $139^{th} - 142^{th}$, d) A zoom-in of constellation graph into the interested frames.

than that of the respiratory/swaying-body motion signals. Based on these constellation diagrams'

characteristics, we propose a method to automatically extract the HBT:

(i) As distances between two consecutive constellation points due to heartbeat are much closer

than the ones produced by respiration/RBSM. By setting a threshold value d_{th}, if $d_{j,j+1} \leq d_{th}$,

then frames j^{th} and $(j+1)^{th}$ are valid for a HBT.

(ii) Similarly, given that angles formed between two vectors from three adjacent constellation

points change much faster due to heartbeat signals than those generated from respiration/RBSM.

Then upon setting a threshold value θ_{th}, if $\theta_{j,j+1,j+2} \geq \theta_{th}$, then frames j^{th} and $(j+1)^{th}$ are

considered appropriate for a possible HBT.

(iii) A frame that can be considered valid for a possible HBT must satisfy conditions (i) and (ii).

Additionally, an HBT is considered valid if there is at least 2 seconds of constellation data

(equivalent to 40 frames) that satisfy conditions (i), (ii). This is because the 2-second templates

should contain at least one cycle of heartbeat signal [21]. It should be noted that there is no upper

limit duration for extracting the HBT. As long as the frames satisfy the above conditions, they will

be considered valid for the HBT. Take Figure 5.7, which shows the chest displacement signal of a

sitting SUT as an example. There are four valid HBT satisfying conditions (i)-(iii). HBTs #1 and

#2 have 2.5-second duration while HBT #3 and HBT #4 have 3-second duration. Also, if any

channel does not produce a valid HBT, it is eliminated from the estimating procedure.

From Figure 5.7, several observations are made:

Observation 1: Multiple HBTs can be extracted from the original physiological signals. Thus,

making the HR estimation more accurate as there is more heartbeat information from different

HBTs. Because we only deal with quasi-static or with RBSM scenarios from SUT in this

dissertation, there always exists signal segments which contain only respiratory and heartbeat signals [53]. Thus, valid HBT can always be extracted if only these scenarios are considered.

Observation 2: Figures 5.7b and 5.7c demonstrate how the selected regions comply with conditions (i) and (ii). Although more robust analysis can be done to find optimal values of d_{th} and θ_{th}, we simply choose d_{th} and θ_{th} as the mean values of all frames' distances and angles in this dissertation. It should be noted that while most of the distances $d_{j,j+1} \leq d_{th}$ (condition (i) is satisfied) as the magnitude of heartbeat signal is small, there are few numbers of frames that have angles $\theta_{j,j+1,j+2} < \theta_{th}$ (condition (ii) is not satisfied) but they are still considered valid. This can be explained by the fact that while constellation points due to heartbeat may change their direction faster and more frequently, there are still frames where their angles do not change that significantly as the nature of the heartbeat signal is oscillatory and might still be on an circular arc. Thus, for a given frame j^{th} that only comply with condition (i), we should check several adjacent frames $j^{th} + 1, j^{th} + 2$, etc. to make sure any valid frame is not overlooked. To make sure each HBT has at least 2-second duration (i.e. 40 time frames) to comply with condition (iii), for potential HBT with more than 30 frames, we extended 5 frames at the beginning and at the end of the HBT so that we do not leave out potential HBT that already has more than 30 frames. This explain why the boundaries of the HBTs shown in Figure 5.7b have several frames that do not comply with conditions (i) and (ii).

Observation 3: A closer look at Figure 5.7b shows that the periodicity of distances data also correlates well with that of the phase variation data in Figure 5.7a, i.e. both have similar periodicity T_{RR} of respiratory signal. This makes sense as the distances $d_{j,j+1}$ between constellation points j^{th} and $(j + 1)^{th}$ should also reflect the periodicity of all physiological motions during the measurements. While this is an interesting observation and might be useful for RR estimation, we
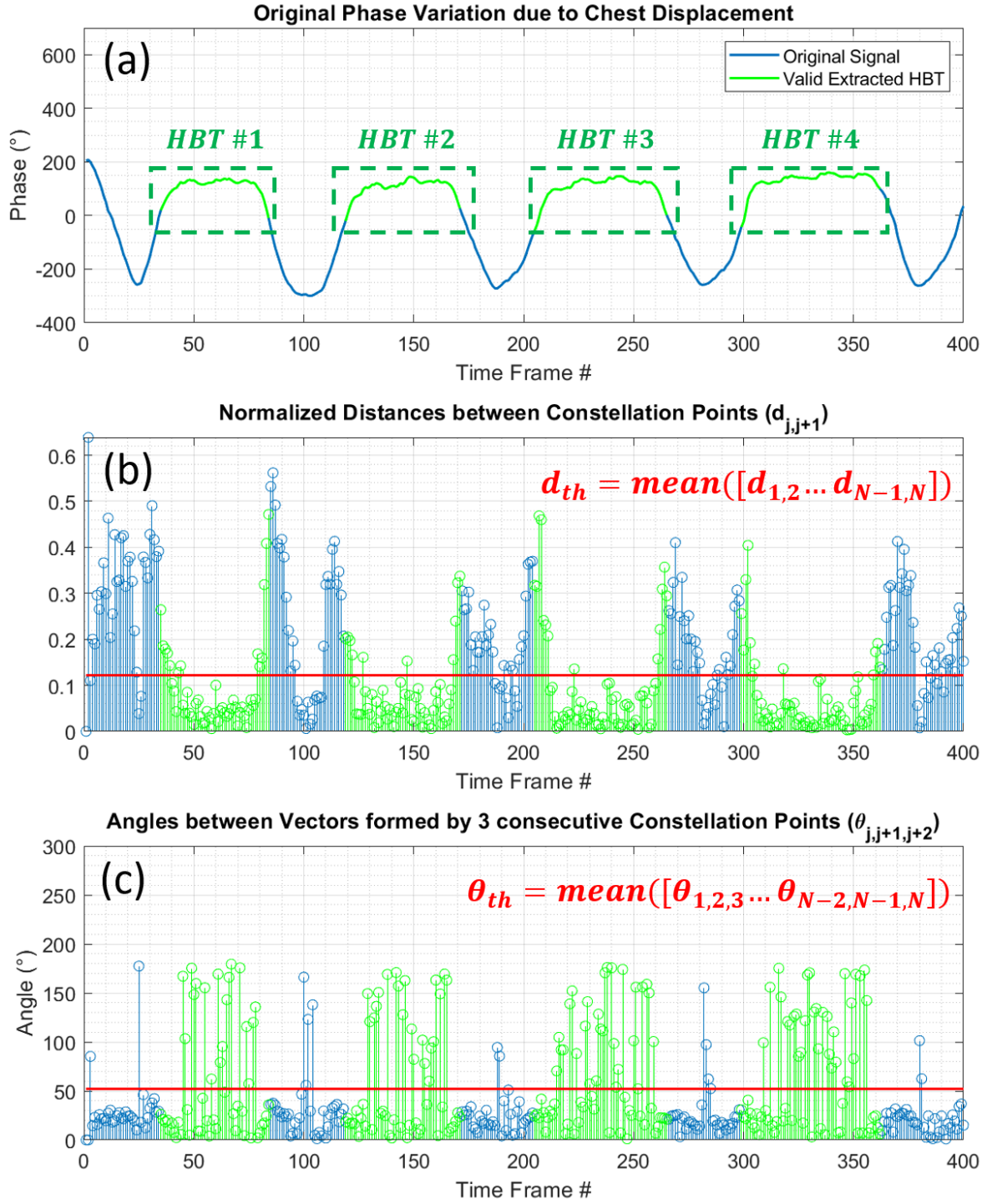
Figure 5.7. Signal Analysis for Sitting Subject, a) Chest displacement obtained using AD method, b) Normalized distances $d_{j,j+1}$ between consecutive constellation points, c) Angles between vectors formed by consecutive constellation points $\theta_{j,j+1,j+2}$.

do not investigate this further as it is not challenging to estimate RR even when there are RBSM.

Observation 4: The constellation diagrams are used to determine the *time frames* that are valid for a HBT. The HBT itself is then extracted from the phase variation signal found by using AD method. It can be seen from [53] that while it is challenging to identify a good HBT from physiological waveform that is partly distorted by body motion. The distances/angles data calculated from constellation points make it easier for this task. This way we can avoid extracting the segments that are already distorted by the RBSM.

After extracting the valid HBT, the next step is to pre-process it to remove several low-frequency components. The original HBTs, i.e. HBT_{ori}, still contain information about the respiratory signal and respiratory harmonics, these low-frequency components need to be removed to achieve better performance. This can be done by using a 5th-order polynomial fitting [53, 73] to approximate the initial HBTs. Let the polynomial fitted version of HBT_{ori} be HBT_{fitted}. The final version of HBT can be found by subtracting the initial HBTs with the polynomial fitted version:

$$HBT_{new} = HBT_{ori} - HBT_{fitted} \tag{5.8}$$

Figures 5.8a, 5.8c, 5.8e and 5.8g show the four original HBTs from Figure 5.7 along with their polynomial fitted versions. It can be shown in Figure 5.8 that the polynomial fitting acts as a moving-average filter to find the trend of the HBTs [53, 73]. Then the new HBT after subtraction in equation (5.8) only recover the heartbeat signals as shown in Figures 5.8b, 5.8d, 5.8f and 5.8h. This approach makes sure there are no low-frequency components interfering with the estimation process and only heartbeat components are contained in the HBT_{new}.

5.6.2 Continuous Wavelet Transform (CWT) with Adapted Wavelet

In time-frequency analysis, CWT measures the correlation between input signal s(t) and compressed/stretched/shifted versions of a wavelet $\Phi(t)$ [74]. For a scale parameter, $a > 0$, and position b, 1D-CWT is defined as:

$$W(a,b) = \int_{-\infty}^{\infty} s(t) \frac{1}{a} \Phi^* \left(\frac{t-b}{a}\right) dt \tag{5.9}$$

where $s(t)$ denotes the input signal, $\Phi(t)$ denotes the wavelet, a, b are scale and position parameters. If $s(t)$ is complex, then $*$ denotes the complex conjugate and CWT is a complex-valued function. An advantage of CWT is that with proper use of the wavelet that is specially adapted to the heartbeat signal, it can improve the effectiveness of heartbeat signal extraction [53, 71-73]. So even if the heartbeat signal is dominated by respiratory harmonics, and since these signals do not resemble the shape of chosen wavelet, their correlation will be low. Following are steps to design adapted wavelet from the HBT_{new} from equation (5.8) and employ CWT for HR estimation:

Step 1: Extract HBT_{new} from constellation diagram and phase variation signals as discussed in Section 5.6.1.

Step 2: Design the wavelet $\Phi(t)$ with the extracted HBT_{new}. To be admissible as a wavelet for CWT, $\Phi(t)$ needs to satisfy two main conditions such that [74]:

$$\begin{cases} \int \Phi(t)dt = 0 & (5.10) \\ \int |\Phi(t)|^2 dt = 1 & (5.11) \end{cases}$$

A 10th-degree polynomial is used with least-square optimization to find the polynomial coefficients satisfying the conditions in (5.10) – (5.11) for approximating the wavelet.
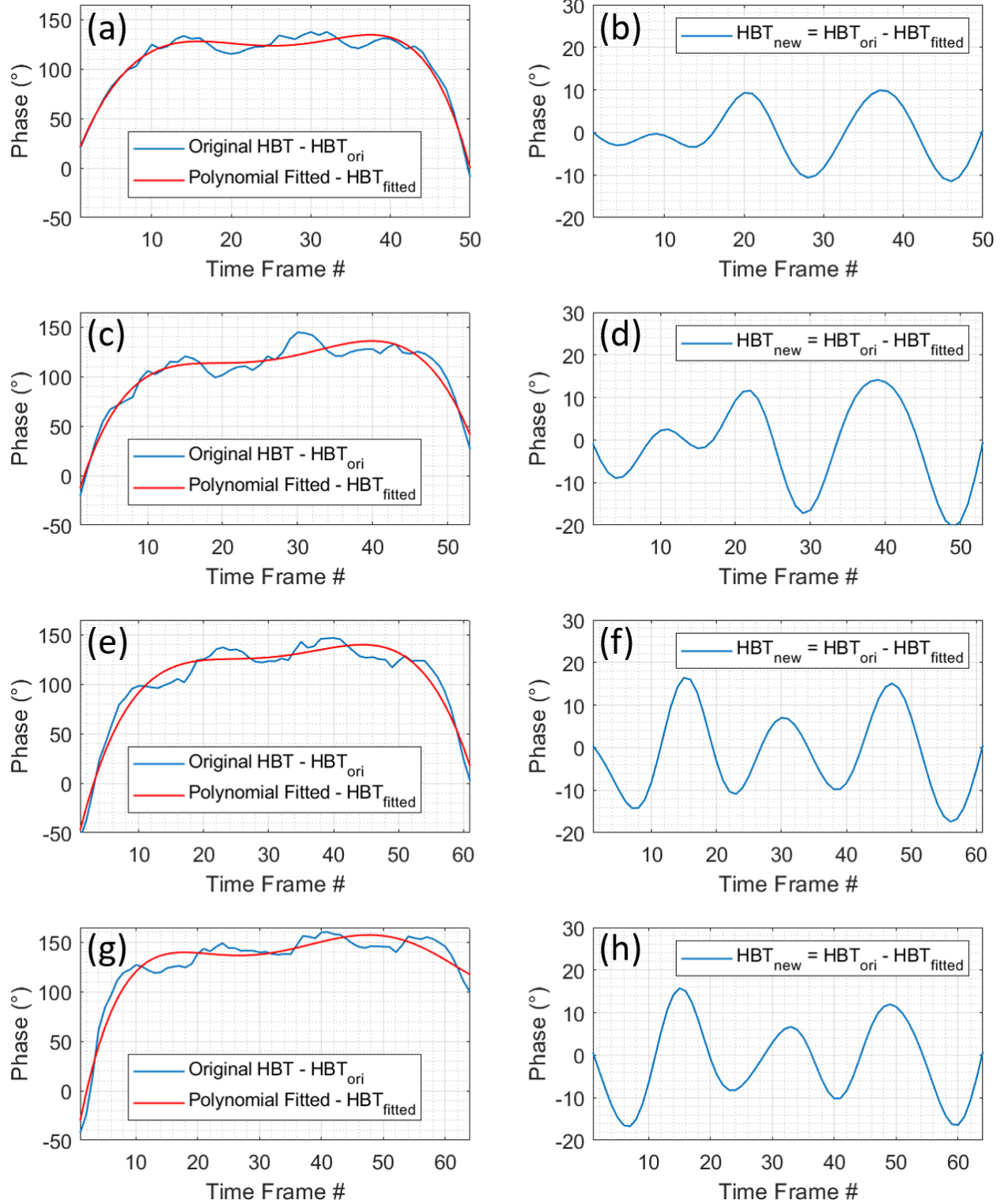
Figure 5.8. a), c), e), g) Original HBT and their polynomial fitted version, b), d), f), h) New HBTs after subtraction using equation (5.8).

Step 3: The combined phase variation signal $\psi_{MRC}(t)$ is first passed through a band-pass filtered with passband 0.75 Hz – 2.5 Hz to filter out lower-frequency components. This is the typical HR range of human subjects [12]. The CWT coefficients $W_1(t)$ is then calculated based on equation (5.9) with $s(t) = \psi_{MRCfilt}(t)$ at scale $a = 1$. This is because adapted wavelet is approximated from the heartbeat waveform, the correlation between itself and the input signal will retain the spectral features of the heartbeat signal. Figure 5.9 shows the magnitude response of the BPF used for HR estimation.

Step 4: As $W_1(t)$ contains the fundamental frequency of the heartbeat signal, Fast Fourier Transform (FFT) is then performed on the wavelet coefficients $W_1(t)$ to estimate HR. To show the effectiveness of the adapted wavelets on suppressing the respiratory harmonics, Figure 5.10 shows a comparison of frequency spectrum between the filtered original phase variation and CWT coefficients $W_1(t)$ calculated using the CWT for each wavelet adapted from $HBT_{new1} - HBT_{new4}$ in Figure 5.8. Figure 5.10 demonstrates reduction of the third/fourth respiratory harmonics level and magnification of heartbeat spectrum. From the normalized spectra in Figure 5.10, heartbeat signals are being interfered by the third/fourth harmonics of the respiratory signals. However, the adapted wavelet reduces these interferences and helps magnify the heartbeat signal so that they can be accurately estimated compared with the ground truth.

5.7 Simulation Results

To validate the robustness of our proposed automatic HBT extraction and CWT with adapted wavelet methods, we first show results with simulated data using the chest displacement and received signal models from equations (4.1), (4.2), and (4.12) – (4.15) that are discussed in Chapter
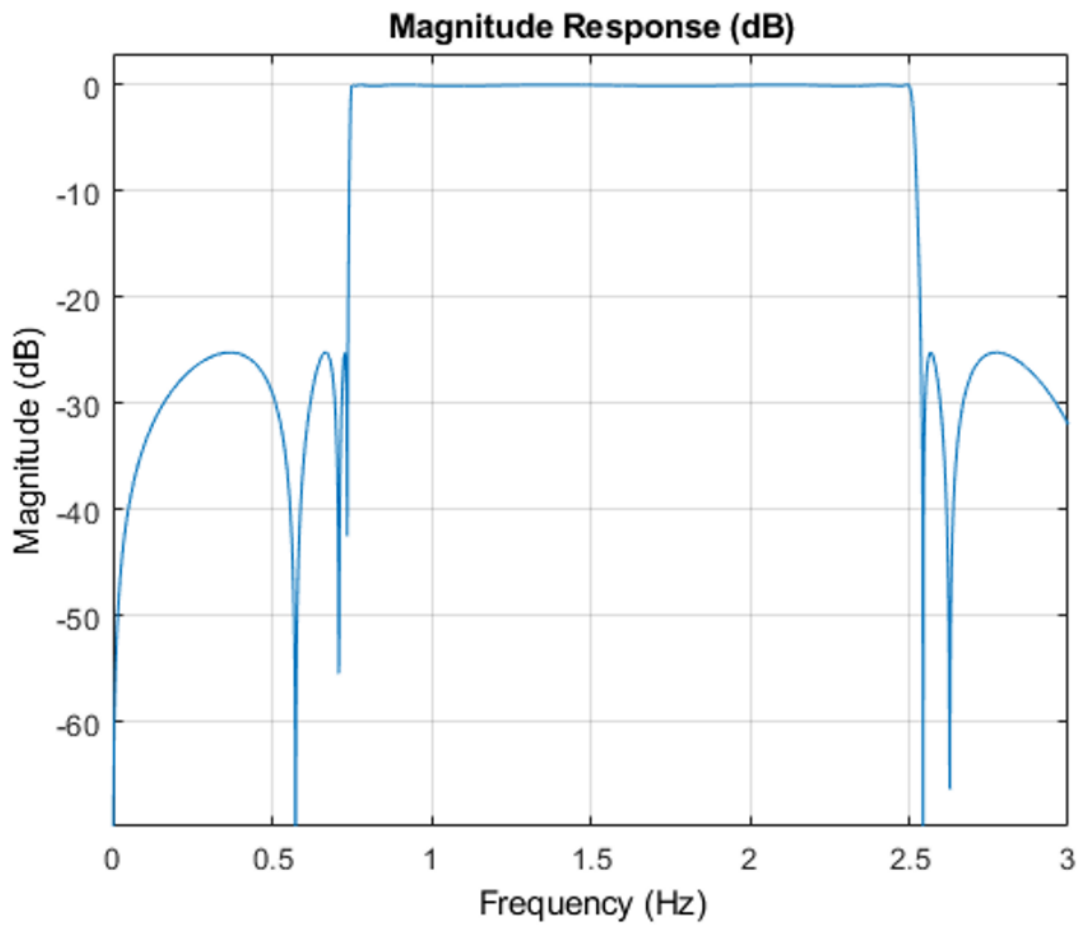
Figure 5.9. Magnitude Response in dB of the BPF with passband 0.75 Hz – 2.5 Hz used for HR estimation
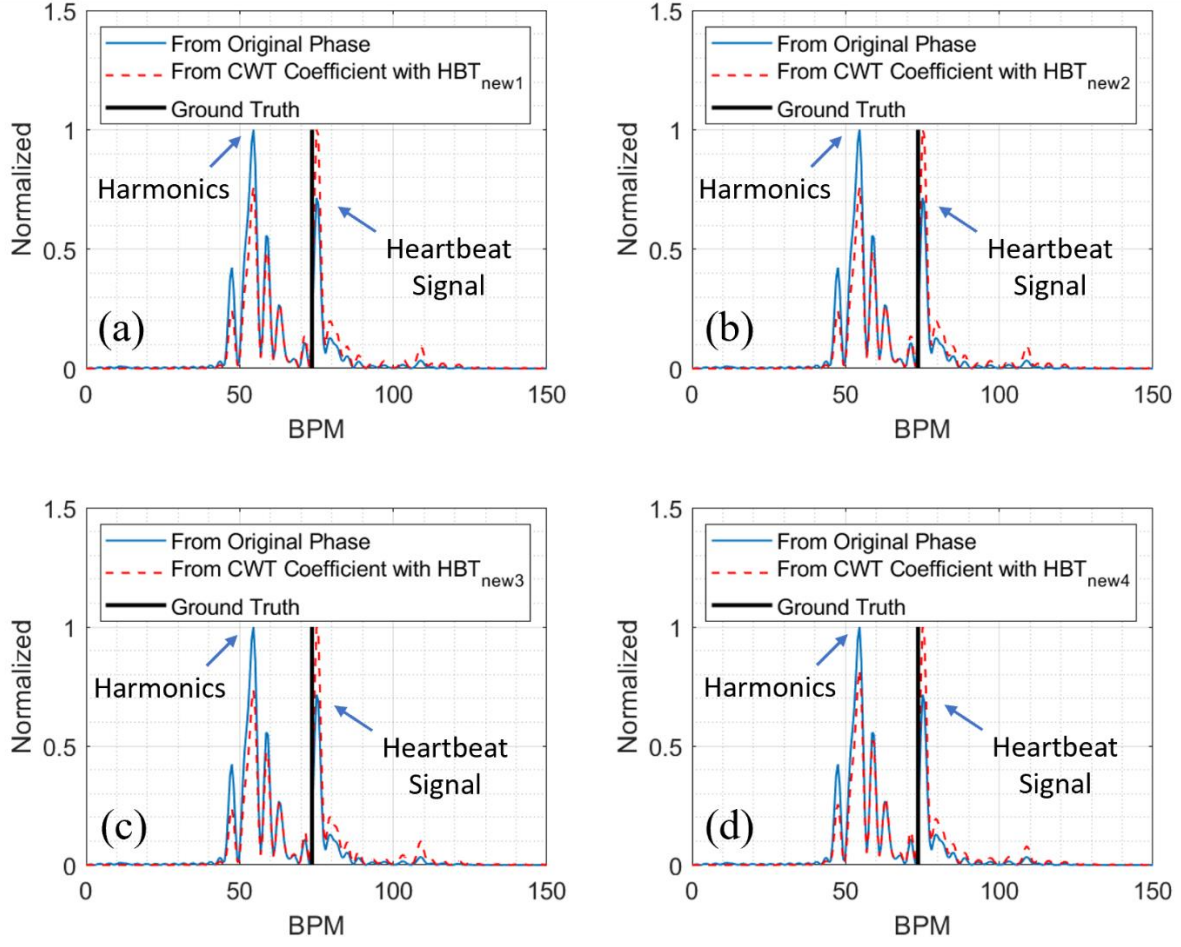
Figure 5.10. Frequency Spectrum of filtered version of original phase variation signal and CWT coefficients with the adapted wavelets from $HBT_{new1} - HBT_{new4}$ shown in Figure 5.8.

4. Since we are considering quasi-static scenarios in this chapter, we will assume that the interfered body movements from RSBM is negligible in these simulations. However, in the next chapter, we will consider the effect of RSBM into the simulated models as well. Table 5.1 shows simulated parameters of chest displacement due to respiration and heartbeat $f_{RR}, f_{HR}, K_b, T_i, T_e, \tau, A_h$ for the 20-second simulation. In this simulation, we select a high value of respiratory rate such as $f_{RR} = 0.18\ Hz$ so that its harmonic components will interfere with the spectrum contents when estimating HR. Therefore, we can show the efficiency of our HBT extraction and CWT with adapted wavelet techniques. Figures 5.11a-c show the simulated chest displacement due to respiratory, heartbeat and combined signal, respectively using equations (4.1) and (4.2) discussed from Chapter 4. In this simulation, the amplitude of displacement due to respiratory signal is almost 30 times higher than that of the heartbeat signal. The constellation from the combined vital sign signals is then calculated using equations (4.12) and (4.13) and is shown in Figure 5.12 below. Since we are neglecting the effect of RSBM, we can see that the constellation is not shifted by body drift effect. Figure 5.13a shows the extracted phase variation by applying AD method to the constellation data in Figure 5.12. Due to phase unwrapping from AD, we observe the vertical offset increasing compared with the original signals in Figure 5.11. It also shows the extracted HBT that comply with the two conditions (i) and (ii) discussed in section 5.6.1 above. We can see that for this simulation, there are 3 HBTs that are considered valid. Figure 5.14 shows the RR estimation by first passing the phase variation signal in Figure 5.13a through the BPF with passband $0.1 - 0.6$ Hz. Then by finding the peak of frequency spectrum, we can determine the RR which agrees well with the true RR (approximately 11 BRPM). Next, the original 3 extracted HBTs shown in Figure 5.13 are further processed by first finding their polynomial fitted versions as shown in Figures 5.15a, 5.15d and 5.15g. Then, the new version HBT_{new} of these HBTs can be found by subtracting

Table 5.1. Simulated Parameters for Chest Displacement due to Respiration and Heartbeat

f_{RR} (Hz)	f_{HR} (Hz)	K_b (mm)	T_i (s)	T_e (s)	τ (s)	A_h (mm)
0.18	1.48	7.65	1.73	3.71	0.23	0.25
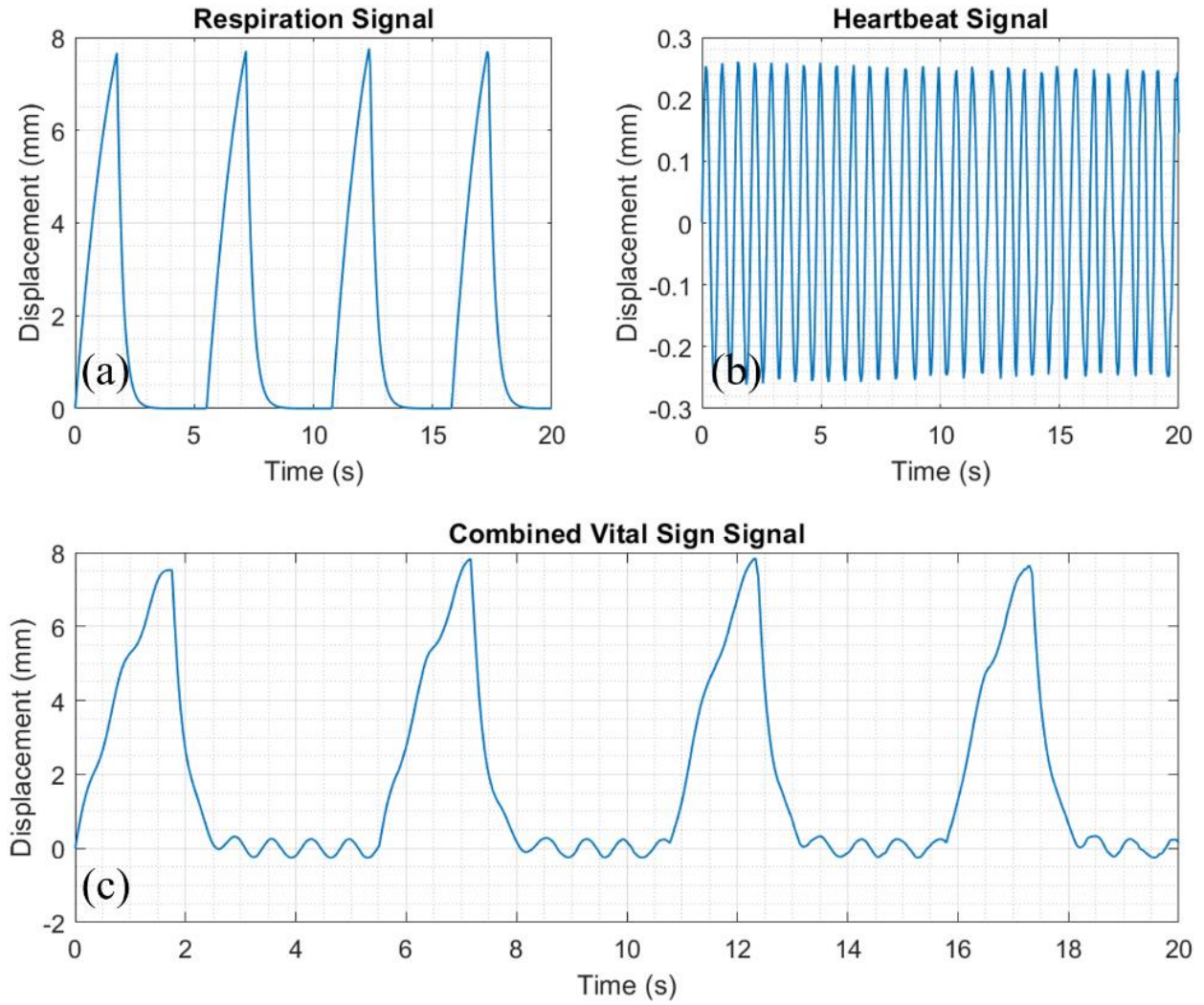
Figure 5.11. Simulated Chest displacement due to, a) Respiration Signal, b) Heartbeat Signal, c) Combined Vital Sign Signal.
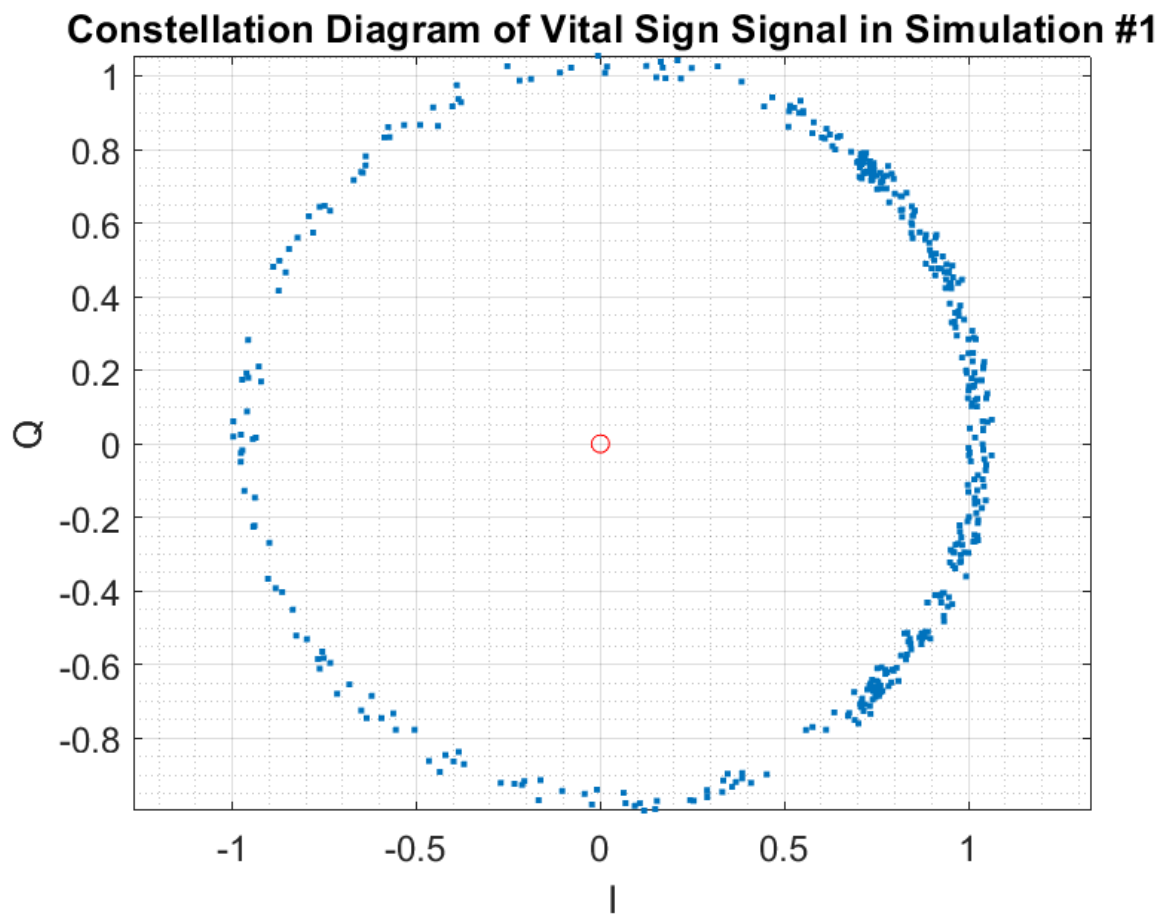
Figure 5.12. Constellation diagram of vital sign signal from simulated data.
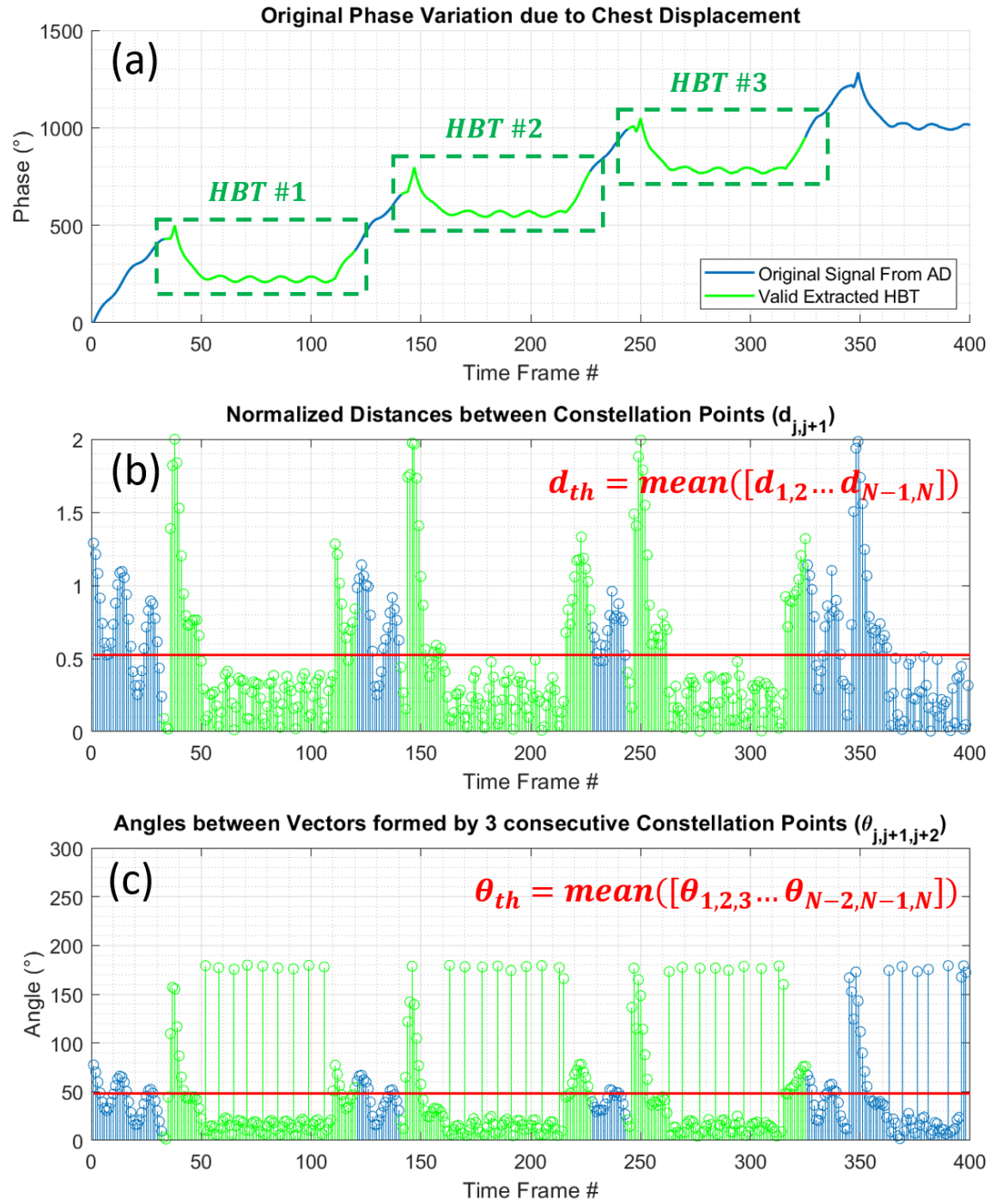
Figure 5.13. Signal Analysis from simulated data, a) Phase variation obtained using AD method, b) Normalized distances $d_{j,j+1}$ between consecutive constellation points, c) Angles between vectors formed by consecutive constellation points $\theta_{j,j+1,j+2}$.
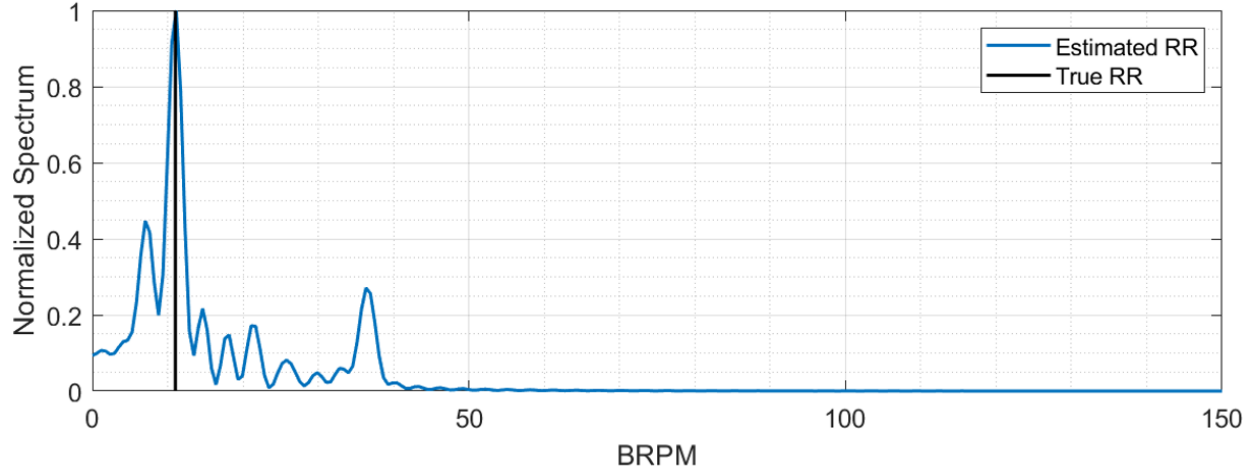
Figure 5.14. Estimation of RR for simulated data.
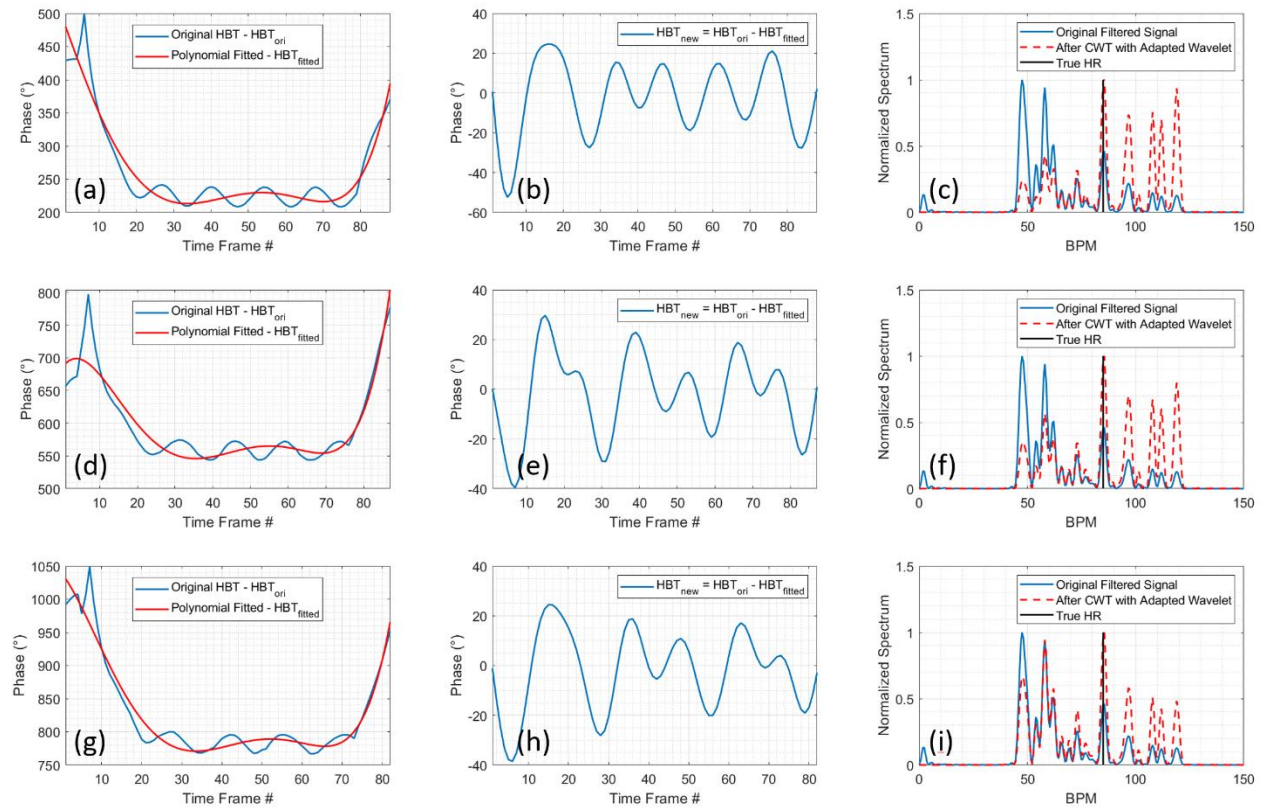
Figure 5.15. a), d), g) Original HBTs and their polynomial fitter versions, b). e), h) New versions of HBTs, c), f), i) Comparisons of frequency spectrum before and after using CWT with adapted wavelet from HBTs.

the original HBT_{ori} with the fitted versions HBT_{fitted} as shown in Figures 5.15b, 5.15e and 5.15h. Figures 5.15c, 5.15f and 5.15i show the comparisons of frequency spectra between the filtered version of the original phase variation and the CWT coefficients using wavelet adapted from the extracted HBT_{new}. We can see that only using the BPF with passband $0.75 - 2.5$ Hz is not sufficient for HR estimation as the $3^{th}/4^{th}$ harmonic components of the respiratory signals are still significantly stronger than the heartbeat signals in some cases. Therefore, by using our HBT-CWT method, we can reduce the harmonic components of the respiratory signal and magnify the heartbeat signal so that HR can be accurately estimated. The final HR values is then determined by finding the average values of the HR estimated from each HBT. It should be noticed that this simulation is only to show the efficiency of the proposed HBT extraction and CWT with adapted wavelet technique in reducing the harmonic of respiratory signals. We do not consider the use of multiple MIMO channels in this situation. However, in the next section, we will also show that by having more radar channels, we can typically improve the accuracy of HR estimation compared with the performance of single channel.

5.8 Experimental Scenarios and Results

Scenarios with single subjects at different postures and radar locations are performed and studied to validate our proposed signal processing chain. Approval of all ethical experimental procedures and protocols was granted by The Institutional Review Board (IRB) of The University of Tennessee – Knoxville, under Applications UTK IRB-14-01040-XM and UTK IRB-22-06785-FB. Respiration waveform from Belt Sensor NUL-236 and photoplethysmogram (PPG) signal from Pulse sensor SEN-11574 are extracted and processed with FFT to estimate RR and HR as our ground truth. Each experiment will last for 1 to 5 minutes so that we can assess the performance

87

of the system in a long-term monitoring manner. The 5-minute collected data will be divided into 20-second sliding windows and RR/HR are then estimated for each sliding window. Two adjacent windows have 19-second overlapped data and 1-second new data. This way for real-time operation, we can estimate and display RR and HR every 1 second.

To assess the estimation performance throughout our experiments, several statistical metrics are used. The mean-error μ_e measures the average of the error vector $\boldsymbol{e} = d_{est} - d_{GT}$ between radar's estimated results d_{est} and ground truth's results d_{GT}. We expect the lower values of mean-error the better the estimated results from radar. The standard deviation (std) of errors σ_e shown in equation (5.12) indicates whether the error of estimation is close to or spread out over wider range away from the mean value μ_e. Thus, the lower values of σ_e the better the estimate.

$$\sigma_e = \sqrt{\frac{1}{P}\sum_{i=1}^{P}(e_i - \mu_e)^2} \tag{5.12}$$

where μ_e is the mean-error calculated above and P is the sample size of the vector. Besides the metrics mentioned above, accuracy rates are also calculated to assess the estimation accuracy of FMCW radar. Accuracy rate for estimated error $<=$ 3 BPM and $>$ 3 BPM compared with the contact sensor reading are considered and shown. We determined this error threshold since this approximates a widely accepted standard within health sciences research for this level of accuracy in measuring HR [75, 76].

Because we are using MIMO configuration with multiple channels, there are different ways to implement the RR/HR estimation. For example, common approach is to first estimate HR for each channel individually. Then, the final HR value can be estimated by finding the average values between the channels after eliminating the outliers. We will call this channel average method. In

this dissertation, instead of merely calculating the HR by channel average method, which is probably time-consuming. We opt for the use of MRC where we combine the phase variation from multiple channels into one for processing. Thus, it will take less processing time. In this section, we will show the comparison of experimental results between the following methods to assess the performance:

1. *MRC with all channels***:** Apply signal processing chain in Figure 5.1 for all MIMO channels. Then, combine the phase variations from all channels into one for processing to find RR and HR.

2. *MRC with selected channels***:** Apply signal processing chain in Figure 5.1 for all MIMO channels. However, only phase variations from selected channels are combined using MRC to estimate RR and HR. This method should produce slightly better results compared with the above as we eliminated some channels that might contribute bad information especially of the heartbeat signals.

3. *Channel average with all channels***:** Apply signal processing chain in Figure 5.1 for all MIMO channels. However, RR and HR are also estimated separately for each channel. Final RR and HR are then found by calculating the average from all channels. As discussed above, while this is a common approach, it may be more time-consuming.

4. *Channel average with selected channels***:** Apply signal processing chain in Figure 5.1 for all MIMO channels. However, RR and HR are estimated separately for only selected channels. Final RR and HR are then found by calculating the average from these selected channels.

5. *Single channel with lowest mean-error***:** This estimates RR and HR separately for each channel then finds the channel with lowest mean-error compared with contact sensors. Finding the channel with lowest mean-error in this case is only for assessing how much better/worse the MRC/channel

average results are compared with the single channel approach. In practical, we do not know which channel will have the best performance.

5.8.1 Scenario #1: Subjects Sitting Down and Withholding Respiration in front of Radar

In this experiment, the SUTs hold their breath for almost 1 minute and sit 1 meter away from the radar as shown in Figure 5.16a. 2D-FFT to show the location of the target during the experiment is shown in Figure 5.16b as an example. For this scenario, three participants are asked to participate. Table 5.2 shows information about genders, ages, weights, and heights of these participants.

The purpose of this experiment is to initially validate if the radar device can estimate HR when there are no interferences from the respiratory signals and RBSM. As the alignment between the radar and upper body of the SUTs are crucial for an accurate HR reading. Figure 5.17 shows the estimated HR results for Participants #1, #2, and #3 from the MRC with selected channels method as function of time. We can see a correlation in trend between the estimated radar and ground truth. Furthermore, because the participants try to hold their breath for 1 minute, their HR increase because the nervous systems are reacting due to the lack of oxygen level for the brain and other organs to function. Figures 5.18a, 5.18c and 5.18e show that HR can be estimated with good accuracy. For participants #1 and #3, the channel with lowest mean-error gives comparable performance compared with other methods based on their accuracy rates, σ_e, μ_e. For participant #2, channel with lowest mean-error performs slightly worse than the channel average with all channels. Thus, it is not the case that channel with lowest mean-error always outperforms other methods. Therefore, we expect that having multiple channels is generally useful for making sure that the estimated results are better than or at least comparable to a single channel. Between MRC

90

Table 5.2. Information of participants in Scenario #1

Participant #	Gender	Age	Weight (lbs)	Height (in)
1	Male	29	125	64
2	Female	30	110	62
3	Male	22	185	70
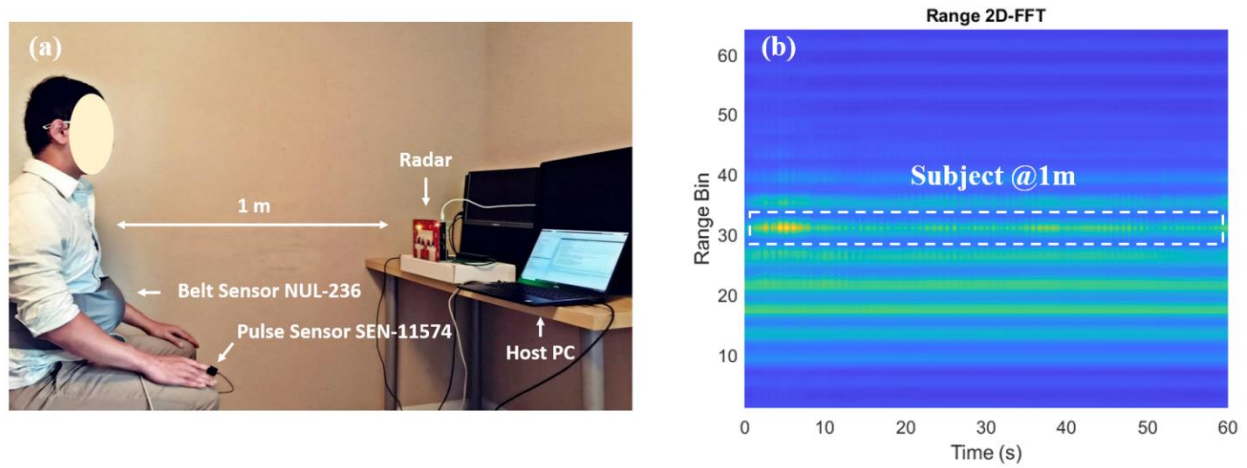
Figure 5.16. a) Experimental Setup of Scenario #1 and #2, b) 2D-FFT Range Profile
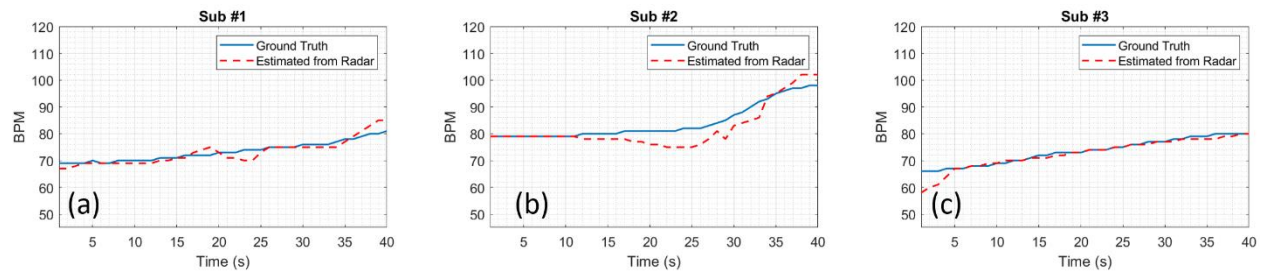
Figure 5.17. HR Estimation compared with ground truth pulse sensor of, a) Subject #1, b) Subject #2, c) Subject #3.

and channel average methods, they have their own advantages and disadvantages. On the one hand, MRC helps reduce complexity of the estimation process as it performs a weighted average of the signals and then HR can be estimated from one combined signal. On the other hand, channel average uses HR estimated from multiple MIMO channels and find the average of those HR values. Therefore, it is not easy to conclude which method will outperform the others. In fact, based on our experimental results, these two methods produce comparable accuracy in estimating HR. However, since MRC requires less computation and processing time, it will be more appropriate for real-time operation which will be discussed shortly. As shown in Figures 5.18c and 5.18d, channel average method with all channels clearly outperforms the others. This result suggests that MRC does not always outperform channel average method in accuracy. Furthermore, as can be shown in all participants, the accuracy rate of MRC with selected channels method usually slightly outperforms the MRC with all Channels. Thus, it shows that our simple channel classification method discussed in section 5.4 is working.

Figure 5.19 shows the comparison of average processing time between methods when 192 channels are used. The processing time shown in Figure 5.19 is approximated on a Dell Latitude 7400 laptop with 8-core Intel Core i7 CPU and a total 16 GB of memory running at 2.1 GHz. The laptop operates on Microsoft Windows 10, and all implementation/calculation is done with MATLAB version R2021b. As expected, channel average requires more time as it has to perform the same processing chain for all channels including the HBT extraction before being able to acquire final HR value.

5.8.2 Scenario #2: Subjects Sitting Down and Normally Breathing in front of Radar

The experimental setup for this scenario is similar to that of Scenario #1 where the SUTs sit in

Figure 5.18. Results of HR Estimation from Scenario #1. a), b) Error Analysis and Accuracy Rate from Subjects #1, c), d), Error Analysis and Accuracy Rate from Subjects #2, e), f) Error Analysis and Accuracy Rate from Subjects #3. ***Horizontal axis shows:*** 1) MRC with all channels, 2) MRC with selected channels, 3) Channel average with all channels, 4) Channel average with selected channels, 5) Channel with lowest mean-error compared with ground truth among all channels.
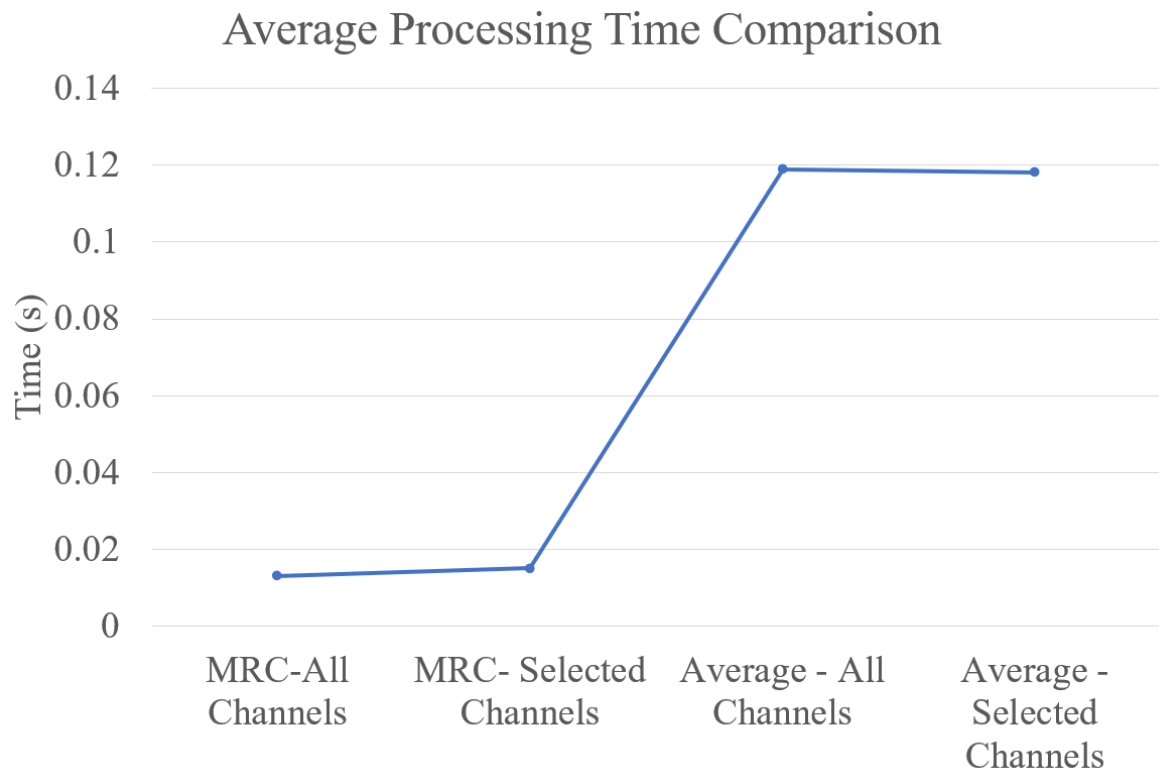
Figure 5.19. Comparison of average processing time between different methods.

front of the radar and is 1 m away. However, they will be asked to normally breath during the 5-minute experiment so that both their RR and HR can be monitored by the radar in a long-term setup. Since this is a common scenario and can be applied to various real-world applications such as at clinics, hospitals, etc., we recruited 10 voluntary participants for this scenario to have a better performance analysis of our proposed hardware and algorithm chains over a wide range of participants. Table 5.3 shows information about genders, ages, weights, and heights of these participants.

Figure 5.20 shows the RR estimation results from radar using MRC with all channels method compared with the ground truth Belt Sensor NUL-236. As reported from literatures [9-11], RR estimation in quasi-static scenarios is relatively straightforward and generally has high accuracy. This can be validated in experimental results where for most the participants, the trend in RR estimated from the radar agrees well with the RR estimated from ground truth. For subjects #7 and #9, there were technical issues where the Belt Sensor does not fit the subjects. Therefore, we could not capture the refence respiratory waveforms for comparison.

Figure 5.21 shows the error analysis of the RR estimation results shown above by calculating the std-error σ_{error} and mean-error μ_{error} of the estimated results. We can see that for all participating subjects, the mean-error of estimated results can be as low as 0.2 BRPM and the worst result is from subjects #8 with mean-error 1.4 BRPM.

Figure 5.22 shows the accuracy rate as another metrics to assess the estimation accuracy compared with the ground truth. We can see that estimated RR from most of the subjects have 100% of error within 3 BRPM compared with the ground truth. Only subject #5 has slightly lower accuracy rate in which only 89% of estimated RR is within 3-BRPM error compared with the ground truth. We can see a good agreement between radar's results and ground truth in first four

Table 5.3. Information of participants in Scenario #2

Participant #	Gender	Age	Weight (lbs)	Height (in)
1	Male	29	125	64
2	Female	30	110	62
3	Male	22	185	70
4	Male	26	150	69
5	Female	54	150	61
6	Female	65	110	64
7	Female	64	235	67
8	Male	23	170	72
9	Male	33	340	73
10	Male	27	125	66

Figure 5.20. RR Estimation compared with Ground Truth from all participating subjects.
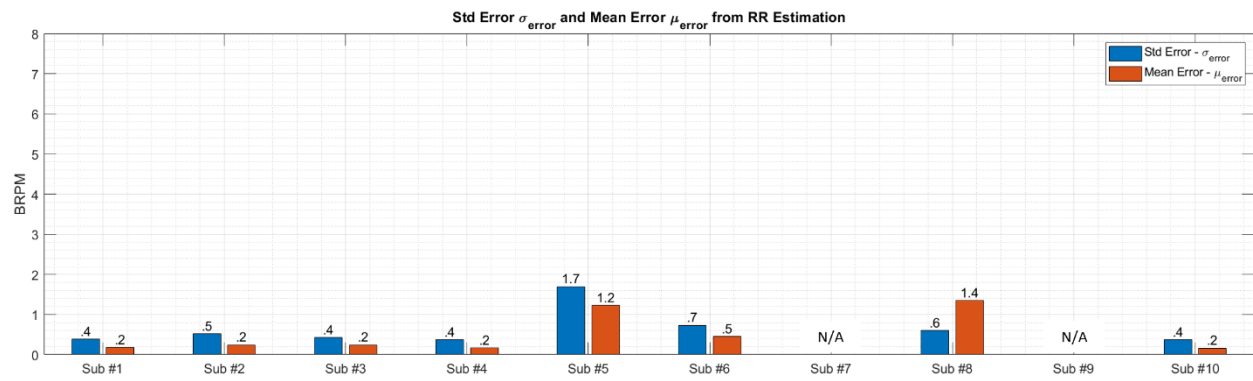
Figure 5.21. Error Analysis of RR Estimation compared with Ground Truth from all subjects.
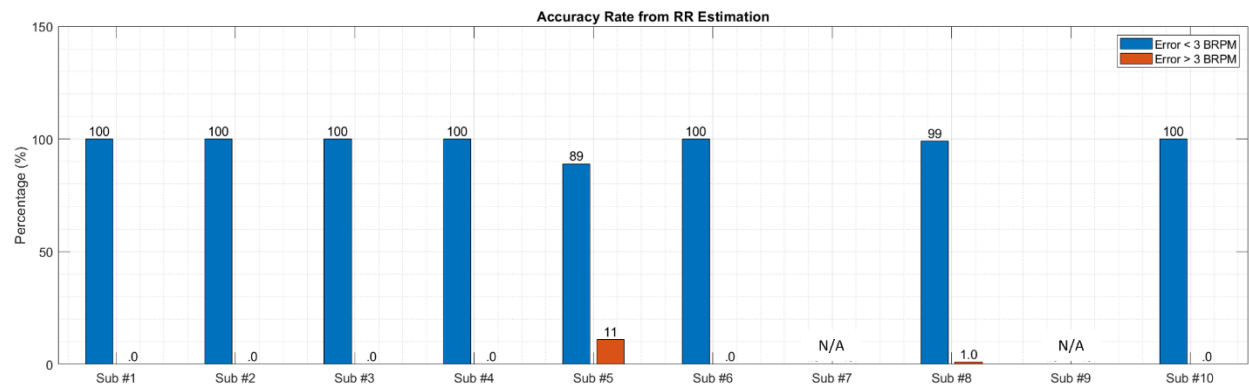
Figure 5.22. Accuracy Rate of RR Estimation compared with Ground Truth from all subjects.

minutes of the experiment of subject #5. However, since the ground truth estimation fluctuates for the last 1 minute, the Belt Sensor may not be able to clearly capture the pressure changed due to respiration. This explains the low agreement between estimated results from radar and belt sensor.

Next, we analyze the performance of HR estimation from all participating subjects for Scenario #2. Figure 5.23 shows the estimated HR from radar using the MRC with selected channels method in comparison with the ground truth Pulse Sensor SEN-11574. We can see that estimated HR using radar from most subjects agree well with the estimated HR from ground truth. However, subjects #8 and #9 show some fluctuations between radar's results compared with ground truth. The difference in accuracy of HR estimation from different subjects under the same scenarios set up has also been reported in literature [79]. While we are not certain what is the main reason that cause this fluctuation, there can be factors that might affect the HR estimation results using radar such as alignment issue between radar and SUT. Thus, better alignment system using simple laser devices can be used to make sure the chest area that cover the heart region is optimally aligned with radar to improve the SNR of the capture heartbeat signals.

Figure 5.24 shows the error analysis using std-error σ_{error} and mean-error μ_{error} from all participating subjects using different methods as discussed above. It can be shown in this experiment with subjects #2, #4, #5, #6, #7 and #8 that results from single channel with lowest mean-error compared with ground truth are worse than the other methods using multiple channels. Therefore, we can see that using more channels can generally help to improve the accuracy of HR estimation. For most subjects, the performance between using MRC method and channel average method is comparable and it is hard to say which one is better in terms of accuracy. However, because MRC method offers less complexity and computation as shown in Figure 5.19, it is more preferable for the real-time operating especially when we want to integrate the radar for multiple
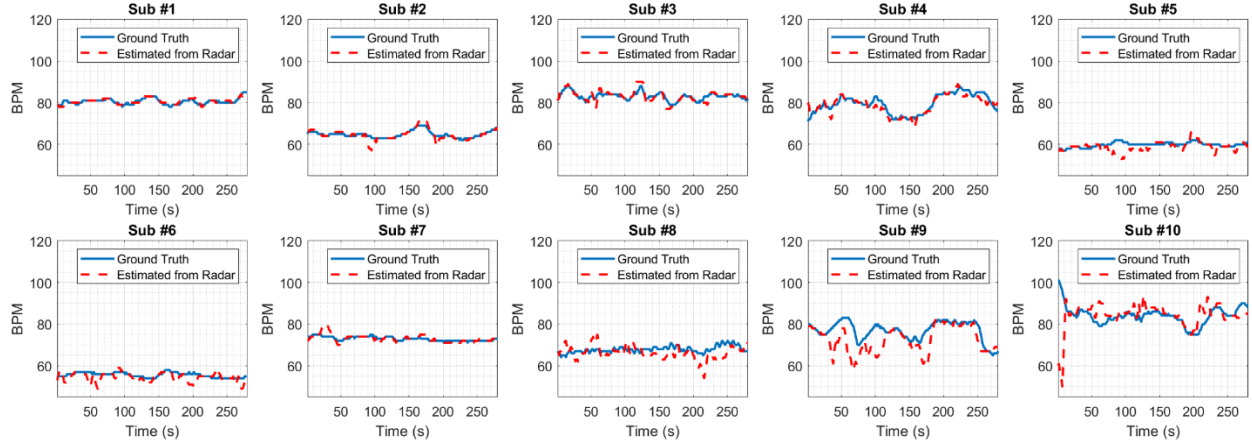
Figure 5.23. HR Estimation compared with Ground Truth from all participating subjects.
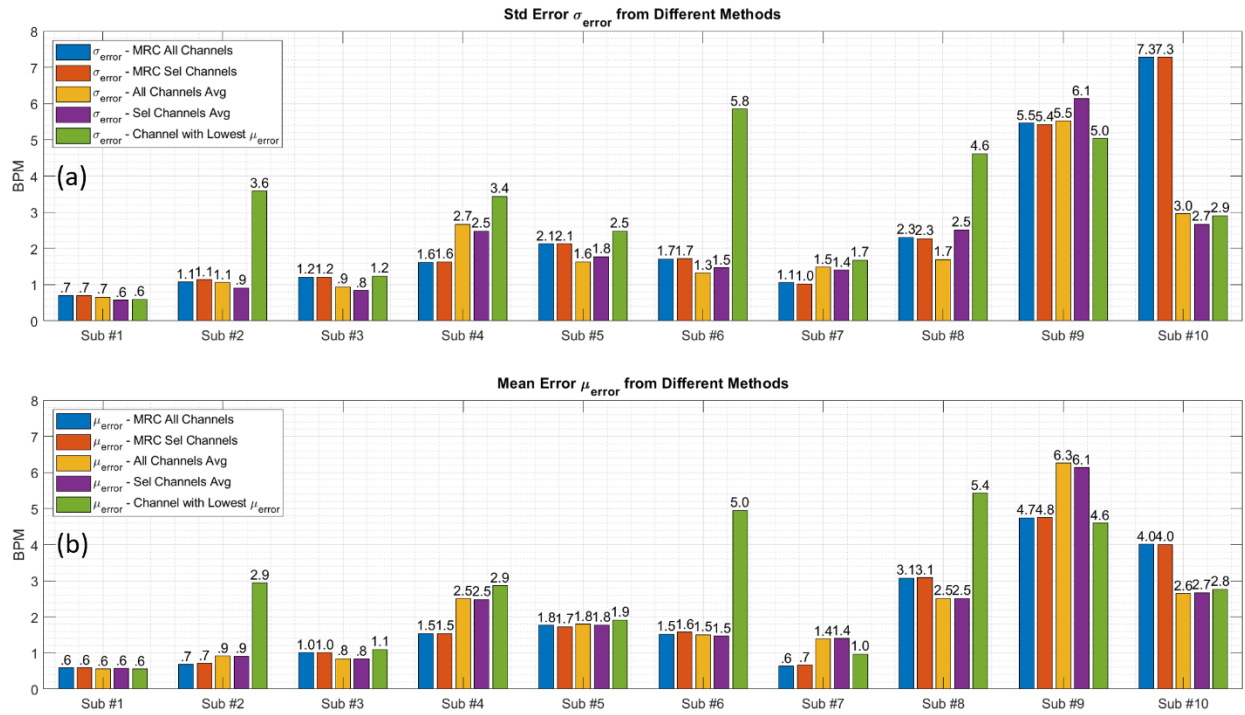
Figure 5.24. a) Std-Error, b) Mean-Error Analysis of HR Estimation compared with Ground Truth from all subjects.

purposes besides vital sign detection such as localization and tracking of multiple subjects using the same radar hardware. In general, estimated HR results from most subjects are less than 3 BPM in average which is satisfactory in terms of accuracy. As discussed above, the mean-error μ_{error} of subjects #8 and #9 are relatively high probably because of the alignment issue. For subject #10, there was a big jump of estimated HR value in the first 5 seconds which makes the total mean-error μ_{error} relatively high. This might be because the subject suddenly makes a movement after sitting down that cause the distortion. However, for the rest of the experiment, the estimated HR from radar agrees well with the ground truth.

Figure 5.25 shows the accuracy rate of error calculation from MRC with selected channel method to show the percentage of errors that are within and beyond 3 BPM threshold. These percentages should be correlated with the mean-error μ_{error} analysis. Therefore, we can see in Figure 5.25 that accuracy rates for the first 7 subjects are high while the last 3 subjects produce lower accuracy rate. This agrees with our observation and discussion based on Figures 5.23 and 5.24 above.

5.8.3 Scenario #3: Subjects Lying Down and Normally Breathing with Radar on the Side

The experimental setup for Scenario #3 is shown in Figure 5.26a. The first three participants from Scenarios #1 and #2 are asked to participate in this experiment. They will lie down for 5 minutes so that the radar can monitor their RR and HR in a long-term setup. The radar is 0.6 meters away from the near edge of the bed. Therefore, distance between radar and subject's chest is approximately 1 meter. The radar is 0.5 meters away from the ground. 2D-FFT of the target is shown in Figure 5.26b as an example. As can be seen from Figure 5.26b, the range bin of the target has stronger reflection than in Scenario #1 shown in Figure 5.16b even though the subject is at roughly the same range. This can be explained by the fact that the reflection from the edge of the
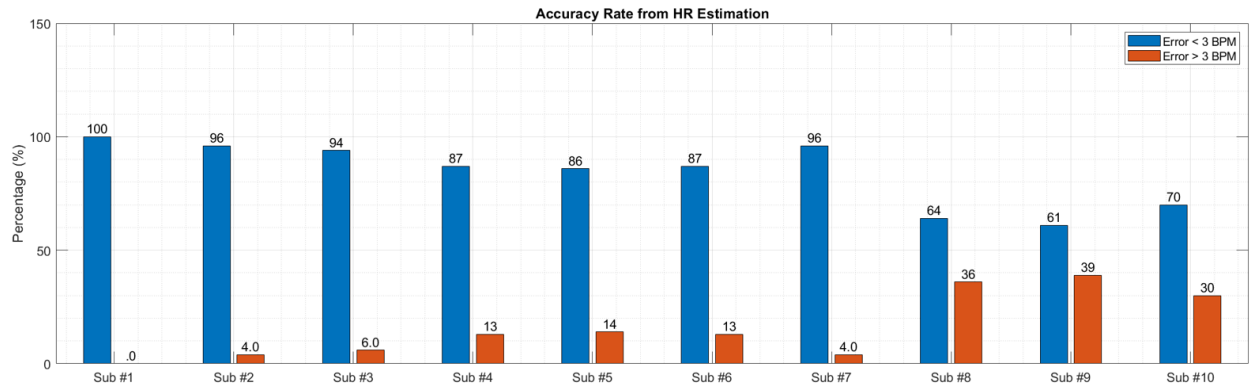
Figure 5.25. Accuracy Rate of HR Estimation compared with Ground Truth from all subjects.
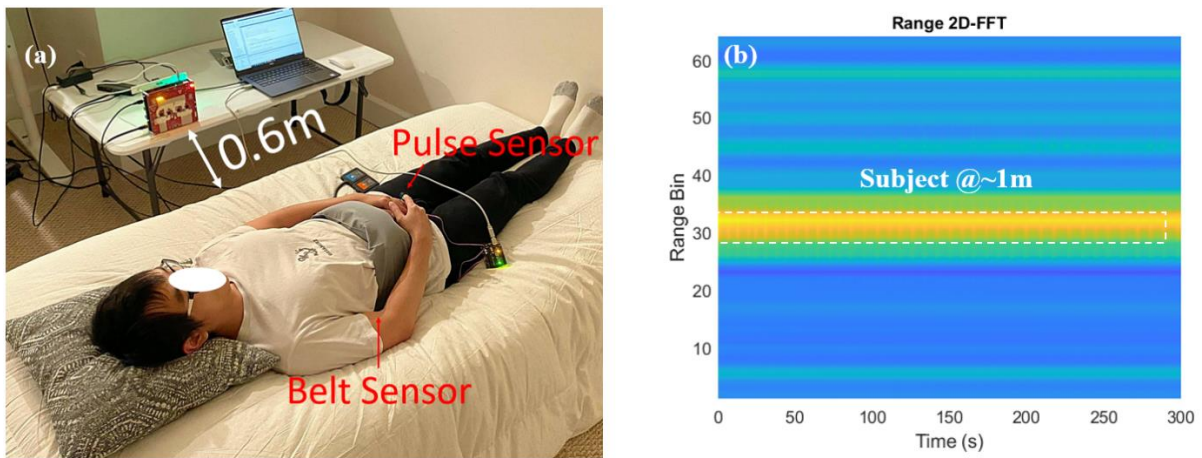
Figure 5.26. a) Experimental Setup of Scenario #3, b) 2D-FFT Range Profile

bed near the subject has made the reflection around the subject range bin stronger. However, this should not impact the target range bin selection as we still select the target range bin based on the variance level in the phase variation. As the bed has no vital sign, it does not produce any changes in phase thus the calculated variance in phase should be very small at the bed's range bin. Experimental results of Scenario #3 are shown in Figures 5.27 – 5.30. As can be shown, when the subjects lie down, we expect minimal amount of RBSM during experiment. Therefore, both RR and HR can be estimated with high accuracy. We can observe comparable performance of HR estimation between different methods. Therefore, in this case, MRC is still preferable as it offers lower computational requirement and processing time.

5.8.4 Scenario #4: Subjects Lying Down and Normally Breathing with Radar on the Ceiling

The setup of Scenario #4 is shown in Figure 5.31a. The same three participants from Scenarios #1 and #3 are asked to participate in this experiment. They will lie down for 5 minutes so that the radar can monitor their RR and HR in a long-term setup. The radar is mounted on the ceiling and looks down at the lying down subject. The radar is 1.7 m away from subject's chest. 2D-FFT of the target is shown in Figure 5.31b as an example. As this experimental setup is similar to Scenarios #1 and #2, the Range 2D-FFT plot should look similar except that the SUT is further away from the radar. Figures 5.32 and 5.33 show the RR estimation from all participants as well as the error analysis and accuracy rate. Since the setup of this scenario is similar to Scenario #2, we observe similar accuracy from RR estimation. HR estimation results from this experiment in Figures 5.34 and 5.35 suggest that as the SUT is further away from the radar, the SNR of the heartbeat signal start decreasing which degrades the accuracy of HR estimation as well. This explains why the accuracy rates of HR estimation are worse than that of Scenario #3. Furthermore,
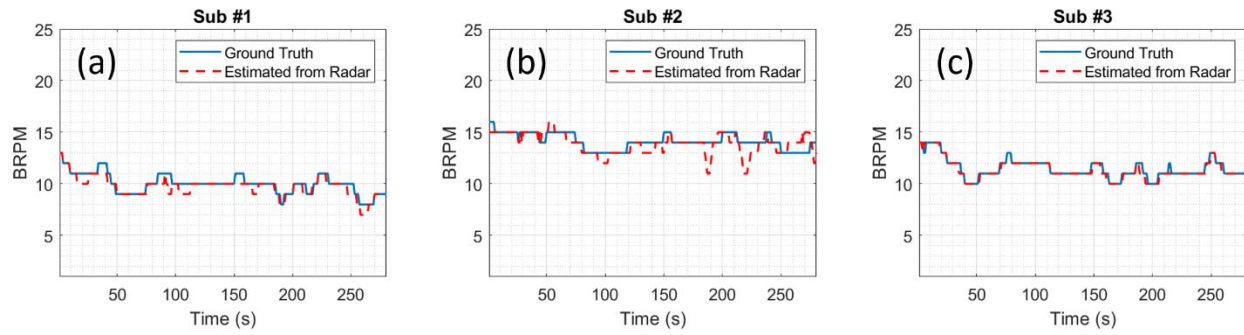
Figure 5.27. RR Estimation compared with Ground Truth from all participating subjects for Scenario #3.
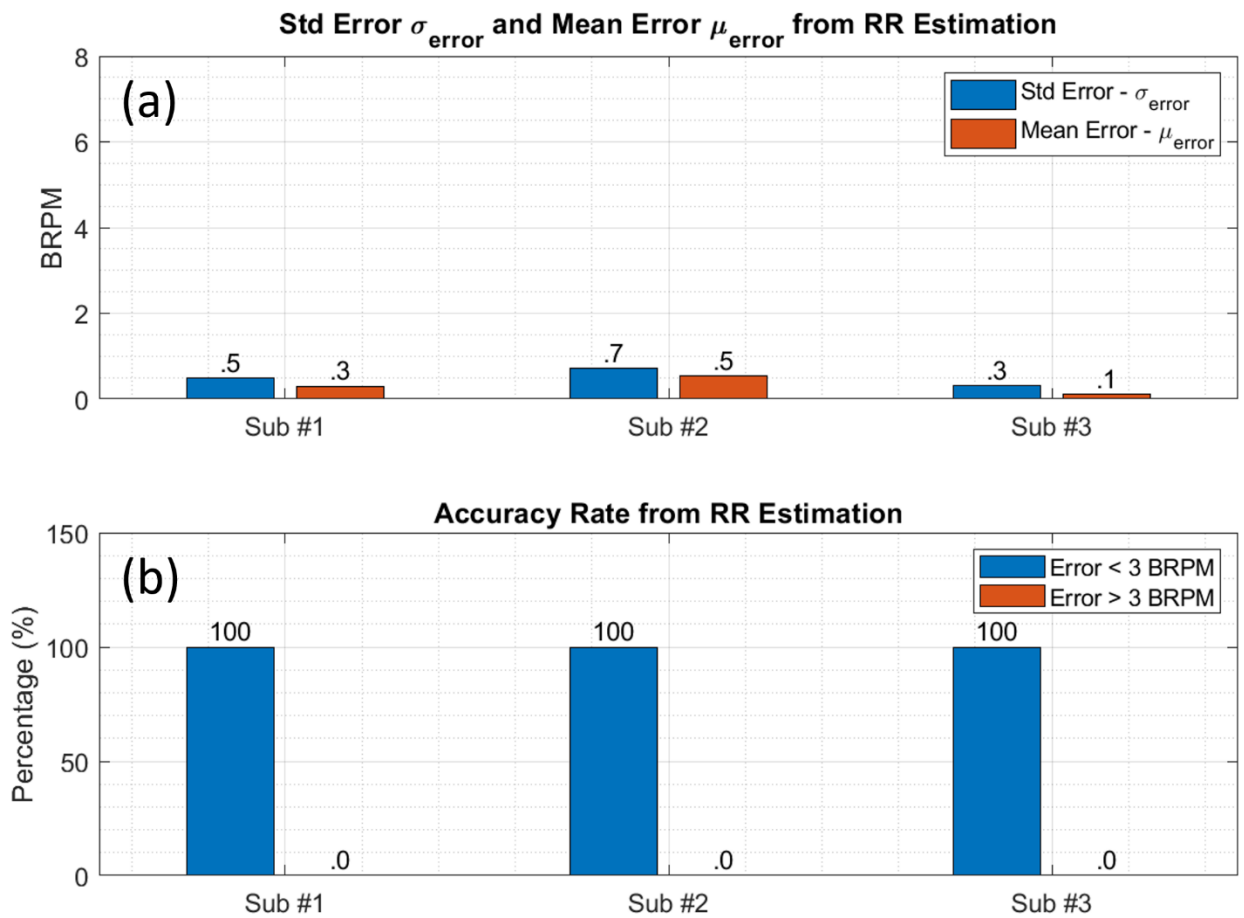
Figure 5.28. Error Analysis and Accuracy Rate for RR Estimation for all subjects for Scenario #3.
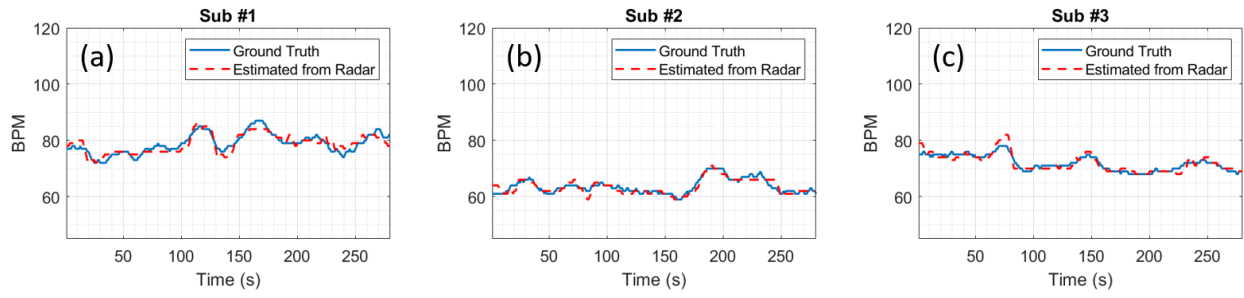
Figure 5.29. HR Estimation compared with Ground Truth from all participating subjects for Scenario #3.
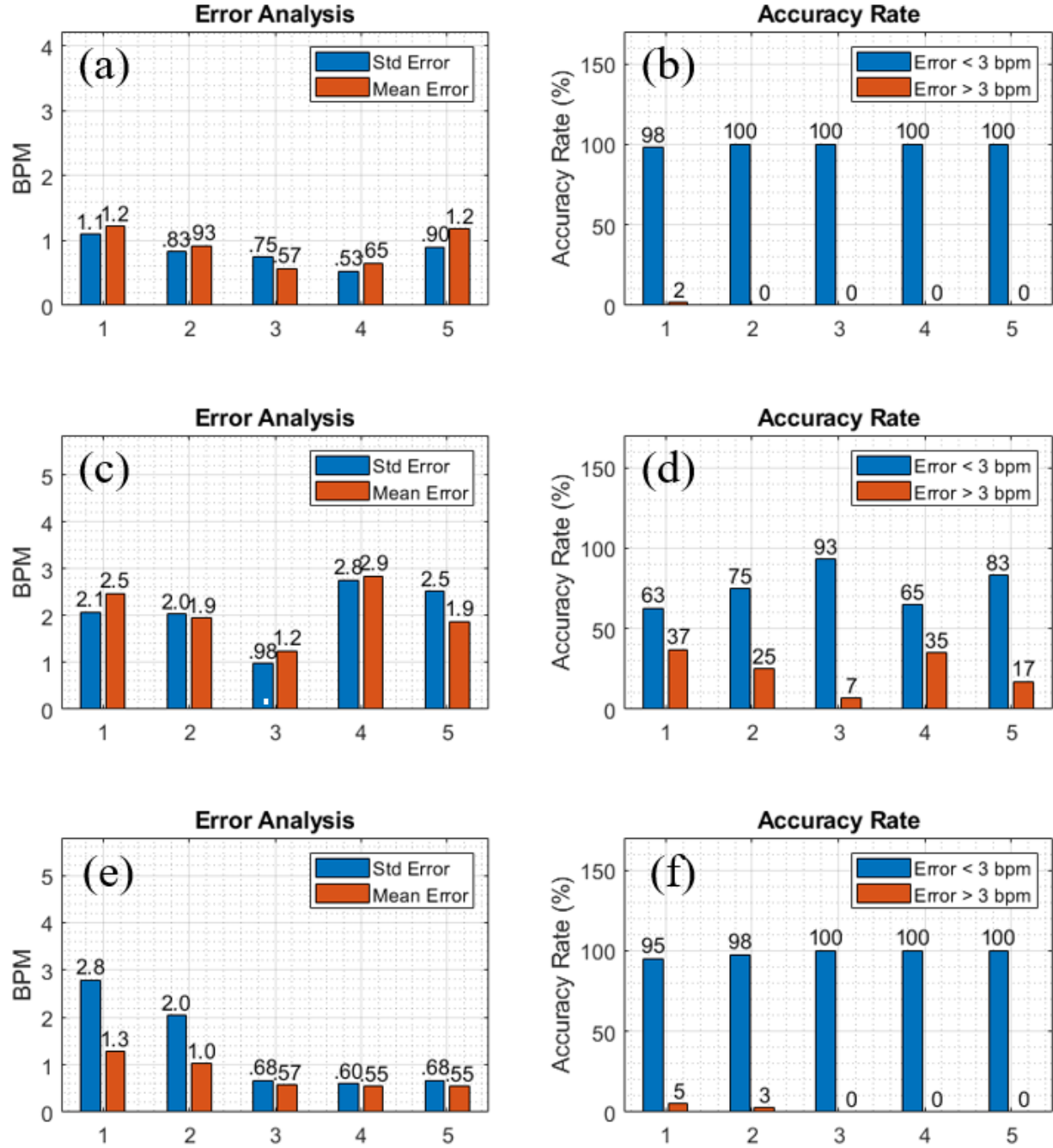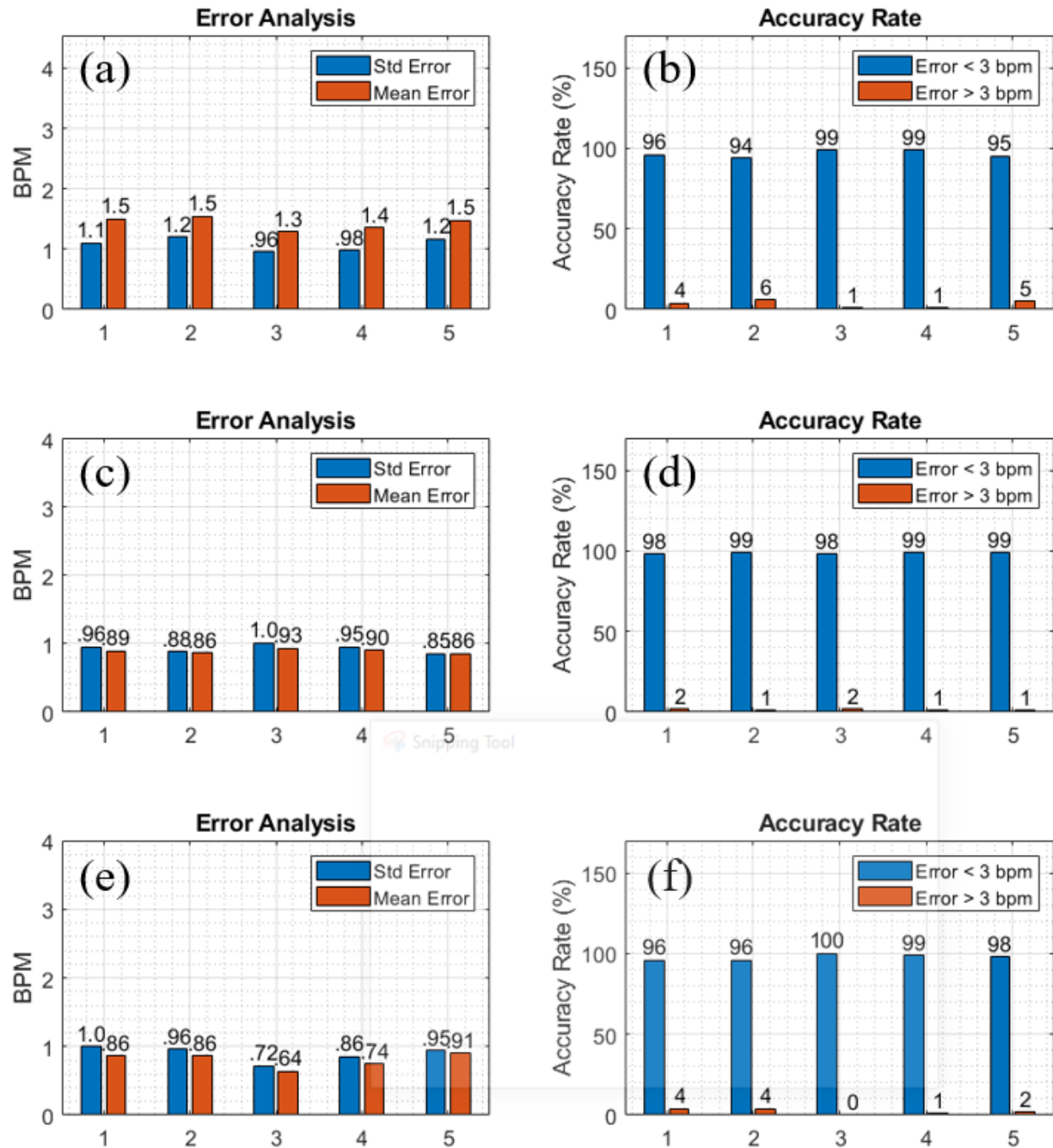
Figure 5.30. Results of HR Estimation from Scenario #3. a), b) Error Analysis and Accuracy Rate from Subjects #1, c), d), Error Analysis and Accuracy Rate from Subjects #2, e), f) Error Analysis and Accuracy Rate from Subjects #3. *Horizontal axis shows:* 1) MRC with all channels, 2) MRC with selected channels, 3) Channel average with all channels, 4) Channel average with selected channels, 5) Channel with lowest mean-error compared with ground truth among all channels.
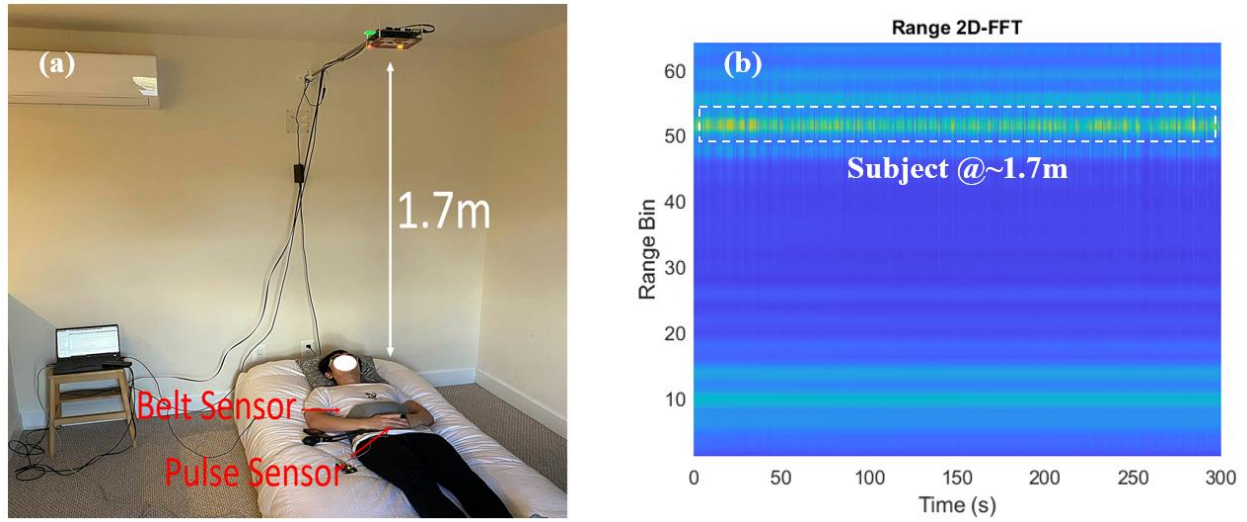
Figure 5.31. a) Experimental Setup of Scenario #4, b) 2D-FFT Range Profile
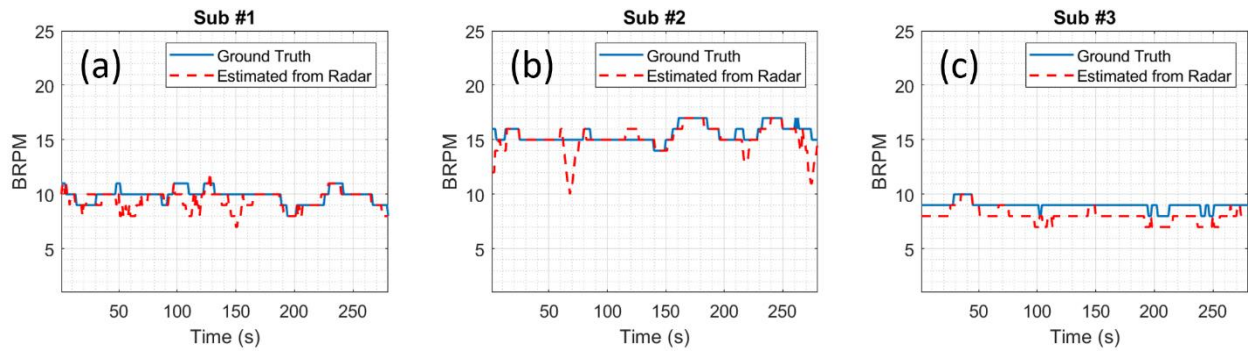
Figure 5.32. RR Estimation compared with Ground Truth from all participating subjects for Scenario #4.
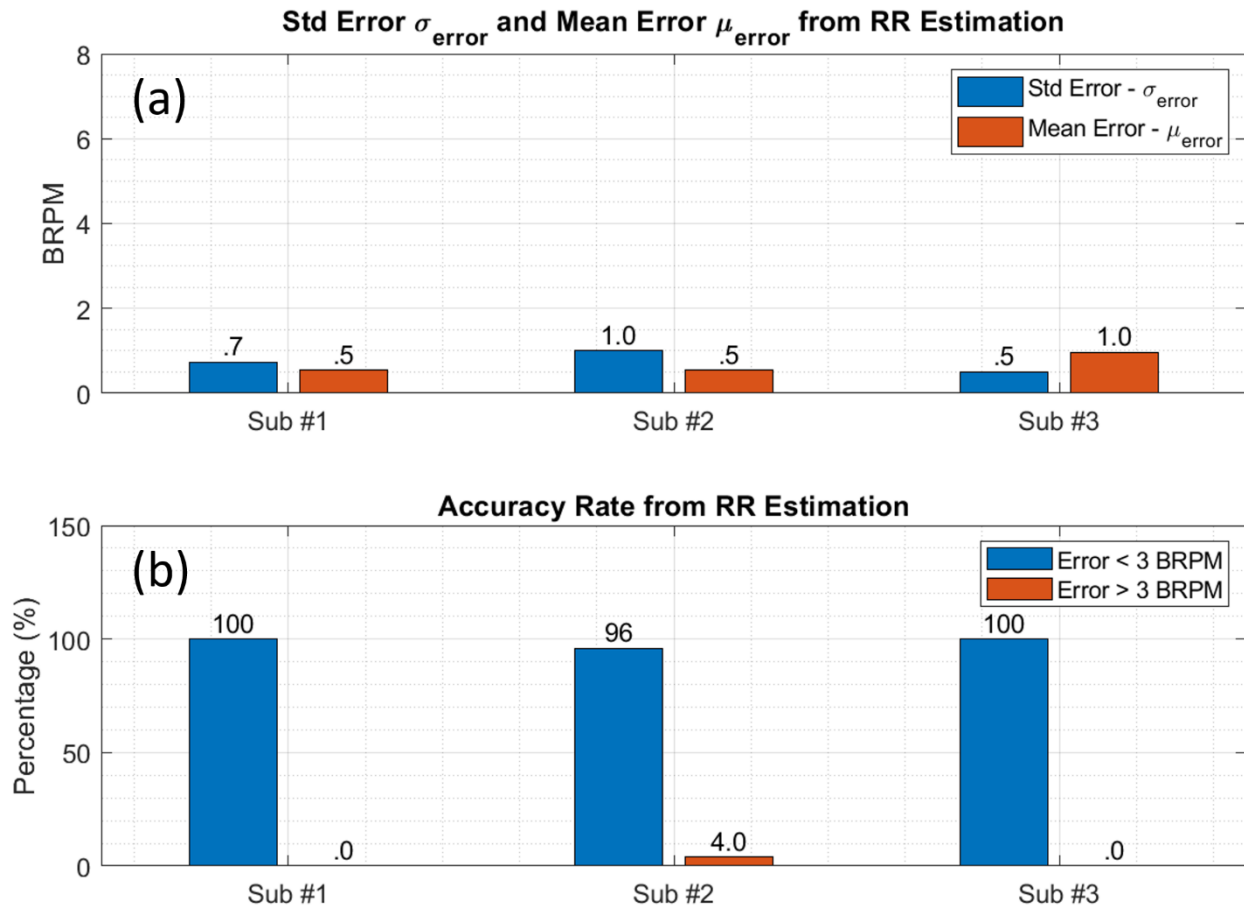
Figure 5.33. a) Error Analysis and b) Accuracy Rate for RR Estimation for all subjects for Scenario #4.
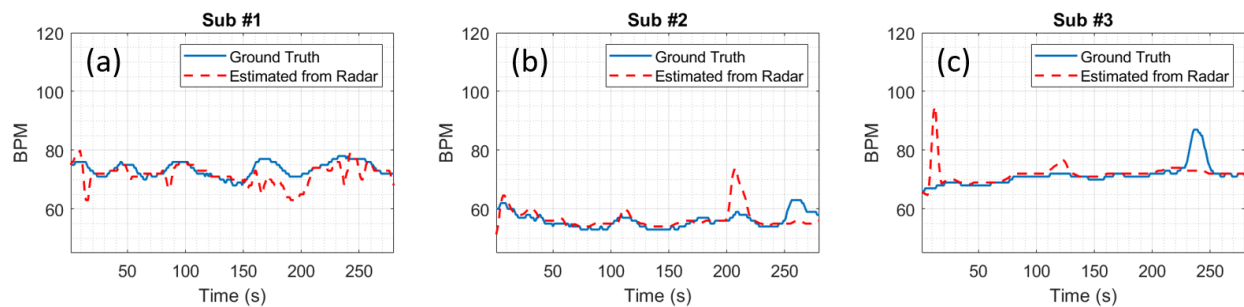
Figure 5.34. HR Estimation compared with Ground Truth from all participating subjects for Scenario #4.
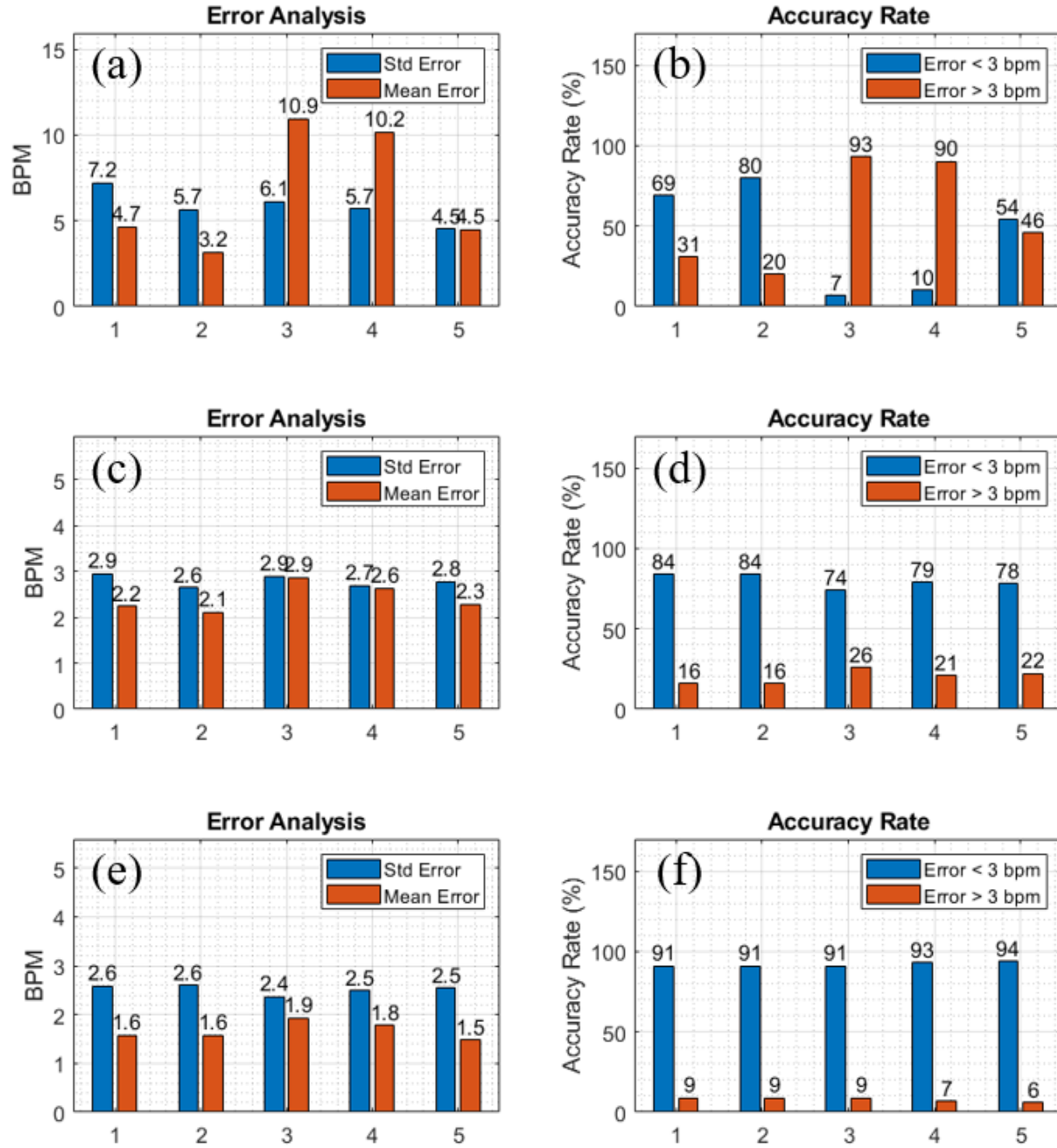
Figure 5.35. Results of HR Estimation from Scenario #4. a), b) Error Analysis and Accuracy Rate from Subjects #1, c), d), Error Analysis and Accuracy Rate from Subjects #2, e), f) Error Analysis and Accuracy Rate from Subjects #3. ***Horizontal axis shows:*** 1) MRC with all channels, 2) MRC with selected channels, 3) Channel average with all channels, 4) Channel average with selected channels, 5) Channel with lowest mean-error compared with ground truth among all channels.

as the radar is mounted on the ceiling, it is more difficult to align the radar and the subjects. This is one factor that affects the HR estimation accuracy. It can also be observed that the HR estimation is highly dependent on the SUT as well as the accuracy of HR estimation are different for the three participants. For participant #3, MRC with all channels and with selected channels produce comparable results with channel average method. For participant #2, MRC with all channels and with selected channels produce similar results and are better than channel average methods and the single channel with lowest mean error. For participant #1, MRC with selected channels significantly outperforms the rest of the methods. Therefore, the results in Scenarios #2 and #4 suggest that while most of the time MRC with selected channels and channel average method have comparable results, MRC is preferable as it requires less complexity and processing time.

5.8.5 Scenario #5: Two Subjects at Different Ranges Sitting Down and Normally Breathing in front of Radar

To demonstrate the capability of the MIMO system, we also show results when participants #1 and #2 sit still in front of the radar as shown in Figure 5.36a. Participant #1 is 0.75m away and participant #2 is 1.5m away from the radar aperture. Separation between them is 0.6m. An example of the range profile calculated from 2D-FFT to find the range bin of each of the two participants is shown in Figure 5.36b.

As the two subjects are in different ranges, it is easy to select the range bin corresponding to each subject and apply the processing chain to each subject's data separately. For scenarios where the two participants are at the same range bin, direction-of-arrival estimation must be performed to estimate the angular location of each participant. Figure 5.37 shows the RR estimation results of the two participating subjects along with the error analysis and accuracy rate. As the experimental
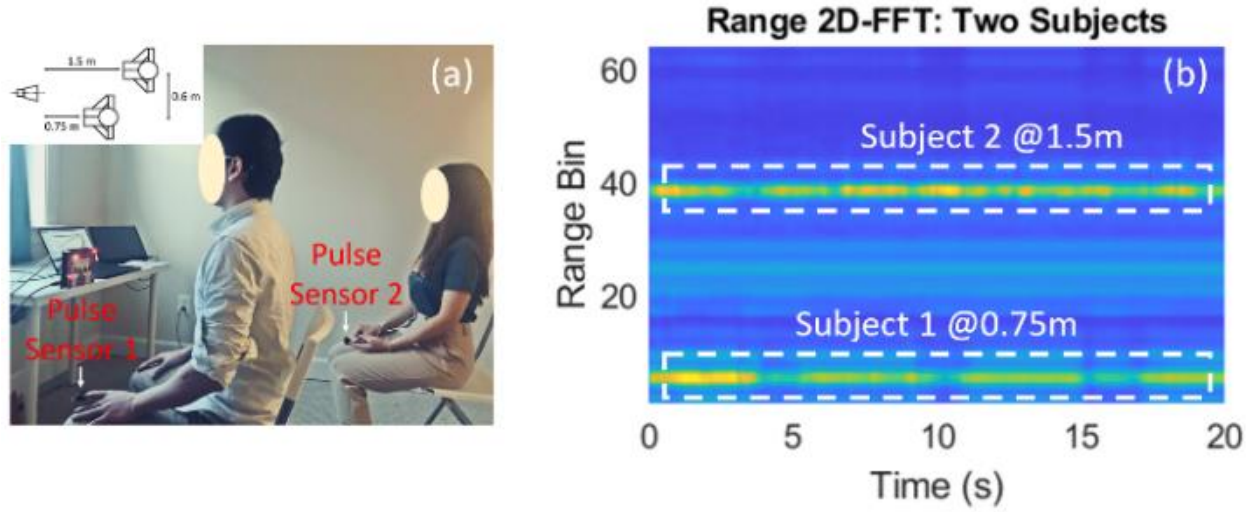
Figure 5.36. a) Experimental Setup of Scenario #5, b) 2D-FFT Range Profile
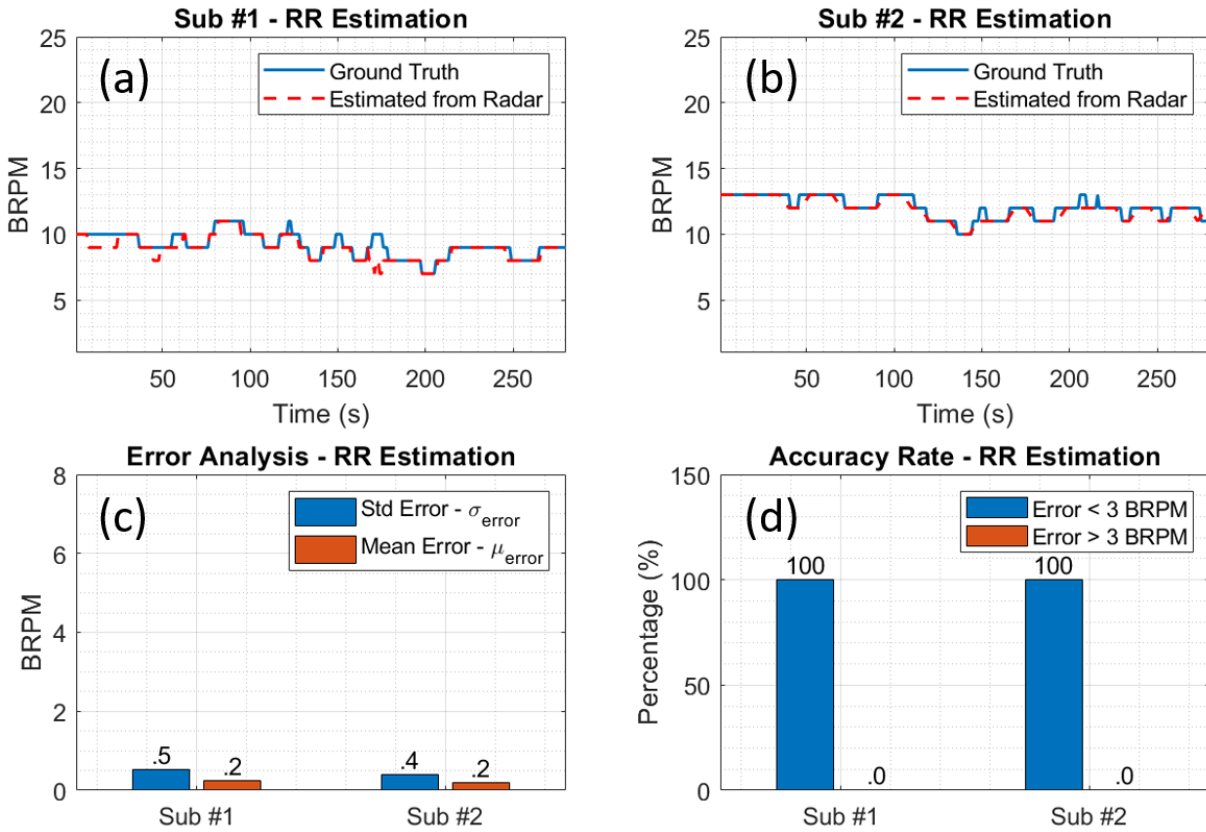
Figure 5.37. a), b) RR Estimation compared with Ground Truth from two participating subjects for Scenario #5, c) Error analysis, d) Accuracy Rate.

setup is similar to Scenarios #2 and #4, we observe high accuracy performance of the RR estimation for both subjects.

For HR estimation, we observe from Figures 5.38 – 5.39 that a comparable performance as what reported in Scenarios #2 and #4 is also achieved here, as the radar is placed in front of the two subjects. Subject #2 still has slightly worse accuracy rates than subject #1 as the subject is 1.7m away. MRC with selected channels method produces comparable results with MRC with all channels. In general, HR estimation performance are satisfactory. Results from Scenario #5 demonstrates the capability of our system and proposed signal processing even for a multi-subject scenario.

5.9 Discussion

5.9.1 Comparison between different methods

Figure 5.40 shows a comparison of average error in HR estimation from all experiments listed above for different methods. We can see that while MRC with selected channels slightly outperforms other methods including channel average method. Furthermore, channel with lowest mean error produces slightly worse result than the others. While we cannot draw a generalized conclusion on whether using MIMO configuration will guarantee an improvement in HR estimation because we do not have a sufficient amount of experimental data to perform statistical inference. However, based on the data collected from the recruited participants in above experiments, we can see having multiple channels generally helps to improve the accuracy of HR estimation. This observation is consistent as reported from other research groups in literature [38-41].
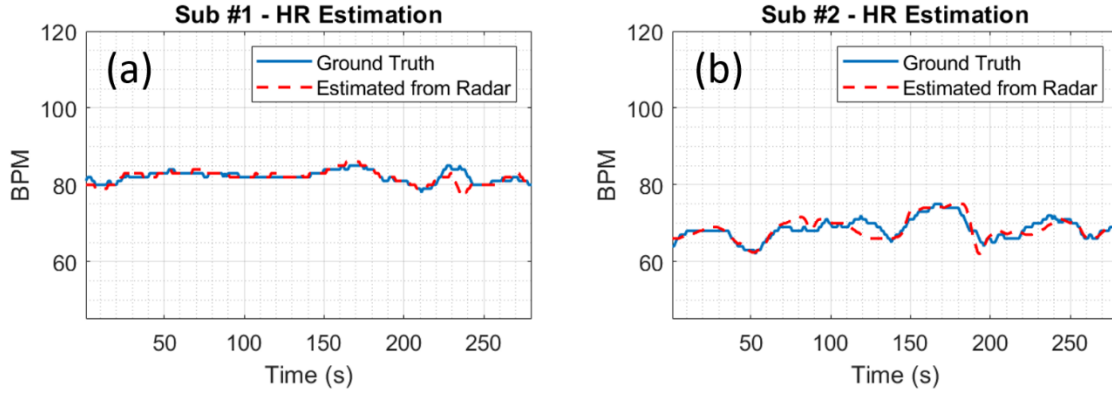
Figure 5.38. HR Estimation compared with Ground Truth from two subjects for Scenario #5.
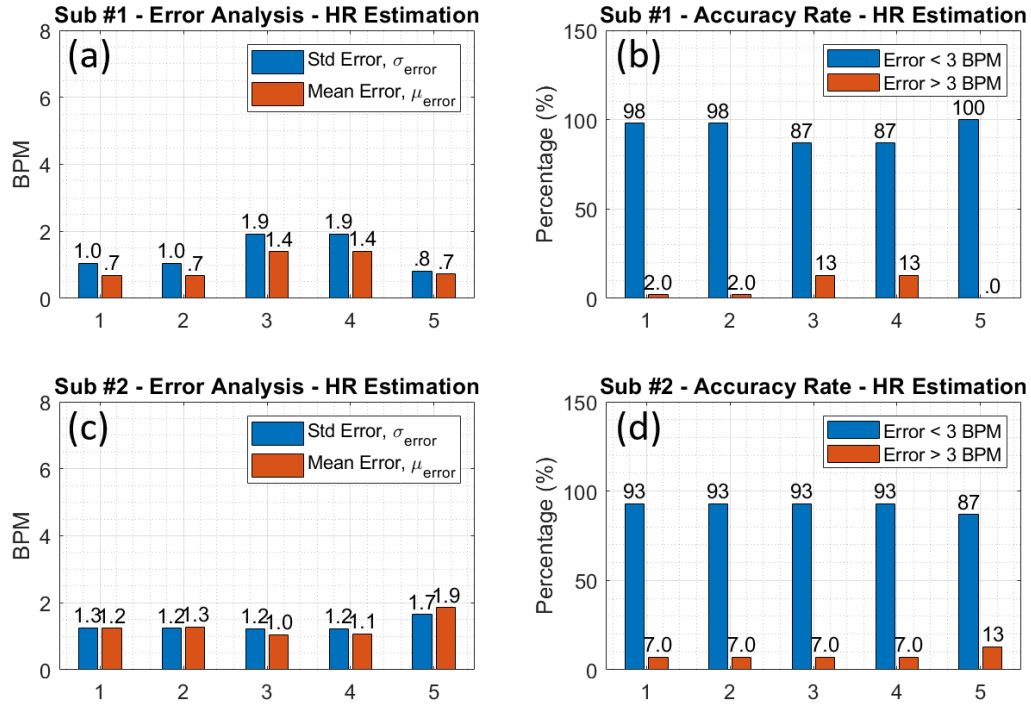
Figure 5.39. Results of HR Estimation from Scenario #5. a), b) Error Analysis and Accuracy Rate from Subjects #1, c), d), Error Analysis and Accuracy Rate from Subjects #2. ***Horizontal axis shows:*** 1) MRC with all channels, 2) MRC with selected channels, 3) Channel average with all channels, 4) Channel average with selected channels, 5) Channel with lowest mean-error compared with ground truth among all channels.
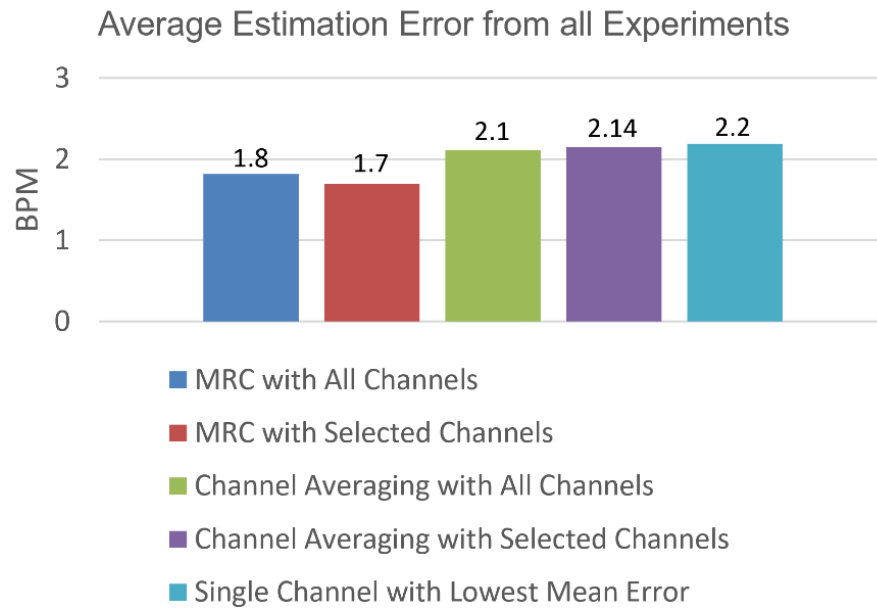
Figure 5.40. Comparisons between different methods for average error of HR estimation from all experiments.

5.9.2 Comparison between experimental results of Scenario #3 to another research group

To show the robustness of our proposed algorithms chain shown in Figure 5.1, this section shows comparisons with some work reported in the literature. To make fair comparison, we opt for the reported results where similar experimental setups were used. Table 5.4 shows a comparison between our experimental results in Scenario #3 and what was reported in [39].

Since the Root-Mean-Square-Error (RMSE) of estimated HR is reported in inter-beat-interval (IBI), we also calculate the RMSE in IBI to compare the results. The IBI is usually determined based on periodicity of waveforms on time domain signals. Therefore, instead of using FFT to find HR on frequency spectrum, we will find local peaks of the CWT coefficients calculated from adapted wavelet in each sliding window. The time steps corresponding to these peaks are used to determine the IBI of cardiac waveform. Table 5.4 shows that RMSE in IBI calculated from our experimental results is lower than what is reported in [39]. This can be explained by the fact that despite similar setup, the hardware system in [39] only has 8 MIMO channels while ours has 192 channels. This increases the number of useful information of heartbeat signal captured by widely distributed radar channels. Furthermore, the results in [39] are acquired without any methods to reduce the interferences from respiratory harmonics. Therefore, as our system has more distributed channels and we carefully use HBT extraction method with CWT to suppress harmonics interferences, we were able to achieve better estimation accuracy.

5.9.3 Comparison between experimental results of Scenario #4 to another research group

Comparison between our Scenario #4 results and reported work in [26] is also shown here in Table 5.5. Despite the similar experimental setup, results from [26] are obtained with a single channel FMCW radar and use Maximum Likelihood to estimate HR. The authors in [26] do not use any methods to suppress interferences from respiratory harmonics. Therefore, by having more

114

Table 5.4. Comparison between Scenario #3 with [39]

	Center Frequency (GHz)	Bandwidth (GHz)	Output Power (dBm)	$N_{TX} \times N_{RX}$
[39]	60	1.5	13	2 x 4
This work	78	3.8	10	12 x 16

	Method	Experimental Setup	Total # of Radar Channels	RMSE in IBI (ms)
[39]	MRC with 8 Channels	Subject is lying on bed ~1m with radar on the side	8	148
This work, Participants #1, #2 and #3.	MRC with Selected Channels + HBT + CWT	Shown in Figure 5.26	192	107 96 90

115

Table 5.5. Results Comparison between Scenario #4 with [26]

	Center Frequency (GHz)	Bandwidth (GHz)	Output Power (dBm)	$N_{TX} \times N_{RX}$
[26]	78	3.9	10	1 x 1
This work	78	3.8	10	12 x 16

	Method	Experimental Setup	Total # of Radar Channels	Accuracy Rate for Error < 3 BPM (%)
[26]	Maximum Likelihood	Subject is lying on bed ~1.7m with radar mounted on the ceiling	1	80
This work, Participants #1, #2 and #3.	MRC with Selected Channels + Adapted CWT	Shown in Figure 5.31	192	80
				84
				91

channels and better estimation method, we can achieve better accuracy than what is reported in [26].

5.10 Conclusion

- This chapter demonstrates that the **use of more MIMO generally produces better accuracy in HR estimation compared with single channel radar**. Accuracy improvement can be achieved in HR estimation when MIMO configuration is used compared with single channel radar.

- While using more channels can help improve the accuracy of HR estimation**, DSP methods such as HBT extraction and Adapted CWT are also needed to reduce the interferences of respiratory harmonics**.

- Five different scenarios with voluntary participants are performed and studied. Experimental results show that **MRC with selected channels is the most preferable method as it consistently produces accurate HR estimation results and require less processing time.**

- Automatic HBT extraction based on constellation is proposed in this chapter to help reduce the impact of respiratory harmonics and does not require human intervention for selecting a good HBT.

- The Channel Classification methods proposed in this chapter can also be improved especially when more complicated scenarios with more interferences from random body motion are introduced.

CHAPTER VI

REDUTION OF RANDOM BODY-SWAYING MOTION

Under scenarios where there is a significant amount of random body-swaying motion (RBSM), these interferences from RBSM need to be considered so that the accuracy of HR estimation can be sustained. In this chapter, we extend the work in Chapter 5 that detects vital signs of quasi-static subjects to include impacts of RBSM. Here, we show that our proposed automatic HBT extraction and CWT with adapted wavelet methods still help to effectively reduce the impact of RBSM. However, under scenarios where the RBSM level is significantly strong, RBSM cannot be completely removed from the frequency spectra. Therefore, we have modified the signal processing chain proposed in previous chapter to add a spectral-based HR selection method which takes advantages of multiple radar channels to determine the HR estimation when there are significantly strong RBSM.

6.1 Impact of RBSM on Constellation and Phase Variation Signals

Before discussing the modification of the processing chain proposed in Chapter 5, we first use the simulated model and experimental data to analyze the impact of RBSM on the constellation and the extracted phase variation that carry information about the chest displacement due to both respiratory and heartbeat. It should be noticed that in this dissertation, we only deal with unintentional body-swaying motions while SUTs are sitting or standing. In other words, the interfered body motions' effects that we are trying to suppress here is a short and aperiodic signal. If the SUT is actively in motion during the monitoring process such as walking or running, it is still a challenging problem to get highly accurate results even for RR estimation using this method.

6.1.1 Analysis of RBSM using Simulated Data

When there are interferences from RBSM, the term ΔR_{RBSM} discussed in equation (4.11) can no longer be neglected. Therefore, the phase variation extracted from AD will be distorted by the RBSM. To show the impact of RBSM, we use the simulated data discussed in Section 5.7 and include two RBSM as interferences. Table 6.1 shows simulated parameters of chest displacement due to respiration and heartbeat $f_{RR}, f_{HR}, K_b, T_i, T_e, \tau, A_h$ for the 20-second simulation.

Table 6.2 shows the simulated parameters of RBSM using equation (4.3), the Gaussian noises are also added to the following parameters T_n, A_n during the 20-second simulation.

To show the impact of RBSM to vital sign signal, Figure 6.1 shows the simulated waveforms of both vital sign signals, RBSM and combined signal. It can be shown in Figures 6.1a, 6.1d and 6.1g that the added RBSM signal will distort the original waveform of vital sign signal.

We also show the frequency spectrum in two passbands $0.1 - 0.6$ Hz and $0.75 - 2.5$ Hz to visualize the impact of RBSM to vital sign signals. These are the passbands that have been used to determine RR and HR in our implementation but could be extended if need be if there are cases with higher HR. Figures 6.1b and 6.1c show that without RBSM, while we can clearly obtain the RR in the passband $0.1 - 0.6$ Hz, the harmonic component of respiratory signal which has Power Spectral Density (PSD) of 5000, interferes with the spectrum of heartbeat signal in the passband of $0.75 - 2.5$ Hz, which has the PSD of 3500. For the RBSM signal only, its spectrum spreads over the two passbands as shown in Figures 6.1e and 6.1f. Due to the random and aperiodic nature of the RBSM that we are considering in this dissertation, its magnitude will not significantly interfere with the RR estimation. As the maximum PSD of RBSM shown in Figure 6.1e is 5×10^4 while the maximum PSD of respiratory signal in the passband $0.1 - 0.6$ Hz from Figure 6.1b is 5×10^5. Thus, as shown in Figure 6.1h, the RR can still be estimated in the passband $0.1 - 0.6$ Hz even

119

Table 6.1. Simulated Parameters for Chest Displacement due to Respiration and Heartbeat

f_{RR} (Hz)	f_{HR} (Hz)	K_b (mm)	T_i (s)	T_e (s)	τ (s)	A_h (mm)
0.18	1.48	7.65	1.73	3.71	0.23	0.25

Table 6.2. Simulated Parameters for Two RBSM for 20 seconds

A_1 (mm)	A_2 (mm)	T_1 (s)	T_2 (s)	t_{d1} (s)	t_{d2} (s)
10.1	6.2	1.4	1.41	6.85	7.14
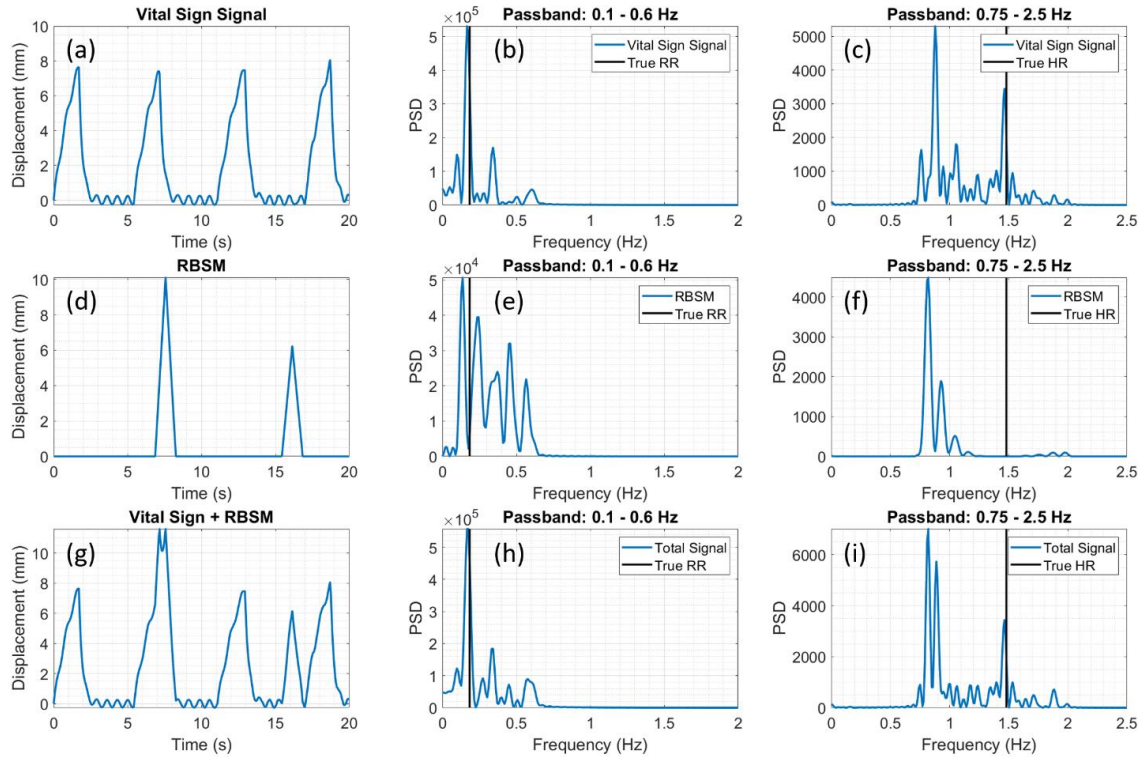
Figure 6.1. a), d), g) Time domain waveforms of vital sign, RBSM and combined signals, b), e), h) The frequency spectrums of corresponding signals in passband $0.1 - 0.6$ Hz, c), f), i) The frequency spectrums of corresponding signals in passband $0.75 - 2.5$ Hz.

when there is RBSM. However, in the passband 0.75 – 2.5 Hz, there are now two interferences from respiratory harmonics and from the RBSM, which makes it even more challenging to determine the HR. Next, based on the original signal in Figure 6.1g, we use equations (4.12) – (4.13) to calculate the constellation diagram and AD method to extract the phase variation. Then, we apply the automatic HBT extraction method discussed in Chapter 5 to show that the extracted HBTs comply with the conditions related to distances and angles between constellation points/vectors. Figure 6.2a shows the comparison between the phase variation signal with and without RBSM in blue and red colors, respectively. The extracted HBTs are shown in green based on the conditions of distances between constellation points and angles between vectors formed by the constellation points. We can see that based on the distances and angles data shown in Figures 6.2b and 6.2c, we can identify the regions that only carry information about heartbeat signals (green regions). For the regions that are interfered by RBSM (black regions), we can see that both the distances between constellation points and angles between vectors formed by constellation points are relatively high. Thus, the black regions shown in Figure 6.2a will not be included in the HBT selection process. At the end, we can extract three HBTs that can be used to reduce the impact of RBSM and magnify the heartbeat signals. As the original 3 extracted HBTs shown in Figure 6.2a are further processed by first finding their polynomial fitted versions as shown in Figures 6.3a, 6.3d and 6.3g. Then, the new version HBT_{new} of these HBT can be found by subtracting the original HBT_{ori} from the fitted version HBT_{fitted} as shown in Figures 6.3b, 6.3e and 6.3h. Figures 6.3c, 6.3f and 6.3i show comparisons of the frequency spectra between the filtered version of the original phase variation and the CWT coefficients using wavelet adapted from HBT_{new}. We can see that with our HBT-CWT method, we can reduce the interferences from the harmonics and RBSM as well as magnify the heartbeat signal so that HR can be accurately estimated.
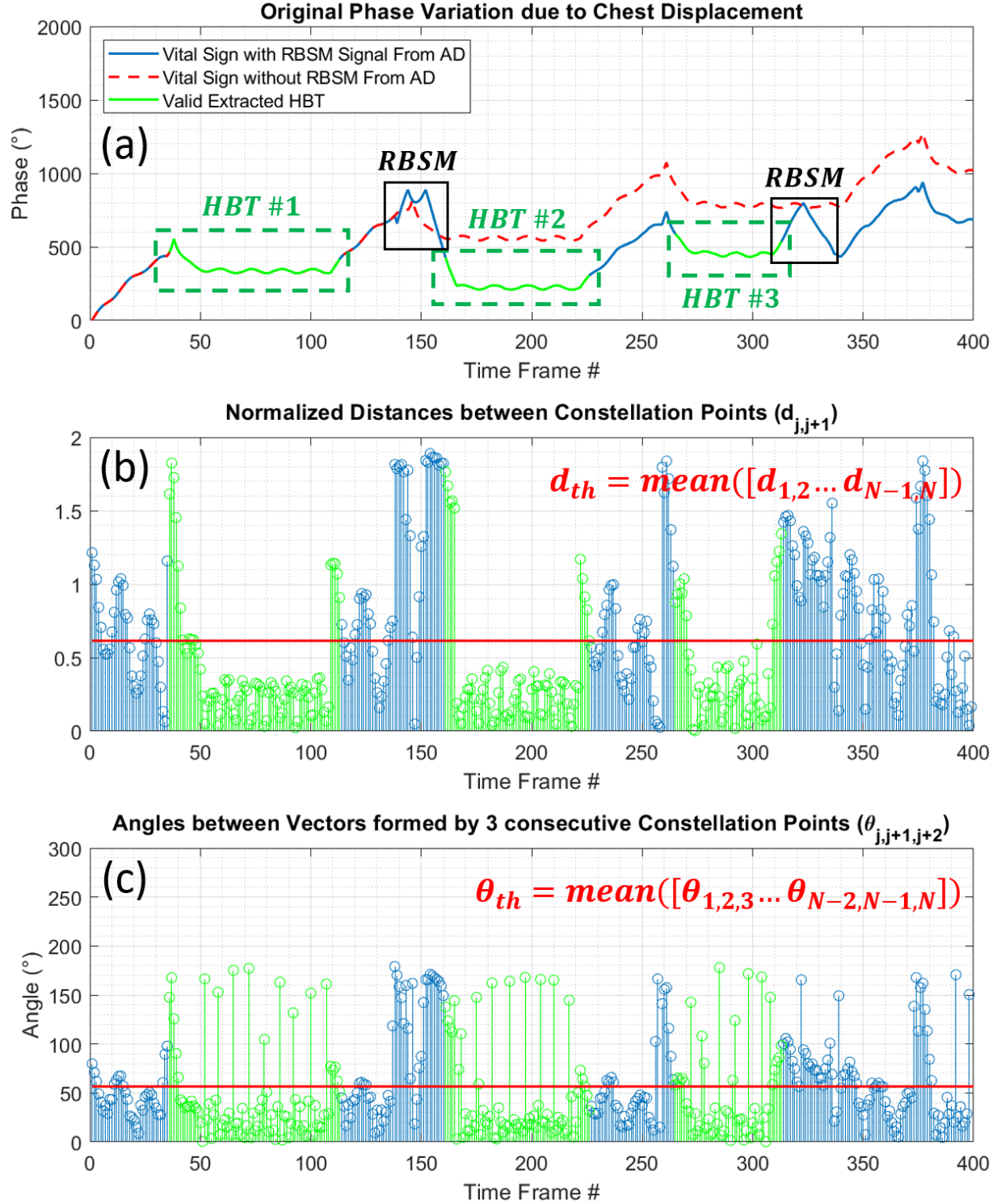
Figure 6.2. Signal Analysis for Simulated Data, a) Chest displacement obtained using AD method, b) Normalized distances $d_{j,j+1}$ between consecutive constellation points, c) Angles between vectors formed by consecutive constellation points $\theta_{j,j+1,j+2}$.
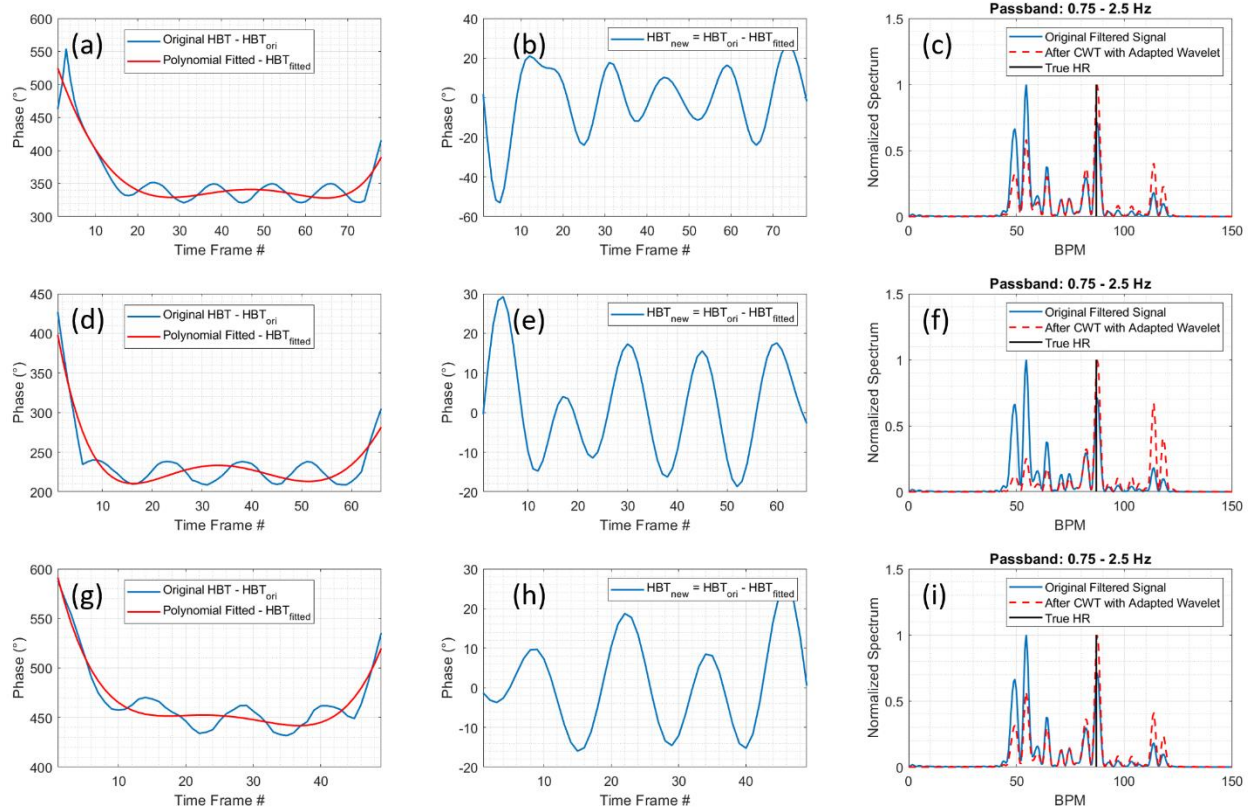
Figure 6.3. a), d), g) Original HBTs and their polynomial fitter versions, b). e), h) New versions of HBTs, c), f), i) Comparisons of frequency spectrum before and after using CWT with adapted wavelet from HBTs.

6.1.2 Analysis of RBSM using Experimental Data for Standing Subject with Significant RBSM

Next, we analyze the impact of RBSM based on experimental data when SUT is standing. To show the distortion of RBSM to vital sign signal (blue line), we show the reference respiratory signal from contact Belt Sensor (red line) in Figure 6.4a. Although it is difficult to identify the portions where RBSM interferes with the vital sign signal, we can see the distortion of RBSM to the vital sign signal by comparing with respiratory waveform from the Belt Sensor. Regardless, with the help of the distances and angles parameters calculated from the constellation diagram shown in Figures 6.4b and 6.4c, the selection of HBTs can be carried out.

The same approach is then employed here in which the polynomial fitted version of the extracted HBTs are calculated and are shown in Figures 6.5a and 6.5d below. Then the new versions HBT_{new} of the original templates HBT_{ori} are found by calculating the difference between $HBT_{ori} - HBT_{fitted}$ as shown in Figures 6.5b and 6.5e. These newly calculated HBT_{new} are then used for adapted wavelet to the CWT calculation in which the input signal to the CWT is the band-pass filtered phase variation with passband $0.75 - 2.5$ Hz. The frequency spectrum of the CWT coefficients are then calculated with FFT. After this step, the frequency spectrum should reveal the magnified heartbeat spectrum, as well as the reduction of the magnitude of interferences from respiratory harmonics and RBSM as shown in Figures 6.5c and 6.5f.

With results from simulated and experimental data from sections 6.1.1 and 6.1.2, we can see that even when there are RBSM which happens unintentionally especially when the SUTs are standing, our proposed HBT extraction method and CWT with adapted wavelet can help to magnify the heartbeat signal and reduce impacts from RBSM.
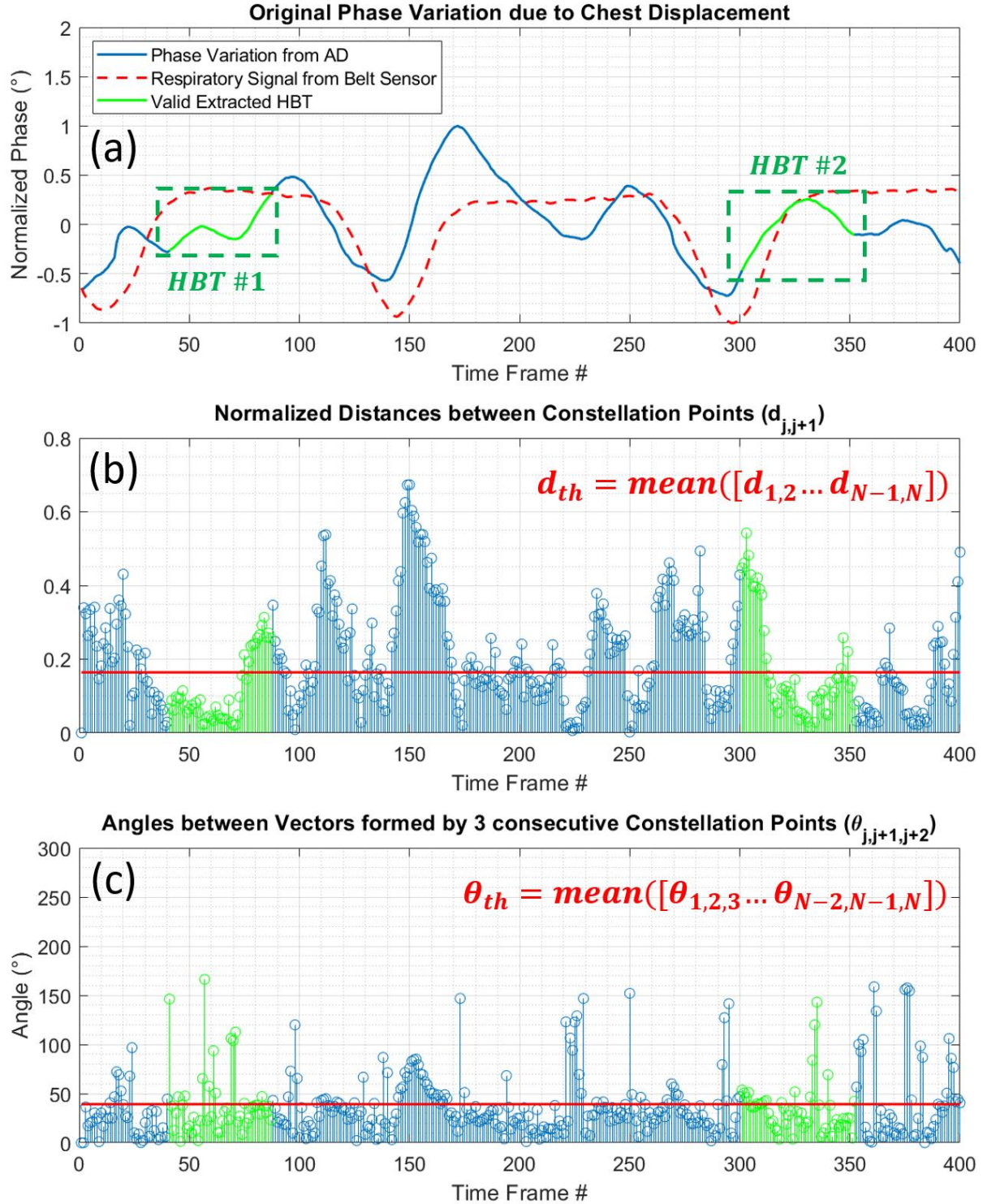
Figure 6.4. Signal Analysis for Standing Subject, a) Chest displacement obtained using AD method [22], b) Normalized distances between consecutive constellation points, c) Angles between vectors formed by consecutive constellation points.

Figure 6.5. a), d), Original HBTs and their polynomial fitter versions, b), e), New versions of HBTs, c), f), Comparisons of frequency spectrum before and after using CWT with adapted wavelet from HBTs.

6.2 Spectral-based Heart Rate Selection Method

With the magnitude of RBSM being unpredictable and significantly higher than heartbeat signals, not all extracted HBT will help to completely suppress interferences from RBSM and magnify the heartbeat signal to the peak of frequency spectrum. Since the magnitude from RBSM can overwhelm the heartbeat signal even after being magnified by HBTs, RBSM's spectrum might still occupy the highest PSD within a frequency spectrum. Therefore, when there are interferences from RBSM, simply assuming that the peak of frequency spectrum always occur at the heartbeat frequency is not a good approach. Because if the peak of the frequency spectrum is occupied by RBSM instead of heartbeat signal, there will be inaccurate HR estimation contributing to the estimation process and make it more difficult for us to determine the final HR value. To deal with this issue, we propose a spectral-based HR selection method to better select the HR estimation based on SNR characteristics from their frequency spectra.

The purpose of spectral-based HR selection is to take advantage of two characteristics about our frameworks: 1) the SNR of heartbeat signals are increased after using HBT and CWT, 2) multiple MIMO channels which produce lots of HR estimation from separate channel. Assuming each of the N MIMO channels has K valid extracted HBTs, then there is potentially up to $N \times K$ HR estimation and the SNR corresponding to these HR estimations. We can then select the final HR from among these $N \times K$ estimations based on the two characteristics discussed above. The procedure of the spectral-based HR selection can be divided into three steps:

Step 1: After HBT extraction, we can find the frequency spectrum of the CWT coefficients for each pair of band-pass filtered phase variation signals with passband $0.75 - 2.5$ Hz and the extracted HBTs.

Step 2: For each set of normalized frequency spectrum, create a set of potential HR values $\varepsilon = \{HR_1, HR_2, ..., HR_M\}$ where M is the total number of potential HR values. These potential HR values are selected if they are local maxima within the frequency spectrum with a normalized PSD at least equals 0.5. This value is chosen to make sure even if the PSD of the heartbeat signal is not at a peak after the CWT calculation using the extracted HBT, it is still selected as a potential HR value.

Step 3: Let $countPeak_{HR_j}$ be the number of occurrences that the PSD of the spectrum located at HR_j is the peak. Let $countPSD_{HR_j}$ be the number of occurrences that the magnitude of the spectrum located at HR_j increases after CWT calculation. The final HR values is selected as:

$$HR_{final} = argmax\left\{countPeak_{HR_j} + countPSD_{HR_j}\right\} \tag{6.1}$$

With this approach, even if the PSD at the right HR is not peaked within a frequency spectrum, by combining the two metrics reflected through $countPeak_{HR_j}$ and $countPSD_{HR_j}$, it helps to bring up the total occurrence of the accurate HR compared with the others. This is similar to a scoring mechanism where the potential HR's score is increased if it receives an upvote from different pairs of phase variation and HBT. To have its score increases, the potential HR must either peak in one frequency spectrum or have its normalized PSD increases higher than 0.5 after CWT calculation in another frequency spectrum. In the next section 6.4, we will demonstrate the spectral-based HR selection with a particular simulation set.

6.3 Modification of the Signal Processing Chain

In the previous chapter, we considered quasi-static scenarios when there are minimal RBSM, we can use MRC to combine the phase variation signal into one. The combined phase variation is then

passed through a band-pass filter with a passband 0.75 – 2.5 Hz. The filtered signal is used as input

for CWT with an extracted HBT to magnify the heartbeat signal. The HR from each pair of phase

variation and HBT is determined by finding the highest peak of frequency spectrum. Then final

HR is determined by taking the average of all HR estimation from each pair of phase variation and

HBTs.

   With the interferences of RBSM, the proposed signal processing chain in Chapter 5 needs to be

modified to deal with the unpredictable and random nature of the RBSM especially when the SUTs

are standing. As discussed above, the extracted HBTs along with CWT with adapted wavelet can

be used to magnify the heartbeat signal and reduce the interferences from respiratory harmonics.

However, because of the unpredictable interferences from RBSM, just finding the HR by looking

for the highest peak within a frequency spectrum is not an optimal approach. Therefore, to address

the RBSM issue, we want to combine the use of CWT method with the extracted HBTs as wavelets

and spectral-based HR selection for better HR estimation accuracy. In other word, we are fully

taking advantage of the MIMO's spatial diversity to implement the spectral-based HR selection

method in which the final HR is selected if it receives the highest scores from all channels based

on its spectral characteristics. Figure 6.6 shows the modified signal processing chain for RR/HR

estimation under scenarios with significant RBSM. As shown in Figure 6.6, we can observe several

differences compared with the processing chain proposed in Chapter 5. Most importantly, we do

not use MRC to combine the phase variation signals from multiple channels anymore. This is

because combining the signals in this case limits the amount of heartbeat information that can be

extracted separately from each channel. As RBSM might severely impact accuracy of HR

estimation, we need as much useful information as we can get from multiple channels to be able

to get accurate HR estimation. As a result, the adapted wavelet designed from HBTs and its CWT
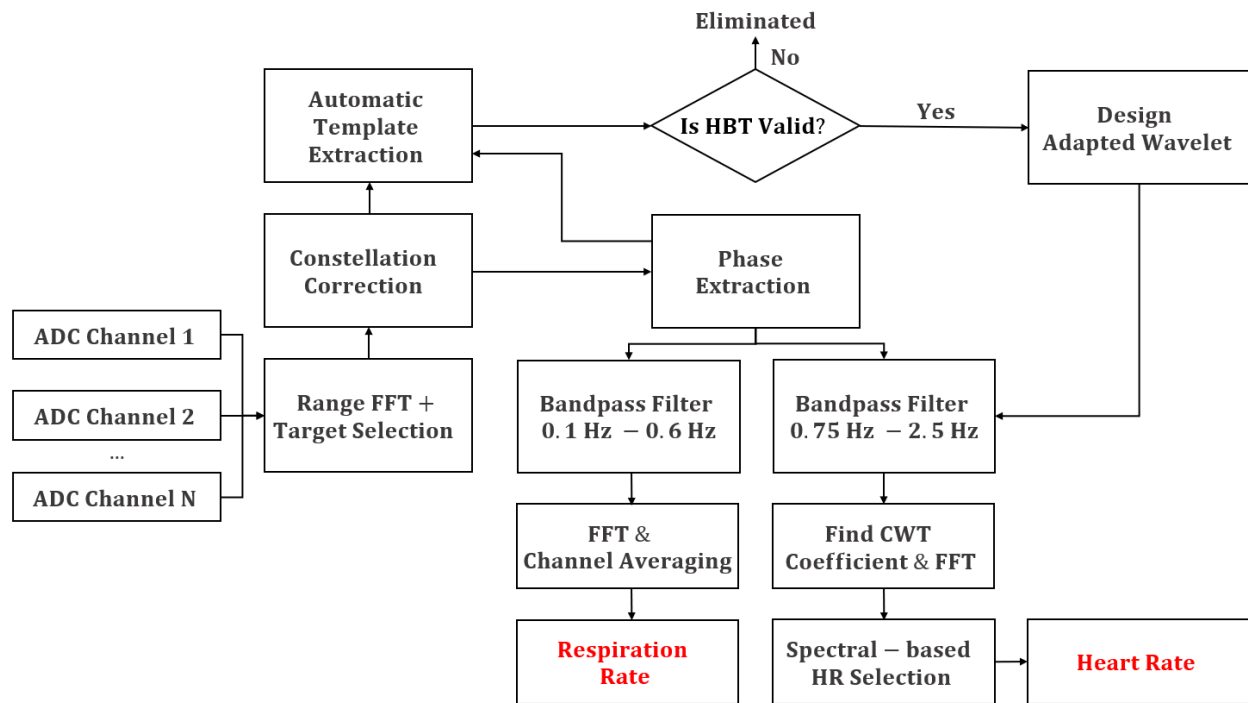
Figure 6.6. Block diagram for RR/HR estimation processing chain when there are RBSM.

coefficients are also calculated separately. The FFT spectrum of CWT coefficients from all MIMO channels are then passed through the Spectral-based HR selection to determine the final HR estimation.

6.4 Simulation Results

To validate the robustness of our proposed processing chain discussed above, we first show results with simulated data that also consider interferences from RBSM. Tables 6.3 and 6.4 show simulated parameters of chest displacement due to respiration and heartbeat and RBSM for the 20-second simulation, respectively. To make the RBSM level more pronounced, we increase the magnitude of the two RBSM as well as their duration so that their interferences are more significant. Figures 6.7 shows the simulated waveform of both vital sign signals and RBSM combined signal. Figures 6.7a, 6.7d and 6.7g show that the added RBSM signal distorts the waveform of vital sign signal.

Here, similar observations from section 6.1.1 can be made where respiratory harmonics and RBSM exist, the heartbeat signal is heavily concealed by these interferences hence it is hard to identify the heartbeat spectrum by just looking for the highest peak in the frequency spectrum as shown in Figure 6.7i. This observation from RBSM and its slow characteristics as well as wide-band behavior was also reported in [53].

Figure 6.8a shows a comparison between the phase variation signal with and without RBSM in blue and red colors, respectively. The extracted HBTs are shown in green based on the conditions of distances between constellation points and the angles between the vectors formed by constellation points as previously described in Chapter 5. We can see that based on the distances and angles data shown in Figures 6.8b and 6.8c, we can identify the regions that would only carry information about heartbeat signals (green regions). For the regions that are interfered by RBSM

131

Table 6.3. Simulated Parameters for Chest Displacement due to Respiration and Heartbeat

f_{RR} (Hz)	f_{HR} (Hz)	K_b (mm)	T_i (s)	T_e (s)	τ (s)	A_h (mm)
0.2	1.5	3.96	1.6	3.47	0.21	0.15

Table 6.4. Simulated Parameters for Two RBSM for 20 seconds

A_1 (mm)	A_2 (mm)	T_1 (s)	T_2 (s)	t_{d1} (s)	t_{d2} (s)
5.6	9.8	3.6	3.3	2.38	7.84
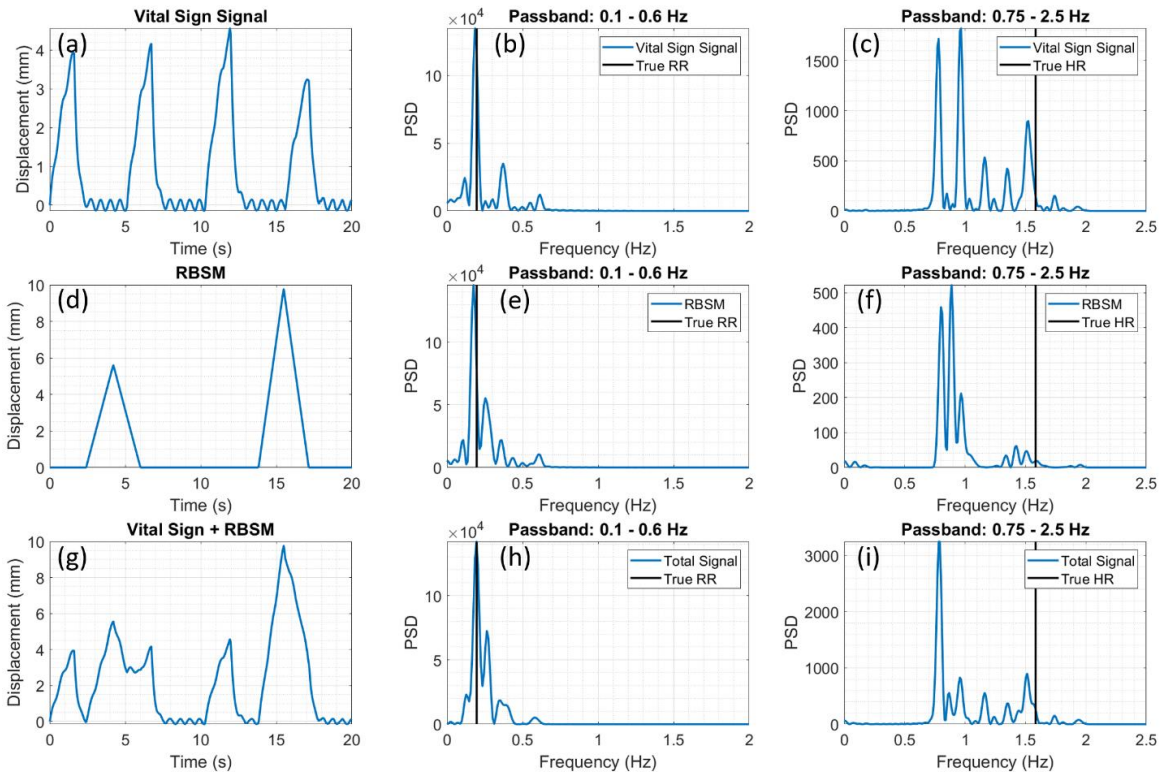
Figure 6.7. a), d), g) Time domain waveforms of vital sign, RBSM and combined signals, b), e), h) The frequency spectrums of corresponding signals in passband 0.1 – 0.6 Hz, c), f), i) The frequency spectrums of corresponding signals in the passband 0.75 – 2.5 Hz.
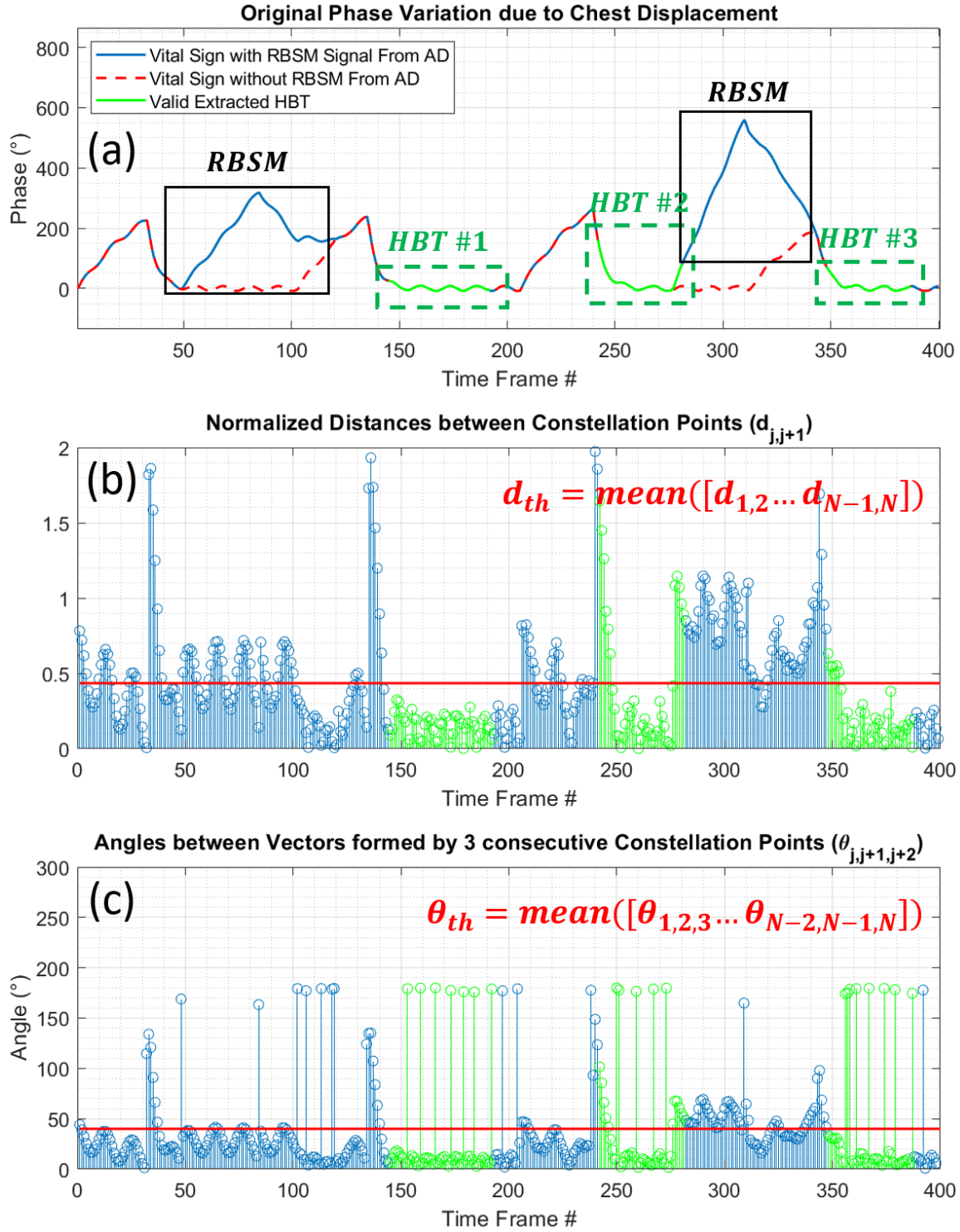
Figure 6.8. Signal Analysis for Simulated Data, a) Chest displacement obtained using AD method, b) Normalized distances $d_{j,j+1}$ between consecutive constellation points, c) Angles between vectors formed by consecutive constellation points $\theta_{j,j+1,j+2}$.

(black regions), we can see that both the distances between constellation points and angles between vectors formed by constellation points are relatively high. Thus, the black regions shown in Figure 6.8a will not be included in the HBT selection process. At the end, we can extract three HBTs that can be used to adapt corresponding wavelets and thus help to reduce the impact of RBSM and magnify the heartbeat signals.

Next, the original 3 extracted HBTs shown in Figure 6.8a are further processed by first finding their polynomial fitted versions as shown in Figures 6.9a, 6.9d and 6.9g. Then, the new version HBT_{new} of these HBT can be found by subtracting the original HBT_{ori} from the fitted version HBT_{fitted} as shown in Figures 6.9b, 6.9e and 6.9h. Figures 6.9c, 6.9f and 6.9i show comparisons of frequency spectra between the filtered version of the original phase variation and the CWT coefficients using wavelets adapted from the extracted HBT_{new}. These three frequency spectra are now passed through the spectral-based HR selection to pick the final HR value. As discussed above, the spectral-based selection will first create a list of potential HR values by finding local maxima within the spectra that has normalized PSD higher than 0.5. In this simulation, the list of potential HR includes two HR values which are 47 BPM and 91 BPM. Their corresponding PSD before the CWT are 1 and 0.25 for all three spectra, respectively. After CWT, their PSDs are 0.97 and 1 which still makes it challenging to pick the correct HR by looking for the peak of the frequency spectrum. In this case, the PSD of HR at 47 BPM decreases after CWT calculations, while PSD at 91 BPM significantly increases after the CWT calculation. Thus, even though the PSDs at the two potential HR values are approximately the same in the spectra, based on the spectral characteristics, we can conclude that the final HR should be 91 BPM, which is close to the true HR value, which is 90 BPM.

Finally, Figure 6.10 shows the RR estimation by passing the phase variation signal through the
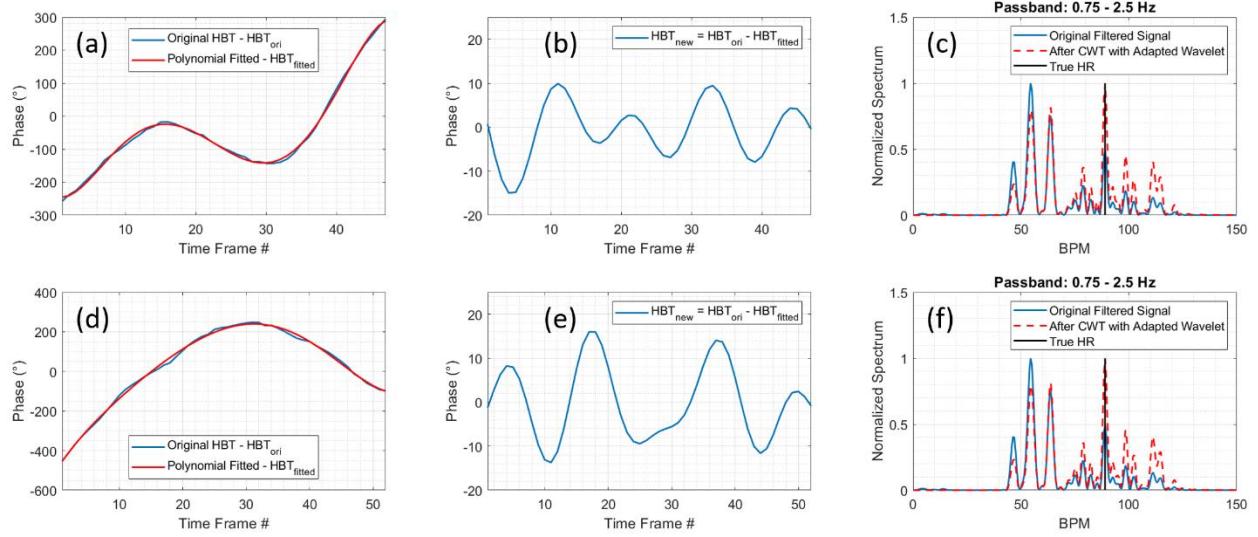
134
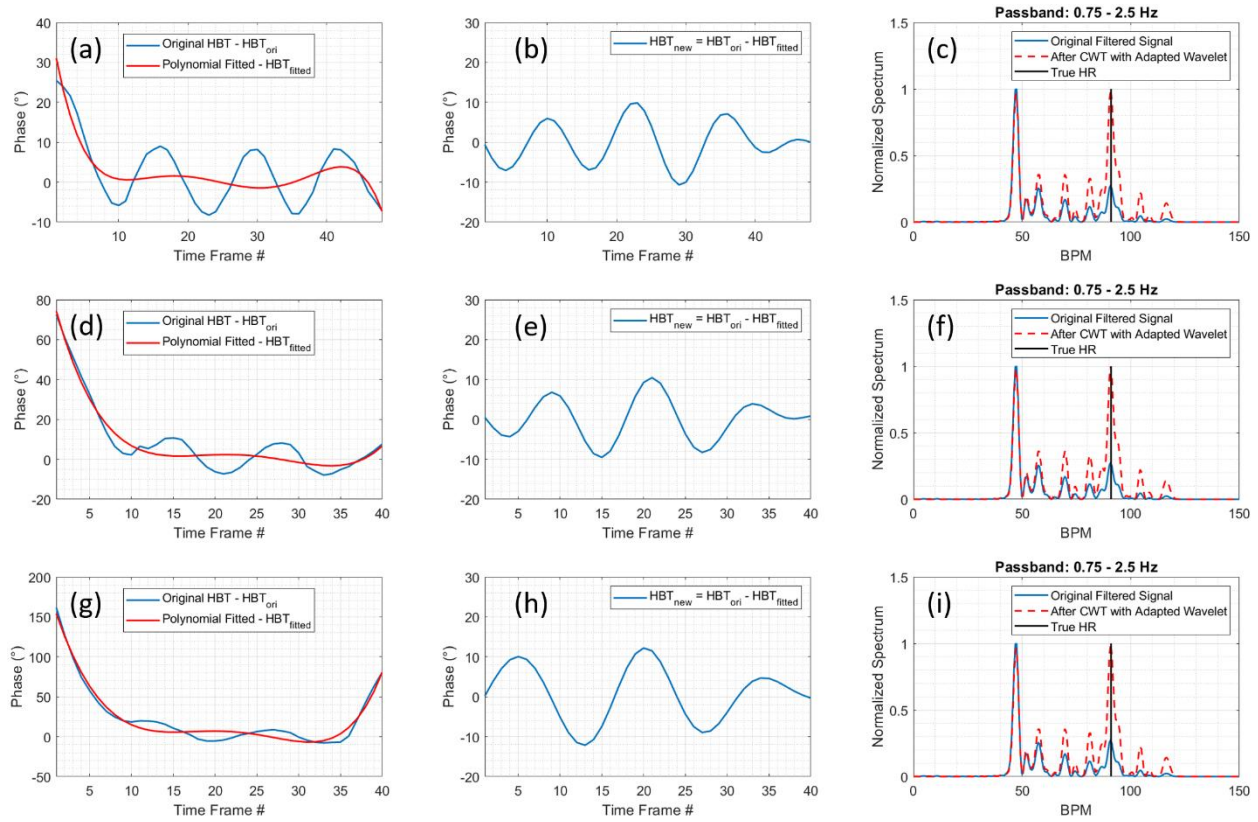
Figure 6.9. a), d), g) Original HBTs and their polynomial fitter versions, b). e), h) New versions of HBTs, c), f), i) Comparisons of frequency spectrum before and after using CWT with adapted wavelet from HBTs.
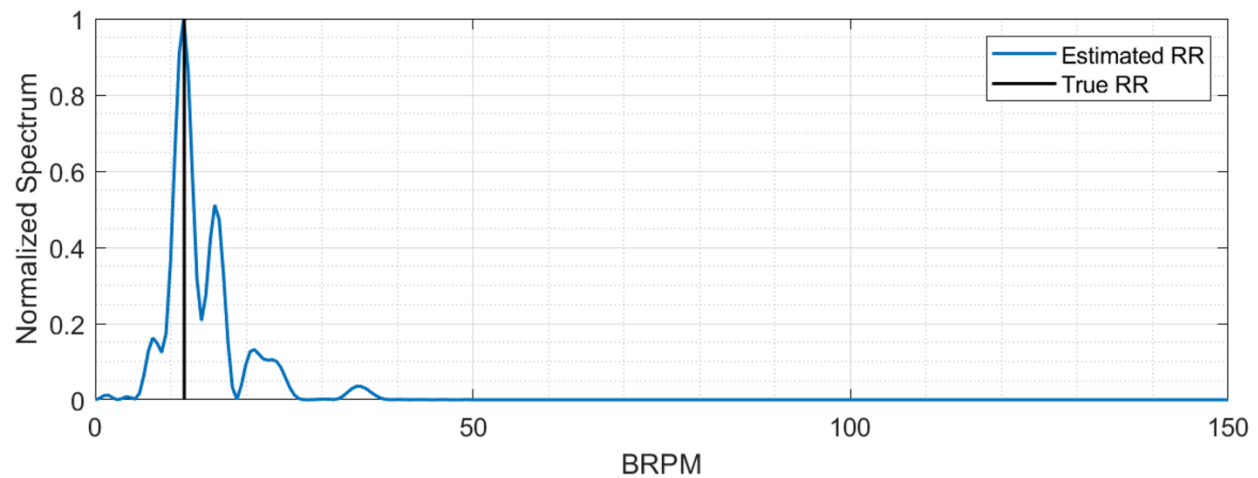
Figure 6.10. Estimation of RR for simulated data.

BPF with passband 0.1 – 0.6 Hz. Then by finding the peak of frequency spectrum, we can determine the RR which agrees well with the true RR (approximately 12 BRPM). From this simulation, we can show that even with more pronounced RBSM, we are still able to estimate RR/HR with high accuracy. Next, we will validate the robustness of our proposed processing chain using experimental data.

6.5 Experimental Scenarios and Results

Scenarios with single and multiple subjects standing in front of the radar are performed and pursued to validate our proposed signal processing chain in this chapter. Similar to Chapter 5, Respiration waveform from Belt Sensor NUL-236 and photoplethysmogram (PPG) signal from Pulse sensor SEN-11574 are extracted and processed with FFT to estimate RR and HR as our ground truth. 20-second window is used at a time to estimate RR and HR. Two adjacent windows have 19-second overlapped data and 1-second new data. To assess the estimation performance throughout our experiments, statistical metrics such as mean-error μ_e, standard deviation (std) of errors σ_e, accuracy rate for estimated error $<= 3$ BPM and > 3 BPM compared with the contact sensor reading are discussed. Comparisons between the modified algorithm chain proposed in this chapter will be presented along with the algorithm chain discussed in the Chapter 5.

6.5.1 Scenario #1: Subjects Standing and Withholding Respiration in front of Radar

In this experiment, the SUTs hold their breath for almost 1 minute and stand 1 meter away from the radar as shown in Figure 6.11a. A 2D-FFT to show the location of the target during the experiment is shown in Figure 6.11b as an example. For this scenario, the same three participants from experimental scenario #1, #3 and #4 from Chapter 5 are asked to participate. Table 6.5 shows

136
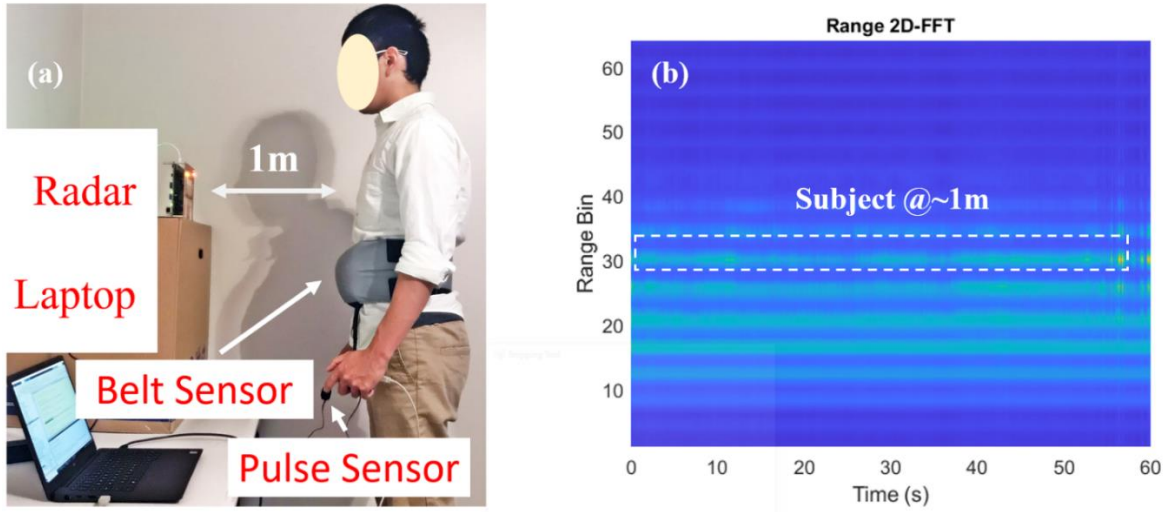
Figure 6.11. a) Experimental Setup of Scenario #1 and #2, b) 2D-FFT Range Profile

Table 6.5. Information of participants in Scenario #1

Participant #	Gender	Age	Weight (lbs)	Height (in)
1	Male	29	125	64
2	Female	30	110	62
3	Male	22	185	70

information about genders, ages, weights, and heights of these participants. To show the significant impact of the RBSM to the vital sign signals, Figure 6.12 shows a comparison between the scenarios when the SUT withhold their breath while sitting/standing in front of the radar. It can be observed in Figure 6.12a that while sitting, the upper body of the SUT does not sway too much, the phase variation signal clearly reflects the chest displacement due only to heartbeat signal. This can also be confirmed by comparing the phase variation signal with the ground truth signal from the Pulse Sensor in Figure 6.12b. Figure 6.12c shows the frequency spectrum of the original phase variation and the CWT coefficients, we see that there is no significant interfered signals and the heartbeat spectrum is clearly shown which agrees with the ground truth result. As seen in Figure 6.12d, although the SUT is withholding their breaths during the experiment, since they are standing, their upper bodies tend to sway back and forth unintentionally, which creates a strong interfering signal. Figures 6.12d and 6.12e show the time domain signal captured by the radar which is not correlated with the ground truth time-domain signal. Figure 6.12f shows the frequency spectrum of the phase variation signal in Figure 6.12d. It can be seen that there are two significant large low-frequency components due to RBSM. However, with proper HBT extraction, the CWT coefficient has been able to reduce the first interference at around 50 BPM. And more importantly, the heartbeat spectrum is magnified to become the highest peak in the spectrum. It should be noticed that the result shown here is for one channel, additionally with multiple MIMO channels producing similar performance, the probability of correct HR estimation is significantly higher.

Figure 6.13 shows the estimated HR results for 3 subjects compared with ground truth. We can see a correlation in the trend between the estimated radar and ground truth. Furthermore, because the participants try to hold their breath for 1 minute, their HR increases because their nervous systems are reacting due to the lack of oxygen level for the brain and other organs to function.
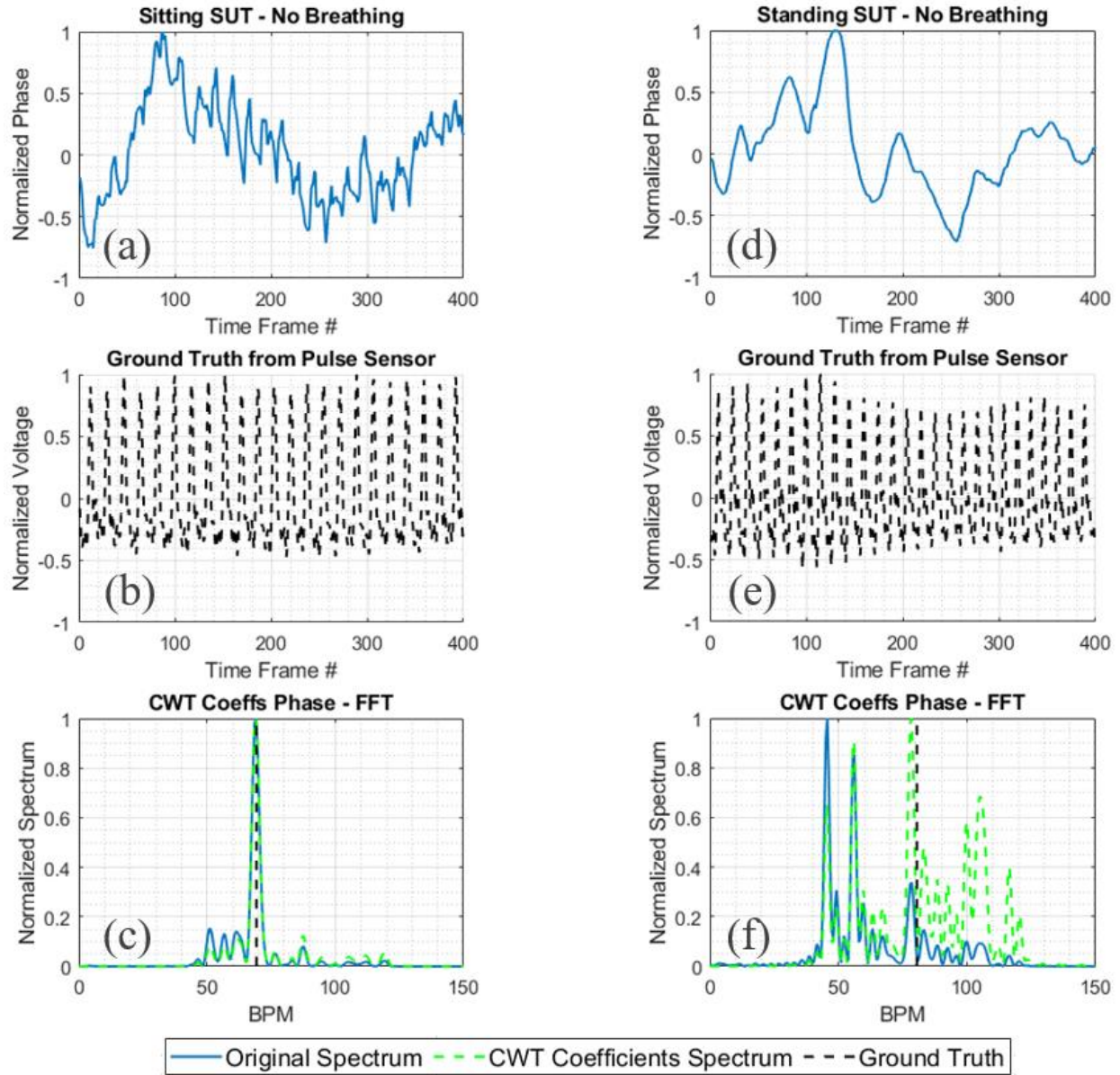
Figure 6.12. a) Phase variation of a sitting SUT and not breathing, b) Its corresponding ground truth, c) Frequency spectrum of original phase variation and CWT coefficient, d) Phase variation of a standing SUT and not breathing, e) Its corresponding ground truth, f) c) Frequency spectrum of original phase variation and CWT coefficient.
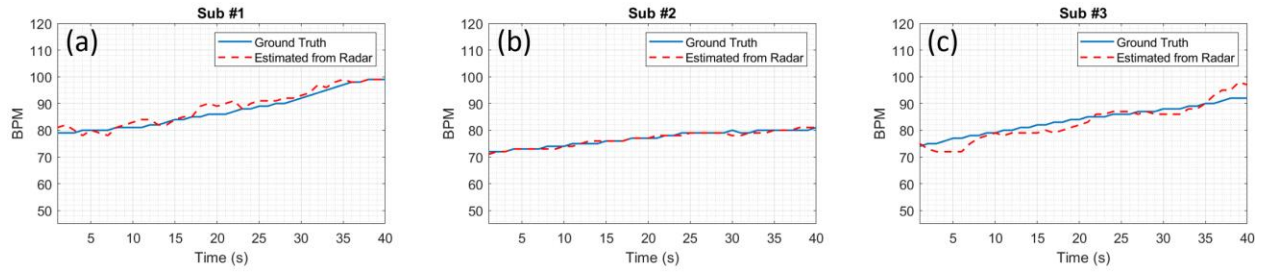
Figure 6.13. HR Estimation compared with ground truth pulse sensor of, a) Subject #1, b) Subject

#2, c) Subject #3.

Figure 6.14 shows the error analysis and accuracy rate for the three subjects from top to bottom when all the 192 MIMO channels are used. It can be observed that for standing subjects, the methods used in Chapter 5 are no longer efficient due to the strong interferences of RBSM. This explains why HR estimated from these methods have very high std- and mean-error compared with ground truth. With proper adaptive HBT extraction and spectral-based HR selection method, the proposed processing chain in this chapter has successfully estimated HR with significantly higher accuracy. The HR estimated from the proposed methods in this chapter typically outperforms the accuracy of the Channel with Lowest Mean-Error. This again validates the efficiency of using multi-channel radars instead of single-channel radar. Overall, our proposed method in this chapter has demonstrated satisfactory performance for the scenario where SUTs stands in front of radar and withholds their breaths.

A disadvantage of the proposed method in this chapter is that it requires more computational and processing time. As shown in Figures 6.15, the average processing time for the proposed method in this chapter is approximately 1.4s when all 192 channels are used while the others require only less than 0.2s on average to produce HR estimation. The processing time is approximated on a Dell Latitude 7400 laptop with 8-core Intel Core i7 CPU and a total 16 GB of memory running at 2.1 GHz. The laptop operates on Microsoft Windows 10, and all implementation is done with MATLAB version R2021b. This is expected because the proposed method must adaptively identify and extract multiple HBTs from different MIMO channels separately. To expedite the proposed method, parallelization of the whole process can be done so that the HBT extraction from different channels can be executed at the same time.

Another approach is to reduce the numbers of channels used for processing. For example, not all 192 channels are needed for accurate HR estimation. This is because if the two receiving antennas
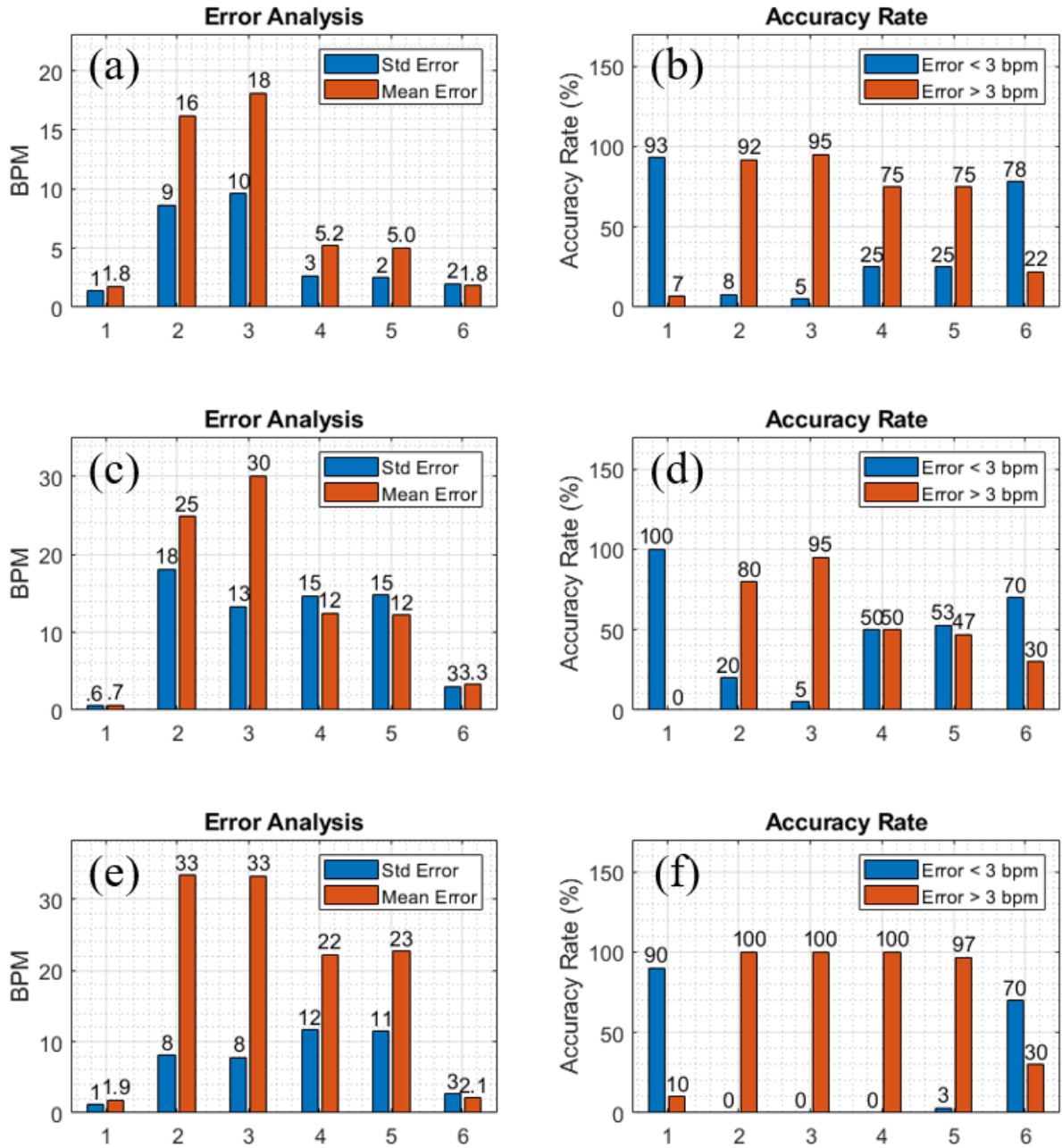
Figure 6.14. Results of HR Estimation from Scenario #1. a), b) Error Analysis and Accuracy Rate from Subjects #1, c), d), Error Analysis and Accuracy Rate from Subjects #2, e), f) Error Analysis and Accuracy Rate from Subjects #3. ***Horizontal axis shows:*** 1) Modified Processing Chain 2) MRC with all channels, 3) MRC with selected channels, 4) Channel average with all channels, 5) Channel average with selected channels, 6) Channel with lowest mean-error compared with ground truth among all channels.
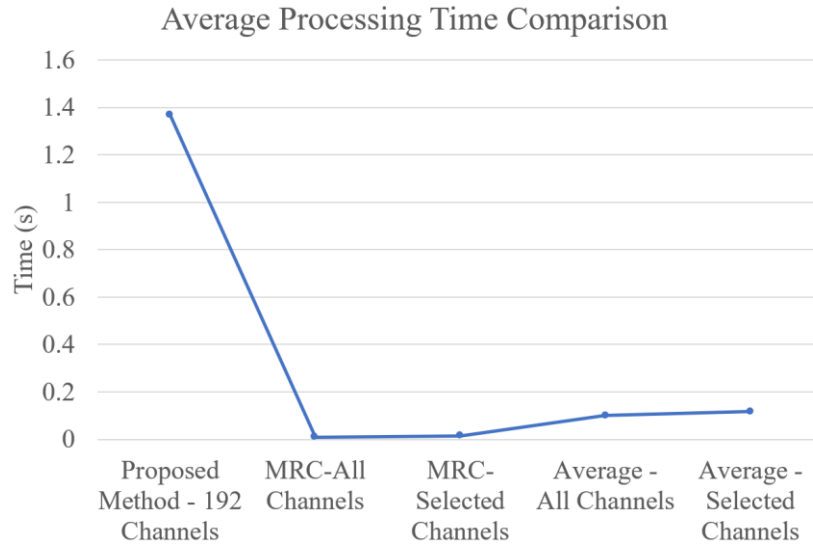
Figure 6.15. Comparison of average processing time between different methods.
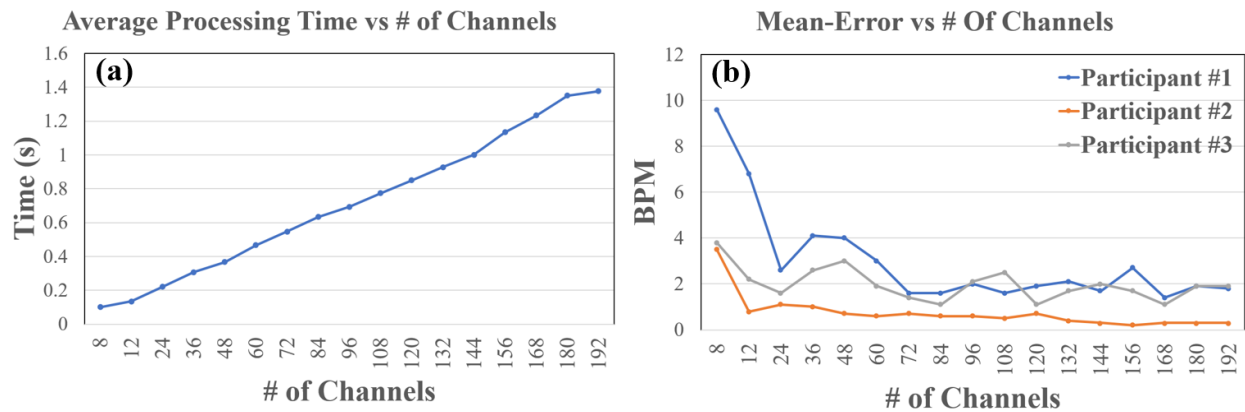
Figure 6.16. a) Comparison of average processing time when different # of channels are used, b) Mean-Error of Scenario #1 from three different participants when different # of channels are used.

are physically close to each other (less than λ_0-spacing) they will receive redundant information. Thus, by reducing the redundant channels, we can speed up the computation without losing useful information. Figure 6.16a shows the average processing time increases as the number of channels increases. Therefore, reducing the number of channels used form processing can significantly speeds up the HR estimation. Figure 6.16b shows the analysis of mean-error in HR estimation compared with the number of channels used for processing. It can be seen for Participants #1 and 2, up to 60 channels are needed to acquire satisfactory performance while for Participant #3 there are 24 channels needed. Therefore, we can see that it is not necessary to use all 192 channels for HR estimation. However, proper number of channels is still required. Furthermore, selecting the channel that has good information about HR also helps to reduce the number of channels needed. In the next chapter, we will discuss a deep learning (DL) framework to support the processing chain proposed in this chapter. The DL framework will be designed to identify good channels prior to processing so that channels that do not have strong information about HR will be eliminated. Hence, the processing can be speed up and accuracy can be improved further.

6.5.2 Scenario #2: Subjects Standing and Normally Breathing in front of Radar

The experimental setup for this scenario is similar to that of Scenario #1 where the SUTs stands in front of the radar and is 1 m away. However, they will be asked to normally breath during the 5-minute experiment so that both their RR and HR can be monitored by the radar in a long-term setup. Since this is a common scenario and can be applied to various real-world applications such as at clinics, hospitals, etc., we recruited 10 voluntary participants for this scenario to have a better performance analysis of our proposed hardware and algorithm chains. Table 6.6 shows information about genders, ages, weights, and heights of these participants. Figure 6.17 shows the RR

144

estimation results from radar using MRC with all channels method compared with the ground truth Belt Sensor NUL-236. As shown in the simulation results, RBSM is aperiodic and random which should not significantly interfere with the RR estimation. This can be validated in experimental results where for most the participants, the trend in RR estimated from the radar agrees well with the RR estimated from ground truth. For subjects #7 and #9, there were technical issues where the Belt Sensor does not fit the subjects. Therefore, we could not capture the refence respiratory waveforms for comparison.

Figure 6.18 shows the error analysis of the RR estimation results shown above by calculating the std-error σ_{error} and mean-error μ_{error} of the estimated results. We can see that for most participating subjects, the mean-error of estimated results can be as low as 0.5 BRPM and the worst result is from subjects #5, #6 and #8 with mean-error 1.1 BRPM.

Figure 6.19 shows the accuracy rate as another metrics to assess the estimation accuracy compared with the ground truth. We can see that estimated RR from most of the subjects have over 96% estimations with error within 3 BRPM compared with the ground truth.

Next, we analyze the performance of HR estimation from all participating subjects for Scenario #2. Figure 6.20 shows the estimated HR from radar using the proposed processing chain in this chapter compared with the ground truth Pulse Sensor SEN-11574. We can see that estimated HRs are not as good compared with HR results from quasi-static scenario is Chapter 5. However, the estimated HRs from radar are still following the trend relative to the ground truth. Figures 6.21 and 6.22 show the error analysis using std-error σ_{error} and mean-error μ_{error} from all participating subjects using different methods as discussed above. It can be observed that for all subjects, the proposed processing chain in this chapter outperform the methods used in Chapter 5. This was due to the unpredictable interferences from RBSM. By just finding the HR by looking up the highest

Table 6.6. Information of participants in Scenario #2

Participant #	Gender	Age	Weight (lbs)	Height (in)
1	Male	29	125	64
2	Female	30	110	62
3	Male	22	185	70
4	Male	26	150	69
5	Female	54	150	61
6	Female	65	110	64
7	Female	64	235	67
8	Male	23	170	72
9	Male	33	340	73
10	Male	27	125	66

Figure 6.17. RR Estimation compared with Ground Truth from all participating subjects.
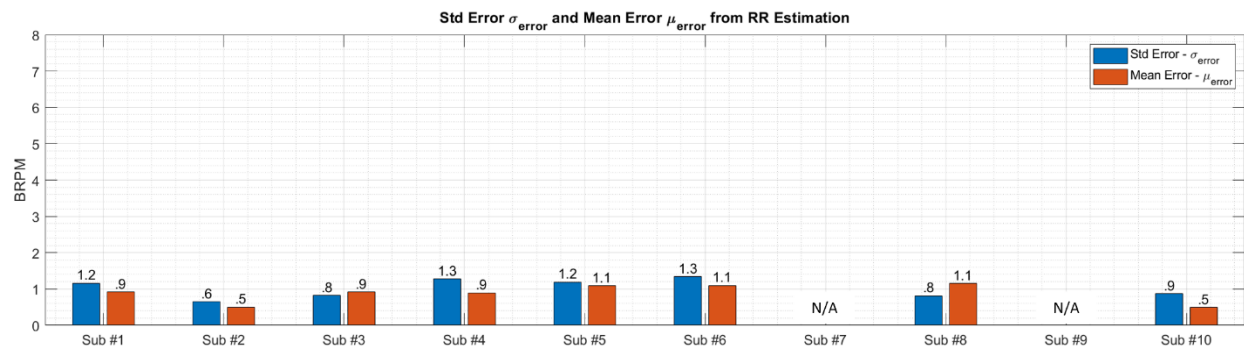
Figure 6.18. Error Analysis of RR Estimation compared with Ground Truth from all subjects.
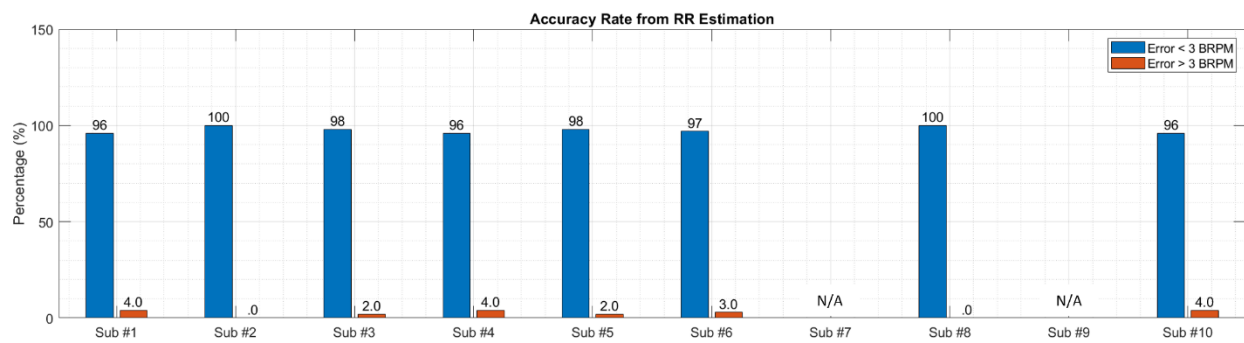
Figure 6.19. Accuracy Rate of RR Estimation compared with Ground Truth from all subjects.
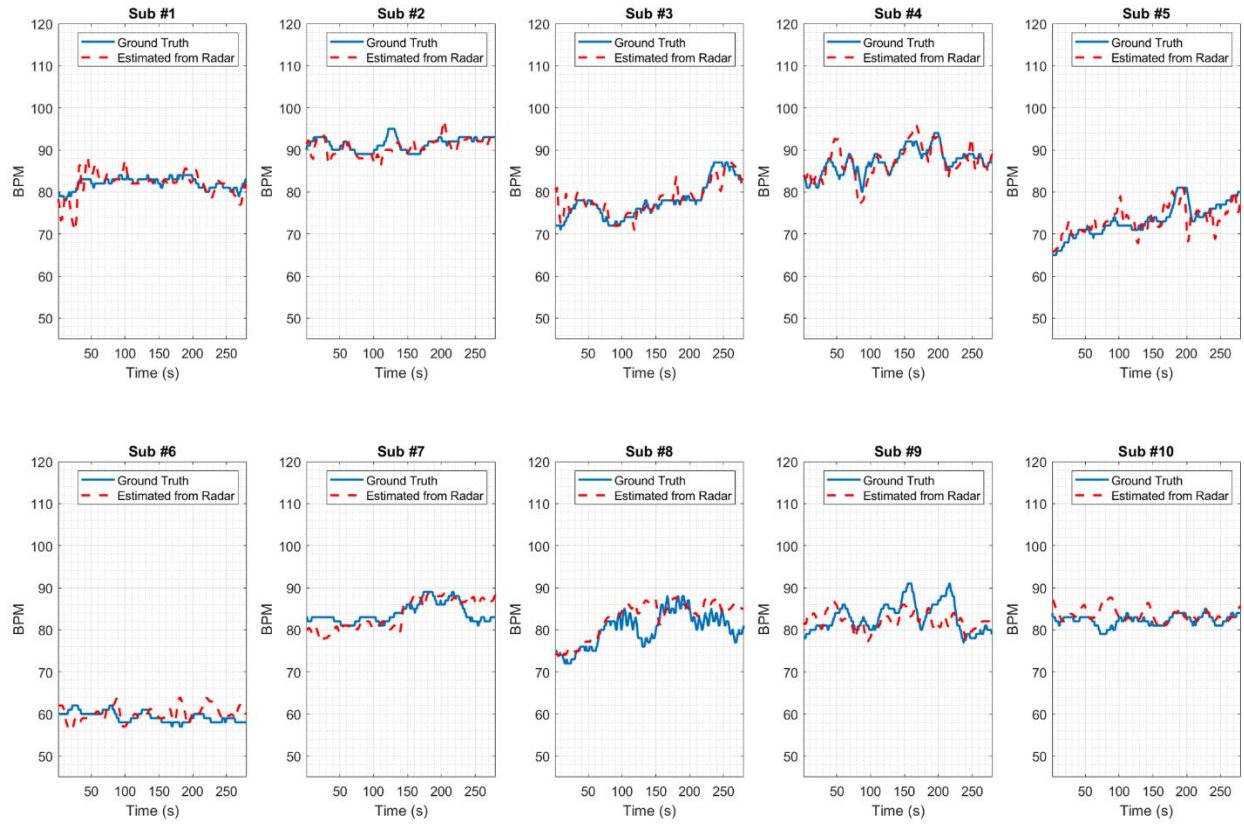
Figure 6.20. HR Estimation compared with Ground Truth from all participating subjects.

peak within a frequency spectrum is not an optimal approach. Therefore, in the current processing chain, the combination of CWT method with extracted HBT as wavelet and spectral-based HR selection help to produce better HR estimation accuracy. It can also be shown from Figures 6.21 and 6.22 that results from single channel with lowest mean-error compared with ground truth are worse than the current processing chain which employs multiple MIMO channels. Thus, we can confirm that using more channels and appropriate processing technique can generally help to improve the accuracy of HR estimation especially when there is significant amount of RBSM.

Finally, Figure 6.23 shows the accuracy calculation using the proposed processing chain in this chapter for the percentage of errors that are within and beyond 3-BPM threshold. These percentages should be correlated with the mean-error μ_{error} analysis. For most subjects, accuracy is typically higher than 80%. While this is certainly lower than the average accuracy rate compared with results from quasi-static scenarios, we still consider these as satisfactory results based on comparison with other research groups in terms of reported performances and hardware requirements for similar experimental setup which will be shown in the next section.

6.6 Discussion

6.6.1 Comparison between different methods

Figure 6.24 shows a comparison of average error in HR estimation from all experiments listed above for different methods. The proposed processing chain in this chapter outperforms the methods used in Chapter 5. This was due to the unpredictable interferences from RBSM which makes finding the HR by looking up the highest peak within a frequency spectrum is not an optimal approach. Furthermore, channel with lowest mean-error produces worse result than the modified processing chain. While we cannot draw a generalized conclusion because we do not have sufficient amount of experimental data to perform statistical inference. However, based on the data
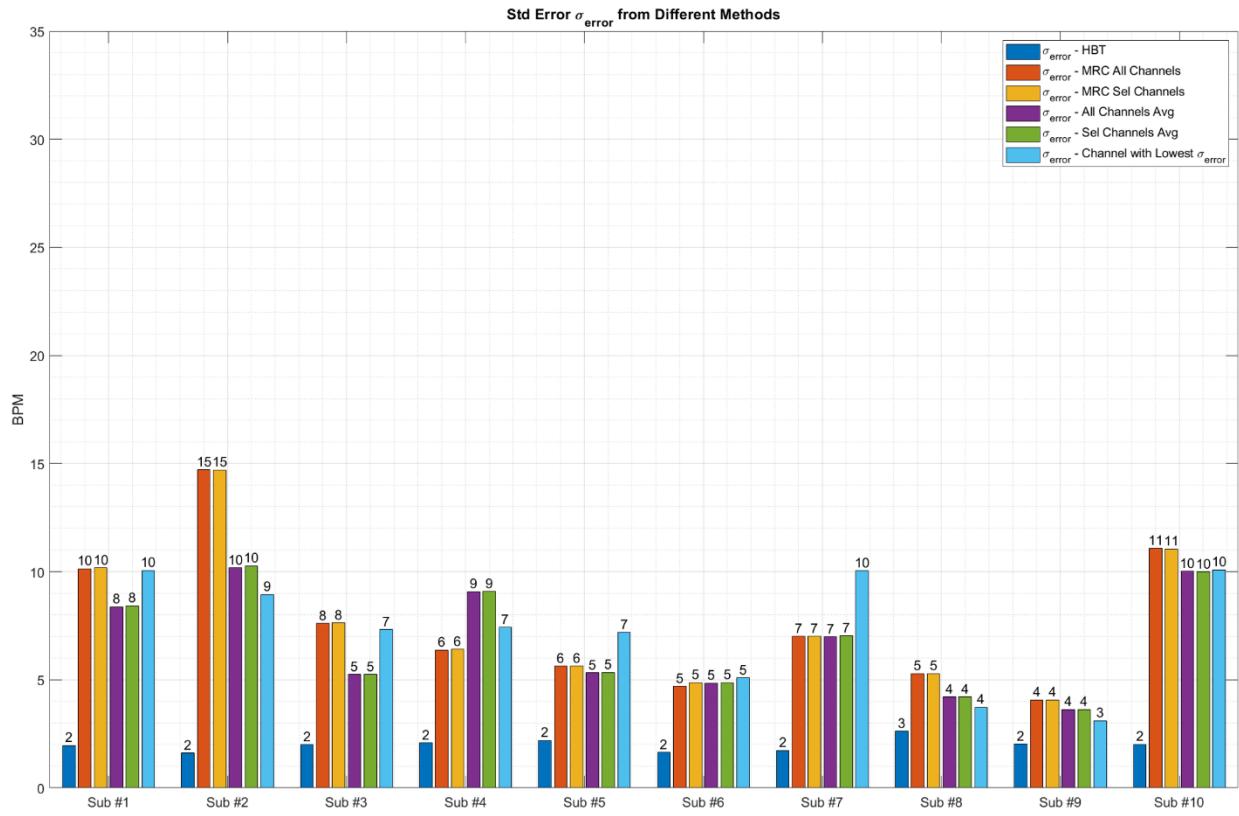
Figure 6.21. Std-Error Analysis of HR Estimation compared with Ground Truth from all subjects.
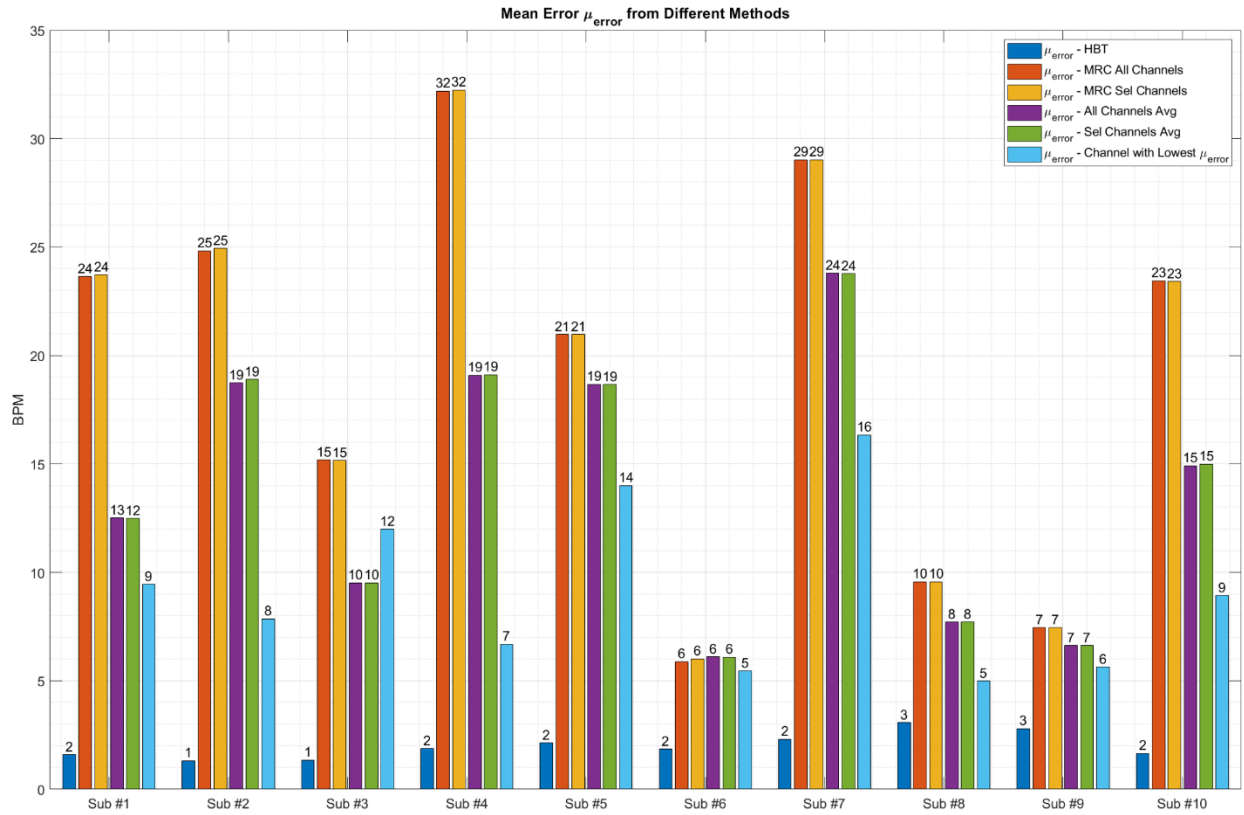
Figure 6.22. Mean-Error Analysis of HR Estimation compared with Ground Truth from all subjects.
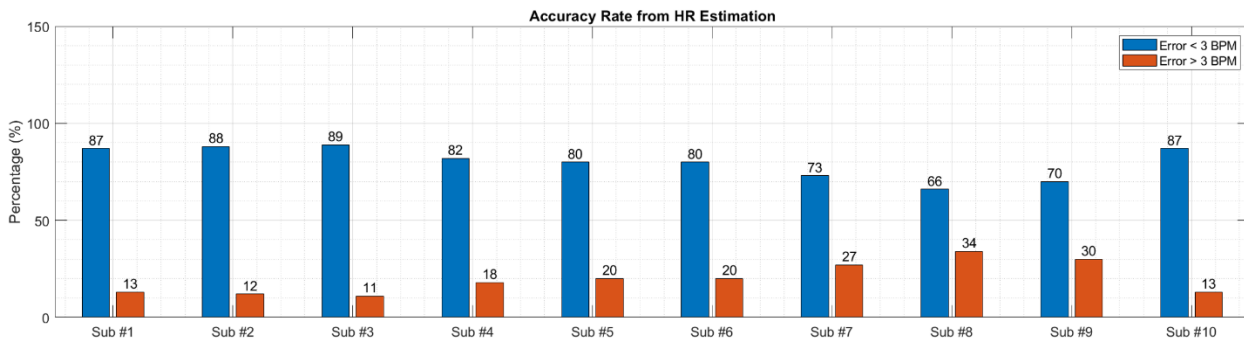
Figure 6.23. Accuracy Rate of HR Estimation compared with Ground Truth from all subjects.

151
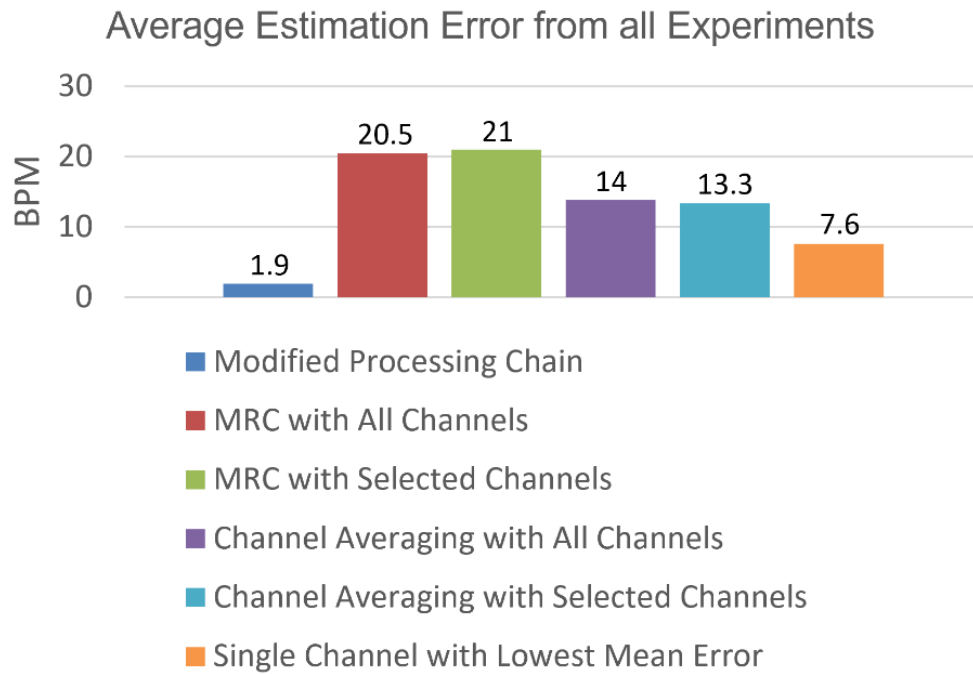
Figure 6.24. Comparisons between different methods for average error of HR estimation from all experiments.

collected from the recruited participants in above experiments, we can see that having multiple channels and appropriate processing technique helps to improve the accuracy of HR estimation especially when there are significant interferences from RBSM. This observation is consistent as reported from other research groups in literature [12, 44-53].

6.6.2 Comparison with reported performances from literature

Table 6.7 provides a summary of the methods used for RR/HR estimation in the presence of RBSM from various research groups along with their reported performances, hardware description, advantages, and limitations of their proposed methods. Unlike most of the current approaches in the literature to cancel RBSM, where multiple radar devices are placed around the SUT so that RBSM can be canceled, our proposed method in this chapter does not require additional radar systems which reduces the hardware complexity and the need for alignment/calibration between these radar devices [10-16]. Furthermore, our HBT extraction method does not require human intervention as the one used in [21]. Therefore, it is more suitable to be implemented for real-time and automatic operation. It should be noted that, however, our method relies on constellation diagram to identify and select good HBTs. Therefore, with RBSM, we are certain that there will be a time interval when there is minimal amount of RBSM and the HBT can be selected from these time intervals [53]. Thus, under scenarios where there are various motions involved, such as when subjects are actively walking or running, our proposed method probably fails as it is challenging to use constellation diagrams to identify valid HBTs because there are velocity components from different body parts interfering with the respiratory/heartbeat signals. Another limitation is that our proposed method requires multiple MIMO channels to estimate HR accurately. These MIMO channels need to be widely distributed similarly to the antenna configuration of the MMWCAS-RF-EVM that we are using in this dissertation. This is

Table 6.7. Comparison with other groups that address RBSM from SUT for RR/HR estimation

Groups	# of Subjects	Distances	Hardware	Software	Type of RM	Advantages	Limitation	Reported Performances
This work	2	1 m	FMCW MIMO 77-81 GHz	HBT-CWT-FFT-Spectral-based HR Selection	RBSM	Reduce RBSM, Improve SNR of heartbeat signals	Require widely distributed MIMO in front of SUT	Improving up to 89% of accuracy
Li et al. [12]	1	Up to 2 m	CW Dual Front-Back Radar 2.4 GHz	AD-FFT	RBSM	Cancel RBSM	Require dual devices in front and back of SUT	N/A
Wang et al. [44]	1	1 m	CW Dual Front-Back Radar 2.4 GHz	AD-FFT	RBSM	Cancel additional motion	Require dual devices in front and back of SUT	97% RM Reduction
Tang et al. [45]	1	1 m	CW Dual Top-Bottom Radar 2.4 GHz	AD-FFT	RBSM	Cancel RBSM	Require separated dual devices in front of SUT	85% RM Reduction
Rich et al. [47]	1	0.5 m	CW Dual Top-Bottom Radar 2.4 GHz	AD-FFT	RBSM	Cancel RBSM	Require separated dual devices in front of SUT	N/A
Rong et al. [48]	1	0.6 m	UWB Dual Left-Right Radar 7.3 GHz	AD-FFT + HR harmonics	RBSM	Cancel RBSM	Require separated dual devices in front of SUT	Improve up to 70% Accuracy
Xiaogang et al. [49]	1	N/A	CW 4 Radars at 4 sides	AD-FFT	RBSM	Cancel RBSM	Require 4 separated devices in front of SUT	N/A
Changzhan et al. [50-51]	1	Up to 1.5 m	Camera + CW Radar @ 2.4 GHz	AD-FFT	RBSM	Cancel RBSM	Users privacy + Sensitive to Lighting	N/A
Qinyi et al. [53]	1	1 m	CW Radar @5.8 GHz	Matched Filter with HBT - FFT	RBSM	Reduce RBSM effects and Improve heartbeat's SNR	HBT are Manually extract	N/A

because collocated antennas (with less than a wavelength spacing) usually receive redundant information from the scenario and are not useful for this application. Our proposed method also takes more time to produce HR estimation compared with other methods used in Chapter 5, as each channel needs to extract their own HBTs and applies the same processing chain to obtain a list of potential HRs, which will then be passed through the spectral-based HR selection to determine final HR values.

6.7 Conclusion

- This chapter demonstrates that the **use of more MIMO generally produces better accuracy in HR estimation compared with a single channel radar**. Especially when there are significant interferences from RBSM of SUTs' upper bodies. Up to 89% of accuracy improvement can be achieved in HR estimation with MIMO configuration and our proposed method when the SUTs stand in front of the radar compared with other methods.

- S**pectral-based HR selection method also plays an important role in helping in the determination of the final accurate HR** as it takes frequency spectrums from multiple MIMO channels and analyzes the SNR level from potential HR to determine the most accurate HR values of SUTs.

- Simulated results with synthesized data are first shown to prove the robustness of the proposed processing chain in this chapter. After that, two different scenarios with voluntary participants are performed and studied. Experimental results show that **our proposed processing chain produces satisfactory performances for standing SUTs.**

- Further improvements can be made by having a robust Channel Classification method to identify the good channels and eliminates the bad ones so that less MIMO channels are needed

155

while increasing the overall accuracy.

CHAPTER VII

DEEP LEARNING TO IMPROVE HEART RATE ESTIMATION

This chapter discusses the Deep Learning Framework using convolutional neural network (CNN) and multilayer perceptron (MLP) neural network that can be used to expedite and improve the accuracy of our proposed processing chain in Chapters 5 and 6. As discussed from previous chapters, if there exists a method to help select only the channels that carry good information about the heartbeat signal and eliminate the others, the overall processing can be reduced significantly while also improving the accuracy of HR estimation. Therefore, in this chapter, we propose a channel classification framework using a CNN. This CNN will be trained using experimental data collected from previous chapters.

Besides the CNN for MIMO channel classification, another add-on framework is also proposed in this chapter where a MLP neural network is used to reconstruct the heartbeat signals when they are interfered by RBSM or respiratory harmonics. It will be shown in this chapter that these modules are shown to be useful in improving the HR estimation accuracy. In this dissertation, these deep learning frameworks are considered add-on to the signal processing chain proposed in chapters 5 and 6. It should also be noticed that the results from these works are preliminary and can be further improved. In the author's opinion, deep learning techniques are extremely useful in HR estimation using radar-based techniques in scenarios where the SUTs are actively moving such as walking, running, or exercising.

7.1 Overview and Proposed Framework

Under the impact of the RBSM, deterministic algorithms may not perform consistently especially in HR estimation. Therefore, adaptive learning methods based on artificial intelligence

can be useful since they are able to learn the regularities that characterize the radar signals and then automatically extract useful information from the learnt features. There have been works in literature that employs different machine learning or deep learning techniques for variety of tasks such as recovering heartbeat signals embedded in respiratory signals and its harmonics under quasi-static scenarios [78] of with body movements involved [79]. Multiple neural networks architectures are employed such as cascaded 1D-CNN [78], hybrid CNN-LSTM [79], cascaded LSTM [80], multi-layer perceptron [39, 81], adaptive gamma filtering [82], and other hybrid architectures [83-89] to deal with heartbeat signals reconstruction with or without interferences from body movements. Table 7.1 summarizes the state-of-the-art machine learning/deep learning methods in radar-based monitoring of RR/HR along with their reported performances and limitations. Interestingly, while all the works listed below proposed the use of complex neural networks architecture for heartbeat signals reconstruction, the radar systems used in these works are single channel radars. This means that to compensate for lack of collected heartbeat information from single channel radar, the authors from listed works below must use more complex NN along with an extensive amount of experimental data for training and validating their proposed NN.

In this dissertation, since we have multiple radar channels that are widely distributed, we can collect more heartbeat information from the SUTs compared with single-channel radar. Furthermore, as we currently consider RBSM, which is simpler than other types of motions such as walking, exercising, etc., we propose a supervised learning framework where simpler CNN and MLP architectures are used to perform two separate tasks. The first task is channel classification to help eliminate the channels that do not carry sufficient heartbeat information for accurate HR estimation. This classification process will help decrease the numbers of channels required from

Table 7.1. Machine Learning/Deep Learning methods in radar-based monitoring of RR/HR

Group	Radar Config	Contributions	Methods	Limitations	Performances
Chen et al. [78]	FMCW, 77GHz, Single Channel	Reconstruct ECG from Radar Device	Cascaded 1D-CNNs	Only for quasi-static, lying down SUTs	91% correlation between reconstructed and ground truth
Chen et al. [79]	UWB - 7GHz FMCW-24/77GHz, Single Channel	Reconstruct Heartbeat signals under ambulant conditions	Self-Supervised Contrastive-Learning and Multi-Layer Perceptron	Require extensive amount of experimental data for training	90% correlation between recovered heartbeat signals and ground truth
Gong et al. [80]	FMCW, 77 GHz, Single Channel	Detect and remove motions for RR/HR estimation in ambulant conditions	Cascaded LSTMs	Improvement is needed for generalizing network	Average HR Error is 4.22 BPM for walking SUTs
Gu et al. [39]	CW, 2.4 GHz, Single Channel	Recover Respiratory Signal when there is RBM	Multi-Layer Perceptron	Only Respiration Information is extracted	N/A
Malesevic et al. [81]	CW, 24 GHz, Single Channel	Detect heartbeats in real-time	Multi-Layer Perceptron	Interferences from RBM is not considered	Up to 2% error was achieved
Saluja et al. [82]	CW, 5.8 GHz, Single Channel	Recover heartbeat waveform from radar signals	Adaptive Gamma Filter	Interferences from Body Motion is not considered	Average error was 3.8% for estimated HR
Toda et al. [83]	FMCW, 79 GHz, Single Channel	Reconstruct ECG from radar signals	CNN	Network is trained and tested on semi-experimental data	86% of correlation between reconstructed and ground truth
Wang et al. [84]	UWB, 7 GHz, Single Channel	Reconstruct heartbeat waveform from radar signals	Convolution Sparse Coding	Interferences from Body Motion is not considered	Average error was 4.5% for estimated HR
Wu et al. [85]	UWB, 79 GHz, 16 Channels	Reconstruct heartbeat waveform	CNN	Interferences from RBM is not considered	Improve 69% of accuracy
Yamamoto et al. [86]	CW, 24 GHz, Single Channel	Reconstruct heartbeat waveform	LSTM	Interferences from RBM is not considered	Average HR Error is 3.84 BPM
Yamamoto et al. [87]	CW, 24 GHz, Single Channel	Reconstruct ECG from radar signals	CNN-LSTM	Only for lying down SUTs	86% of correlation between reconstructed and ground truth
Yang et al. [88]	UWB - 7GHz FMCW-77GHz, Single Channel	Recover heartbeat waveform from radar signals with RBM	Cascaded CNN and LSTM	Require 3 separate radar devices	Up to 95% of HR estimation accuracy for moving SUTs

Table 7.1. Continued

Group	Radar Config	Contributions	Methods	Limitations	Performances
Ye et al. [89]	CW, 24 GHz, Single Channel	Recover heartbeat waveform from radar signals of typewriting SUT with random body movements	LSTM and K-means algorithm	Require short distances for good accuracy (30 cm)	Average HR Error is 3.56 BPM for typewriting SUTs
Yin et al. [90]	UWB, Single Channel	Reconstruct ECG from radar signals	Cascaded CNNs	Only for quasi-static, sitting SUTs	Up to 91% accuracy compared with ground truth ECG

processing and as a result reduce the processing time as shown in Chapter 6.

The second task is reconstruction of heartbeat signal under the interferences of RBSM. It should be noticed that the deep learning framework proposed in this chapter is not intended to replace the processing chain in Chapter 6 but a support framework to increase the confidence level in estimated results from its. Figure 7.1 shows the block diagram of the two deep learning modules proposed in this dissertation and how they can be deployed as add-ons to the proposed processing chain in Chapter 6.

7.2 MIMO Channel Classification with CNN

The purpose of channel classification is to determine if a channel is good or bad based on the amount of heartbeat information they carry. Since this is a supervised learning procedure, we will first label the phase variation of each channel with the help of HBT extraction technique discussed in chapters 5 and 6. Next, we calculate the Scalogram of the labeled phase variations using CWT. The calculated scalograms are then converted into RGB images. These RGB images are used as input to train the proposed CNN so that it can learn high-level characteristics that can be used to distinguish between good and bad channels. Once trained, the CNN will be deployed to the processing chain so that it can frequently perform the channel classification during the experiment. Because during the experiment the SUT might unintentionally adjust their standing/sitting position and we do not know when they move, frequently performing the channel classification can help to adaptively identify good/bad channels for calibration purposes. The concept of CNN model is widely discussed and employed for classification task in different areas such as computer vision [91-92], audio [93-94], or communication [95-96], etc. Figure 7.2 shows the working principle of
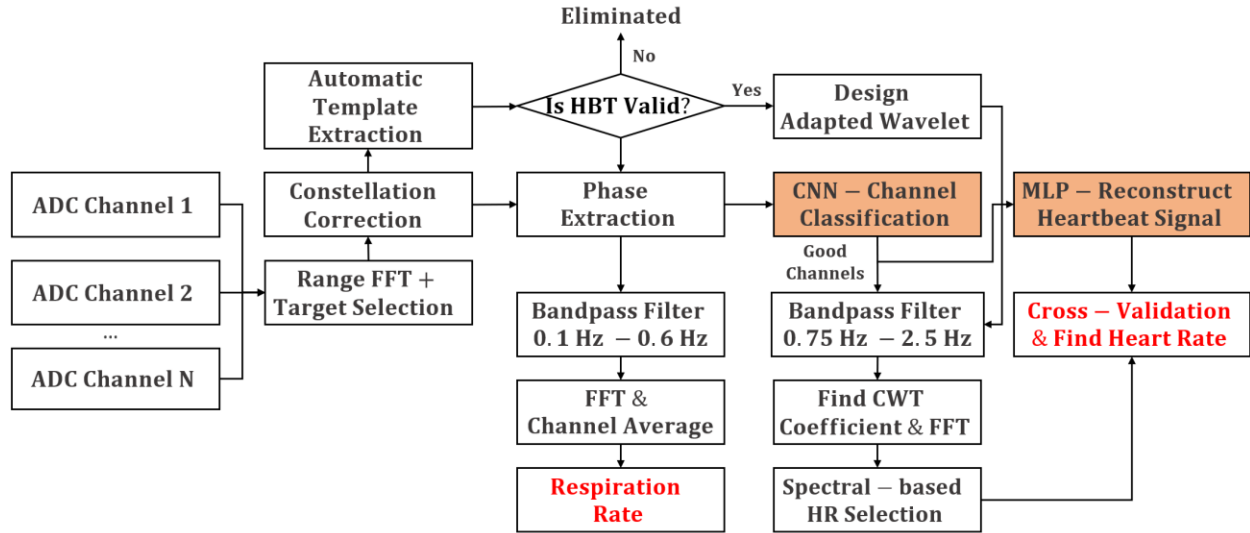
Figure 7.1. Block Diagram of processing chain in Chapter 6 that includes the DL framework
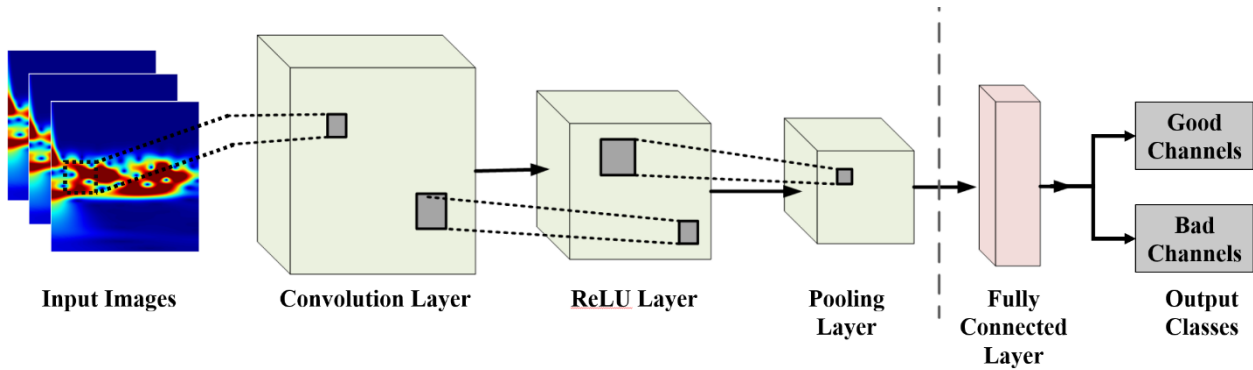
Figure 7.2. CNN is performed as Good/Bad channel classifier.

162

the CNN for our proposed channel classification task.

Generally, a typical deep neural network training procedure includes several main steps [91-96]:

- Labeling and pre-processing training data to suit with input requirements of CNN architecture.

- Determine the architecture of the networks such as number convolution layers, pooling layers, and type activation function.

- Train the network with the labeled data and selected network architecture, training options.

- Once trained, the network can be deployed to the application to predict the labels of unseen data and calculate the classification accuracy.

7.2.1 Criteria for Determining Good/Bad Channels

As discussed earlier, the purpose of the CNN is to help identify if the phase variation from a channel carries a good amount information of heartbeat signal because if it does, it will be easier to estimate accurate HR from these channels. Thus, there are two output classes for the CNN which are **Good Channel** and **Bad Channel** as shown in Figure 7.2. To label the phase variation data, we first define the criteria of how we, as a human, identify if a phase variation is **Good** or **Bad**. Because the trained network will follow the criteria designed by human to classify the input, it is important that we clearly define the criteria before we design and use the data to train the neural network.

- **Good Channel**: A channel is considered good, 1) if we can identify the HR from the peak of frequency spectrum of its phase variation or, 2) if its phase variation is significantly interfered by RBSM, there should exist at least one HBT that can be reduce the impact of the RBSM's interferences.

- **Bad Channel**: A channel is considered bad if we cannot identify the HR from the peak of

163

frequency spectrum of its phase variation or there are no HBTs that can be extracted to easily identify the HR information.

Figures 7.3 demonstrates examples of phase variations from channels that are considered good based on our discussed criteria. It can be shown in Figure 7.3a and 7.3c that by just looking at the phase variations in time domain, it is difficult to identify if the channels are good or bad even with human intervention. However, based on the constellation diagram method discussed in Chapters 5 and 6, we can extract some HBTs that can be used to magnify the heartbeat signals. Figures 7.3b and 7.3d show frequency spectrums of the corresponding phase variations as well as the CWT coefficient calculated with the extracted HBTs as wavelet. By comparing the peaks of these spectrums with HR values from ground truth, we can determine that these phase variations from these channels can be considered good. Once we know that these channels are good, we can label them as GOOD and move on to next channels. Figure 7.4 shows examples of phase variations from channels that are considered BAD. There can be multiple factors that impact the quality of the phase variations such as RBSM or the TX-RX pair of that channel just does not get a good reading of the heartbeat signals as its beam to the heartbeat region on the upper body of the SUT might be limited. Therefore, if we can eliminate these channels prior to the signal processing, we can reduce the chance that these bad channels contribute inaccurate HR estimation. As shown in Figures 7.4a and 7.4c, the phase variations look similar compared with the ones in Figures 7.3a and 7.3c because they still carry the respiratory signals information. However, when looking at their frequency spectrum before and after the CWT calculation with several extracted HBTs, we still cannot identify the HR accurately. Thus, these channels will be labeled as BAD for the classification process.
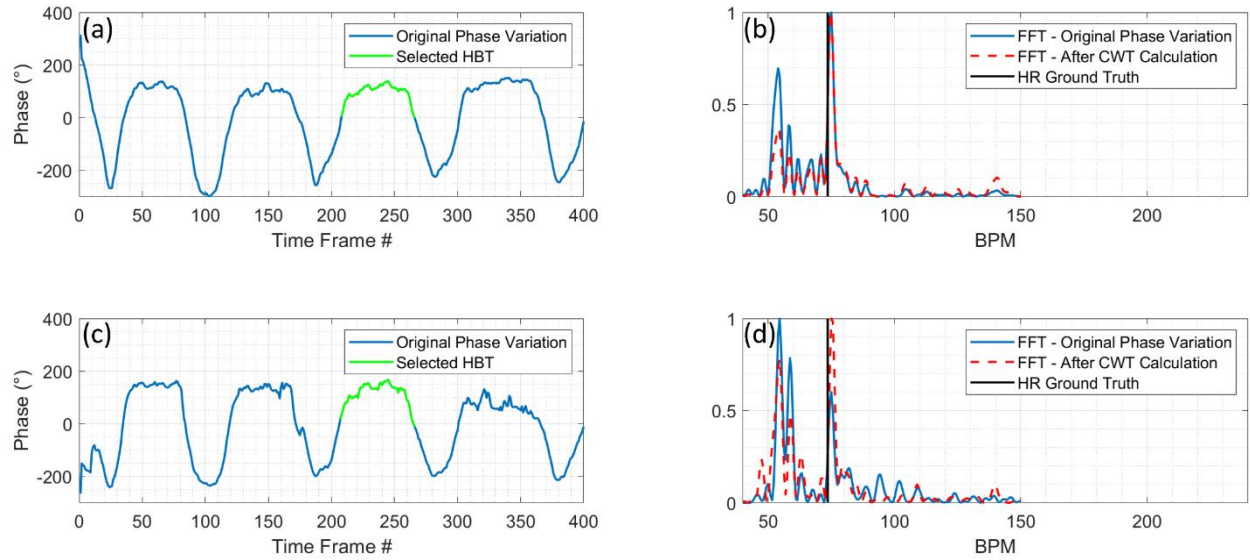
Figure 7.3. Examples of two channels that are considered **Good** channels where a), b) the heartbeat spectrum can be clearly identify and c), d) a HBT can be used to magnify the heartbeat spectrum.
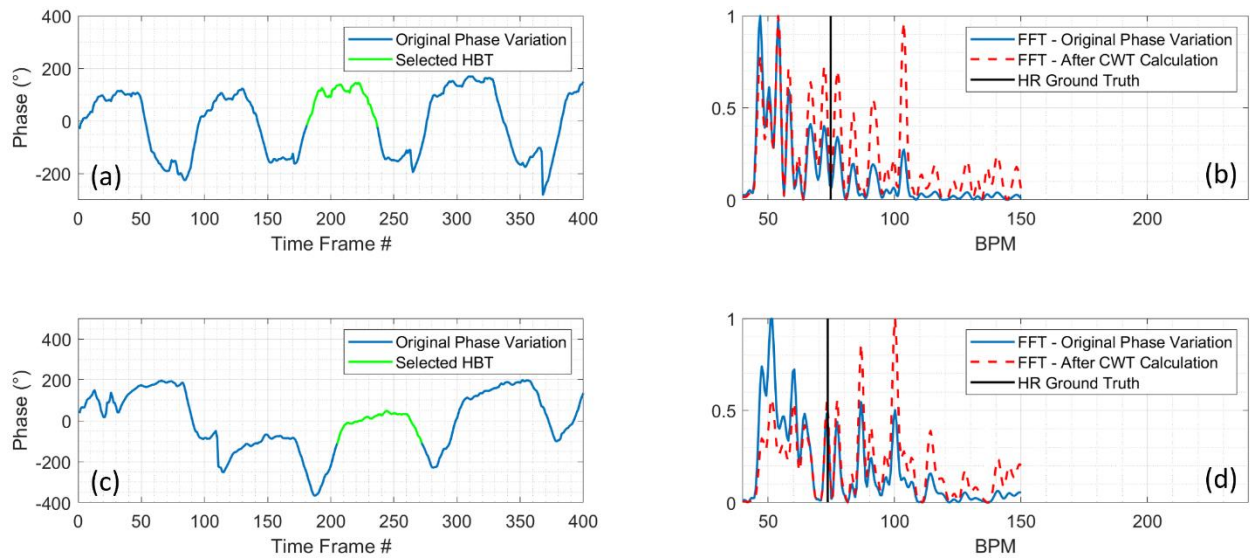
Figure 7.4. Examples of two channels that are considered **Bad** channels where a), b), c), d) the heartbeat spectrum cannot be clearly identify even if HBT is used.

7.2.2 Data Labeling for Phase Variation Data

After figuring out the criteria mentioned above that we use to determine if a channel is considered Good/Bad, we next discuss the labeling and pre-processing techniques to prepare the data to train the CNN. It should be noticed that the labeling step is done manually by human. We must look at each channel's phase variation, find and extract any valid HBTs, then calculate frequency spectrums of its phase variation and CWT coefficient with the extracted HBTs. This way we can be certain that the channel is accurately labeled so that the CNN can learn to optimally classify the channel from the training data. This is like the classic image classification of dogs and cats' images where the human must first go through images to create label of dog/cat before the training process. To generalize the classification capability of the trained CNN, data sets from different subjects can be used so that the CNN is able to classify channels' data collected from different subjects.

To make it easier and faster for the labeling process, a simple interface in MATLAB was built for this task. This interface allows users to look at the phase variation from each channel and manually select the HBT. If a channel is Good, the user will assign letter "G" for that channel and store the valid HBT of that channel. If the channel is considered Bad, the user will assign letter "B" and move on to the next channel. After the labeling step, we can establish a table that contains all the information about the phase variations from each channel, their labels of "G" or "B", and the HBTs if the label is "G".

7.2.3 CNN Architecture for Channel Classification

There are various architectures of deep neural network that can perform two-class classification problem such CNN [97], LSTM [98] or Temporal Convolutional Network (TCN) [99]. LSTM and TCN are trained to identify the high-level characteristics of time-domain signals by leaning the

individual time step of the signals. A CNN typically takes in an input image, assigns learnable weights and biases to various aspects/objects in the image and be able to differentiate one from the other. To perform MIMO channel classification, as was shown in [100] that simply use of raw phase variation as input for LSTM or TCN does not yield the best classification performance as the amount information from the time-domain signals is limited. Therefore, feature extraction from the data can help improve the training and testing accuracies of the classifier. As a result, extracting both time and frequency information from the phase variation should give the classifier more information and improve the training accuracy. Thus, the phase variation will be transformed into RGB images using CWT to extract its time-frequency information. With RGB images as input, we opt for CNN architecture for our classifier. Since this is a two-class classifier, typical CNN proposed in [97] can be used. This CNN architecture has been used widely in various classification problems in computer visions [91], audio signals [93], and communication [95]. Figure 7.5 shows the CNN layers that we want to use for our channel classification problem. The CNN architecture consists of several layers (or so-called multi-building blocks). Each layer in the CNN architecture is briefly described below.

- Input Layer: The input layer in a CNN model is organized in three dimensions: height, width, and depth. For an RGB image as input, height and width are the dimensions of the image and depth is equal to three which are the red, green, blue channels of the images.

- Convolutional Layer: This is the most significant component of the CNN model. It consists of a collection of convolutional filters that are used to convolve with the input images to generate the output feature maps. These output feature maps are used to characterize and distinguish between different images.
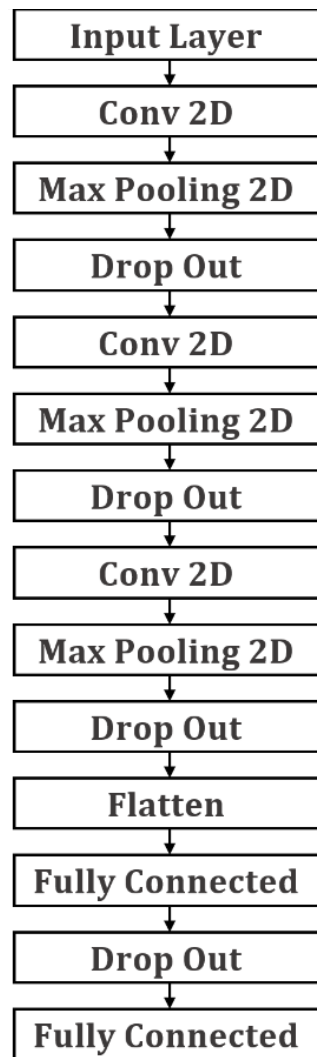
Figure 7.5. Layers of CNN for Channel Classification

- Pooling Layer: Since the feature maps from the convolutional layers have large size, pooling layers are usually used next to them to sub-sample the feature maps. In other words, the pooling layers shrinks large-size feature maps to create smaller feature maps. As a result, the overall trainable weights can be reduced.

- Dropout Layer: For CNN model, over-fitting is an issue associated with achieving well-behaved generalization. The model is over-fitted when the model executes especially well on training data but does not perform well on unseen data. Dropout is a widely used regularization method that reduces overfitting of the training dataset and makes the model more robust. This is done during training, where random number of layer outputs are dropped out. As a result, the layers have different number of nodes and connectivity to the prior layers during training. By contrast, the full-scale network is utilized to perform prediction during the testing process and reduces the chance of over-fitting in the trained network.

- Flatten Layer: This layer reshapes the input data into one-dimension matrix to prepare the connection to Fully Connected Layer.

- Fully Connected Layer: This layer is typically located at the end of each CNN model. Inside this layer, each neuron is connected to all neurons of the previous layer. It is utilized as the CNN classifier.

7.2.4 Create Images for Input Layer of CNN

As discussed above, the input layer to CNN requires RGB images. In this dissertation, we will extract the time-frequency features from the phase variations. There are various ways to do this such as calculating spectrogram using Short Time Fourier Transform (STFT) or scalogram using CWT. As CWT offers more time-resolution compared with STFT, we opt for using CWT to extract

169

time-frequency features of the phase variations. Figure 7.6 shows the examples of the RGB images which show the scalograms of the phase variation from a good channel and a bad channel. From Figure 7.6, we can see that while it is difficult to tell the difference between them, the CNN will extract features from these images and learn a way to distinguish them.

7.3 Performances of CNN for Channel Classification

7.3.1 Evaluation Metrics

The evaluation metrics is utilized to measure the efficiency of the classifier within the model testing stage using unseen data. Let True Positive (TP) and True Negative (TN) are number of positive and negative instances, which are successfully classified. False Positive (FP) and False Negative (FN) are number of misclassified positive and negative instances. Below we show the metrics that are widely used to assess the performance of classifier [101].

- Accuracy: Calculates the ratio of correct predicted classes to the total number of samples evaluated.

$$Accuracy = \frac{TP + TN}{TP + TN + FP + FN} \tag{7.1}$$

- Precision: Calculate the positive patterns that are correctly predicted by all predicted patterns in a positive class.

$$Precision = \frac{TP}{TP + FP} \tag{7.2}$$

- Recall: Calculate the fraction of positive patterns that are correctly classified.

$$Recall = \frac{TP}{TP + FN} \tag{7.3}$$
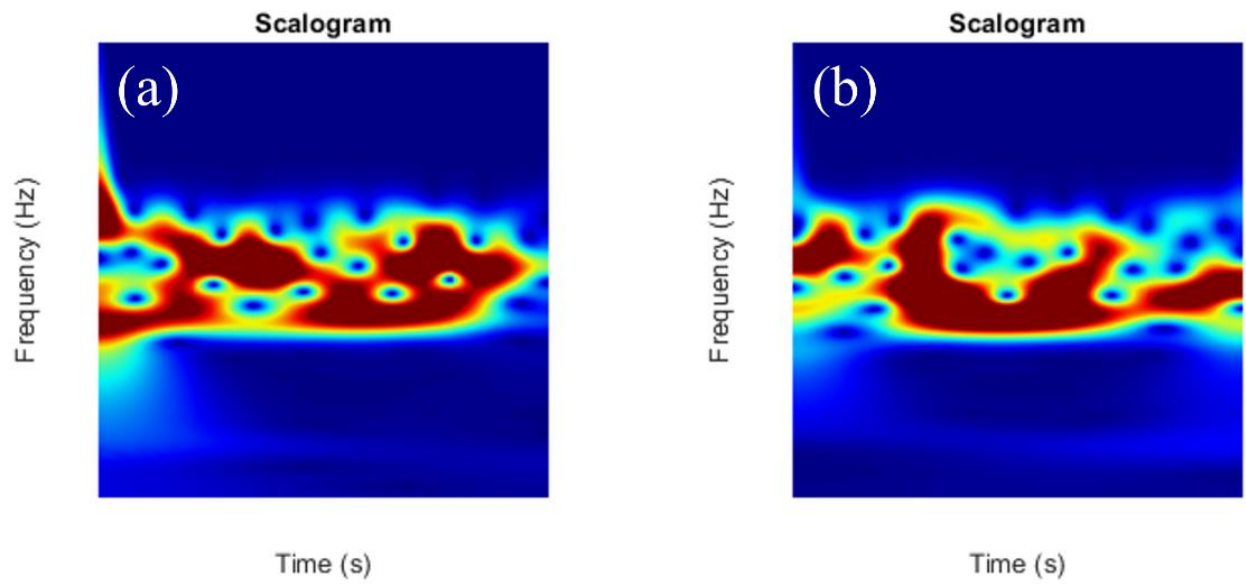
Figure 7.6. Examples of Scalogram for the phase variations from a) Good Channel and b) Bad

Channel

- F1-Score: Calculate the harmonics average between recall and precision rates.

$$F1_{score} = 2 \times \frac{Precision \times Recall}{Precision + Recall} \tag{7.4}$$

7.3.2 Channel Classification with Experimental Data

To show the robustness of the proposed CNN architecture, we use the collected data discussed in Chapter 5 where the SUTs sit in quasi-static positions. The experimental data from quasi-static SUTs help us evaluate the overall performance of the CNN. In total, about 35 minutes of experimental data from 10 participants are used for training. In other words, an overall 5040 data sets of 20-second time sequences from 48 channels are used for training. Meanwhile, 15 minutes of experimental data are separated for testing which corresponding to 2160 data sets of 20-second time sequences from 48 channels. The percentage between good channels and bad channels are 50% - 50% to avoid biasing from the trained CNN.

Table 7.2 discusses parameters used for training the CNN for channel classification task. These are typical settings for a two-class classifier with CNN [101]. We implement the network by using the Tensor Flow – Keras library and use the Stochastic Gradient Descent (SGD) optimizer to minimize the loss function and to update the network parameters iteratively. Figure 7.7 shows the training curve of the CNN of channel classification task with the training data sets that are collected from quasi-static, sitting SUTs from Chapter 5. In Figure 7.7, the blue line shows the performance to validate our model performance during training. This validation process gives information that helps us tune the model's hyperparameters and configurations accordingly. It is like a critic that helps keep track of the training procedure and tells us if the training is going in the right direction or not. From Figure 7.7a, we see that around epoch 16, the model starts over-fitting because even when training loss keeps decreasing, the validating loss starts saturating. This means that the model

Table 7.2. Hyper Parameters used for Training the CNN

Optimizer	Stochastic Gradient Descent (SGD)
Learning Rate	0.001
Momentum	0.9
Mini Batch Size	16
Number of Epochs	20
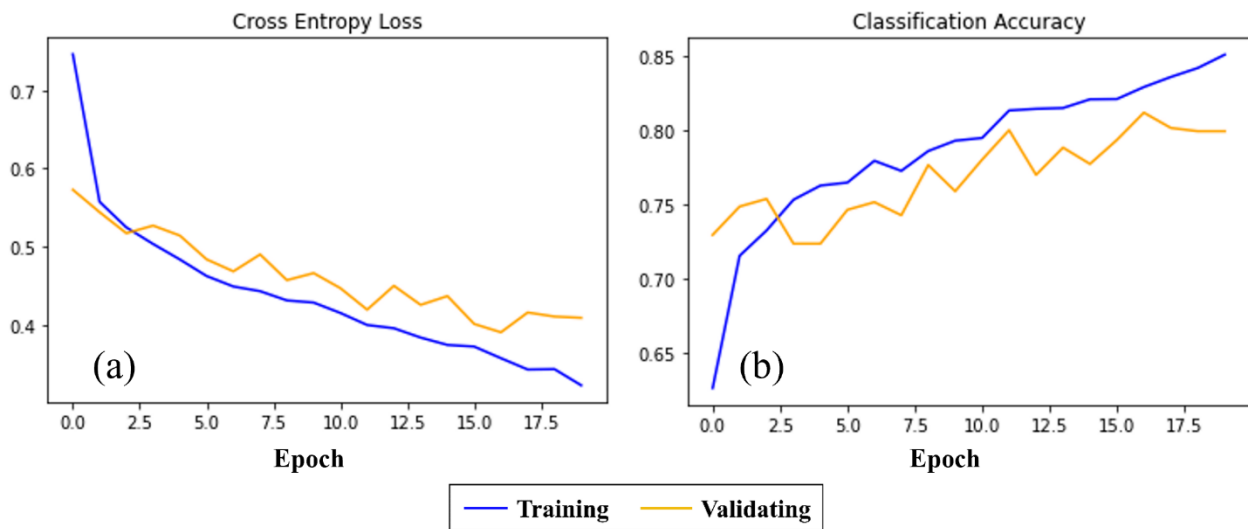
Figure 7.7. a) Training and Validation Cross-Entropy Loss, b) Classification Accuracy for Training and Validation

will end up memorizing the training data patterns and will fail to generalize and perform well in the case of unseen data. Therefore, it is a good idea to terminate the training around epoch 16 or 17 to stop the over-fitting. Figure 7.7b shows the classification accuracy of the training and validation data. We can also see the over-fitting issue around epoch 16 which suggests we should terminate the training around epoch 16 or 17.

Table 7.3 shows the evaluation metrics discussed in equations (7.1) – (7.4) to better quantify the testing performance of our trained classifier. The accuracy of the classifier is 80% which means that on average, there are 80% of correct classification to the total number of predictions. Other metric calculated here is precision of 89% which means that up to 89% of Good Channels are correctly classified among all samples classified as Good Channels (correctly of incorrectly). This means that among all channels that are classified as Good, 89% of them are Good Channels and 11% are not. This means that our classifier can classify the Good Channel accurately. Other metrics are the recall of 75% which shows the classifier's ability to detect the Good Channel and $F1_{score}$ of 81% which shows the balance of the classifier in equally being able to classify both Good/Bad Channel. Finally, Figure 7.8 shows the confusion matrix which is the summary of classification results from our trained CNN based on the testing (unseen data). We can see that our trained CNN did a good job in correctly classifying Good and Bad channels from the testing data set.

7.4 Heartbeat Signal Reconstruction Using Multiple-Layer Perceptron

As shown in Figure 6.1, another deep learning framework that we are interested in is the use of a multilayer perceptron (MLP) neural network to help denoise the phase variation signals and only reconstruct the heartbeat waveforms. This approach has been proposed in [39] for recovering the respiratory signals under the interference of the body motions or in [81] where heartbeat signals

Table 7.3. Testing Performance from the trained CNN

Accuracy	80 %
Precision	89 %
Recall	75 %
$F1_{score}$	81 %
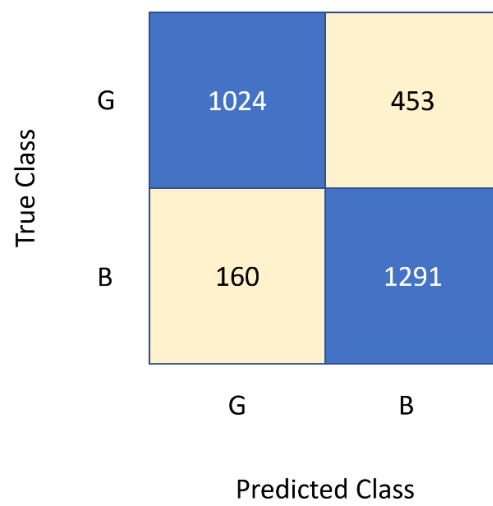
Figure 7.8. Confusion Matrix of the classification result.

are reconstructed from the captured radar signals. In this dissertation, we want to extend the approach in [39] so that we can extract the heartbeat waveform when there are interferences from RBSM. Thus, when looking at the phase variations, only heartbeat signals are of interests while the others such as respiratory signals, random body movements are considered noises. Therefore, we aim to remove noises from the heartbeat signals to enhance the accuracy of HR estimation. This is a regression problem where the neural network will learn the relationship between a noisy signal and a corresponding clean signal so that it can predict the clean version of a new signal when it sees a noisy one [39].

Figures 7.9 and 7.10 summarizes the working principle of our proposed framework for denoising the heartbeat signal with neural networks. To train the deep neural network for a regression task, it typically requires two sets of input, the first set is the noisy signal (predictor) that we are trying to denoise, and the second set is the clean version of that noisy signal (target). A feature extraction technique such as STFT or CWT can be used to extract time-frequency information from the signals so that it is easier for the neural network to learn from. These input sets will be fed into the neural network so that it can learn the relationship between the predictors and targets. This is done by using the predictor input to minimize the mean squared error between its output and the input target. After the training process, the trained neural network can be used to denoise unseen phase variation to reconstruct the heartbeat waveform as shown in Figure 7.10. For example, if a time-frequency image from unseen phase variation is inputted to trained network, it will be able to output/predict a denoised time-frequency image. The denoised heartbeat signal is converted back to the time domain using inverse operation of the feature extraction techniques (ISTFT or ICWT). Next, we will discuss steps for our heartbeat waveform reconstruction framework using the MLP:

- Pre-processing predictor and target data to suit with input requirements of MLP architecture.

176
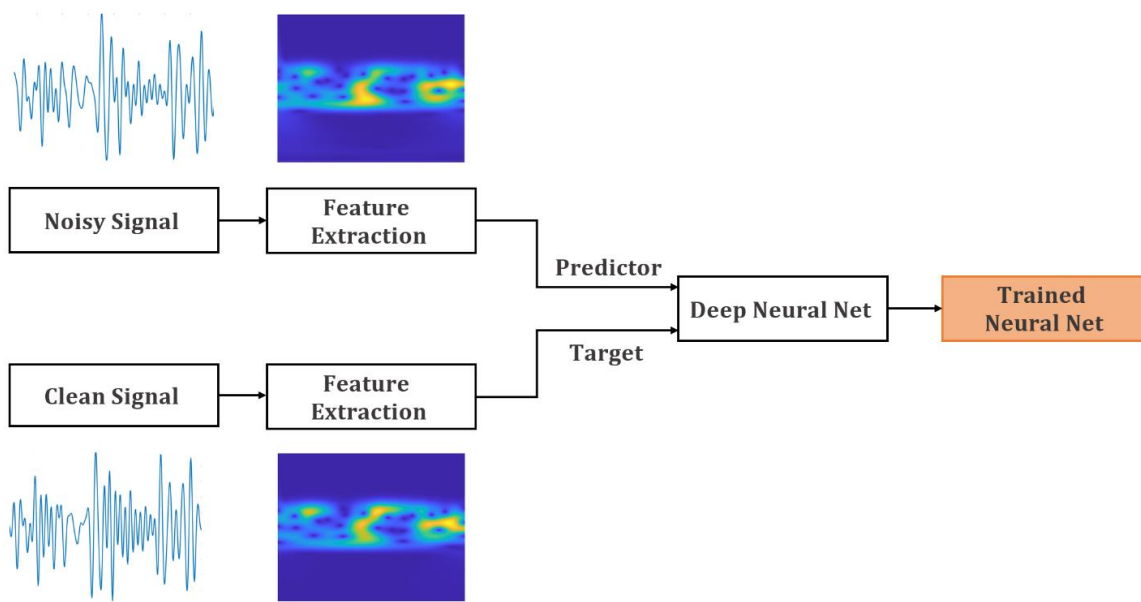
Figure 7.9. Training principle of the deep learning framework for denoising heartbeat signal.
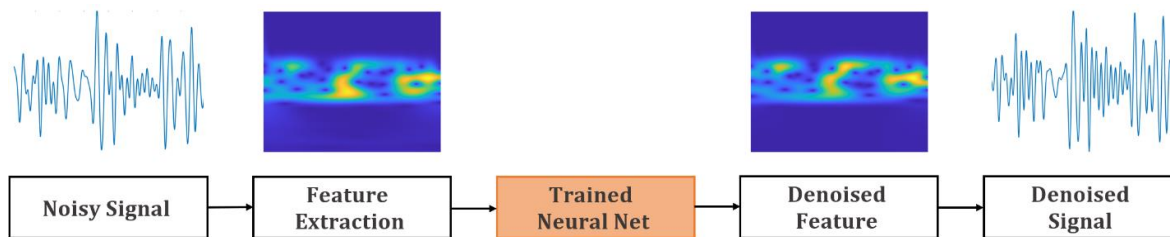
Figure 7.10. Testing/Deploying principle of the deep learning framework for denoising heartbeat signal.

- Determine the architecture of the networks such as number of hidden layers and type of activation function.

- Specify training options such as which solver to use, number of mini batch size, number of epochs, etc.

- Train the network with the predictor/target data and selected network architecture, training options. Depends on hardware availability and the size of input data, the training procedure can be expedited if GPU platform are used.

- Once trained, the network can be deployed to the application to predict the denoised heartbeat signals.

7.4.1 Pre-processing of Predictor/Target Data

The first step is to prepare the predictor and target data for training the MLP. It should be noticed that we have already eliminated bad channels from the CNN discussed in previous section. Thus, we only take input from the classified good channels. From the labeling step in the Channel Classification task with CNN, we already have information about the phase variations (predictor) and the CWT coefficients calculated from the stored HBTs which can be used as the clean version of the phase variations (target). While the ground truth signal from contact Pulse Sensor can also be used as target signal, it requires precise synchronization between radar device and contact pulse sensor. Figure 7.11 shows an example of the predictor and target signals obtained from the selected HBT along with their frequency spectrums. It can be observed that the phase variation (predictor) has several interferences (noises) while the corresponding signal from CWT coefficient only carries heartbeat information (target). Thus, we expect the deep neural network to learn the relationship between the predictor and the target so that it can reduce the impact from interferences

178
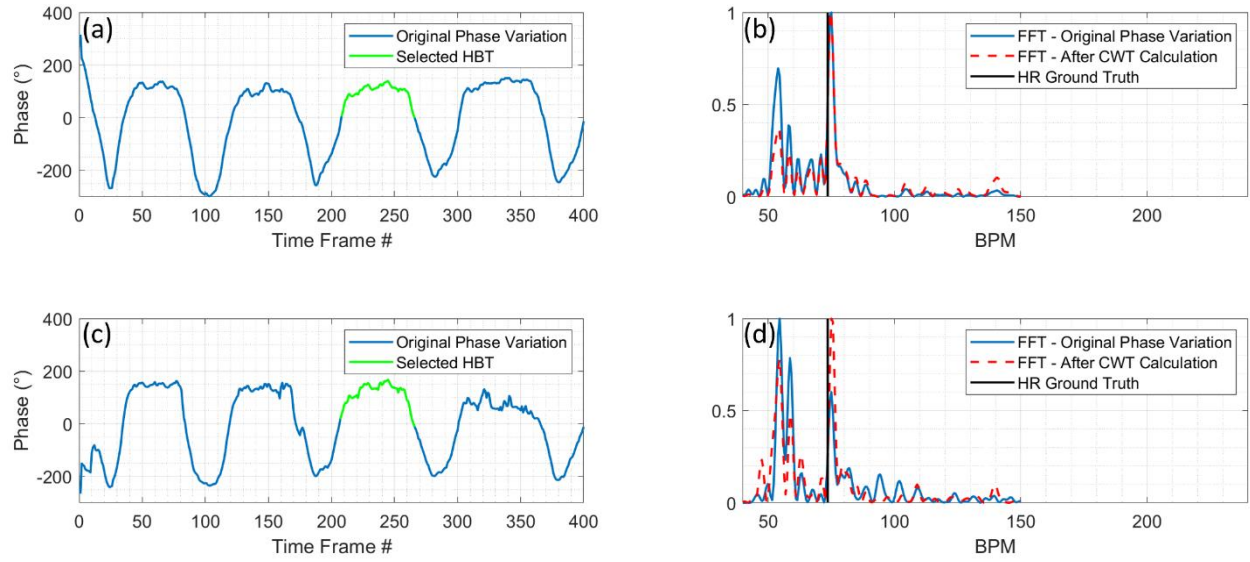
Figure 7.11. Examples for data used for training the MLP-NN, a), c) Phase variation for predictor and the selected HBTs used to calculate the CWT coefficient to find target signal, b), d) Frequency spectrum of the predictor and target compared the ground truth.

and improve the SNR of heartbeat signal. This way, when combined with the processing chain in Chapter 6, we can increase the confidence level of the HR estimation.

7.4.2 MLP Architecture for Regression Task

There are various architectures of deep neural network that can perform this type of regression task. However, we decide to adopt the classic MLP neural network as it is straightforward and easier to understand [39]. As shown in Figures 7.9 and 7.10, feature extraction from the data can help improve the training and testing accuracies of the MLP. Thus, both the predictor and target will be transformed into RGB images using CWT to extract its time-frequency information. These transformed images of the predictor and target will be fed to the input layer of the MLP model. Figure 7.12 shows the MLP layers that we want to use for our regression task. The MLP architecture consists of several layers (or so-called multi-building blocks).

7.4.3 Create Images for Input Layer of MLP-NN

This step is discussed in Section 6.2.4 where CWT is used to extract time-frequency features of the predictor and target signals. Figure 7.13 shows an example RGB images from predictor and target signals.

7.5 Performances of MLP for Reconstruction of Heartbeat Waveform

7.5.1 Regression Performance with Synthesized Data

To first validate the efficiency of our proposed MLP architecture for the regression task, we try to train the network with synthesized data using simulated models of chest displacement from respiratory signals, heartbeat signals and interferences from RBSM as discussed in Chapter 4. The
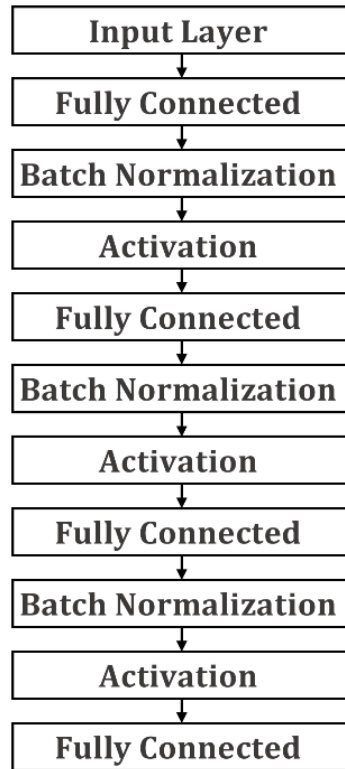
Figure 7.12. Layers of MLP for Regression Task
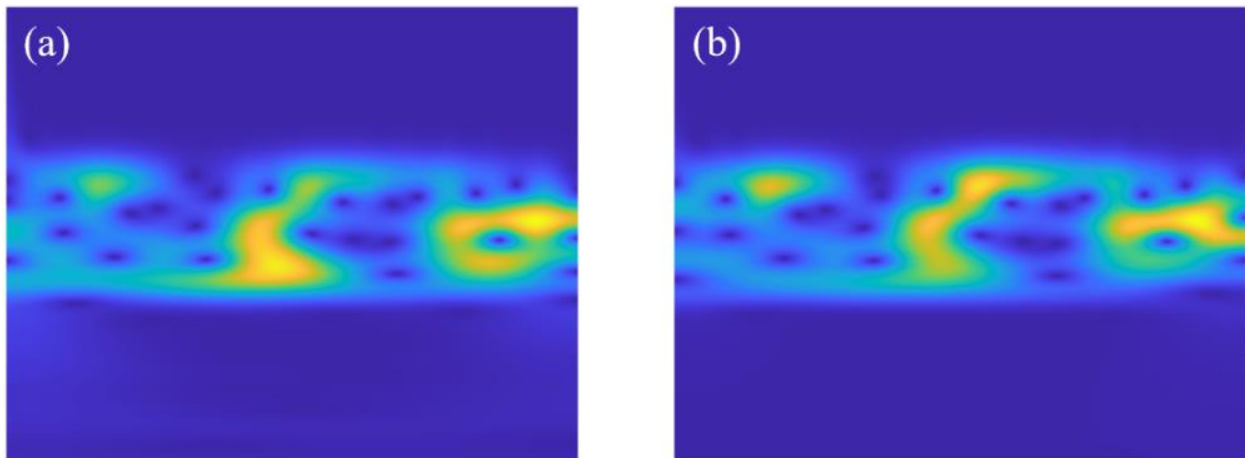
Figure 7.13. Examples of Scalogram from a) predictor and b) target signals

neural network in this case is expected to predict the original HR that is disrupted by the harmonic components of respiratory signal as well as interferences from RBSM. To train the network with the synthesized data, we create 1500 sets of 20-second data with random values of parameters for simulated that will be listed in Table 7.4.

Table 7.5 discusses parameters used for training the MLP-NN for regression task. These are typical settings for a regression network with MLP [39]. We implement the network by using the Tensor Flow – Keras library and use the Adam optimizer to minimize the loss function and to update the network parameters iteratively.

Figure 7.14 shows the training loss and validating lost when training with the synthesized data. To test the trained network, we show the predicted *HR* results from 100 test signals of 20-second phase variation with random simulated parameters shown in Table 7.4. Figure 7.15a shows the average error over 100 test signals in BPM is 3.7 and Figure 7.15b shows the fitted line between predicted HR from MLP-NN with the true HR. This confirms that our proposed MLP-NN works well for simple synthesized data.

7.5.2 Regression Performance with Experimental Data

Next, we validate the proposed MLP architecture using the collected data discussed in Chapter 5 where the SUTs sit in quasi-static positions. The experimental data from quasi-static SUT helps us evaluate the overall performance of the MLP. In total, about 35 minutes of experimental data from 10 participants are used for training and 15 minutes are used for testing. An overall 5000 data sets of 20-second time sequences from 48 channels are used for training. Figure 7.16 shows the training loss and validating lost when training with the synthesized data. To test the trained network with experimental data, we use 15-minute unseen experimental data to try to predict HR results for 20-second phase variation signals. Figure 7.17a shows the average error from 15-minute test

Table 7.4. Simulated Parameters used for Synthesizing Training Data for the MLP-NN

Respiratory Rate (RR)	8 – 20 BRPM
Chest displacement due to Respiration (A_{RR})	1 – 12 mm
Ratio of Inhalation and Exhalation Period (T_{ratio})	0.3 – 0.5 s
Decay rate of exhalation period (τ_{RR})	0.1 – 0.3 s
Heart Rate (HR)	50 – 100 BPM
Chest displacement due to Heartbeat (A_{HR})	0.1 – 0.5 mm
Number of Interferences from RBSM	0 – 3
Magnitude of Interferences from RBSM (A_{RBSM})	5 – 12 mm
Duration of Interferences from RBSM (T_{RBSM})	1 – 4 mm
Time Delay between RBSM ($t_{d_{RBSM}}$)	2 – 10 mm

Table 7.5. Hyper Parameters used for Training the MLP

Optimizer	Adam
Learning Rate	0.001
Momentum	0.9
Mini Batch Size	16
Number of Epochs	20
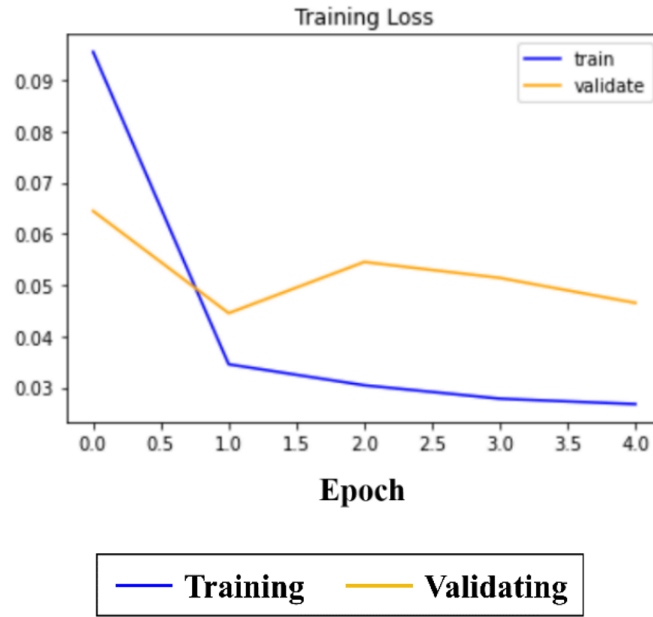
Figure 7.14. Training and Validation Cross-Entropy Loss
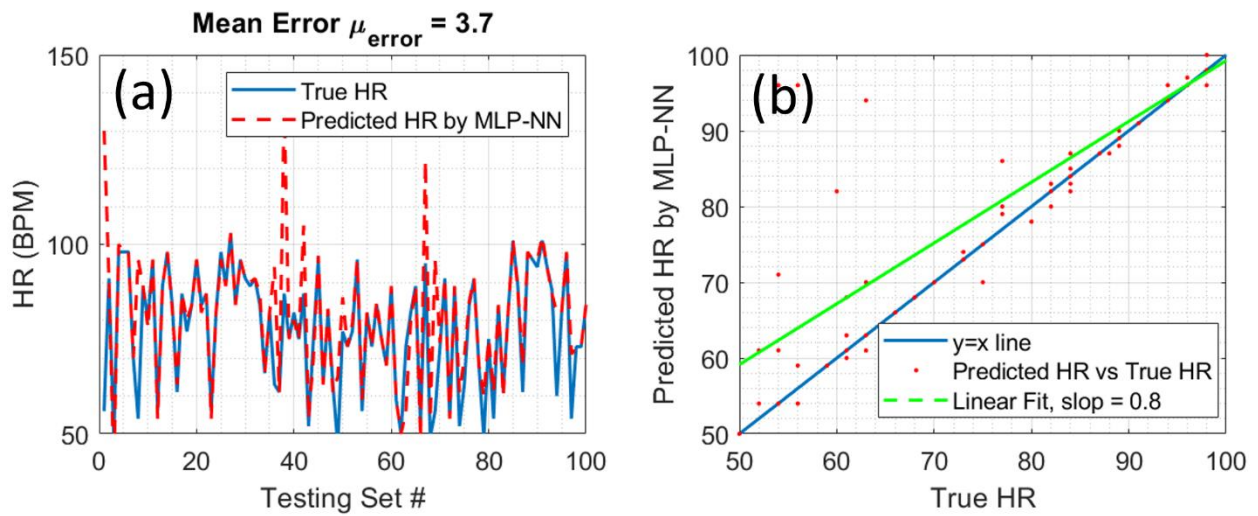
Figure 7.15. a) Predicted HR from MLP-NN compared with True HR, b) Plot of Predicted HR vs True HR and fitted line with 80% match.

184
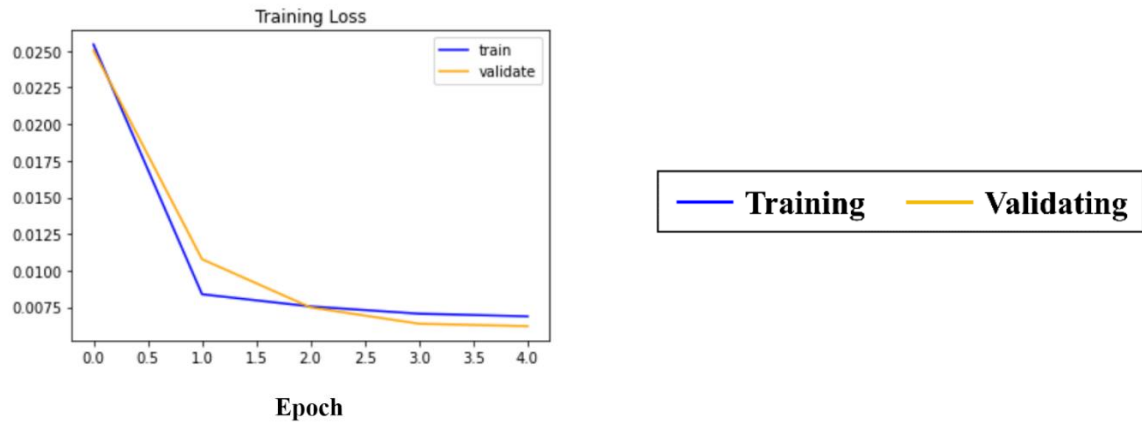
Figure 7.16. Training and Validation Cross-Entropy Loss
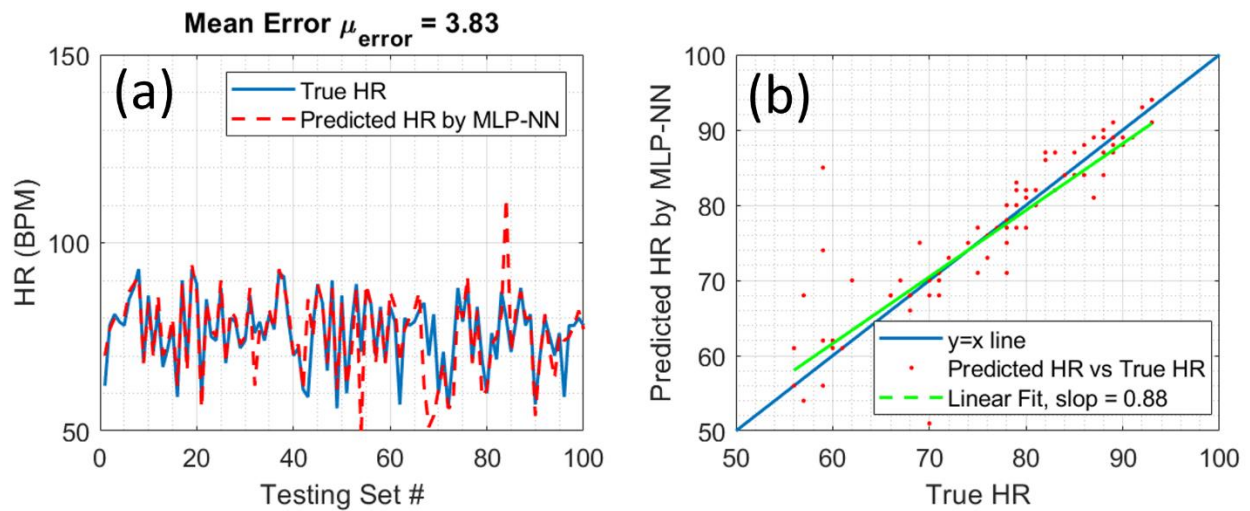
Figure 7.17. a) Predicted HR from MLP-NN compared with True HR, b) Plot of Predicted HR vs True HR and fitted line with 88% match.

signals in BPM are 3.7 and Figure 7.17b shows the fitted line between predicted HR from MLP-NN with the true HR. This confirms that our proposed MLP-NN works well for simple synthesized data.

7.6 Discussion

To assess the performance of our proposed MLP-NN for reconstructing the heartbeat signals in quasi-static scenarios, we show a comparison between our work with other research groups that report similar machine learning/deep learning frameworks for recovering heartbeat signals when there are minimal interferences from random body motions. Table 7.6 lists the comparisons between radar configurations, methods, amount of data needed for training and reported performances between different research groups and ours. Here, we show that our proposed framework achieves comparable accuracy in reconstruction of heartbeat signals while requires significantly less amount of data sets required form training the MLP. Therefore, we can show the advantages of using MIMO configurations and our HBT extraction method for reconstruction of heartbeat signals using artificial intelligence. Since most results from other groups are reported using the average relative error (*ARE*) in percentage, we also calculate this as [86]:

$$ARE = mean\left(\frac{\left|HR_{predicted} - HR_{true}\right|}{HR_{true}}\right) \tag{7.5}$$

7.7 Conclusion

- This chapter discusses the Deep Learning Framework using convolutional neural network (CNN) and multilayer perceptron (MLP) neural network that can be used to expedite and improve the accuracy of our proposed processing chain in Chapters 5 and 6.

Table 7.6. Comparison between our proposed MLP-NN with other research groups

Group	Radar Config	Contributions	Methods	Data required for training	Data for Testing	ARE
This work	FMCW, 77 GHz. Up to 192 Channels	Recover heartbeat waveform from radar signals	Multi-Layer Perceptron	35 minutes	15 minutes	4.8% compared with ground truth
Malesevic et al. [81]	CW, 24 GHz, Single Channel	Detect heartbeats in real-time	Multi-Layer Perceptron	70 minutes	35 minutes	Up to 2% compared with ground truth
Saluja et al. [82]	CW, 5.8 GHz, Single Channel	Recover heartbeat waveform from radar signals	Adaptive Gamma Filter	250 minutes	250 minutes	3.8% compared with ground truth
Yamamoto et al. [86]	CW, 24 GHz, Single Channel	Reconstruct heartbeat waveform	LSTM	32 minutes + 800 minutes of augmented data	51 minutes	4% compared with ground truth

- The trained CNN can classify good/bad channels with accuracy of 80% which means that on average, there are 80% of correct classification to the total number of predictions. This is satisfactory for our application as if 80% of bad channels are correctly classified and eliminated prior to processing, we can save more computational time as well as reduce the contribution from these bad channels to the HR estimation results.

- The proposed MLP neural network for reconstructing the heartbeat signals also works as expected. We first use synthesized data to train the proposed MLP neural network to show that even with interferences from respiratory harmonics and RBSM, the trained MLP network is still able to reconstruct the heartbeat signal and estimate the HR. Next, experimental data are used to train the same MLP neural network. Experimental results show a mean error of 3.8 BPM from predicted HR from the trained MLP network compared with the ground truth and a 88% match between predicted HR and true HR.

- Results from this chapter are preliminary and show the potential of using deep learning frameworks for improving accuracy of HR estimation using radar-based techniques.

CHAPTER VIII

CONCLUSION AND FUTURE WORK

This chapter discusses the contribution, concluding remarks of this dissertation as well as potential future work to further improve the proposed approach for monitoring RR/HR with radar-based techniques especially with the interferences from RBSM.

8.1 Summary of Results

It was shown that the MMWCAS-RF-EVM radar device used in this work could accurately detect human RR and HR. However, while the respiratory rate can be accurately estimated with band-pass filtering and Fourier Transform, significant work still needs to be done to improve the accuracy of HR estimation under the impact of random body-swaying motion. Respiratory harmonics and random body-swaying motion can negatively affect the estimation accuracy of heart rate and they need to be suppressed. From this dissertation, we propose an automatic heartbeat template extraction technique to identify the signals' portion that carry sufficient amount of heartbeat signals. These heartbeat templates are then used as adapted wavelet for CWT calculations to reduce the interferences from respiratory harmonics and random body-swaying motion while magnifying the magnitude level of heartbeat signals.

Under quasi-static scenarios where there is a minimal amount of random body-swaying motion, presences from respiratory harmonics are the main factor that can plague the estimation accuracy. Under quasi-static scenarios, we can first use MRC technique to combine the phase variation from different MIMO channels to reduce the total processing time. Then the combined phase variation from MRC will be used with the extracted HBT to magnify the heartbeat signal by calculating its

CWT using the HBTs as adapted wavelets. The HR can then be determined by finding the highest peak within the frequency spectrum of the calculated CWT coefficients.

In scenarios where the SUTs are standing in front of the radar, the effect of RBSM becomes more significant and the HR cannot be determined by simply finding the highest peak within the frequency spectrum of the calculated CWT coefficients. This is because the RBSM is relatively large in magnitude and its spectrum can occupy the highest peak within the frequency spectrum. Therefore, the processing chain was modified to further address the interferences from RBSM. For scenarios where SUTs are standing, MRC is dropped and a spectral-based HR selection technique is added so that it helps to search and determine the accurate HR value even if the spectral components at correct HR are not highest peak within the frequency spectrum. This is done based on the fact that the power spectral densities of heartbeat signals generally increase after the CWT calculation using HBTs as adapted wavelets. Therefore, by using different MIMO channels to search for HR values that tend to increase its power spectral density values after CWT calculation, the spectral-based HR selection technique can help to find the accurate HR value.

To improve the accuracy of HR estimation, we also investigate different applications of deep learning frameworks. In this dissertation, two deep learning architectures have been studied for two different tasks: MIMO Channel Classification and HR Prediction. The first deep learning architecture is CNN where we try to train the CNN to learn time-frequency characteristics that associate with Good/Bad Channels from the scalograms images calculated from the CWT. With the CNN trained using experimental data, the classification accuracy of 80% is achieved. This means the trained CNN can correctly classify if a channel is good or bad with 80% accuracy. The second task is HR prediction which is performed by training the MLP-NN to also learn the time-frequency characteristics of phase variation signals through scalograms calculated using CWT.

The trained MLP-NN is then able to predict HR from unseen phase variation data for up to 88% match.

8.2 Contribution

The contributions of this dissertation include:

- The MMWCAS-RF-EVM offers the use of a compact, portable, widely distributed MIMO radar system operating at 77-81 GHz to improve the respiratory/heart rate estimation results. We show that by using more widely distributed MIMO channels, better estimation accuracy especially for heart rate can be achieved compared with single channel systems especially in scenarios where there are pronounced random body-swaying motion that interfere with the respiratory and heartbeat signals. The exploration of this device on monitoring vital sign of human subjects have not been widely published in the literature and this dissertation is one of the first work that investigate the use of this device.

- We propose a novel automatic heartbeat template extraction method based on constellation diagram of the received radar signal to adaptively identify the corrupted signal portions due to random swaying body motion and extract the templates that contain heartbeat signal to magnify its magnitude. The idea of using heartbeat template and matched filtering for magnifying heartbeat signals is not novel. However, the works in the literature require human intervention to extract a heartbeat template which are certainly not practical for real-time operation while our method is completely automatic and does not require human intervention.

- We develop a spectral-based heart rate selection to adaptively search for accurate heart rate based on the spectral characteristics of the wavelet transformed signal to address the interfered random body-swaying motion. Under the strong impact from the random body-swaying motion, the power spectral density of the heartbeat signals can be concealed by the

interferences given that simply picking the highest peak within the frequency spectrum do not guarantee accurate heart rate estimation. While most of the work using MIMO in the literature are not fully taking use of the spatial diversity of the system, our developed spectral-based heart rate selection can be implemented in different widely distributed MIMO devices to improve accuracy of the heart rate estimation.

- Develop and analyze a convolutional neural network (CNN) for channel classification in which channels with low signal-to-noise ratio of heartbeat signals are identified and excluded from the estimating procedure to reduce the error of HR detection. Currently in the literature, deep learning frameworks are mostly applied for single-channel radar which results in the requirement for large amount of data sets for certain tasks. With the advantages of having more information from different radar channels, we are among the first research groups that steers the effort of using deep learning for simpler tasks such as channel classification where there is no need for extensive amounts of data while still improving heart rate estimation's accuracy.

- We also utilize a multi-layer perceptron neural network to reconstruct the heartbeat signals and predict heart rates from subjects under test. While there have been works in the literature that use neural network for heartbeat signals' reconstruction, most of them use single-channel radar which eventually require an extensive amount of data for reconstructing the heartbeat signals, especially under scenarios with moving subjects under test. Our proposed framework addresses the challenge that extensive amount of radar data collected from different subjects do not currently exist, hence by using more information from different MIMO channels and extracted information about our heartbeat template extraction method, we reduce the amount of training data needed while still achieving satisfactory performance for heartbeat signals reconstruction.

8.3 Future Work

Additional work which would be complementary to the work presented here includes:

- Digital beamforming on the receive end so that we can monitor the respiratory rate and heart rate of multiple subjects at the same ranges, which was not done in this work.

- Development of a real-time operating system using this radar device or radar devices with similar antenna configuration so that it can be deployed in multiple places.

- Analysis on the efficiency of CNN for Channel Classification on how it can really help to expedite the overall procedure of estimating HR. While the CNN can help to reduce the number of required channels while maintaining the estimation accuracy, current implementation of preparing the RGB images from phase variation signals to perform classification still requires significant amount of processing time. Therefore, timing analysis and how frequent the trained CNN should be used during the experiment to minimize the overall processing time are necessary, which has not been done in this dissertation.

- Furthermore, research on more complex deep learning frameworks is also required to further improve the accuracy of our classification and prediction task. This will be beneficial for scenarios when SUTs are actively moving during the experiment.

LIST OF PUBLICATIONS

Journals

- **T. K. V. Dai,** Y. Yu, P. Theilmann, A. E. Fathy and O. Kilic, "Remote Vital Sign Monitoring With Reduced Random Body Swaying Motion Using Heartbeat Template and Wavelet Transform Based on Constellation Diagrams," in IEEE Journal of Electromagnetics, RF and Microwaves in Medicine and Biology, doi: 10.1109/JERM.2022.3140900.

- **T. K. V. Dai et al.,** "Enhancement of Remote Vital Sign Monitoring Detection Accuracy Using Multiple-Input Multiple-Output 77 GHz FMCW Radar," in IEEE Journal of Electromagnetics, RF and Microwaves in Medicine and Biology, vol. 6, no. 1, pp. 111-122, March 2022, doi: 10.1109/JERM.2021.3082807.

- **T. K. Vo Dai**, T. Nguyen, and O. Kilic, "A Non-Focal Rotman Lens Design to Support Cylindrically Conformal Array Antenna", ACES Express Journal, 2016, vol. 1, No. 7, pp. 205-208, July 2016.

- **T. K. Vo Dai**, O. Kilic. "Compact Rotman Lens Structure Configurations to Support Millimeter Wave Devices", Progress in Electromagnetics Research B 71 (2016).

- **T. K. Vo Dai**, A. Thai, T. Phan, O. Kilic, and K. Russo, "Construction of an Inexpensive Anechoic Chamber and Its Applications in Undergraduate Research [Education Corner]", IEEE Antennas and Propagation Magazine, 60. 4, (2018): 102-112

- **T. K. Vo Dai**, Ozlem Kilic, and Hang Liu. "Improved Cell Search for mmWave Cellular Networks Using Deterministic Scanning Algorithm with Directional Array Antenna." *Electronics* 6.2 (2017): 42.

- **T. K. Vo Dai**, T. Nguyen, and O. Kilic, "Compact multi-layer microstrip Rotman lens design using coupling slots to support millimetre wave devices", IET Microwave, Antennas and Propagation 12.8 (2018): 1260-1265.

- T. Nguyen, **T. K. Vo Dai** and O. Kilic, "Design of a 360° Scanning Circularly Symmetric Polygon Lens", IEEE Transactions on Antennas and Propagation 66.9 (2018).

Conferences

- **T. K. V. Dai** et al., "Analysis of Signal Processing Methods on the Improvement of Noncontact Vital Sign Estimation using 24/60-GHz FMCW Radar." *2020 IEEE International Symposium on Antennas and Propagation and North American Radio Science Meeting, July 2020.*

- **T. K. Vo Dai**, T. Nguyen, K. Cao, T. Le, O. Kilic, "A Conformal Micro-strip Rotman Lens design using Particle Swarm Optimization (PSO)," U.S. National Committee on International Union of Radio Science (USNC-URSI) Meeting, Boulder, CO, USA, January 2016.

- **T. K. Vo Dai**, O. Kilic and M. Mirotznik "Designing Folded Rotman Lenses" APS-URSI 2016, Fajardo, Puerto Rico, USA, 26 June- 1 July 2016.

- T. Nguyen, **T. K. Vo Dai** and O. Kilic "Rotman Lens-Fed Aperture Coupled Array Antenna at Millimeter Wave", APS-URSI 2016, Fajardo, Puerto Rico, USA, 26 June- 1 July 2016.

- **T. K. Vo Dai**, and O. Kilic "Directional Array for Millimeter-Wave Cellular Networks", U.S. National Committee on International Union of Radio Science (USNC-URSI) Meeting, Boulder, CO, USA, January 2017.

-   **T. K. Vo Dai**, T. Nguyen, and O. Kilic "A Compact Microstrip Rotman Lens Design", U.S. National Committee on International Union of Radio Science (USNC-URSI) Meeting, Boulder, CO, USA, January 2017.

-   **T. K. Vo Dai**, T. Nguyen, and O. Kilic "Compact Antenna System Fed by Dual-layer Rotman Lens to Support Millimeter Wave Devices", APS-URSI 2017, San Diego, California, USA, 8 July- 13 July 2017.

-   **T. K. Vo Dai**, O. Kilic, and H. Liu "Clusters Effect in Urban Environments on Initial Cell Searching Procedure using Directional Array in mmWave Cellular Networks", URSI-GASS 2017, Montreal, Canada, August 19-26, 2017.

-   **T. K. Vo Dai**, O. Kilic, and H. Liu "Low-Cost Anechoic Chamber Construction and its Applications for Educational Purposes", URSI-GASS 2017, Montreal, Canada, August 19-26, 2017.

LIST OF REFERENCES

[1] Snyder, Frederick, et al. "Changes in respiration, heart rate, and systolic blood pressure in human sleep." *Journal of applied physiology* 19.3 (1964): 417-422.

[2] Allataifeh, Areen, and Mahmoud Al Ahmad. "Simultaneous piezoelectric noninvasive detection of multiple vital signs." *Scientific reports* 10.1 (2020): 1-13.

[3] Ojarand, J., et al. "Magnetic induction sensor for the respiration monitoring." *Proc. of 10th Int. Conf. on Bioelectromagnetism (icBEM). Tallinn.* 2015.

[4] Grlica, Josip, Toni Martinović, and Hrvoje Džapo. "Capacitive sensor for respiration monitoring." *2015 IEEE Sensors Applications Symposium (SAS).* IEEE, 2015.

[5] Krehel, Marek, et al. "An optical fibre-based sensor for respiratory monitoring." *Sensors* 14.7 (2014): 13088-13101.

[6] Serhani, Mohamed Adel, et al. "ECG monitoring systems: Review, architecture, processes, and key challenges." *Sensors* 20.6 (2020): 1796.

[7] Kebe, Mamady, et al. "Human vital signs detection methods and potential using radars: A review." *Sensors* 20.5 (2020): 1454.

[8] Castaneda, Denisse, et al. "A review on wearable photoplethysmography sensors and their potential future applications in health care." *International journal of biosensors & bioelectronics* 4.4 (2018): 195.

[9] Money, Eugene W., Roger Caldwell, and Michael Sciarra. "Vital sign remote monitoring device." U.S. Patent No. 5,919,141. 6 Jul. 1999.

[10] Li, Changzhi, et al. "Radar remote monitoring of vital signs." *IEEE Microwave Magazine* 10.1 (2009): 47-56.

[11] Li, Changzhi, et al. "A review on recent advances in Doppler radar sensors for noncontact healthcare monitoring." *IEEE Transactions on microwave theory and techniques* 61.5 (2013): 2046-2060.

[12] Li, Changzhi, and Jenshan Lin. "Random body movement cancellation in Doppler radar vital sign detection." *IEEE Transactions on Microwave Theory and Techniques* 56.12 (2008): 3143-3152.

[13] Banet, Matthew, and Henk Visser. "Wireless, internet-based system for measuring vital signs from a plurality of patients in a hospital or medical clinic." U.S. Patent Application No. 11/162,719.

[14] Genc, Sahika, et al. "Continuous remote vital sign/environment monitoring for returning soldier adjustment assessment." *2011 Annual International Conference of the IEEE Engineering in Medicine and Biology Society*. IEEE, 2011.

[15] Tarassenko, Lionel, et al. "Non-contact video-based vital sign monitoring using ambient light and auto-regressive models." *Physiological measurement* 35.5 (2014): 807.

[16] Bartula, Marek, Timo Tigges, and Jens Muehlsteff. "Camera-based system for contactless monitoring of respiration." *2013 35th Annual International Conference of the IEEE Engineering in Medicine and Biology Society (EMBC)*. IEEE, 2013.

[17] Li, Changzhi, Yanming Xiao, and Jenshan Lin. "Experiment and spectral analysis of a low-power Ka-band heartbeat detector measuring from four sides of a human body." *IEEE Transactions on Microwave Theory and Techniques* 54.12 (2006): 4464-4471.

[18] Vinci, Gabor, et al. "Six-port radar sensor for remote respiration rate and heartbeat vital-sign monitoring." *IEEE Transactions on Microwave Theory and Techniques* 61.5 (2013): 2093-2100.

[19] Naishadham, Krishna, and Jean E. Piou. "A robust state space model for the characterization of extended returns in radar target signatures." *IEEE Transactions on Antennas and Propagation* 56.6 (2008): 1742-1751.

[20] Naishadham, Krishna, et al. "Estimation of cardiopulmonary parameters from ultra-wideband radar measurements using the state space method." *IEEE transactions on biomedical circuits and systems* 10.6 (2016): 1037-1046.

[21] Ren, Lingyun, et al. "Non-invasive detection of cardiac and respiratory rates from stepped frequency continuous wave radar measurements using the state space method." *2015 IEEE MTT-S International Microwave Symposium*. IEEE, 2015.

[22] Tateishi, Naoyuki, et al. "Microwave measurement of heart beat and analysis using wavelet transform." *2007 Asia-Pacific Microwave Conference*. IEEE, 2007.

[23] Tomii, Shoichiro, and Tomoaki Ohtsuki. "Heartbeat detection by using Doppler radar with wavelet transform based on scale factor learning." *2015 IEEE International Conference on Communications (ICC)*. IEEE, 2015.

[24] Mogi, Eriko, and Tomoaki Ohtsuki. "Heartbeat detection with Doppler sensor using adaptive scale factor selection on learning." *2015 IEEE 26th Annual International Symposium on Personal, Indoor, and Mobile Radio Communications (PIMRC)*. IEEE, 2015.

[25] Ahmad, Adeel, et al. "Vital signs monitoring of multiple people using a FMCW millimeter-wave sensor." *2018 IEEE Radar Conference (RadarConf18)*. IEEE, 2018.

[26] Alizadeh, Mostafa, et al. "Remote monitoring of human vital signs using mm-Wave FMCW radar." *IEEE Access* 7 (2019): 54958-54968.

[27] Alizadeh, Mostafa. *Remote vital signs monitoring using a mm-wave FMCW radar*. MS thesis. University of Waterloo, 2019.

[28] Kellen, O. "Vital Sign Detection Using Millimeter Wave Radars." MS Thesis, University of Tennessee, Knoxville, 2020.

[29] Nosrati, Mehrdad, et al. "A concurrent dual-beam phased-array Doppler radar using MIMO beamforming techniques for short-range vital-signs monitoring." *IEEE Transactions on Antennas and Propagation* 67.4 (2019): 2390-2404.

[30] Yuan, Yichao, et al. "Multi-target concurrent vital sign and location detection using metamaterial-integrated self-injection-locked quadrature radar sensor." *IEEE Transactions on Microwave Theory and Techniques* 67.12 (2019): 5429-5437.

[31] Fishler, Eran, et al. "Spatial diversity in radars—Models and detection performance." *IEEE Transactions on signal processing* 54.3 (2006): 823-838.

[32] Fishler, Eran, et al. "Performance of MIMO radar systems: Advantages of angular diversity." *Conference Record of the Thirty-Eighth Asilomar Conference on Signals, Systems and Computers, 2004.*. Vol. 1. IEEE, 2004.

[33] Frankford, Mark T., et al. "Numerical and experimental studies of target detection with MIMO radar." *IEEE Transactions on Aerospace and Electronic systems* 50.2 (2014): 1569-1577.

[34] Su, Wei-Chih, et al. "Human tracking and vital sign monitoring with a switched phased-array self-injection-locked radar." *2020 IEEE/MTT-S International Microwave Symposium (IMS)*. IEEE, 2020.

[35] Walterscheid, Ingo, and Graeme E. Smith. "Respiration and heartbeat monitoring using a distributed pulsed MIMO radar." *2017 39th Annual International Conference of the IEEE Engineering in Medicine and Biology Society (EMBC)*. IEEE, 2017.

[36] Liu, Qiwei, et al. "Non-contact non-invasive heart and respiration rates monitoring with MIMO radar sensing." *2018 IEEE Global Communications Conference (GLOBECOM)*. IEEE, 2018.

[37] Shah, Amit, and Alexander M. Haimovich. "Performance analysis of maximal ratio combining and comparison with optimum combining for mobile radio communications with cochannel interference." *IEEE Transactions on Vehicular Technology* 49.4 (2000): 1454-1463.

[38] Holtzman, M., R. Goubran, and Frank Knoefel. "Maximal ratio combining for respiratory effort extraction from pressure sensor arrays." *2011 IEEE International Symposium on Medical Measurements and Applications*. IEEE, 2011.

[39] Sakamoto, Takuya. "Noncontact Measurement of Human Vital Signs during Sleep Using Low-power Millimeter-wave Ultrawideband MIMO Array Radar." *2019 IEEE MTT-S International Microwave Biomedical Conference (IMBioC)*. Vol. 1. IEEE, 2019.

[40] Sakamoto, Takuya, and Kosuke Yamashita. "Noncontact Measurement of Autonomic Nervous System Activities Based on Heart Rate Variability Using Ultra-Wideband Array Radar." *IEEE Journal of Electromagnetics, RF and Microwaves in Medicine and Biology* (2019).

[41] Vodai, Toan Khanh, et al. "Enhancement of remote vital sign monitoring detection accuracy using multiple-input multiple-output 77 GHz FMCW radar." *IEEE Journal of Electromagnetics, RF and Microwaves in Medicine and Biology* (2021).

[42] I. Mostafanezhad, O. Boric-Lubecke, V. Lubecke and A. Host-Madsen, "Cancellation of unwanted motion in a handheld Doppler radar used for non-contact life sign monitoring," *2008 IEEE MTT-S International Microwave Symposium Digest*, 2008, pp. 1171-1174, doi: 10.1109/MWSYM.2008.4633266.

[43] I. Mostafanezhad, O. Boric-Lubecke, V. Lubecke and D. P. Mandic, "Application of empirical mode decomposition in removing fidgeting interference in doppler radar life signs monitoring devices," *2009 Annual International Conference of the IEEE Engineering in Medicine and Biology Society*, 2009, pp. 340-343, doi: 10.1109/IEMBS.2009.5333206.

[44] F. Wang, T. Horng, K. Peng, J. Jau, J. Li and C. Chen, "Single-Antenna Doppler Radars Using Self and Mutual Injection Locking for Vital Sign Detection With Random Body Movement Cancellation," in *IEEE Transactions on Microwave Theory and Techniques*, vol. 59, no. 12, pp. 3577-3587, Dec. 2011, doi: 10.1109/TMTT.2011.2171712.

[45] Mu-Cyun Tang, Chao-Yun Kuo, Da-Cian Wun, F. -K. Wang and T. -S. Horng, "Same side dual SIL-radar system for real-time vital sign monitoring with random body movement cancellation," *2016 IEEE MTT-S International Microwave Symposium (IMS)*, 2016, pp. 1-4, doi: 10.1109/MWSYM.2016.7540003.

[46] M. Tang, C. Kuo, D. Wun, F. Wang and T. Horng, "A Self- and Mutually Injection-Locked Radar System for Monitoring Vital Signs in Real Time With Random Body Movement Cancellation," in *IEEE Transactions on Microwave Theory and Techniques*, vol. 64, no. 12, pp. 4812-4822, Dec. 2016, doi: 10.1109/TMTT.2016.2623612.

[47] R. Fletcher and Jing Han, "Low-cost differential front-end for Doppler radar vital sign monitoring," *2009 IEEE MTT-S International Microwave Symposium Digest*, 2009, pp. 1325-1328, doi: 10.1109/MWSYM.2009.5165949.

[48] Y. Rong, A. Dutta, A. Chiriyath, D.W.Bliss, "Motion-Tolerant Non-Contact Heart-Rate Measurements from Radar Sensor Fusion," in *Sensors (Basel)*. 2021 Mar 4;21(5):1774. doi: 10.3390/s21051774. PMID: 33806426; PMCID: PMC7961631.

[49] X. Yu, C. Li and J. Lin, "Two-dimensional noncontact vital sign detection using Doppler radar array approach," *2011 IEEE MTT-S International Microwave Symposium*, 2011, pp. 1-4, doi: 10.1109/MWSYM.2011.5972723.

[50] C. Gu, G. Wang, T. Inoue and C. Li, "Doppler radar vital sign detection with random body movement cancellation based on adaptive phase compensation," *2013 IEEE MTT-S International Microwave Symposium Digest (MTT)*, 2013, pp. 1-3, doi: 10.1109/MWSYM.2013.6697618.

[51] C. Gu, G. Wang, Y. Li, T. Inoue and C. Li, "A Hybrid Radar-Camera Sensing System With Phase Compensation for Random Body Movement Cancellation in Doppler Vital Sign Detection," in *IEEE Transactions on Microwave Theory and Techniques*, vol. 61, no. 12, pp. 4678-4688, Dec. 2013, doi: 10.1109/TMTT.2013.2288226.

[52] C. Gu, J. Wang and J. Lien, "Deep Neural Network based Body Movement Cancellation for Doppler Radar Vital Sign Detection," *2019 IEEE MTT-S International Wireless Symposium (IWS)*, 2019, pp. 1-3, doi: 10.1109/IEEE-IWS.2019.8803973.

[53] Q. Lv *et al.*, "Doppler Vital Signs Detection in the Presence of Large-Scale Random Body Movements," in *IEEE Transactions on Microwave Theory and Techniques*, vol. 66, no. 9, pp. 4261-4270, Sept. 2018, doi: 10.1109/TMTT.2018.2852625.

[54] Kuo, Hsin-Chih, et al. "A 60-GHz CMOS direct-conversion Doppler radar RF sensor with clutter canceller for single-antenna noncontact human vital-signs detection." *2015 IEEE Radio Frequency Integrated Circuits Symposium (RFIC)*. IEEE, 2015.

[55] Chan, Kevin Khee-Meng, Adrian Eng-Choon Tan, and Karumudi Rambabu. "Circularly polarized ultra-wideband radar system for vital signs monitoring." *IEEE Transactions on microwave theory and techniques* 61.5 (2013): 2069-2075.

[56] Ren, Lingyun, et al. "Phase-based methods for heart rate detection using UWB impulse Doppler radar." *IEEE Transactions on Microwave Theory and Techniques* 64.10 (2016): 3319-3331.

[57] Dang, Vinh Quang. *Detection and Tracking of Moving Targets Behind Cluttered Environments Using Compressive Sensing*. 2015.

[58] Peng, Zhengyu, et al. "A portable FMCW interferometry radar with programmable low-IF architecture for localization, ISAR imaging, and vital sign tracking." *IEEE transactions on microwave theory and techniques* 65.4 (2016): 1334-1344.

[59] Fishler, Eran, et al. "MIMO radar: An idea whose time has come." *Proceedings of the 2004 IEEE Radar Conference (IEEE Cat. No. 04CH37509)*. IEEE, 2004.

[60] White, Langford B., and Pinaki S. Ray. "Receiver design for MIMO tracking radar." *2004 International Waveform Diversity & Design Conference*. IEEE, 2004.

[61] Hefnawi, Mostafa, et al. "MIMO radar using a vector network analyzer." *Electronics* 8.12 (2019): 1447.

[62] Bliss, D. W., and K. W. Forsythe. "Multiple-input multiple-output (MIMO) radar and imaging: degrees of freedom and resolution." *The Thrity-Seventh Asilomar Conference on Signals, Systems & Computers, 2003*. Vol. 1. IEEE, 2003.

[63] Texas Instruments, "Application Report – SWRA554A – MIMO Radar," *Revised July 2018*

[64] Texas Instruments, "Application Report – SWR553A – AWRx Cascaded Radar RF Evaluation Module (MMWCAS-RF-EVM)," *Revised February 2020.*

[65] Texas Instruments, "Application Report – SWRA553A – Programming Chirp Parameters in TI Radar Devices," *Revised February 2020.*

[66] Albanese, Antonio, et al. "An integrated mathematical model of the human cardiopulmonary system: model development." *American Journal of Physiology-Heart and Circulatory Physiology* 310.7 (2016): H899-H921.

[67] Petrović, Vladimir L., et al. "High-accuracy real-time monitoring of heart rate variability using 24 GHz continuous-wave Doppler radar." *IEEE Access* 7 (2019): 74721-74733.

[68] Nam, K. "Direct down-conversion system with I/Q correction." *Texas Instruments, http://www. ti. com/lit/ug/slwu085/slwu085. pdf*.

[69] Singh, Aditya, et al. "Data-based quadrature imbalance compensation for a CW Doppler radar system." *IEEE Transactions on Microwave Theory and Techniques* 61.4 (2013): 1718-1724.

[70] Rong, Yu. *Remote sensing for vital signs monitoring using advanced radar signal processing techniques*. Diss. Arizona State University, 2018.

[71] Will, Christoph, et al. "Advanced template matching algorithm for instantaneous heartbeat detection using continuous wave radar systems." *2017 First IEEE MTT-S International Microwave Bio Conference (IMBIOC)*. IEEE, 2017.

[72] Sakamoto, Takuya, et al. "Feature-based correlation and topological similarity for interbeat interval estimation using ultrawideband radar." *IEEE Transactions on Biomedical Engineering* 63.4 (2015): 747-757.

[73] Yang, Zi-Kai, et al. "Accurate Doppler radar-based heart rate measurement using matched filter." *IEICE Electronics Express* 17.8 (2020): 20200062-20200062.

[74] Mallat, Stéphane. *A wavelet tour of signal processing*. Elsevier, 1999.

[75] Shcherbina, Anna, et al. "Accuracy in wrist-worn, sensor-based measurements of heart rate and energy expenditure in a diverse cohort." *Journal of personalized medicine* 7.2 (2017): 3.

[76] Rosenberger, Mary E., et al. "24 hours of sleep, sedentary behavior, and physical activity with nine wearable devices." *Medicine and science in sports and exercise* 48.3 (2016): 457.

[77] Schellenberger, Sven, et al. "A dataset of clinically recorded radar vital signs with synchronized reference sensor signals." *Scientific data* 7.1 (2020): 1-11.

[78] Chen, Zhe, et al. "MoVi-Fi: motion-robust vital signs waveform recovery via deep interpreted RF sensing." *Proceedings of the 27th Annual International Conference on Mobile Computing and Networking*. 2021.

[79] Chen, Jinbo, et al. "Contactless Electrocardiogram Monitoring with Millimeter Wave Radar." *arXiv preprint arXiv:2112.06639* (2021).

[80] Gong, Jian, et al. "RF Vital Sign Sensing under Free Body Movement." *Proceedings of the ACM on Interactive, Mobile, Wearable and Ubiquitous Technologies* 5.3 (2021): 1-22.

[81] Malešević, Nebojša, et al. "Contactless real-time heartbeat detection via 24 GHz continuous-wave Doppler radar using artificial neural networks." *Sensors* 20.8 (2020): 2351.

[82] Saluja, Justin, Joaquin Casanova, and Jenshan Lin. "A supervised machine learning algorithm for heart-rate detection using Doppler motion-sensing radar." *IEEE Journal of Electromagnetics, RF and Microwaves in Medicine and Biology* 4.1 (2019): 45-51.

[83] Toda, Daiki, et al. "ECG Signal Reconstruction Using FMCW Radar and Convolutional Neural Network." *2021 20th International Symposium on Communications and Information Technologies (ISCIT)*. IEEE, 2021.

[84] Wang, Pengfei, et al. "Noncontact heart rate measurement based on an improved convolutional sparse coding method using IR-UWB radar." *IEEE Access* 7 (2019): 158492-158502.

[85] Wu, Shuqiong, et al. "Person-specific heart rate estimation with ultra-wideband radar using convolutional neural networks." *IEEE Access* 7 (2019): 168484-168494.

[86] Yamamoto, Kohei, and Tomoaki Ohtsuki. "Non-Contact Heartbeat Detection by Heartbeat Signal Reconstruction Based on Spectrogram Analysis With Convolutional LSTM." *IEEE Access* 8 (2020): 123603-123613.

[87] Yamamoto, Kohei, Ryosuke Hiromatsu, and Tomoaki Ohtsuki. "ECG signal reconstruction via doppler sensor by hybrid deep learning model with CNN and LSTM." *Ieee access* 8 (2020): 130551-130560.

[88] Yang, Xiuzhu, et al. "Indoor Activity and Vital Sign Monitoring for Moving People with Multiple Radar Data Fusion." *Remote Sensing* 13.18 (2021): 3791.

[89] Ye, Chen, Guan Gui, and Tomoaki Ohtsuki. "Deep clustering with lstm for vital signs separation in contact-free heart rate estimation." *ICC 2020-2020 IEEE International Conference on Communications (ICC)*. IEEE, 2020.

[90] Yin, Wenfeng, et al. "ECG monitoring system integrated with IR-UWB radar based on CNN." *IEEE Access* 4 (2016): 6344-6351.

[91] Nanni, Loris, Stefano Ghidoni, and Sheryl Brahnam. "Handcrafted vs. non-handcrafted features for computer vision classification." *Pattern Recognition* 71 (2017): 158-172.

[92] Khan, Salman, et al. "A guide to convolutional neural networks for computer vision." *Synthesis Lectures on Computer Vision* 8.1 (2018): 1-207.

[93] Hershey, Shawn, et al. "CNN architectures for large-scale audio classification." *2017 ieee international conference on acoustics, speech and signal processing (icassp)*. IEEE, 2017.

[94] Kwon, Soonil. "A CNN-assisted enhanced audio signal processing for speech emotion recognition." *Sensors* 20.1 (2019): 183.

[95] Hermawan, Ade Pitra, et al. "CNN-based automatic modulation classification for beyond 5G communications." *IEEE Communications Letters* 24.5 (2020): 1038-1041.

[96] Zheng, Shilian, et al. "Fusion methods for CNN-based automatic modulation classification." *IEEE Access* 7 (2019): 66496-66504.

[97] Esteva, Andre, et al. "Dermatologist-level classification of skin cancer with deep neural networks." *nature* 542.7639 (2017): 115-118.

[98] Nagabushanam, Perattur, S. Thomas George, and Subramanyam Radha. "EEG signal classification using LSTM and improved neural network algorithms." *Soft Computing* 24.13 (2020): 9981-10003.

[99] Deng, Shumin, et al. "Knowledge-driven stock trend prediction and explanation via temporal convolutional network." *Companion Proceedings of The 2019 World Wide Web Conference*. 2019.

[100] Chauhan, Sucheta, and Lovekesh Vig. "Anomaly detection in ECG time signals via deep long short-term memory networks." *2015 IEEE International Conference on Data Science and Advanced Analytics (DSAA)*. IEEE, 2015.

[101] Hossin, Mohammad, and Md Nasir Sulaiman. "A review on evaluation metrics for data classification evaluations." *International journal of data mining & knowledge management process* 5.2 (2015): 1.

VITA

Toan K. Vo Dai was born and grew up in Da Nang, Viet Nam. He received his B.Sc. degree in Electrical Engineering from The Catholic University of America in 2015. He joined the University of Tennessee, Knoxville in 2019 to continue his education towards Ph.D. degree in Electrical Engineering. His interests are vast and ever changing but his primary focus at the moment is on Microwave Radar/Digital Signal Processing for Remote Sensing Applications.